Electronic spectroscopy of small carbocations

Giel Muller

Orcid 0000-0003-1173-6825

This thesis is submitted in total fulfillment of the requirements of the degree of

Doctor of Philosophy

March 2021

School of Chemistry
University of Melbourne

Dedicated to Truus, Ben, Loes, Daan, Allie, Max, and Daniel Lucas Muller.

Abstract

This work focuses on the measurement and analysis of gas-phase electronic spectra of $C_4H_2^+$, $C_4H_4^+$, $C_4H_5^+$, and $C_6H_4^+$ cations. The spectra are recorded by photodissociating the cations, or their messenger tagged complexes, in a tandem mass spectrometer and monitoring the photofragment signal as a function of laser wavelength. Ultimately, structural and energetic information extracted from these spectra, complemented by quantum chemical calculations, may provide insights into the roles of cations in the chemistry of flames, plasmas, and extraterrestrial environments. Understanding the vibronic structures of the cations is also fundamental for facilitating their possible detection in remote environments.

Electronic spectra of $C_4H_2^+$-Ar_n (n = 1-3) and $C_4H_2^+$-$(N_2)_n$ (n = 1-2) complexes are recorded over the 290-530 nm range by monitoring $C_4H_2^+$ photofragments. Intense narrow bands in the visible region arise from the $\tilde{A}^2\Pi_u \leftarrow \tilde{X}^2\Pi_g$ electronic transition of the diacetylene cation, HC_4H^+. Vibronic transitions are compared with previous results and theoretical predictions for the $\tilde{A}^2\Pi_u \leftarrow \tilde{X}^2\Pi_g$ band system based on calculations at the CCSD/cc-pCVTZ and EOM-CCSD/cc-pCVTZ levels of theory. Hole burning experiments confirm that the weak, broad bands in the ultraviolet region also correspond to excitations of HC_4H^+. These bands are assigned to the $2^2\Pi_u \leftarrow \tilde{X}^2\Pi_g$ electronic transition based on calculated energies and oscillator strengths, previous experiments, and spectra of isoelectronic molecules. The origin transition is observed at 29723 cm^{-1} (336.44 nm) for HC_4H^+-Ar, followed by a progression in the symmetric C-C stretch vibration, spaced by 906 cm^{-1}. Spectral congestion observed toward shorter wavelengths is possibly due to the presence of close-lying electronic states, vibronic coupling effects, and HC_4H^+ being bent in the $2^2\Pi_u$ electronic state.

Electronic spectra of Ar- and N_2-tagged $C_4H_4^+$ cations, generated from acetylene ion-molecule reactions, are recorded over the 296-550 nm range by monitoring $C_4H_4^+$ and $C_4H_3^+$ / $C_4H_2^+$ photofragments. The spectra exhibit a clearly resolved band system commencing at 511 nm, a set of weak bands around 410 nm, and an intense broad band in the UV. Band assignments are based on previous spectroscopic studies and calculations for the four lowest energy $C_4H_4^+$ isomers. The visible region of the spectrum is dominated

by the $\tilde{B}^2A''\leftarrow\tilde{X}^2A''$ electronic transition of the vinylacetylene cation (**VA**$^+$) whose origin transition occurs 19558 cm^{-1} (511.30 nm) for **VA**$^+$-Ar and at 19551 cm^{-1} (511.48 nm) for **VA**$^+$-N_2. The spectrum features a strong progression in the central C-C stretching vibration spaced by $\approx$ 806 cm^{-1} and well defined vibronic transitions associated with two bending vibrational modes. The weaker 410 nm system is assigned to the $\tilde{D}^2B_3\leftarrow\tilde{X}^2B_2$ electronic transition of the butatriene cation (**BT**$^+$). Two broad bands, following the origin transition at 24399 cm^{-1} (409.85 nm) in the $C_4H_4^+$-Ar spectrum, arise from excitation of a symmetric C=C stretching vibration and possibly the CH_2 twisting vibration. The observation of $C_4H_4^+$ and $C_4H_3^+$ / $C_4H_2^+$ photofragments following excitation of **BT**$^+$-Ar complexes over the 380-410 nm range accords with calculated dissociation pathways on the ground state $C_4H_4^+$ potential energy surface. The broad band appearing at wavelengths below 320 nm is predicted to be due to electronic transitions of all four of the lowest energy $C_4H_4^+$ isomers, including the **VA**$^+$ and **BT**$^+$ cations.

The $\tilde{B}^2A'\leftarrow\tilde{X}^2A'$ electronic spectrum of the 1-butyn-3-yl cation ($H_3CCHCCH^+$) is recorded over the 245-285 nm range by photodissociating the bare cation and its Ne- and Ar-tagged complexes. Origin transitions for $H_3CCHCCH^+$ and $H_3CCHCCH^+$-Ne are observed at 35936 cm^{-1} (278.27 nm) and 35930 cm^{-1} (278.32 nm), respectively. Additional bands in the spectra are assigned to vibronic transitions of $H_3CCHCCH^+$ through quantum chemical calculations and comparison of the spectra with those of similar molecules, the propargyl ($C_3H_3^+$) and methyl propargyl ($H_3C_4H_2^+$) cations. Excitation of $H_3CCHCCH^+$ produces $C_2H_3^+ + C_2H_2$ (protonated acetylene + acetylene) and $C_4H_3^+ + H_2$ (protonated diacetylene + hydrogen molecule) photofragments. The preferred formation of $C_2H_3^+ + C_2H_2$ photofragments is correctly predicted by master equation simulations, generated from calculated dissociation pathways on the ground state $C_4H_5^+$ potential energy surface.

Electronic spectra of Ar- and N_2-tagged $C_6H_4^+$ cations, generated from acetylene ion-molecule reactions, are recorded over the 265-700 nm range by monitoring $C_6H_4^+$ and $C_4H_2^+$ photofragments. Bands are assigned to transitions of five isomers based on previous spectroscopic studies, calculated stationary points on the ground state $C_6H_4^+$ potential energy surface, hole burning experiments, and spectral simulations generated from TD-DFT calculations. In the $C_6H_4^+$-Ar spectrum, bands over the 526-700 nm range arise from the $\tilde{B}^2A'' \leftarrow \tilde{X}^2A''$ electronic transition of the 1-hexene-1,3-diyne cation ($CH_2CHCCCCH^+$) and the $\tilde{C}^2B_g \leftarrow \tilde{X}^2A_u$ electronic transition of the *trans*-3-hexene-1,5-diyne cation ($HCCCHCHCCH^+$), with origin transitions occurring at 604 and 581 nm, respectively. Over the 375-460 nm range, broad bands at 440, 425, and 423 nm are assigned to vibronic transitions within the $\tilde{C}^2A'' \leftarrow \tilde{X}^2A''$ band system of the 1-ethynyl-3-methylene-cyclopropa-1,2-diene cation ($H_2C[c-C_3H]CCH^+$).

Sharper bands at 416, 407, and 400 nm are ascribed to the $\tilde{B}^2A'' \leftarrow \tilde{X}^2A''$ electronic transition of the propargyl cyclopropene cation ($[c-C_3H_2]CHCCH^+$). Between 265 and 375 nm, several bands appear, superimposed on a broad band that extends for several thousand wavenumbers. The 371 nm band is assigned to the $\tilde{B}^2A'' \leftarrow \tilde{X}^2A''$ origin transition of the 1-hexene-1,3-diyne cation ($CH_2CHCCCCH^+$), agreeing with previous assignments. In light of the TD-DFT calculations, the bands at 365 and 357 nm are tentatively reassigned to the $\tilde{C}^2B \leftarrow \tilde{X}^2B$ electronic transition of the propadienylidene cyclopropene ($[c-C_3H_2]CCCH_2{}^+$) isomer. The underlying band possibly arises from the $\tilde{C}^2B_g \leftarrow \tilde{X}^2A_u$ electronic transition of the *trans*-3-hexene-1,5-diyne ($HCCCHCHCCH^+$) cation, which undergoes a reduction in symmetry upon photoexcitation. Formation of $C_4H_2{}^+$ photofragments at wavelengths below 426 nm (2.91 eV) agrees with calculated $C_6H_4{}^+$ dissociation pathways on the ground state $C_6H_4{}^+$ potential energy surface.

Declaration

I hereby declare that:
(i) this thesis comprises only my original work towards the PhD except where indicated in the preface;

(ii) due acknowledgement has been made in the text to all other material used; and

(iii) this thesis is fewer than 100,000 words, exclusive of tables, maps, bibliographies and appendices.

Giel Muller
Orcid 0000-0003-1173-6825
March 2021

Preface

Spectroscopic studies presented in this work have been, or will be, published in peer-reviewed journals. A full list of publications is provided below. Studies of the $C_4H_2^+$ and $C_4H_5^+$ cations, published in the Journal of Physical Chemistry A, are reproduced in this document as Chapters 3 and 5, respectively, with permission. Minor changes were made to these articles to improve readability. In particular, the numbers for figures, tables, and references were adjusted to match their positions in this work. Ions labeled [0] and [1] in Figure 5.6 were relabeled **BT** and **MP**, respectively. Original copies of the publications are provided in the Appendix (page 209). Supporting information, originally published with the main articles, are included at the ends of Chapters 3 and 5.

Chapter 1 features 7 non-original images that are used with permission from the relevant third parties. Citation information for this material is provided in Table 1.

This research was conducted with the support of Australian Research Council's Discovery Project funding scheme (Project Numbers DP150101427 and DP160100474) and the Australian Government Research Training Program Scholarships (formerly the International Postgraduate Research Scholarship and Australian Postgraduate Award) which include stipend and fee offsets.

The following individuals are acknowledged for their invaluable contributions to the work presented in this thesis:
Katherine J. Catani, for sharing her expertise of the tandem mass spectrometer, her meticulous scrutiny/editing of drafts and figures, and her valuable advice for all projects in this work. Michael S. Scholz for calculating one-dimensional potential energy curves for HC_4H^+. Ugo Jacovella for discussions that helped understand possible Renner-Teller effects for HC_4H^+ and vibronic transitions of $C_4H_4^+$ and $C_4H_5^+$ cations. Nastasia I. Bartlett for helping conduct spectroscopic measurements of HC_4H^+. Gabriel da Silva for modeling branching ratios of $C_4H_5^+$ and providing invaluable insights into dissociation processes.

List of Publications

- G. Muller, U. Jacovella, K. J. Catani, G. da Silva, E. J. Bieske, "The Electronic Spectrum and Photodissociation Chemistry of the 1-butyn-3-yl cation, $H_3CCHCCH^+$" *Journal of Physical Chemistry A*, **124**, 2366-2371, 2020.
- G. Muller, K. J. Catani, M. S. Scholz, U. Jacovella, N. I. Bartlett, E.J. Bieske, "Electronic Spectra of Diacetylene Cations (HC_4H^+) Tagged with Ar and N_2" *Journal of Physical Chemistry A*, **123 (33)**, 7228-7236, 2019.

Additional publications produced during my PhD candidature that are not discussed in this thesis:

- G. Muller, G. Pullen, G. Sun, "Session Viewpoints on the 2019 International Symposium on Free Radicals Conference" *Journal of Physical Chemistry A*, **124 (3)**, 465-471, 2020.
- U. Jacovella, G. Muller, K. J. Catani, N. I. Bartlett, E. J. Bieske, "Electronic Spectra of the Triacetylene Cation (HC_6H^+) and Protonated Triacetylene ($HC_6H_2^+$) Tagged with Ar" *Australian Journal of Chemistry*, **72 (4)**, 260, 2018.
- K. J. Catani, G. Muller, P. Jusko, P. Theulé, E. J. Bieske, C. Jouvet, "Electronic Spectrum of the Protonated Diacetylene Cation $H_2C_4H^+$" *The Journal of Chemical Physics*, **147**, 084302, 2017.
- K. J. Catani, G. Muller, G. da Silva, E. J. Bieske, "Electronic Spectrum and Photodissociation Chemistry of the Linear Methyl Propargyl Cation $H_2C_4H_3^+$" *The Journal of Chemical Physics*, **176**, 044307, 2017.
- M. Winfough, K. Voronova, G. Muller, G. Laguisma, B. Sztáray, A. Bodi, G. Meloni, "Furfural: The Unimolecular Dissociative Photoionization Mechanism of the Simplest Furanic Aldehyde" *The Journal of Physical Chemistry A*, **121**, 3401, 2017.

Table 1 Third party copyright material used in this thesis.

citation information	location of item in thesis	permission granted (Y/N)
Hubble Space Telescope image of NGC 3603, NASA Goddard Center for Astrobiology, https://astrobiology.gsfc.nasa.gov/images/NGC3603.png.	Fig. 1.1, page 2	Y
Synthetic observations of star formation and the interstellar medium by T. J. Haworth and others in New Astronomy Reviews vol. 82. License 4751120554043 provided by Elsevier.	Fig. 1.2, page 4	Y
Recent progress in astrochemistry by B. E. Turner in Space Science Reviews vol. 51 (3). License 4767311157041 issued by Springer Nature.	Fig. 1.3, page 5	Y
Chemical reactions leading to the formation of Titan's haze, the European Space Agency ATG Medialab, https://sci.esa.int/s/WEqqJvW. Authorized for use in this thesis by the European Space Agency, reference 20191220-00341.	Fig. 1.4, page 6	Y
Hubble's scientific instruments analyze different types of light ranging from ultraviolet (UV) to infrared (IR), NASA's Goddard Space Flight Center, https://www.nasa.gov/mission_pages/hubble/observatory	Fig. 1.5, page 9	Y
A study on the unimolecular decomposition of the $(C_2H_2)_3$ complex by Y. Ono and C. Y. Ng in the Journal of the American Chemical Society vol. 104 (18). Copyright 1982 American Chemical Society.	Fig. 1.7, page 11	Y
The C_4H_4 potential energy surface. 3. The reaction of acetylene with its cation by V. Hrouda and others in the Journal of Physical Chemistry A vol. 101. Copyright 1997 American Chemical Society.	Fig. 1.9, page 14	Y

Acknowledgements

Infinitesimal yet significant.
We wield the power to probe the cosmos
and take glimpses into times well before our own inception.
Perhaps to no better end than to understand the beginning.

I am grateful for the opportunity to have carried out this research with a grand sense of purpose and childlike wonder. Thank you to the University of Melbourne, the Australian Research Council, and the Commonwealth Department of Education & Training for recognizing the value of this research and providing funding and scholarships that made it possible.

The journey has been equally long and arduous as it has been fleeting and joyful. The four studies presented in this work are products of an environment where scientific rigor and innovation were balanced by valuable personal relationships, which have reminded me that, above all – we're human.

I begin by expressing my deepest appreciation for Professor Evan Bieske. Thank you for your friendship, encouragement, wisdom, and patience over the past several years. Your high standards have led me to develop a new understanding of my potential.

Gabriel da Silva, thank you for helping me see chemistry through a different lens, often with a perspective that clarifies the bigger picture. Your collaboration and mentorship were key to the success of my research.

Katherine J. Catani, you have been a staple of my academic life at the University of Melbourne even prior to my arrival. In many ways, you have been a mentor to me and have significantly contributed to my growth as a scientist. Thank you for being an emotional anchor for me, particularly when the tides were unpredictable.

Ugo Jacovella, your arrival at UniMelb brought fine understanding of quantum mechanics and small hydrocarbons. Fittingly, it was accompanied by a fiery personality with bottomless energy and passion – that provided much of the fuel for the research we've accomplished together. Thank you for being one of my greatest advocates.

Michael S. Scholz, thank you for the incredible advice and camaraderie over the years. You, along with other former members of the spectroscopy group, have blazed the trail for me.

To the rest of the laser spectroscopy group, notably Nastasia I. Bartlett, your invaluable contributions and friendship have helped shape me to be the young researcher I am today. You are deeply appreciated.

to my family

To Mom, Dad, Daan, Loes, Allie, and uncle Michael, you are my rock and my best friends. You are there at every step along the way. Thank you for your undying support and inspiration.

Finally, to my wonderful husband, Daniel Lucas, this work would not be possible without you by my side. The gratitude I have for you cannot be adequately expressed here; for once, I'm speechless.

Table of contents

List of figures

List of tables

Chapter 1

Introduction

This thesis details spectroscopic studies of cold, small carbocations – particularly those which can be generated through ion-molecule reactions involving acetylene. The first section provides a general description of how hydrocarbons can be formed and how they shape our universe. It briefly introduces how spectroscopy is used to study the composition of extraterrestrial environments and emphasizes the need for robust databases of laboratory spectra of known molecules. Finally, the chapter outlines the motivation to measure and study the electronic spectra of $C_4H_2^+$, $C_4H_4^+$, $C_4H_5^+$, and $C_6H_4^+$ ions generated from ion-molecule reactions involving acetylene. Chapter 2 describes basic concepts related to resonance-enhanced photodissociation (REPD) spectroscopy and the experimental and computational approaches used to produce this body of work. The following four chapters (3-6) are comprised of the spectroscopic studies of $C_4H_2^+$, $C_4H_4^+$, $C_4H_5^+$, and $C_6H_4^+$ ions.

1.1 Motivation to study hydrocarbons

Hydrocarbons are abundant on Earth, where they are involved in combustion,[1,2] atmospheric,[3,4] and plasma[5–7] reactions. They also exist in extraterrestrial environments such as circumstellar envelopes,[8–10] protoplanetary nebulae,[11,12] comets,[13] planetary atmospheres,[14–16] and molecular clouds.[17–21] The prevalence of hydrocarbons throughout the universe suggests they play important roles in its evolution, and that a better understanding of hydrocarbon reactions in specific environments would help inform the formation and destruction of molecular clouds, stars, planets, moons – and even life. This section describes how hydrocarbons are involved in the stellar life cycle, depicted in Figure 1.1, and where they are likely to exist.

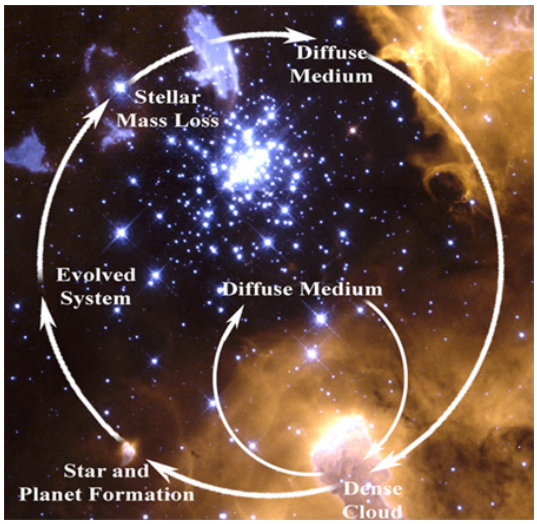

Fig. 1.1 The cyclic process of star formation and destruction. Reprinted with permission from NASA Goddard Center for Astrobiology (GCA).

1.1.1 Importance of hydrocarbons

A general description of the stellar life cycle, as it relates to hydrocarbons, is provided here. The cycle was initiated shortly after the birth of the universe ≈ 13.8 billion years ago when tiny, hot particles reacted with energy and light in an event coined "the Big Bang." Tremendous amounts of energy and particles were expelled from the center, with residual cosmic microwave background (CMB) radiation still observable today.[22,23] The young universe was comprised mostly of ionized plasma. As the universe inflated and cooled, gases rich in H atoms condensed to form molecular clouds. Because some locations in clouds possessed more energy than others, there were pockets of gas molecules known as "cores" that were more dense than the surrounding gases. These cores continued to increase in density until they imploded to form protostars. Toward the outer regions of a protostar core, gas molecules had sufficient angular momentum to overcome the gravitational forces dragging them toward the center. This resulted in a thin disk orbiting the core. On occasion, stellar winds ejected gases from the disk into the cold interstellar medium (ISM), giving rise to both diffuse and dense molecular clouds – the latter of which can birth new stars.[24]

The formation of atoms larger than hydrogen was made possible through the collapse of a protostar core under strong gravitational force. The star, through proton-proton thermonuclear fusion, released radiation, heat, and helium atoms into the ISM. The presence of heavier helium atoms in star-forming regions opened new fusion pathways, such that younger stars in the universe, once having burned through their supply of hydrogen, can fuse three helium

atoms together to generate carbon through the so-called "triple-alpha" process.[25] It is through this process, as well as through supernova explosions, that hydrogen and carbon atoms are among the most abundant in the universe, facilitating formation of hydrocarbons in various environments including molecular clouds that can spawn new stars.

In addition to their relevance to stellar destruction and formation, hydrocarbons are involved in the formation of moons, asteroids, comets, Pluto, and the gas planets.[26–32,32,33] When gas molecules in a protostar disk interact with small dust grains to form planetesimals, the gravitational pull of the object on the surrounding gases become stronger, increasing the probability that the object will develop an atmosphere. Identifying which molecules comprise atmospheres of other planets, moons, and comets is useful to determine how the respective object was formed.[34,35]

One planetary body has gained significant attention, in part due to the hydrocarbon chemistry occurring on its surface and in its atmosphere.[36,37] Titan, a moon of Saturn, is the only planetary object in the solar system (aside from Earth) with liquid lakes and a dense atmosphere. Geochemical data suggest that Titan is similar to Archaen Earth, therefore an understanding of its chemical makeup can provide insight into Earth's past and possibly the emergence of life.[38,39]

1.1.2 Hydrocarbon chemistry in extraterrestrial environments

Hydrocarbon formation in remote environments can occur through different mechanisms, depending on the temperature and density of the environment. In HII regions of stars (see Figure 1.2), where the temperature and density of ionized gas (mostly H^+) and electrons are high, the strong ionizing photon flux heats the gaseous mix to produce high temperature ionic and neutral molecules similar to those formed in combustion reactions.[40] One of the most accepted mechanisms for hydrocarbon growth reactions occurring in circumstellar outflows is the H-abstraction-C_2H_2-addition (HACA) mechanism.[3,4,10,41,42] Molecules and ions escaping this portion of the circumstellar orbit are eventually ejected into the ISM, or, in the case of late-stage red giants, the mass loss may ionize and envelop to form a planetary nebula.[43]

Hydrocarbon formation and growth in cold environments, such as molecular clouds (10-100 K)[40] and the atmosphere of Titan ($\approx$ 90 K),[44] are induced by absorption of UV radiation.[40] In diffuse molecular clouds, which have gas densities of 100 cm^3 or less, hydrocarbon formation is likely to be initiated through the reaction between C^+ and H_2, based on the lower ionization potential of C compared to that of H_2:[45–47]

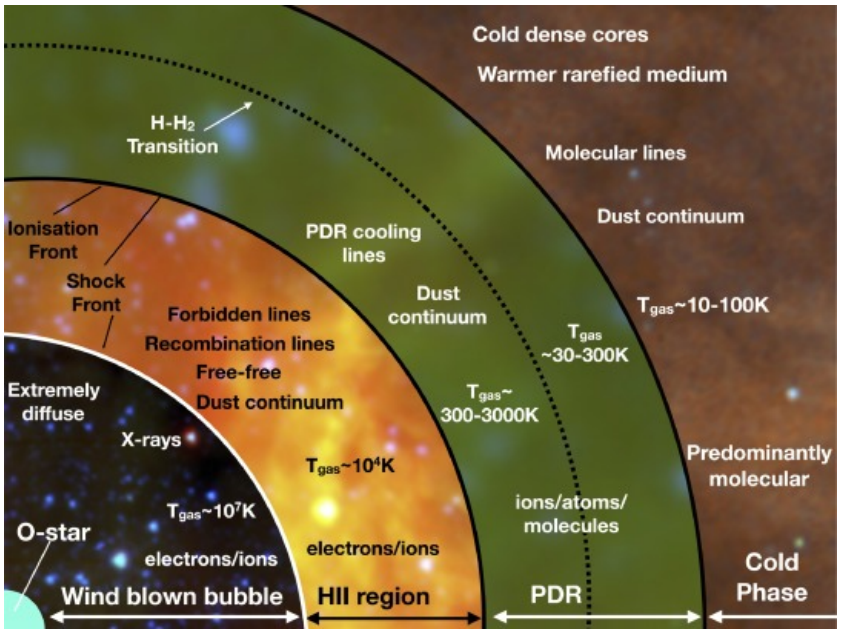

Fig. 1.2 Regions around a star in which different reactions occur. Reprinted with permission from ref. 40. Copyright Elsevier 2018.

$$C^+ + H_2 \rightarrow CH^+ + H \tag{1.1}$$

and

$$C^+ + H_2 \rightarrow CH_2{}^+ + h\nu \tag{1.2}$$

Despite the reaction in eq. 1.1 being endothermic by ≈ 0.4 eV,[48–50] and the radiative association reaction in eq. 1.2 being slow (with rate coefficient, k, $\approx 1 \times 10^{-15}$ cm^{3}s^{-1}),[51] they are believed to be competitive due to tunneling effects[52] and interstellar shocks that provide enough energy for the reactions to proceed unhindered.[53–55] In dense clouds better shielded from UV radiation but penetrated by cosmic rays, hydrocarbon growth is initiated through ionization of hydrogen molecules:[52]

$$H_2 + h\nu \rightarrow H_2{}^+ \tag{1.3}$$

$$H_2{}^+ + H_2 \rightarrow H_3{}^+ + H \tag{1.4}$$

$$H_3{}^+ + C \rightarrow CH^+ + H_2 \tag{1.5}$$

$$CH^+ + H_2 \rightarrow CH_2{}^+ + H \tag{1.6}$$

Once CH_2^+ ions are formed in cold environments, they can undergo fast secondary reactions to form CH_3^+ and CH_5^+:[56]

$$CH_2^+ + H_2 \rightarrow CH_3^+ + H \tag{1.7}$$

$$CH_3^+ + H_2 \rightarrow CH_5^+ + h\nu \tag{1.8}$$

$$CH_5^+ + e^- \rightarrow CH_4 + H \tag{1.9}$$

The reaction between CH_3^+ and H_2 to form CH_4 is endothermic, and therefore the slow radiative association reaction in eq. 1.8 is predicted to be more competitive.[56,57]

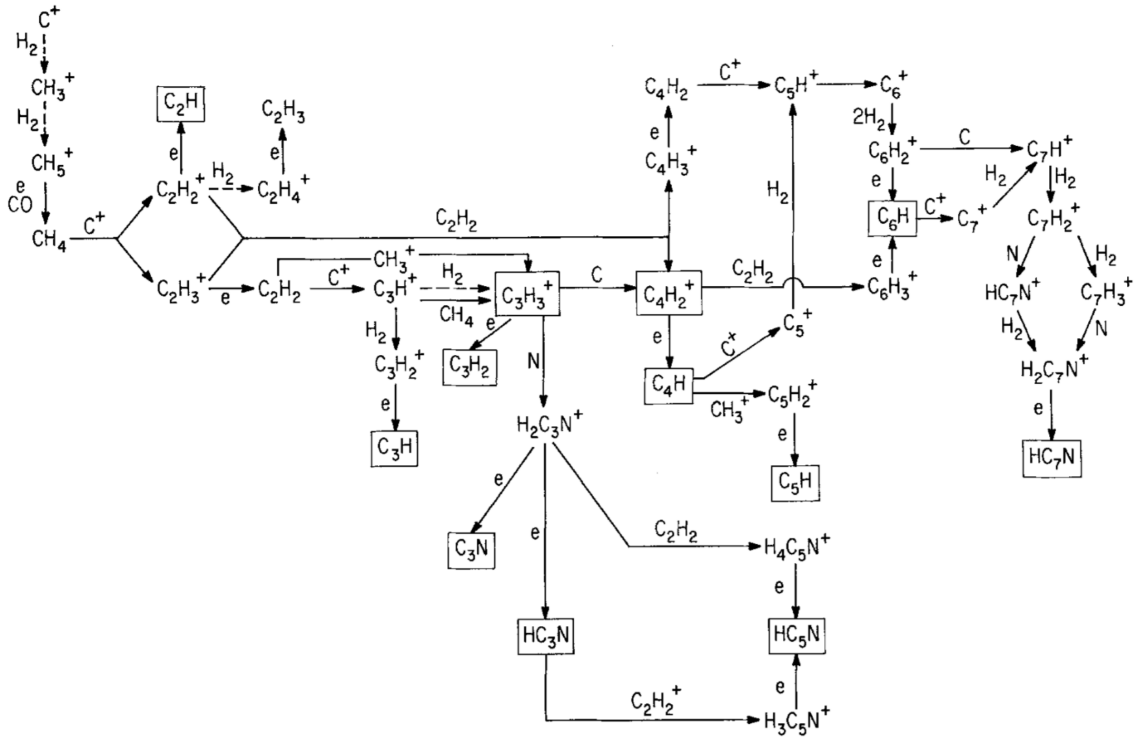

Fig. 1.3 Schematic representation of ion-molecule reactions occuring in the ISM. Hydrogenation and acetylene addition reactions are primary mechanisms for hydrocarbon ion growth. Reprinted with permission from ref. 58. Copyright Springer Nature 1989.

Following the formation of the fundamental CH_5^+ carbocation, several reactions, including those shown in the reaction scheme in Figure 1.3, have been proposed to occur in low temperature environments.[47,58–61] Hydrocarbons present in the ISM, if not formed in stellar winds, are generally understood to form through ion-molecule reactions, which are on the order of ten times faster than neutral-neutral reactions at low temperatures.[62–64] The rate coefficients of reactions involving nonpolar neutrals are well-described by the Langevin theory,[52,65] and

reactions between ions and molecules with permanent dipoles are particularly fast, owing to long-range attractions.[66] Ion-molecule reactions relevant to interstellar chemistry have been extensively studied using laboratory experiments and computational approaches.[45,67]

Photodissociation, a unimolecular reaction occurring when a molecule or ion absorbs a photon of sufficient energy to rupture a bond, is important in driving astrophysical chain reactions, including ion-molecule reactions.[68–71] This process is likely to occur in environments where molecules or ions are exposed to visible ($380 < \lambda < 740$ nm), near UV ($380 < \lambda < 240$ nm) and far UV (FUV, $91 < \lambda < 240$ nm) light.

The reactions in Titan's atmosphere are similar to those occurring in the ISM, but with the major source of hydrocarbons being methane (CH_4) that is released from volcanic eruptions and evaporated from lakes. The CH_4 cycle on Titan functions similarly to the water cycle on Earth, with a major difference being that CH_4 is a sink in its cycle – once CH_4 is consumed it is not reformed.[72,73] When CH_4 encounters solar radiation, cosmic rays, or charged particles from Saturn's magnetosphere as shown in Figure 1.4, it is photolyzed to form the reactive methyl radical (CH_3) and a hydrogen atom (H).[74,75] Reactions involving the CH_3 radical generate larger hydrocarbons, including polyacetylene and polycyclic aromatic hydrocarbons (PAHs) that in the presence of nitriles give rise to Titan's haze layers.[72,76,77] Solar and cosmic radiation and charged particles can also ionize hydrocarbons, particularly those located in the upper atmosphere (ionosphere-thermosphere), increasing the probability that ion-molecule and unimolecular reactions occur similar to those proposed in Figure 1.3.[78–82]

To understand hydrocarbon reactions in extraterrestrial environments, numerous chemical models[83–90] have been developed that take into account important factors such as temperature, density, and chemical composition – all of which can be informed through spectroscopy.

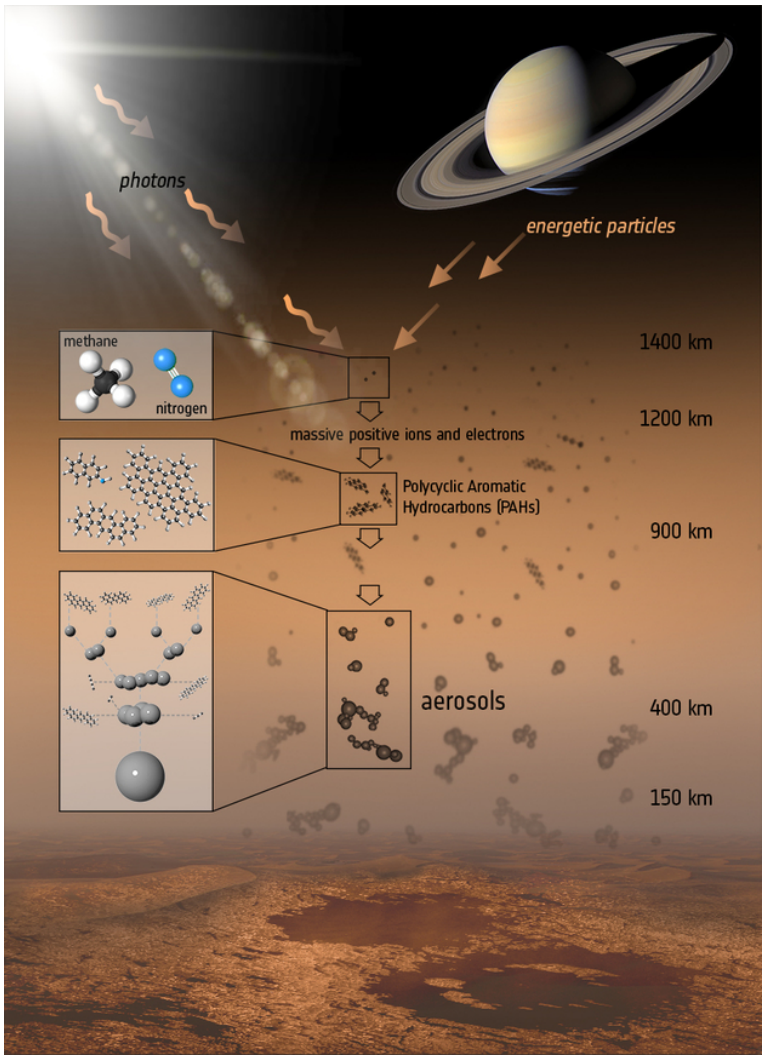

Fig. 1.4 Overall hydrocarbon growth mechanism leading to the formation of Titan's haze layer. Reprinted with permission. Copyright ESA/ATG medialab.

1.1.3 Using light to understand reactions

An understanding of how each molecule or ion interacts with light provides insight into its stability, which can inform the likelihood of its presence in certain environments and how it may participate in reactions. For example, the reaction scheme in Figure 1.3 includes empirical formulas for molecules suspected to be involved in reactions but does not specify their structures, which influence the chemical reactions that occur. An ion such as $C_3H_3^+$ may take a linear or cyclic form, although each isomer has been shown to have different reactivities.[91] In addition, dissociation energy thresholds vary depending upon the structure

of the molecule, which can affect which fragments result and which subsequent reactions occur.

To better model chemical reactions, it is necessary to consider the structures of the molecules involved, which in the case of remote environments may be informed by comparing emission and absorption spectra with laboratory spectra. As each molecule can only emit and absorb light of specific frequencies, related to its structure and quantized energy levels, its recorded spectrum is often considered a "molecular fingerprint." The comparison of spectra recorded in remote environments with those measured in laboratories has, as Professor Henry Draper described in 1866, "made the chemist's arms millions of miles long".[92]

Astronomical emission and absorption spectra can be generally described by Kirchoff's laws of spectroscopy. Stellar emission lines, such as those emanating from hot HII regions where the temperature is on the order of 10^4 K, are often broad, unresolved, or continuous, and are therefore typically used as background radiation for absorption spectroscopy of colder regions. Stellar absorption spectra can be generally categorized into three denominations: stellar lines arising from gases in circumstellar envelopes, terrestrial lines arising from gases in a planetary atmosphere, and interstellar lines of gases in (typically diffuse) molecular clouds.[93] Reduced intensities or extinction of light at specific wavelengths are caused by absorption of photons by molecules positioned between the light source and the observer. As diffuse molecular clouds are cold (between 10 and 10^2 K), the Maxwell-Boltzmann energy distribution for molecules is small, with the zero vibrational energy level of the ground state being the most populated. Consequently, the spectral lines are narrow and can be matched with known vibrational or electronic transitions of molecules. In addition, the timescale of chemical reactions in diffuse clouds is relatively long, due to the low temperature and gas density, such that astronomical spectra may capture chemistry that has not reached an equilibrium state. Intermediate molecules considered unstable and transient in other conditions may be as observable as stable reaction products. A cold molecule may also be identified by comparing laboratory and emission spectra in the case where it fluoresces (emits one or more photons of lower energies) following photon absorption.

Until the 1930s, only a few stellar and interstellar bands could be explained – those arising from transitions of neutral sodium[94] and calcium.[95] Interstellar molecules were first detected when absorption lines between 387 and 431 nm were recorded using a spectrograph mounted on the 60-inch telescope at Mount Wilson Observatory and assigned to electronic transitions of CN, CH, CH^+, and NaH.[96–99] Because the absorption lines correspond to transitions from the lowest rotational level in the zero vibrational level of their ground electronic states,[96] the temperature of the ISM in the direction was deduced to be ≈ 2 K.[98] Perhaps the most famous

set of interstellar bands are those recorded in the direction of reddened stars, the diffuse interstellar bands (DIBs), which have perplexed scientists since their initial observation in the early 1920s.[94] The bands have been postulated to arise from electronic transitions of neutral and/or cationic carbon chain molecules, as well as PAHs.[100–106] Only recently, since 2015, has there been a positive match between five DIBs and the recorded electronic absorption spectrum of the Buckminsterfullerene cation (C_{60}^+).[107–110]

Several spectrographs have been used to obtain astronomical spectra, including the Ralph infrared and Alice ultraviolet imaging spectrometers aboard the New Horizons spacecraft (exploring Pluto, its moons, and the Kuiper belt), the Infrared Spectrograph aboard the Spitzer Space Telescope, and the Visible and Infrared Imaging Spectrometer, the Ultraviolet Imaging Spectrograph, and the Composite Infrared Spectrometer aboard the Cassini spacecraft that orbited Saturn. The instruments installed on the Hubble Space Telescope, including the Space Telescope Imaging Spectrograph (STIS), the fine guidance sensors (FGSs), wide field cameras (WFC3), and the Advanced Camera for Surveys (ACS) and the wavelength ranges in which they operate are shown in Figure 1.5. Based on comparison of astronomical spectra with laboratory spectra compiled in databases such as GEISA,[111] HITRAN,[112,113] the NASA Ames PAH database,[114–116] and the Cologne Database for Molecular Spectroscopy,[117,118] numerous molecules have been detected by their rotational spectra,[17–21,119] several by their vibrational spectra,[120] but only a few by their electronic spectra.[121]

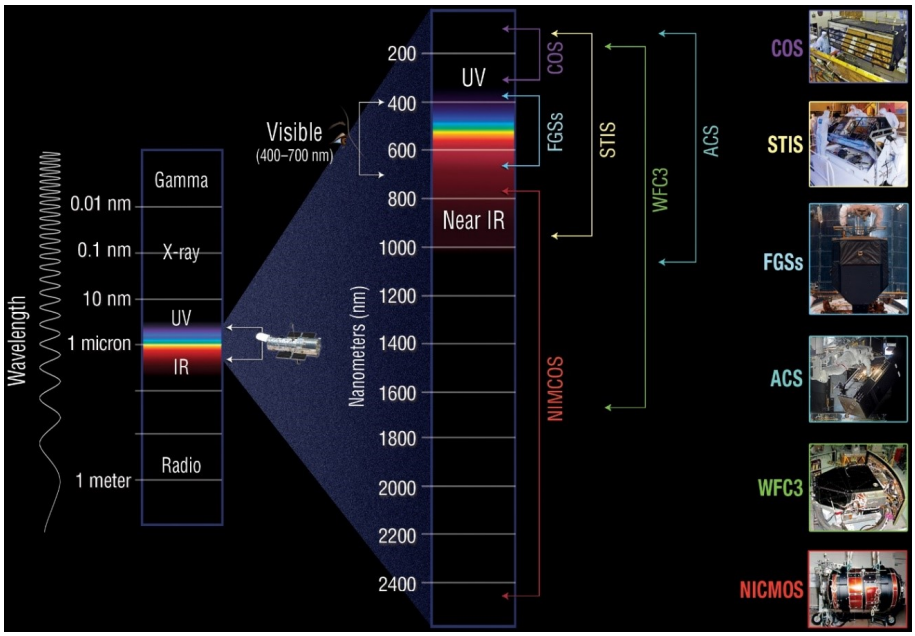

Fig. 1.5 Instruments aboard the Hubble space craft that can detect different wavelengths of light. Reprinted with permission from NASA.

1.2 Electronic spectroscopy of acetylenic cations

This work focuses on the electronic spectroscopy of small carbocations that can be generated from acetylene (HCCH), the smallest unsaturated hydrocarbon. Neutral and ionic forms of acetylene exist in circumstellar envelopes,[122] the ISM,[13,123] on Titan,[124–127] and possibly other environments where methane is abundant.[128,129] Both neutral and charged forms of acetylene are involved in hydrocarbon growth processes, such as those shown in Figure 1.3.[3,4,52,52,130–134] Because ion-molecule reactions are expected to be dominant in low-temperature environments, carbocation intermediates along acetylene growth pathways are likely to be important in the chemistry of the ISM and Titan's atmosphere. The growth process can be initiated by the carbon insertion reaction between C^+ and methane:[52]

$$C^+ + CH_4 \rightarrow C_2H_4{}^+ \rightarrow C_2H_2{}^+ + H_2 \tag{1.10}$$

with subsequent reactions also demonstrated in Fig. 1.3. Numerous experiments and ab initio calculations have been conducted to characterize acetylene ion-molecule reactions and their intermediates and products.[45,81,82,132,135–151]

Prior to conducting the spectroscopic experiments described in this work, a preliminary electron impact (EI) mass spectrum of a dilute acetylene mixture (in Ar and N_2) was recorded, shown in Figure 1.6, to gain insight into the types of carbocations that can be investigated. Note that water vapor was a trace impurity. The experimental approach for obtaining the spectrum is described in the following chapter. The mass spectrum is similar to previously recorded spectra of acetylene [144,152,153] and another obtained using a mixture of acetylene and H_2 to investigate protonated acetylene clusters.[154]

In Figure 1.6, the acetylene dimer and trimer species, $(C_2H_2)_2{}^+$ and $(C_2H_2)_3{}^+$ have lower abundances than do ions one mass unit lower ($C_4H_3{}^+$ and $C_6H_5{}^+$, respectively), highlighting the importance of carbon insertion reactions that typically produce H or H_2 fragments that do not rapidly react with larger ions.[71] The fragmentation of the acetylene trimer cation was described in a dissociative photoionization experiment by Ono *et al.*,[155] wherein the photoionization efficiency (PIE) curves of the trimer and several of its ionic fragments were recorded. A simple pseudo-potential energy surface is depicted in Figure 1.7 to describe the process. The measured appearance energies of $C_6H_5{}^+$, $C_6H_4{}^+$, $C_4H_4{}^+$, and $C_3H_3{}^+$ fragments were all in the vicinity of 10.10 eV, suggesting a small entrance barrier (≈ 0.26 eV above the energy of the trimer) to the covalent $C_6H_6{}^+$ surface. It was postulated that the energy of this barrier lies higher than the dissociation limits for various product sets, and therefore $C_6H_6{}^+$,

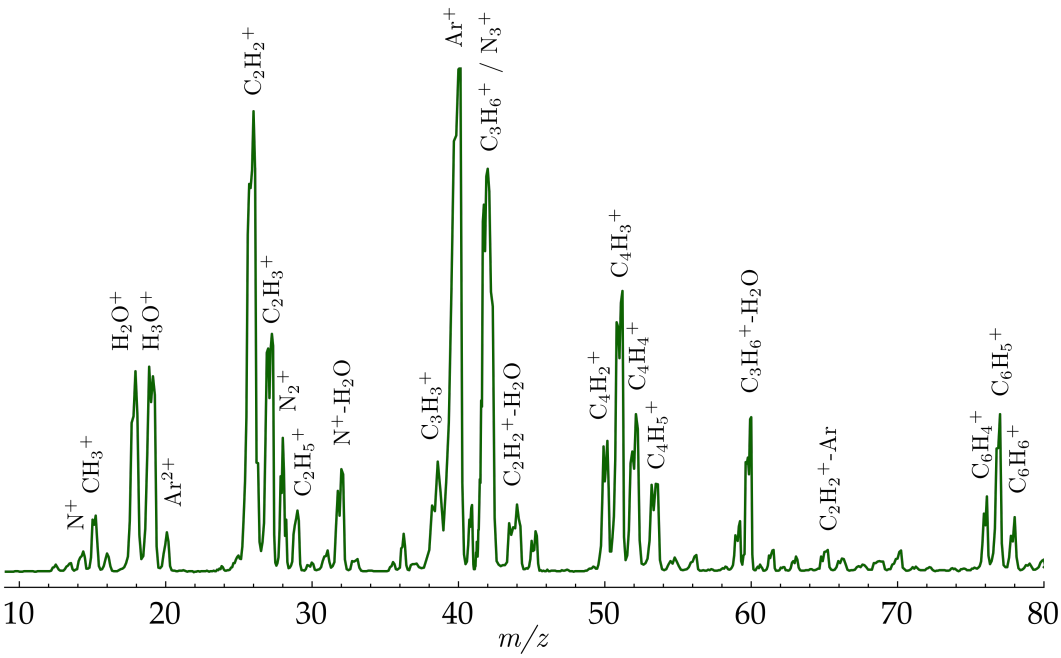

Fig. 1.6 Electron impact mass spectrum of a dilute acetylene/argon mixture in N_2.

once formed, possesses sufficient internal energy to fragment. In general, this underscores the complexity of ion-molecule reactions, in that ions such as $C_6H_4^+$ and $C_4H_4^+$ may be formed through several mechanisms involving acetylene. The mechanisms are described in more detail for the ions investigated in this work: $C_4H_2^+$, $C_4H_4^+$, $C_4H_5^+$, and $C_6H_4^+$.

The electronic spectra of $C_4H_2^+$, $C_4H_4^+$, and $C_6H_4^+$ presented in Chapters 3, 4, and 6 are those of ions generated from an acetylene source. Spectra of $C_4H_5^+$ ions generated from acetylene were also recorded as part of this work, however the transitions matched those previously recorded by Catani *et al.*,[156] confirming formation of the methyl propargyl cation ($H_3C_4H_2^+$). Another energetically low-lying $C_4H_5^+$ isomer was investigated using a brominated precursor as described in Chapter 5.

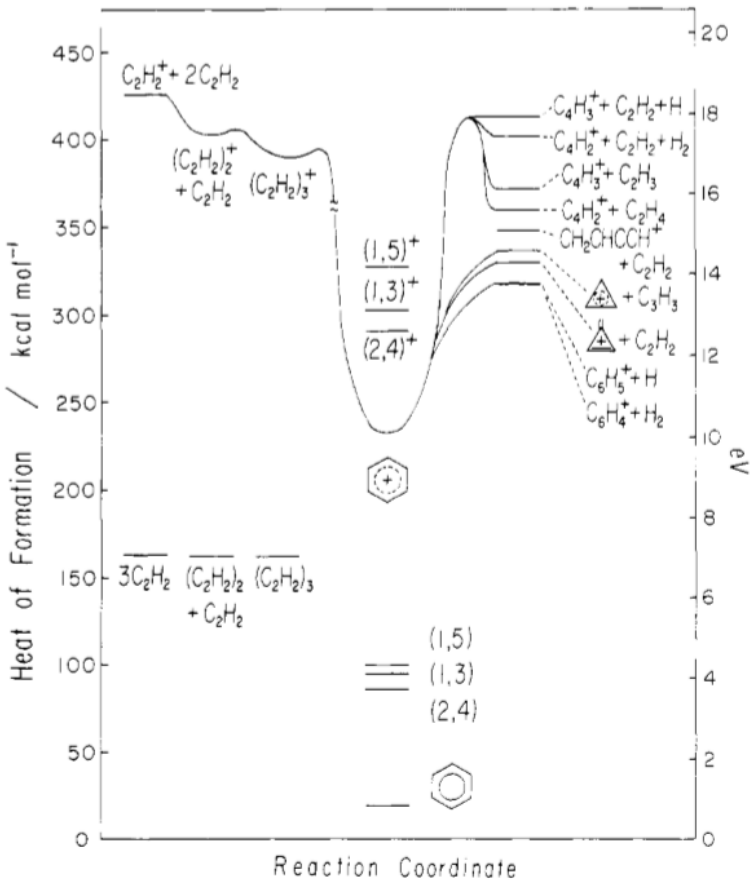

Fig. 1.7 A pseudo reaction scheme of the dissociation of an acetylene trimer cation, $(C_2H_2)_3^+$. Reprinted with permission from Ono and Ng.[155] Copyright 1982 American Chemical Society.

1.2.1 $C_4H_2^+$

Neutral C_4H_2 isomers have been identified in the atmosphere of Titan and protoplanetary and protostellar nebulae.[14,21,157] The two lowest energy isomers take the forms of diacetylene (HC_4H) and a carbene structure ($CCCCH_2$), with diacetylene lying ≈ 1.9 eV lower in energy.[63,158] The exposure of molecules in these environments to strong ionizing UV light and X-rays increases the probability that $C_4H_2^+$ radical cations are also present.

There are several possible mechanisms for the formation of $C_4H_2^+$ in the ISM, some of which are outlined in Figure 1.3. Interaction between ionic and neutral acetylene molecules leads to a dimer cation $(C_2H_2)_2^+$ that enters the covalent $C_4H_4^+$ surface and eliminates H_2:

$$C_2H_2^+ + C_2H_2 \rightarrow (C_2H_2)_2^+ \rightarrow C_4H_4^+ \rightarrow C_4H_2^+ + H_2 \tag{1.11}$$

Fragmentation of larger acetylenic cations, such as $C_6H_4^+$ described in Section 1.2.4, can also be a source of $C_4H_2^+$.[159]

The role of $C_4H_2^+$ in the formation of larger polyacetylenes in the ISM has been previously investigated.[160] In Titan's upper atmosphere, $C_4H_2^+$ is postulated to give rise to the benzene cation through a series of reactions:[82,161,162]

$$C_4H_2^+ + C_2H_4 \rightarrow C_6H_5^+ + H \tag{1.12}$$

$$C_6H_5^+ + H_2 \rightarrow C_6H_7^+ \tag{1.13}$$

$$C_6H_7^+ + e^- \rightarrow C_6H_6^+ + H \tag{1.14}$$

The identity of $C_4H_2^+$ ions becomes important in modeling the chemistry occurring in remote areas. Although the ground state $C_4H_2^+$ potential energy surface has not been thoroughly explored, quantum chemical calculations underscore the stability of the diacetylene radical cation (HC_4H^+) compared to its isomers, and vertical excitation calculations predict it has the strongest oscillator strength of the $C_4H_2^+$ species.[163] Therefore, it is the most likely $C_4H_2^+$ structure to exist and be spectroscopically detected.

The electronic configurations of the first five doublet electronic states of HC_4H^+ are depicted in Figure 1.8, and are based on computational and spectroscopic studies. Photoelectron spectroscopy, IR spectroscopy, and quantum mechanical calculations agree that the ground electronic state is linear and centrosymmetric ($D_{\infty h}$ symmetry) with an electronic configuration of $5(\sigma_g)^4 4(\sigma_u)^4 1(\pi_u)^4 1(\pi_g)^3$.[164,165]

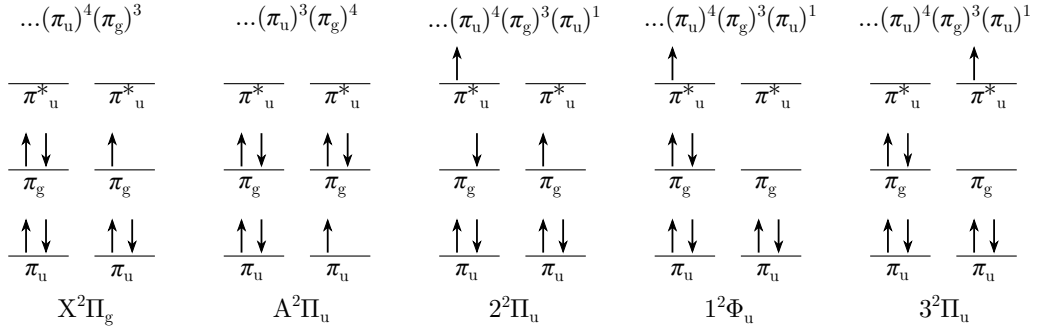

Fig. 1.8 Dominant electronic configurations of the five lowest doublet electronic states of the diacetylene radical cation.

The first electronic spectrum of HC_4H^+ was obtained in the 1950s in a discharge of organic vapors, and the emitted light around 507 nm (2.45 eV) was assigned to the $\widetilde{A}^2\Pi_u \rightarrow \widetilde{X}^2\Pi_g$ transition.[166,167] Since then, several studies have examined spectral bands in the IR and

visible regions to improve understanding of the structure of the $\widetilde{X}^2\Pi_g$ and $\widetilde{A}^2\Pi_u$ states of HC_4H^+.[103,168–172]

Higher excited states, including $2^2\Pi_u$, $1^2\Phi_u$, and $3^2\Pi_u$, are more complicated to measure experimentally and are also more difficult to describe using electronic structure calculations. Because the $2^2\Pi_u$ state and the $1^2\Phi_u$ state have been predicted to lie energetically close to one another, the energetic ordering of the states is unclear. Therefore, the labeling convention used by Bally *et al.*[173] in a study of HC_4H^+ is adopted for electronic states above the $\widetilde{A}^2\Pi_u$ state. The $2^2\Pi_u$, $1^2\Phi_u$, and $3^2\Pi_u$ excited states are non-Koopmans' states, in that an electron occupies a molecular orbital (π_u*) that is not occupied in the ground electronic state. These excited electronic states cannot be reached through single photon ionization of the ground state neutral. Therefore, photoelectron spectra of HC_4H typically exhibit a gap of ≈ 4 eV between the bands associated with the $\widetilde{A}^2\Pi_u$ state and the next accessible excited electronic state (≈ 6.45 eV above the $\widetilde{X}^2\Pi_g$ state).[165] Instead, the non-Koopmans' $^2\Pi_u$ states can be accessed from excitation of the $\widetilde{X}^2\Pi_g$ state using electronic spectroscopy, whereas transitions to the $1^2\Phi_u$ state are electric-dipole forbidden. Vertical excitation calculations confirm that transitions to the upper $^2\Pi_u$ states have significantly lower oscillator strengths than the $\widetilde{A}^2\Pi_u \leftarrow \widetilde{X}^2\Pi_g$ transition. The $2^2\Pi_u \leftarrow \widetilde{X}^2\Pi_g$ band system has been recorded using matrix isolation spectroscopy,[173,174] however the weakness of the transitions compromised its interpretation. Obtaining spectra of HC_4H^+ ions in the gas phase may help facilitate understanding of the transitions induced by UV light and detection of the cation in remote environments.

1.2.2 $C_4H_4^+$

Although $C_4H_4^+$ has not been detected in the ISM, it is likely to exist in Titan's atmosphere based on the abundance of acetylene[86,175] and other small hydrocarbons.[80] One possible mechanism to formation involves an acetylene ion reacting with a neutral acetylene molecule to form an acetylene dimer complex that can enter the covalent $C_4H_4^+$ surface (see Figure 1.9) and undergo additional acetylene-growth processes or, with sufficient internal energy, unimolecular dissociation to $C_4H_3^+$, $C_4H_2^+$, and $C_2H_2^+$ (see equation 1.11).[135,176–184] Another pathway to $C_4H_4^+$ formation in the atmosphere of Titan involves a reaction between the diacetylene cation, possibly formed through eq. 1.11, and ethene:[82]

$$C_4H_2^+ + C_2H_4 \rightarrow C_4H_4^+ + C_2H_2 \tag{1.15}$$

Dissociative photoionization studies of acetylene trimers [155,185] (see Fig. 1.7) and tetramers [185] suggest that $C_4H_4^+$ can also be generated from larger acetylenic cations.

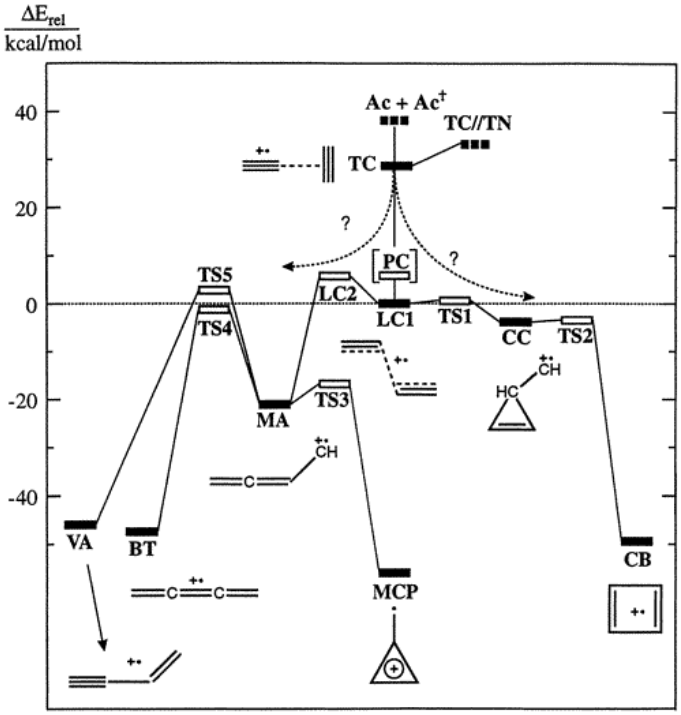

Fig. 1.9 Pseudo potential energy surface of the acetylene dimer cation, $(C_2H_2)_2^+$. Reprinted with permission from ref. 178. Copyright 1997 American Chemical Society.

Results of ion mobility and vibrational predissociation spectroscopy experiments indicate several $C_4H_4^+$ isomers can form from acetylene interactions. [152,180] Of the $C_4H_4^+$ isomers, the vinylacetylene (1-buten-3-yne) cation (**VA**$^+$) may be particularly likely to exist in remote environments, as it is a known photofragment of $C_6H_6^+$, and can be formed in areas where acetylene and/or benzene are exposed to ultraviolet photons, including the atmosphere of Titan. [148,155,176,177,186–193] Inclusion of the neutral vinylacetylene molecule (**VA**) into atmospheric models of Titan and PAH formation mechanisms in the ISM suggests an increased probability for **VA**$^+$ presence. [9,193–196]

VA is the global minimum on the neutral C_4H_4 potential energy surface, [197,198] whereas **VA**$^+$ lies higher in energy than three of its $C_4H_4^+$ isomers, based on measured ionization potentials and quantum mechanical calculations. [176,178,179,187,191,199–202] Photodissociation studies have outlined that the formation of linear $C_4H_4^+$ isomers, including **VA**$^+$, is favorable over cyclic isomers when the internal energy of the precursor is high. [176,188,203,204] The preference for **VA**$^+$ can partially be explained by its deep energy well, underscoring its stability.

Calculations of the ground state $C_4H_4^+$ potential energy surface predict isomerization of $\mathbf{VA}^+$ to require at least 2 eV,[191,202] and the measured photoionization potential of **VA** and appearance energies of $C_4H_3^+$ and $C_4H_2^+$ fragments lead to the prediction that $\mathbf{VA}^+$ requires at least 3 eV of energy to dissociate.[135,178,201]

The ground state of $\mathbf{VA}^+$ is predicted to have a C_s equilibrium geometry.[178,202] A single electron in the highest occupied molecular orbital (HOMO) with a″ symmetry leads to the designation of the ground state as $\tilde{X}^2A''$. Relative energies of several excited electronic states of $\mathbf{VA}^+$ were measured using photoelectron spectroscopy, the first three of which were detected 1.0, 2.4, and 3.2 eV above $\tilde{X}^2A''$, and are referred to in this body of work as the $\tilde{A}^2A'$, $\tilde{B}^2A''$, and $\tilde{C}^2A'$ electronic states, respectively.[201,205] These three lowest energy doublet excited states are reached upon removal of an electron from the HOMO-1, HOMO-2, and HOMO-3 orbitals of the ground state neutral molecule, respectively. The fourth excited state ($\tilde{D}^2A''$) is a non-Koopmans' excited state (see Section 1.2.1) that cannot be accessed by photoionizing the ground state neutral, and therefore has not been observed in photoelectron spectra. Bally *et al.*[173] recorded HOMO→LUMO transitions of $\mathbf{VA}^+$ using matrix isolation spectroscopy and reported this state to lie 4.2 eV above the $\tilde{X}^2A''$ state.

Although electronic transitions of $\mathbf{VA}^+$ have been recorded in the visible and ultraviolet regions, corresponding to the $\tilde{B}^2A'' \leftarrow \tilde{X}^2A''$ and $\tilde{D}^2A'' \leftarrow \tilde{X}^2A''$ band systems, the individual bands have not yet been assigned to vibronic transitions.[173] Araki *et al.*[206] measured a rotationally resolved spectrum of the $\tilde{B}^2A'' \leftarrow \tilde{X}^2A''$ origin band in the gas phase around 513 nm (2.42 eV), in addition to transitions over the 480-520 nm range in a 6 K neon matrix. The matrix isolation spectrum included artefacts due to site structure and contributions from the $\tilde{A}^2\Pi_u \leftarrow \tilde{X}^2\Pi_g$ band system of the diacetylene cation (HC_4H^+), complicating the analysis. In an analogous experiment by Filipkowski *et al.*[207] using 1,4-dichloro,2-butyne as the precursor, transitions of butatriene, vinylacetylene, and diacetylene cations were recorded in the spectrum as a result of sufficient internal energy to isomerize and dissociate.

A spectrum of isolated $\mathbf{VA}^+$ in the gas phase over the visible and ultraviolet regions would significantly improve understanding of its excited states, may provide clues to its photodissociation processes, and would aid its detection in remote environments where it may exist. These are the primary motivations of this study.

1.2.3 $C_4H_5^+$

C_4H_5 radicals are formed as fragments of various combustible hydrocarbons and have been observed in fuel-rich flames.[208,209] In addition to their potential roles in the formation of soot and larger hydrocarbons,[210] these radicals and their corresponding closed-shell cations may form in environments beyond Earth's atmosphere where acetylene and benzene are present.[60,208,209,211–216] In the atmosphere of Titan, reactions of C_4H_5 radicals have been incorporated into chemical models, including the reaction with acetylene to form benzene:[217]

$$C_4H_5 + C_2H_2 \rightarrow C_6H_6 + H \tag{1.16}$$

Some experimental results provide insight into the C_4H_5 isomers that are likely to form. Through crossed-beam experiments, coupled with photoionization time-of-flight mass spectrometry, the identities of C_4H_5 products from various reactions were determined by matching their photoionization efficiency curves with those of known C_4H_5 isomers.[208,218–220]

Regarding $C_4H_5^+$ cations, the INMS aboard the Cassini spacecraft identified molecules in Titan's atmosphere with the mass-to-charge ratio (*m/z*) of 53, supporting assignment of the molecules to $C_4H_5^+$.[221] The cations may form through photoionization of the neutral radicals, dissociation of larger carbocations,[222] or acetylene ion-molecule reactions:[16,184]

$$C_2H_2^+ + C_2H_4 \rightarrow C_4H_5^+ + H \tag{1.17}$$

and

$$C_2H_5^+ + C_2H_2 \rightarrow C_4H_5^+ + H_2 \tag{1.18}$$

However, it is unknown which isomers are formed from these reactions and exist on Titan.

Several $C_4H_5^+$ structures have been elucidated through quantum chemical calculations,[223–228] however most of the available energetic and spectroscopic data pertain to the two low-energy methyl propargyl isomers, shown in Figure 1.10. The photoelectron spectra of the neutral methyl propargyl radicals[229,230] are similar to the spectrum of the propargyl radical,[231–233] suggesting that the substitution of a methyl group for a hydrogen atom has a minor effect on the propargyl chromophore and therefore the three ions should have similar electronic transitions.

Recently, the electronic spectrum of the linear methyl propargyl cation, (**MP**, $H_3C_4H_2^+$ in Fig. 1.10) was recorded using resonance enhanced photodissociation (REPD) spectroscopy,

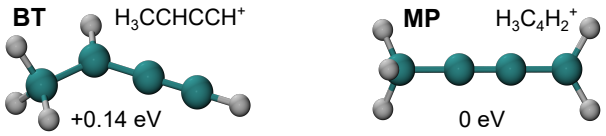

Fig. 1.10 Structures (MP2/aug-cc-pVDZ level of theory) and relative energies (CCSD(T)/cc-pVTZ single point with MP2/aug-cc-pVDZ zero-point energies) of the bent ($H_3CCHCCH^+$) and linear ($H_3C_4H_2^+$) methyl propargyl cations.

an experimental approach that is described in the following chapter.[156] The spectrum is useful for comparison with astronomical spectra, and possible future spectra of Titan, to identify whether the molecular ion is present. The $^1A' \leftarrow ^1A'$ band system was recorded over the 230-270 nm range by monitoring $C_2H_3^+$ and $C_4H_3^+$ photofragments and exhibited a profile that is similar to the electronic spectrum of the propargyl cation[234] occurring in the same spectral region. Quantum chemical calculations were conducted to assign bands in the **MP** spectrum to vibronic transitions. Calculations were also used to explain the fragmentation of **MP** following photoexcitation, through which ≈ 5 times more $C_2H_3^+$ than $C_4H_3^+$ ions were produced over the scanned photon energy range. Assuming the excited ions nonradiatively decay through internal conversion onto the ground state manifold, stationary points on the ground state $C_4H_5^+$ potential energy surface were calculated and used for master equation simulations. The predicted $C_2H_3^+ / C_4H_3^+$ branching ratio of ≈ 2 correctly predicted the favored formation of $C_2H_3^+$ fragments over the investigated range.

To measure the electronic spectrum of **MP**, described above, the $C_4H_5^+$ ions were generated from 1-bromo-2-butyne. Based on the preliminary electron impact mass spectrum shown in Fig. 1.6, and similar mass spectra available in literature,[144] $C_4H_5^+$ ions can also be generated from acetylene which is the main precursor used in this body of work. A preliminary REPD spectrum of $C_4H_5^+$, generated from a ≈ 0.7 % acetylene mixture, was measured over the 225-700 nm range as part of this work and matched that of **MP** without contributions from other isomers. Note that this observation does not imply that **MP** is the only $C_4H_5^+$ isomer generated, but simply the only isomer formed under the particular experimental conditions (see following chapter) that is spectroscopically observable within the investigated wavelength range.

The other methyl propargyl isomer, the bent 1-butyn-3-yl cation (**BT**, $H_3CCHCCH^+$), lies only slightly higher in energy than **MP,** such that its presence in remote environments is also probable. An REPD spectrum of **BT** would aid its possible detection in remote environments, provide additional information on the influence of the methyl group on the

propargyl chromophere through comparison with spectra of **MP** and the propargyl cation, and further our understanding of $C_4H_5^+$ dissociation.

1.2.4 $C_6H_4^+$

Neutral C_6H_4 molecules can form from acetylene and benzene,[235–237] and are believed to play important roles in the formation of larger structures.[237] One isomer, the cyclic *ortho*-benzyne structure shown in Figure 1.11, has been sought out in circumstellar envelopes.[238] The possible presence of C_6H_4 molecules in areas exposed to ionizing radiation ($\lambda < 135$ nm based on measured photoionization energies)[177,239–243] or charged particles increases the likelihood that $C_6H_4^+$ cations exist and participate in reactions. In addition, the radical cations can be generated as fragments of larger carbocations,[159,186,203,244,245] and through acetylene ion-molecule reactions[80,82,140,246–248] such as

$$C_2H_2^+ + C_2H_2 \rightarrow (C_2H_2)_2^+ \rightarrow C_4H_4^+ \tag{1.19}$$

$$C_4H_4^+ \rightarrow C_4H_2^+ + H_2 \tag{1.20}$$

$$C_4H_2^+ + C_2H_2 \rightarrow C_6H_4^+ \tag{1.21}$$

and

$$C_2H_2^+ + 2C_2H_2 \rightarrow (C_2H_2)_3^+ \rightarrow C_6H_6^+ \tag{1.22}$$

$$C_6H_6^+ \rightarrow C_6H_4^+ + H_2 \tag{1.23}$$

Equation 1.22 may also include $C_4H_4^+$ reacting with C_2H_2, where linear $C_4H_4^+$ isomers such as $H_2CCHCCH^+$ (**VA**$^+$, vinylacetylene) are believed to react significantly faster than cyclic isomers with acetylene.[249,250] The reactions proceeding through the generation of the acetylene trimer cation (equation 1.22) are also described in the pseudo potential energy surface[155] in Fig. 1.7 presented at the beginning of Section 1.2.

The identities of $C_6H_4^+$ structures formed through various reactions depend, in part, on their relative stabilities, which were first investigated through calculated equilibrium geometries, heats of formation, and ionization potentials of neutral benzyne molecules.[240] Although the *ortho*-benzyne molecule, shown in Figure 1.11, is the global minimum on the singlet neutral potential energy surface, the calculations[240] predicted the *meta*-benzyne cation (also in Fig. 1.11) to lie nearly 1 eV lower in energy than the *ortho*- form on the doublet

potential energy surface. Based on measured ionization potentials[239] of the *ortho*-benzyne and 3-hexene-1,5-diyne molecules, of which the heats of formation were also available,[251] the benzyne cations were expected to lie lower in energy. In 1980, additional heats of formation were estimated and compared with the appearance energy of $C_6H_4^+$ fragments measured in a photoelectron photoionization coincidence (PEPICO) spectroscopy study of benzonitrile.[252] The $C_6H_4^+$ ions were proposed to be cyclic, based on their predicted lower heats of formation compared to those of acyclic structures.

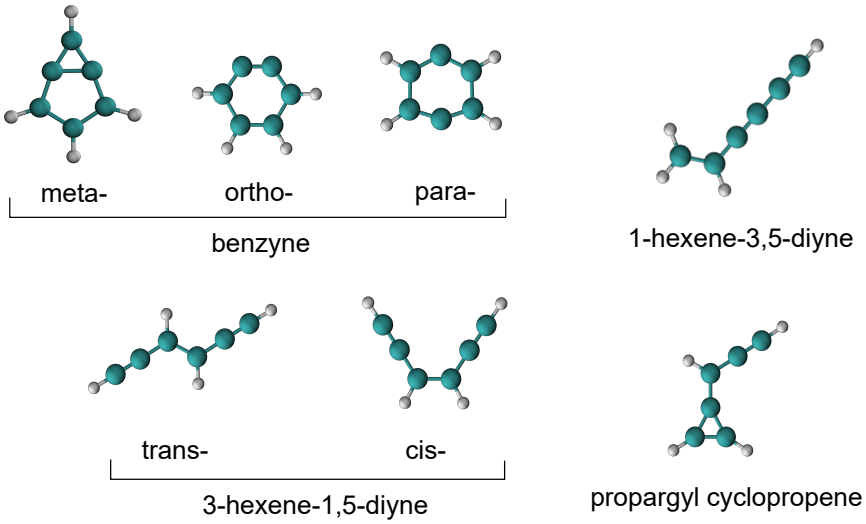

Fig. 1.11 Isomers of $C_6H_4^+$ that have been previously spectroscopically studied.

The understanding that cyclic $C_6H_4^+$ isomers lie lower in energy than acyclic isomers was challenged in the late 1980s when electron impact mass spectra of benzonitrile and 2-ethynylpyridine were observed to be similar.[253] Since a ring-breaking mechanism is necessary for HCN loss from 2-ethynylpyridine, it was proposed that the $C_6H_4^+$ fragments from both precursors are likely acyclic. In a subsequent study, the $C_6H_4^+$ fragments generated from benzonitrile, 2-ethynylpyridine, and other precursors, were photodissociated in a cell of an ion cyclotron resonance spectrometer using visible and near-UV light.[159] The resulting $C_4H_2^+$ ions were recorded as a function of wavelength to generate a photodissociation action spectrum. To help interpret the spectrum, electronic structures and energies for several $C_6H_4^+$ isomers were calculated using the modified neglect of dynamic overlap (MNDO) approach, which predicted acyclic isomers to be lower in energy than cyclic ones. In addition, the predicted energies and oscillator strengths corresponding to electronic transitions of the *cis*- and *trans*- 3-hexene-1,5-diyne isomers were consistent with the spectral maximum occurring around 375 nm. Indeed, previously recorded photoelectron spectra of the 3-hexene-1,5-diyne conformers indicate that at least three electronic states lie between 2-5 eV above the ground

state, such that the states may be reachable from the ground state through excitation with visible or UV light.[201]

In the early 2000s, the 1-hexene-3,5-diyne cation (Fig. 1.11) became the first $C_6H_4^+$ isomer to be spectroscopically identified as an intermediate in hydrocarbon chemistry.[206] An electronic spectrum was recorded by probing a discharge of 0.5 % acetylene in He with visible light, in hopes to measure bands consistent with DIBs. A band occurring at 604 nm exhibited clear rotational structure that was compared with predictions of *ab initio* calculations. To further verify the identity of the isomer, additional electronic transitions were recorded over the 575-620 nm range using matrix isolation spectroscopy, with all bands ascribed to the 1-hexene-3,5-diyne isomer – except one occurring at 585 nm. Subsequent spectroscopic studies assigned the band at 585.3 nm (580.0 nm in the gas phase) to a transition of the *trans*-3-hexene-1,5-diyne cation.[254,255]

The most extensive and recent spectroscopic investigation of $C_6H_4^+$ cations was conducted by performing matrix isolation spectroscopy on ions generated from a variety of precursors.[256] The spectra exhibited numerous bands, including known transitions of $C_6H_2^+$ and $C_4H_2^+$, which were formed as fragments of $C_6H_4^+$ during the deposition of ions into the matrix. To ascertain which $C_6H_4^+$ isomers give rise to the bands, the equilibrium geometries, energies, and harmonic vibrational frequencies of several isomers in their ground and excited states were calculated. Figure 1.12 depicts the electronic excitations of $C_6H_4^+$ isomers that were attributed to bands in the spectra. Transitions in the 570-610 nm region, as well as the 375 nm region, were associated with the 1-hexene-3,5-diyne and *trans*-3-hexene-1,5-diyne isomers, consistent with previous electronic[206,254,255] and photodissociation action spectroscopy studies discussed above.[159] Weak bands at 622 and 385 nm were attributed to transitions of *cis*-3-hexene-1,5-diyne based on spectroscopic evidence of photoisomerization with the *trans*-form. Transitions of the propargyl cyclopropene isomer (Fig. 1.11) occur around 417 nm based on calculated energies, oscillator strengths, and a Franck-Condon simulation. The most puzzling $C_6H_4^+$ transition occurs at 423 nm, which remains unassigned. The intensities of bands in the 417 nm region were independent of the dibromobenzene precursor used to produce the $C_6H_4^+$ ions. Based on calculated energies of $C_6H_4^+$ ions, and on previous work in which $C_6H_4^+$ fragments of dibromobenzene and difluorobenzene isomers were described to preserve the benzyne structure,[257,258] a transition of *ortho*-benzyne was expected to give rise to bands near 417 nm, potentially at 423 nm.

The ground state geometry of the *ortho*-benzyne cation has proven difficult to characterize. Several photoelectron spectra of neutral *ortho*-benzyne have been recorded,[177,241–243] with confusion around a band that ultimately was confirmed to be associated with benzene.[242]

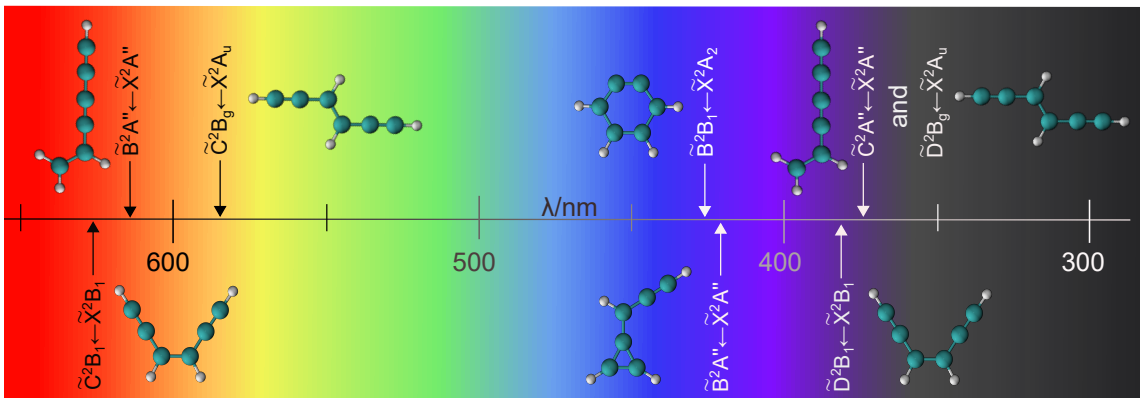

Fig. 1.12 Electromagnetic spectrum with previously investigated electronic transitions of $C_6H_4^+$ isomers.

Quantum chemical calculations[256,259,260] have predicted the ground state to be planar (C_{2v} symmetry), although high level CCSD(T)/cc-pVTZ calculations[151] and a recent photoionization study of neutral *ortho*-benzyne, accompanied by CASPT2(11,14) *ab initio* calculations, revealed that the *ortho*-benzyne cation is twisted in its electronic ground state (C_2 symmetry, $\tilde{X}^2A_2$).[261] Thus, the electronic excitation energies and oscillator strengths for the *ortho*-benzyne cation should be revisited and considered for assignment of the band arising at 423 nm.

Electronic spectra of $C_6H_4^+$ isomers in the gas phase would be useful to aid in their detection in remote environments, should they be present. In addition, REPD spectra, coupled with quantum chemical calculations, would provide meaningful insights into the deactivation of excited $C_6H_4^+$ ions, which has been observed to yield $C_4H_2^+$ and $C_6H_2^+$ fragments – although the energetics and mechanisms are unknown.

Chapter 2

Experimental and computational approach

Most of the previously recorded electronic spectra of $C_4H_2^+$, $C_4H_4^+$, $C_4H_5^+$, and $C_6H_4^+$ ions, described in Chapter 1, were obtained through matrix isolation spectroscopy – a technique that measures light absorption by ions deposited into solid argon or neon matrices. The spectra have provided valuable information on the electronic energies and vibrational frequencies of the cations. However, as previously described, matrix site artefacts and contributions from fragments formed during the deposition process often complicate interpretation of the spectra. In addition, interactions between trapped carbocations and the solid matrix can lead to substantial frequency shifts from gas-phase transitions, typically to lower energies.[262]

Directly measuring light absorption by molecules in the gas phase, where they are free from solvent and matrix effects, is more difficult than measuring absorption by molecules in condensed phases because the density of the target species is low. In lieu of directly measuring absorption, resonance-enhanced photodissociation (REPD) spectroscopy relies on measuring the photofragment signal as a function of excitation light's wavelength. This type of spectroscopy has proven useful to study electronic transitions of small carbocations.[156,171,234] In this chapter, the experimental approach is outlined, followed by a description of electronic spectroscopy, photodissociation, and the messenger tagging technique that greatly enhances the scope of molecules that can be characterized through REPD spectroscopy. The final section of this chapter discusses quantum chemical calculations that have been conducted to help interpret the experimental spectra.

2.1 Experimental methods

The REPD spectra presented in this work were obtained using the custom-built tandem mass spectrometer, illustrated in Figure 2.1.[263] An overview of the experimental approach is provided here, with descriptions of the major components of the apparatus given below (Sections 2.1.1 - 2.1.5).

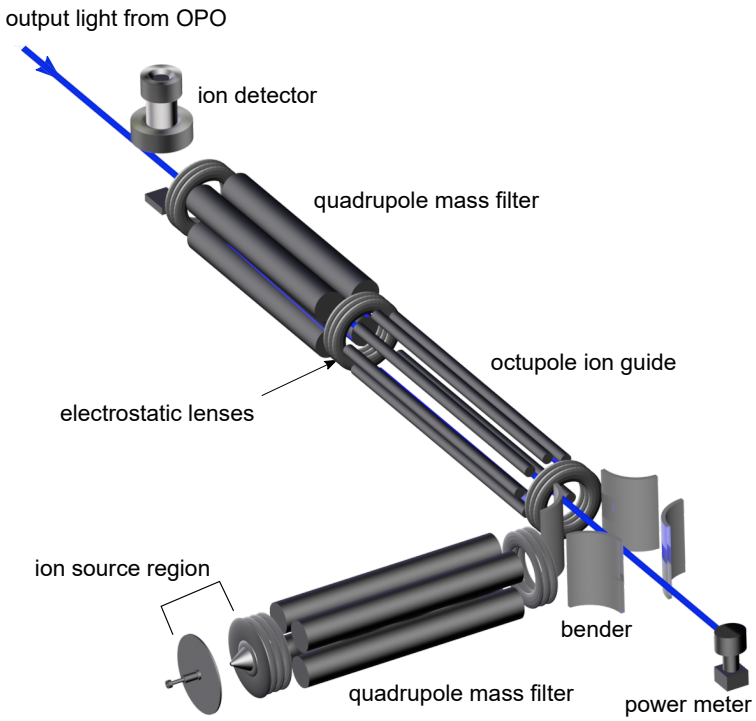

Fig. 2.1 Schematic diagram of the tandem mass spectrometer used in this work to record REPD spectra of carbocations.

A gas mixture of ≈ 0.7% acetylene in Ar (or Ne or N_2) was typically used to produce the $C_4H_2^+$, $C_4H_4^+$, and $C_6H_4^+$ ions described in Chapters 3, 4, and 6, respectively, whereas a brominated precursor (3-bromo-1-butyne in Ar) was used to generate $C_4H_5^+$ cations described in Chapter 5. In each study, the gas mixture, with a stagnation pressure of 4.5 bar, was pulsed into a low pressure chamber to form a supersonic expansion that was intercepted by ionizing electrons. Complexes of the carbocations with carrier gas atoms or molecules were produced and stabilized through three-body collisions in the expansion. The charged molecules in the central part of the expansion, with vibrational and rotational temperatures of 100 and 10-30 K, respectively, were selected by a skimmer and then focused using a set of electrostatic lenses. Cations of interest were selected using a quadrupole mass filter and deflected 90° by

an electrostatic quadrupole bender into an octupole ion guide. There, they were exposed to counterpropagating output light from a tuneable optical parametric oscillator (OPO). The complexes photodissociate at wavelengths resonant with vibronic transitions of the ionic chromophore. The charged photofragments were selected by a second quadrupole mass filter and detected by a microchannel plate. REPD spectra were generated by plotting the photofragment signal, normalized to the laser power, as a function of wavelength.

2.1.1 Light sources

The REPD spectra presented in this work were obtained using light from an EKSPLA NT342B optical parametric oscillator (OPO). A Nd:YAG (yttrium aluminum garnet doped with neodymium Nd^{3+}) laser system produces 1064 nm light, the third harmonic of which (355 nm) is generated using two sequential deuterated potassium dihydrogen phosphate crystals and used to pump the OPO. In the OPO, each 355 nm photon is converted into a longer wavelength signal photon (410-710 nm) and idler photon (710-2600 nm) through parametric down conversion by a pair of type II barium borate (BBO) crystals. A Rochon prism separates the idler and 355 nm beams from the signal beam, which provides the visible output light for experimentation. For experiments requiring UV light, a type I BBO crystal is used for second harmonic generation of the signal beam to produce 225-295 nm light. Sum frequency generation using the signal and fundamental 1064 nm beams produces 296-410 nm light. The EKSPLA OPO delivers output light with a pulse duration of 3-5 ns, a bandwidth of $\approx 8\,\mathrm{cm}^{-1}$, and a maximum repetition rate of 20 Hz. The wavelength of the output beam was calibrated using a High Finesse Ångstrom LSA UVL wavemeter. For hole burning experiments, detailed in Section 2.1.6, hole burning light with a pulse duration of ≈ 5 ns and a 10 Hz repetition rate was provided by an Opotek Vibrant 355 LD OPO, which has components similar to those of the EKSPLA OPO system.

2.1.2 Vacuum systems

The tandem mass spectrometer relies on a diffusion pump and four turbomolecular vacuum pumps to attain the necessary low pressure. A Varian VHS6-0184 (2400 L/s) oil diffusion pump, backed by an Edwards RV12 rotary pump, evacuates the ion source chamber such that the pressure is $1 - 2.5 \times 10^{-4}$ Torr when gas is pulsed into the chamber and $\approx 10^{-6}$ Torr otherwise. A Pfeiffer Balzers TPH330 (330 L/s) turbomolecular pump evacuates the region of the first quadrupole mass filter (QMF), where the pressure is typically

$\approx 5 \times 10^{-6}$ Torr. A Leybold Turbovac 450 (450 L/s) is located beneath the electrostatic quadrupole bender and is backed by a Varian SD-700 rotary pump. Two turbomolecular pumps [Oerlikon Leybold Turbovac 151 (145 L/s) and a Pfeiffer TMH260 (230 L/s)] evacuate the octupole and detector regions, such that the pressure in the octupole region is $\approx 2 \times 10^{-7}$ Torr. These two turbomolecular pumps are backed by an Edwards RV5 rotary pump. To minimize contamination by condensible gases, liquid nitrogen cold traps are affixed near the ion source, first quadrupole, and octupole regions.

2.1.3 Ion generation

The ion source region is illustrated in Figure 2.2. Gas is pulsed into the low pressure source region at a frequency of 20 Hz using a solenoid General Valve Series 9 with an opening time of $\approx 250\,\mu$s. The early part of the isentropic gas expansion is intercepted by electrons produced by thermionic emission from two rhenium filaments (0.2 mm diameter). Molecules are ionized through direct electron impact, charge-transfer, or through Penning ionization reactions involving metastable rare gas atoms in the expansion.[152,264]

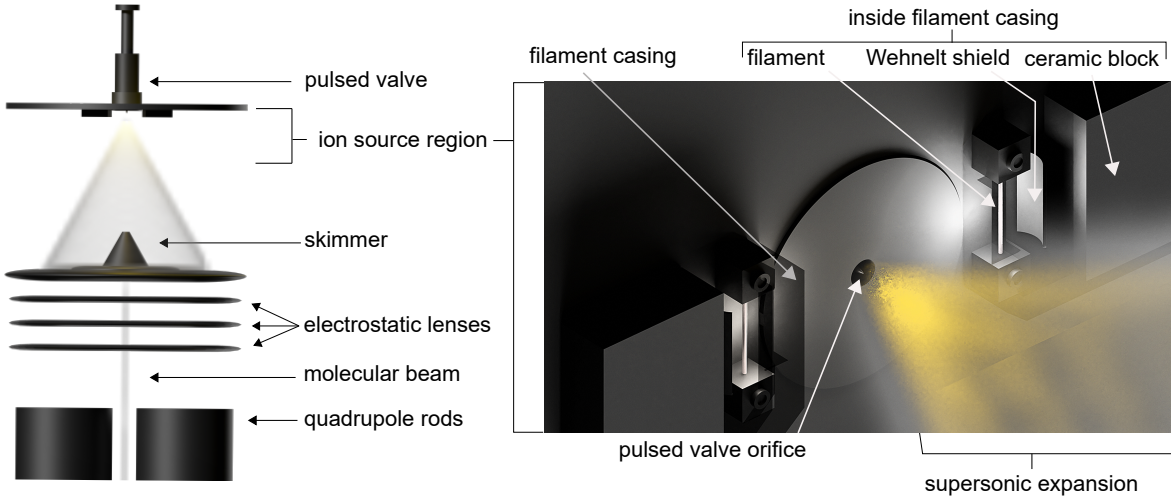

Fig. 2.2 Schematic diagram of the ion source, with the pulsed valve and filaments, from the top (left) and zoomed in at an angle (right). The filament casings are rendered partially transparent to reveal the filaments. Carbocation and ion cluster formation is influenced by the position of the pulsed valve, which controls the portion of the supersonic expansion that is bombarded by electrons. Figures are not to scale.

The valve can be moved back and forth by 10 mm, controlling the portion of the expansion that is bombarded by electrons. Three-body collisions that form charged cluster ions are more

likely to occur when the electrons intercept the expansion near the valve orifice.[152,153,265] The influence of the ionization region, and the concentration of C_2H_2 seeded in Ar on the formation of hydrocarbon ions and Ar-containing ionic clusters, has been described in previous work.[152,153,184]

The central part of the supersonic expansion is selected by a conical skimmer (Beam Dynamics, nickel, 22 mm brim diameter, 14 mm base-to-apex length, 1.5 mm orifice diameter), located 30 mm from the pulsed valve orifice (Figure 2.2). The extracted ions are focused using a set of three stacked electrostatic lenses and introduced into the first QMF (see Fig. 2.1).

2.1.4 Mass selection and beam focusing

The ion beam produced by the source is comprised of many different charged species. The selection of ions of a particular mass-to-charge ratio, *m/z*, is facilitated by quadrupole mass filters (QMFs), the first of which consists of four parallel 250 mm long (19 mm diameter) cylindrical rods (see Fig. 2.1). A radio frequency (RF) voltage and direct current (DC) offset voltage are applied to each set of opposing quadrupole rods:

$$\Psi(t) = U + V cos(2\pi f t) \tag{2.1}$$

using an Extrel (Model 14) power supply, where U is the DC voltage and V is the peak amplitude of the RF voltage with frequency f. Only ions with the selected *m/z* have stable trajectories and pass through the QMF. The transmission of the ions through the QMF is influenced by the kinetic energy of the ions, which can be controlled by a common DC bias applied to all four rods. Increasing the ion energy enhances the transmission of ions at the expense of mass selectivity.

The electrostatic quadrupole bender, comprised of four electrodes as shown in Figure 2.1, deflects the ion beam by 90°. Two additional electrodes, not shown in the figure, are located above and below the bender region to control the vertical alignment of the ion beam. Following deflection, the ions enter the octupole ion guide, which consists of eight parallel cylindrical rods 600 mm in length and 3.2 mm in diameter with centers arranged on a circle (Fig. 2.1). Alternate rods are connected to form two sets of four rods. An alternating RF voltage is applied between the two sets of rods. At an appropriate RF frequency (1.2 MHz in the REPD experiments) and amplitude, the octupole radially confines the ions as they travel down its length. A common DC voltage applied to all eight rods sets the kinetic energy of the ions.

Following exposure to light in the octupole region, the ions enter a second QMF (four parallel rods, 12 mm in diameter and 250 mm in length) that is used to mass select the photofragment ions.

2.1.5 Ion detection and data gathering

Charged photofragments exiting the second QMF are repelled upward by an electrode towards a microchannel plate (MCP, Del Mar Photonics), an electron multiplier with a gain of $\approx 10^6$. The resulting electrons bombard a phosphor-coated scintillator disc, which emits photons that are directed through a glass rod towards a photomultiplier tube (PMT). The PMT output is sent to a digital oscilloscope (Tektronix TDS 620) for signal observation and to a boxcar gated integrator (Stanford Research Systems SR250) that is connected to a National Instruments data acquisition board (DAC). Control of the light source and data acquisition is accomplished using a LabVIEW program (National Instruments, version 11) running on a PC.

2.1.6 Hole burning experiments

Sections 2.1.1 - 2.1.5 outlined the experimental approach for measuring REPD spectra. In the case that several isomers give rise to bands in the spectrum, as is the case for $C_6H_4^+$ (see Section 1.2.4 and Chapter 6), two-color hole burning (HB) experiments were conducted to identify whether particular bands arise from one isomer or another. HB experiments have proven useful in the analysis of bands in spectra of gas-phase ions[266,267] and ion complexes.[268,269]

The HB process is illustrated in Figure 2.3, which shows how vibronic transitions of isomer A (squares) are disentangled from those of isomer B (red circles). The initial step in HB experiments is to measure an REPD spectrum, shown on the left in Figure 2.3a. The solid arrows in the energy level diagram represent vibronic excitations induced by the exposure of the isomers to the probe light in the octupole, giving rise to bands in the spectrum. Bands associated with transitions of isomer B are highlighted by red ovals.

The second step, illustrated in Figure 2.3b, is to record another REPD spectrum, but with the introduction of HB light (supplied by the output of an OPOTEK Vibrant OPO) directed along the axis of the first QMF toward the ion source and tuned to a wavelength resonant with a vibronic transition of isomer B (represented by the dotted arrow in the energy level diagram). Following absorption of HB light, isomer B photodissociates and its fragments

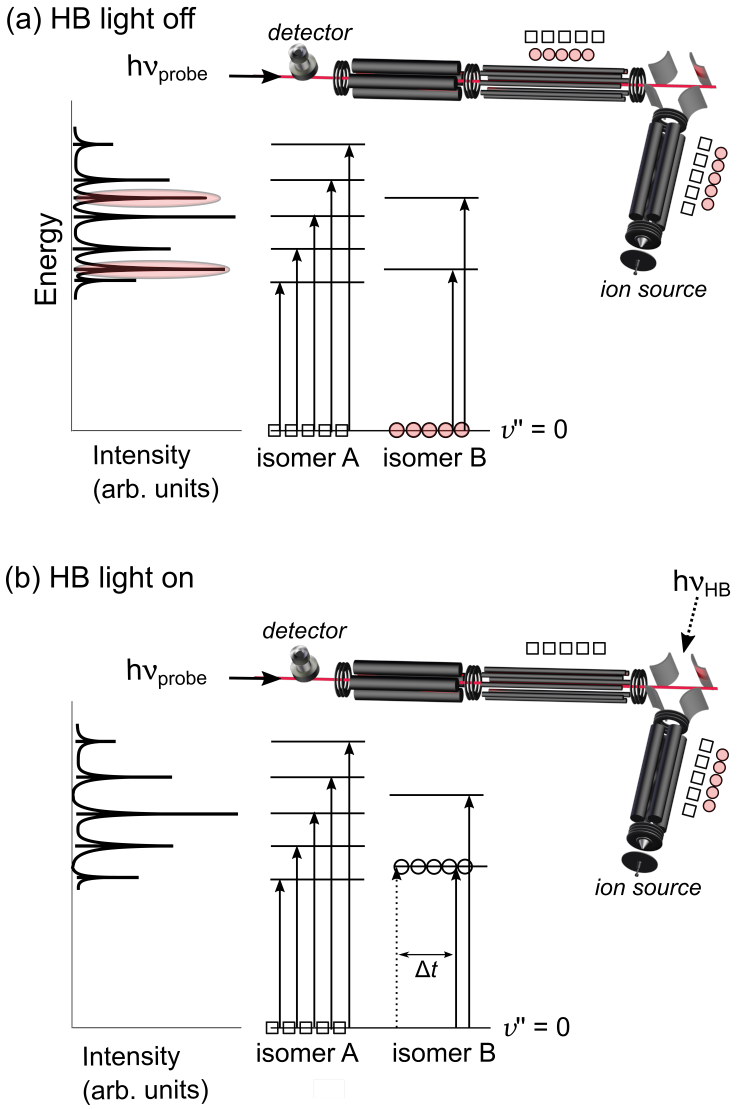

Fig. 2.3 Scheme for hole burning (HB) experiments. The effect of the HB beam (dotted arrow) on the intensity of spectral bands is assessed by comparing spectra recorded using (a) only the probe light (solid arrows) and (b) both the probe and HB light sources, with HB light tuned to a wavelength resonant with a vibronic transition. See Section 2.1 for a description of the tandem mass spectrometer.

are filtered out prior to reaching the electrostatic quadrupole bender such that the octupole is devoid of isomer B and its transitions are absent from the REPD spectrum (left side of Fig. 2.3b). Thus, comparison of band intensities in REPD spectra recorded with and without HB light (Figs. 2.3a and b) facilitates identification of bands arising from different isomers.

2.2 Concepts associated with REPD spectroscopy

2.2.1 Energy levels and nomenclature

To describe the electronic transitions measured in this work, basic details of energy levels and nomenclature associated with electronic spectroscopy are provided here. These are discussed in the context of hypothetical potential energy surfaces of a triatomic cation (ABC^+) in its ground and excited electronic states along the AB-C internuclear coordinate, shown in Figure 2.4.

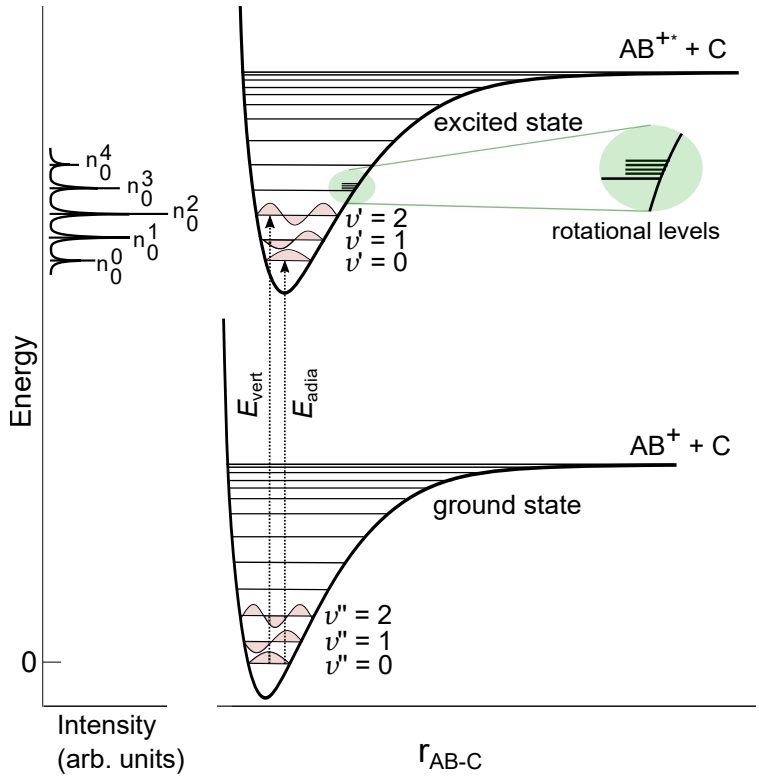

Fig. 2.4 Hypothetical potential energy curves of a cation, ABC^+, along the AB-C stretch coordinate in the ground and excited electronic states. Energies corresponding to adiabatic (E_{adia}) and vertical (E_{vert}) excitations are shown. The intensities of the bands in the spectrum, shown on the left, are dictated by the Franck-Condon principle.

Regarding the nomenclature used throughout this work, the ground electronic state of a molecule is designated as the $\tilde{X}$ state, and unless otherwise noted (as in the case of $C_4H_2^+$ discussed in Section 1.2.1 and Chapter 3), higher lying electronic states of the same multiplicity are labeled $\tilde{A}$, $\tilde{B}$, $\tilde{C}$, ... in order of increasing energy.[270] The vibrational energy levels of a molecule in the ground electronic state are referred to using the quantum number

v'' (0, 1, 2, ...) and those in an excited electronic state using the quantum number v' (0, 1, 2, ...) as shown in Figure 2.4. Vibronic transitions are denoted by $n_{v''}^{v'}$ with n corresponding to a specific vibrational normal mode, ν_n, that is defined using the Mulliken convention.[271] This convention orders vibrational modes first by symmetry based on the molecule's point group and then by frequency, such that ν_1 corresponds to the highest frequency mode with totally symmetric representation.

Rotational, vibrational, and electronic energy levels of ABC^+ are depicted in Figure 2.4, with the vibrational energy levels corresponding to the AB-C stretching vibration. In general, rotational energy levels are closely spaced and transitions between them can be induced for polar molecules by exposing them to light in the microwave region with wavelengths between 0.03 and 30 cm (30-0.03 cm^{-1}). Vibrational energy levels are spaced more widely and transitions between them, within the same electronic state, can be induced by infrared light with typical wavelengths between 100 and 2.5 μm (100-4000 cm^{-1}) if the excitation induces a net change in dipole moment. Subject to selection rules,[272] excited electronic energy levels can be accessed by exposing a molecule in its ground electronic state to visible or UV light (700-200 nm).

The vibrational energy levels can usually be described using a harmonic oscillator model. Solving the Schrödinger equation for the simple harmonic oscillator approach gives the following expression for vibrational energy levels:

$$E_v = \left(v + \frac{1}{2}\right) h\nu \tag{2.2}$$

with $v = 0, 1, 2, ...$ and with the harmonic vibrational frequency given by

$$\nu = \frac{1}{2\pi}\sqrt{\frac{k}{\mu}} \tag{2.3}$$

where k is the force constant and μ is the reduced mass. Note that in the ground vibrational state, $v = 0$, the vibrational zero-point energy (ZPE) is $\frac{1}{2}$ hν. For polyatomic molecules with several vibrational degrees of freedom, the total ZPE is the sum of the ZPEs for the individual vibrational modes.

The arrows in Figure 2.4 represent vertical and adiabatic electronic excitations of a molecule. The vertical excitation energy (E_{vert}) corresponds to the energy difference between the ground and excited electronic states with nuclear coordinates (Q) frozen to the ground

state equilibrium geometry:

$$E_{\text{vert}} = E_{\text{excited}}^{\text{Q}_{\text{eq(ground)}}} - E_{\text{ground}}^{\text{Q}_{\text{eq(ground)}}} \tag{2.4}$$

From the $v'' = 0$ vibrational level, the lowest energy electronic transition corresponds to excitation to the $v' = 0$ level (Fig. 2.4). Therefore, the adiabatic excitation energy (E_{adia}) is defined as the difference in the vibrational zero-point corrected energies of the ground and excited electronic states at their respective equilibrium geometries:[273]

$$E_{\text{adia}} = \left[E_{\text{excited}}^{\text{Q}_{\text{eq(excited)}}} + ZPE_{\text{excited}}\right] - \left[E_{\text{ground}}^{\text{Q}_{\text{eq(ground)}}} + ZPE_{\text{ground}}\right] \tag{2.5}$$

Depending upon the change in geometry between ground and excited electronic states, the difference between E_{adia} and E_{vert} can be substantial, as can be the difference in ZPEs (second term of eq. 2.5). In cases where there are small changes in the geometry and vibrational frequencies between ground and excited electronic states, E_{adia} and E_{vert} are similar.

2.2.2 Transition intensities

The intensities of vibronic transitions are dictated by the Franck-Condon principle, which is briefly formalized in this section. Subject to selection rules, an electronic transition is induced when electrons and nucleii of a molecule interact with the oscillating electric field component of incident radiation. The photon energy must correspond to the energy difference between the lower (Ψ'') and upper (Ψ') eigenstates. The strength of the interaction is described by the transition dipole moment, R:

$$R = \int \Psi'^{*}\, \hat{\mu}\, \Psi'' d\tau \tag{2.6}$$

where $\hat{\mu}$, the dipole moment operator, represents the interaction of the light with the dipole of the molecule, and $d\tau$ describes the spatial coordinates of the electrons and nucleii. If $R > 0$, the transition is electric-dipole allowed, whereas if $R = 0$ the transition is electric-dipole forbidden and is unlikely to occur.

Based on the Born-Oppenheimer approximation that electronic motion is rapid compared to nuclear motion, the total wavefunction for each eigenstate involved in a vibronic transition (neglecting rotation) can be separated into electronic (Ψ_e) and nuclear (Ψ_v) wavefunctions:

$$\Psi_{ev} = \Psi_e(q, Q)\Psi_v(Q) \tag{2.7}$$

with q and Q representing all electronic and nuclear coordinates, respectively. The dipole moment operator in eq. 2.6 is also separated into electronic and nuclear components:

$$\hat{\mu} = \hat{\mu_e} + \hat{\mu_v} \tag{2.8}$$

such that the transition dipole moment can be represented through $\hat{\mu_e}$ and $\hat{\mu_v}$ operating on Ψ_e and Ψ_v, respectively:

$$R_{ev} = \int \Psi_v'^* \Psi_v'' \, d\tau_v \int \Psi_e'^* \, \hat{\mu}_e \, \Psi_e'' \, d\tau_e + \int \Psi_e'^* \Psi_e'' \, d\tau_e \int \Psi_v'^* \, \hat{\mu}_v \, \Psi_v'' \, d\tau_v \tag{2.9}$$

For a given geometry Q, the eigenfunctions = Ψ_e'' and Ψ_e' are orthogonal to one another, rendering $\int \Psi_e'^* \Psi_e'' d\tau_e = 0$. Consequently, the second term of eq. 2.9 vanishes such that

$$R_{ev} = \int \Psi_v'^*(Q') \Psi_v''(Q'') \, d\tau_v \int \Psi_e'^*(q,Q) \, \hat{\mu}_e \, \Psi_e''(q,Q) \, d\tau_e \tag{2.10}$$

The first integral depends on the nuclear coordinates and describes the overlap of vibrational wavefunctions for the lower and upper electronic states. The second integral (R_e) depends mostly on the electronic coordinates and in the absence of vibronic coupling is the same for all vibronic transitions associated with an electronic transition. Therefore, the intensity of a vibronic transition is proportional to the Franck-Condon (FC) factor, the square of the vibrational overlap integral:[274]

$$FC\ factor \propto \left[\int \Psi_v'^*(Q) \Psi_v''(Q) d\tau_v \right]^2 \tag{2.11}$$

In the case that the potential energy functions of the ground and excited electronic states are similar, the 0_0^0 transition is the strongest of the electronic band system, as Ψ_v' ($v' = 0$) is similar to Ψ_v'' ($v'' = 0$). Alternatively, if the equilibrium geometries and vibrational levels differ substantially between electronic states, transitions from the $v'' = 0$ to several v' levels carry appreciable intensity, with the most intense transition corresponding to the vertical excitation (e.g. n_0^2 in Fig. 2.4).

FC factors, associated with vibronic transitions of a particular molecule, are predicted as part of the quantum chemical calculations, described in Section 2.3. The FC factors of the vibronic transitions are used to simulate an electronic spectrum ("molecular fingerprint")

that is characteristic of the molecule. The simulated spectrum can be compared with the REPD spectrum to identify the molecule giving rise to the bands and to assign the bands to particular vibronic transitions.

2.2.3 Deactivation of the excited electronic state

As mentioned previously, REPD spectroscopy relies on the production and detection of photofragments following excitation of a molecule with light. Dissociation is one possible consequence of photon absorption, and can be accompanied by – or be in competition with – radiative decay processes (fluorescence and phosphorescence). A simple scheme for the deactivation of gas-phase molecules is provided in the Jablonski diagram shown in Figure 2.5, which for simplicity does not include intersystem crossing between electronic states of different multiplicities. For most doublet radical cations, such as $C_4H_2^+$, $C_4H_4^+$, and $C_6H_4^+$, quartet states lie higher in energy than one or more doublet excited electronic states such that intersystem crossing and phosphorescence are generally not observed.[275] However, these pathways may play a role following excitation to higher excited electronic states.

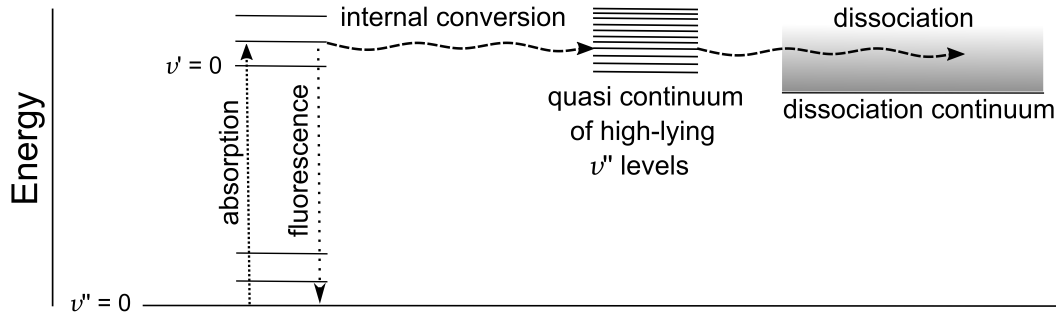

Fig. 2.5 Fluorescence and unimolecular dissociation mechanisms for an electronically excited gas-phase molecule.

The mechanisms shown in Figure 2.5 are based on the excitation of a molecule from one bound electronic state to another. A molecule in a vibrational level of the excited electronic state (v') can either fluoresce to the ground electronic state or internally convert to a quasi-continuum of high-lying vibrational levels of the ground electronic state ($v'' \gg 0$).[276] The rate of the internal conversion has been described by an energy gap law that predicts the process to be faster with larger excess internal energy and smaller energy difference between the relevant electronic states.[277] Following internal conversion to the ground state manifold, the electronic energy is redistributed into various vibrational degrees of freedom through intramolecular vibrational energy redistribution.[278,279] If the internal energy of the molecule

exceeds the energy required for dissociation, the bond is ruptured as the energy flows into the dissociation coordinate. Any remaining energy is partitioned into translational, vibrational, and rotational energies of the fragment molecules. This type of spontaneous unimolecular decomposition can be described by the Rice-Ramsperger-Kassel-Markus quasi-equilibrium theory (RRKM/QET).[275]

Unimolecular dissociation following a bound-bound excitation leads to a discrete set of bands in a recorded REPD spectrum, whereas direct dissociation, involving excitation from a bound electronic state to a repulsive electronic state, gives rise to broad bands. Note that the potential energy surfaces of bound and repulsive excited electronic states can intersect, such that an REPD spectrum exhibits narrow vibrational bands at lower energies and broader bands at higher energies. REPD spectra of $C_4H_4^+$, $C_4H_5^+$, and $C_6H_4^+$ ions (Chapters 4-6) exhibit sharp bands, demonstrating that the dissociation of these molecules over the investigated range does not occur through direct excitation to repulsive electronic states.

REPD spectra are measured by monitoring photofragment signal as a function of photon energy (see Section 2.1). Dissociation is often modeled using statistical transition state theories, which are based on the ergodicity assumption that the timescale for energy redistribution is short compared to the unimolecular reaction.[280] The unimolecular microcanonical rate coefficient, $k_{E,J}$, for a dissociation channel with a well-described ("tight") transition state is often predicted using RRKM theory:

$$k_{E,J} = \frac{N^{\ddagger}(E - E_0, J)}{h\rho(E, J)} \tag{2.12}$$

where $N^{\ddagger}$ represents the sum of rovibrational states corresponding to a transition state geometry, E is the total internal energy of the reactant, E_0 is the critical dissociation energy, h is Planck's constant, and $\rho(E, J)$ represents the density of rovibrational states of the reactant. The input values to solve for $k_{E,J}$ are normally provided by predictions from quantum chemical calculations (described in Section 2.3). For systems proceeding through looser transition states, the dissociation dynamics are often modeled using phase space theory.[281]

The resulting $k_{E,J}$ values can be incorporated into stochastic energy grain master equation calculations, which predict rate coefficients that account for temperature and pressure effects.[280] Often, these master equation simulations do not consider the angular momentum, $\overrightarrow{J}$, due to computational restrictions. It is expected that errors associated with omission of $\overrightarrow{J}$ affect the overall error less than do errors in the calculated molecular energies and frequencies.[280,282] To facilitate the calculations, rovibrational states of similar energies are

bundled into energy "grains". Master equation simulation packages, such as MultiWell[282] and MESMER,[280] account for the temperature using a diagonal matrix with elements associated with the Boltzmann distribution for each energy well. To describe the effect of collisions, the energy transfer to bath gas molecules for deactivation from an excited state with energy E' to ground state with energy E'' is described using an exponential down model:

$$P(\mathrm{E''|E'}) = \mathrm{C(E')}^{-\frac{E'-E''}{\Delta E_\mathrm{d}}} \tag{2.13}$$

where C(E′) is the normalization constraint and ΔE_d represents the average energy that is transferred in a deactivation collision.[280] The master equation is solved by diagonalizing a matrix comprised of representations of P(E|E) and k_E. The resulting eigenvalues and eigenvectors are then used to obtain rate coefficients for each dissociation channel. In the case that multiple dissociation channels are energetically accessible, the rate coefficients can be used to predict which channel is preferred. The statistically-derived branching ratio for different photofragments can be compared with the measured branching ratio.

2.2.4 Messenger tagging

For many molecules, the lower excited electronic states lie below the lowest dissociation asymptote so that unimolecular decomposition following excitation to such states is not possible. For example, in the case of the diacetylene cation (HC_4H^+) the energy of the $C_4H^+ + H$ dissociation limit, calculated to be ≈ 6.55 eV at the ωB97X-D/aug-cc-pVTZ level of theory, lies above several lower excited electronic states (see Section 1.2.1). Therefore, transitions to these states cannot be measured using single photon REPD spectroscopy.

The messenger tagging technique[283–285] circumvents the limitations imposed by high-energy intramolecular dissociation thresholds. Normally, a ligand such as He, Ne, Ar, or N_2 is attached to the target ion to form a complex with a low intermolecular dissociation energy, D_0, typically in the 100-1000 cm^{-1} range. Following photoexcitation of the ionic complex, the weak intermolecular bond is severed following vibrational energy redistribution or fluorescence to a vibrationally excited level (Figure 2.6).[286] A REPD spectrum of messenger-tagged ions are obtained by monitoring production of the core "bare" ion as a function of wavelength.

A weakly attached ligand only slightly perturbs the geometry and energy levels of the core chromophore ion. Minor red- or blue-shifting of bands may occur, depending on the relative binding energy in the ground and excited states (D_0'' and D_0', respectively). The low binding

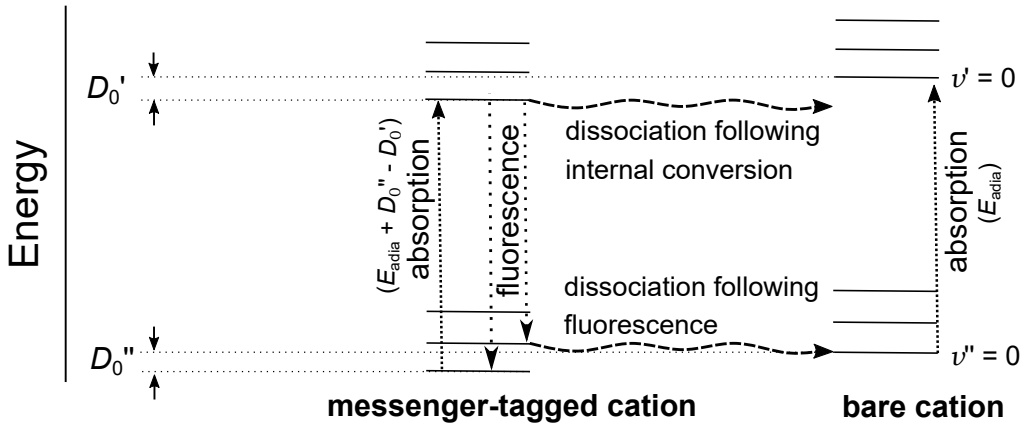

Fig. 2.6 Energy level diagram for a messenger-tagged complex and the bare cation chromophore. The complex has binding energies D_0'' and D_0' in the ground and excited electronic states, respectively.

energy of a ligand also restricts the internal energy of the complexes, as complexes with vibrational energy exceeding D_0'' are not stable. Therefore, REPD spectra of chromophore cations tagged with rare gas atoms (or N_2) typically exhibit minimal contributions from hot bands.[287]

2.3 Computational approach

2.3.1 Exploring the ground state potential energy surface: *ab initio* and density function theory calculations

Interpretation of measured REPD spectra is aided by predictions from quantum chemical calculations, which were conducted using the Gaussian,[288] Psi4,[289] and ORCA[290] programs. *Ab initio* and density functional theory (DFT) methods are used throughout this work to calculate energies, equilibrium geometries, and vibrational frequencies of stable minima, intermediates, transition states, and photofragments.

Ab initio methods are based on Hartree-Fock (HF) calculations, which approximate the wavefunction using a single Slater determinant, simplifying the many-body problem by considering the average potential experienced by a single electron in the presence of other electrons (mean-field or central-field approximation). As a result, HF calculations do not explicitly address electron correlation effects resulting from electron-electron repulsion, with the omission being the major source of error. Electron-correlated *ab initio* calculations

achieve higher accuracy than HF calculations alone. Møller-Plesset (MP_n) calculations introduce a perturbation, based on the Rayleigh-Schrödinger perturbation theory, to the zeroth-order wavefunction obtained as the eigenfunction of the Fock operator, with n being the order of the correlation potential.[291] Coupled-cluster (CC) calculations take the HF molecular orbital approach, but solve for multi-electron wavefunctions through the use of an exponential cluster operator, T, that accounts for electron correlation:

$$T = 1 + T_1 + T_2 \ldots \tag{2.14}$$

where 1 is the reference wavefunction, and T_1 and T_2 are the operators of single and double excitations, respectively. CCSD (coupled-cluster singles and doubles) uses T_1 and T_2, whereas CCSDT introduces the operator for triple excitations, T_3.[292] The most accurate, commonly used method available for small molecules is considered to be CCSD(T), which involves CCSD calculations with an additional 5^{th} order MP term.

Density functional theory (DFT) is an alternative to *ab initio* calculations and is based on the Hohenberg-Kohn theory that the energy of a molecule can be determined by its electron density, ρ(r). Kohn-Sham DFT calculations combine HF methods with density-based exchange-correlation functionals and electrostatic theory, which is used to solve for the Coulomb attraction between electrons and nuclei and repulsion between electrons. The major drawback of DFT is that the exact functionals are not yet known, and therefore are fitted to measured physical properties.[293] Third generation functionals take into account the electron density, its gradient (first derivative), and Laplacian (second derivative). Because the calculation of the Laplacian is challenging, "hybrid" DFT calculations are supported by HF-calculated exchange energy, with its contribution to DFT able to be varied. Fourth generation DFT functionals include dispersion-corrected (DFT-D) density functionals with nonlocal exchange operators, facilitating calculations of van der Waals complexes.[294] Simple calculations to account for basis set superposition errors (BSSE) are often conducted in conjunction with DFT to improve predictions of binding energies.[295,296] A benefit of DFT calculations is that the electron density is independent of the number of electrons in the system, and therefore the resources required for the calculations do not scale in the same way as *ab initio* calculations, rendering DFT less computationally expensive. Although the calculated geometries and vibrational frequencies derived from DFT calculations are generally expected to be as accurate as MP2 calculations, there is a slight sacrifice in the accuracy of energies.

2.3.2 Exploring the excited state potential energy surface: TD-DFT and EOM-CCSD methods

In this work, structural and energetic information associated with electronically excited cations are predicted through the use of time-dependent DFT (TD-DFT) and equation of motion (EOM) methods. Calculating excited state properties requires reliable predictions of ground state equilibrium geometries ($Q_{eq(ground)}$), with TD-DFT using DFT-calculated geometries and EOM relying on geometries determined using CCSD.

Initial calculations of vertical excitation energies (see Fig. 2.4) and oscillator strengths help identify whether electronic transitions occur over a particular energy range. TD-DFT methods make use of a linear-response Casida expression to calculate the vertical excitation energy:

$$\begin{bmatrix} A & B \\ B^* & A^* \end{bmatrix} \begin{bmatrix} \vec{X_I} \\ \vec{Y_I} \end{bmatrix} = \omega_I \begin{bmatrix} 1 & 0 \\ 0 & -1 \end{bmatrix} \begin{bmatrix} \vec{X_I} \\ \vec{Y_I} \end{bmatrix} \tag{2.15}$$

where A and B matrices are associated with excitations and deexcitations, respectively, and ω_I gives the energy difference between the electronic ground and excited states.[297,298] The response of the density matrix to the electric field is given by $\overrightarrow{X_I}$ and $\overrightarrow{Y_I}$. Following these initial calculations, further information can be obtained by optimizing the geometry of a selected electronic state, through the use of analytic gradients,[299–301] and calculating harmonic vibrational frequencies. The calculations are used to predict the adiabatic electronic excitation energy and intensities of vibronic transitions in the band system (see following section).

The single-reference, time-independent EOM method was initially formalized by Emrich[302,303] and further developed by Sekino and Bartlett.[304] It is based on an excitation operator acting on the coupled-cluster (CC) ground state wavefunction derived using a single Slater determinant.[305] The excited state wavefunctions are obtained through diagonalization of an effective Hamiltonian, an approach similar to that used by the configuration interaction (CI) method, with the major difference being that the Hamiltonian for EOM is non-Hermitian and has left- and right-hand eigenvectors.[306–309] Although EOM methods are more accurate than TD-DFT methods for the calculation of excited state properties, they are computationally expensive. EOM-CCSD, the least computationally expensive of the EOM methods, is known to slightly overestimate excitation energies compared to experimental values.[310]

2.3.3 Franck-Condon (FC) simulations

Energies and intensities (Franck-Condon factors, eq. 2.11) of vibronic transitions can be determined based on the calculated geometries and frequencies for the molecule in the ground and excited states.[298] Harmonic vibrational frequencies and coordinates associated with the optimized geometries of the ground and excited electronic states, $Q_{eq(ground)}$ and $Q_{eq(excited)}$, are used to compute Franck-Condon (FC) factors within the Gaussian 16[288] and PGOPHER[311] programs. The $Q_{eq(ground)}$ and $Q_{eq(excited)}$ coordinates are related through a linear transformation:[298]

$$Q_{eq(ground)} = JQ_{eq(excited)} + K \tag{2.16}$$

where J is defined as the Duschinsky rotation matrix,[312] and K is the displacement vector, describing change in equilibrium geometries projected onto the $Q_{eq(ground)}$ normal modes. The vibronic structure is then predicted using the time-independent approach with a sum-over-states (Fermi's Golden Rule) expression, with FC factors determined from the overlap of vibrational wavefunctions (eq. 2.11). Normally, the calculated stick spectrum is convoluted with a Lorentzian function to facilitate comparison with the experimental spectrum.

Chapter 3

Electronic spectra of diacetylene cations (HC_4H^+) tagged with Ar and N_2

Introduction to Chapter 3

This contents of this chapter have been published and are reprinted with permission from:

> G. Muller, K. J. Catani, M. S. Scholz, U. Jacovella, N. I. Bartlett, E.J. Bieske, "Electronic Spectra of Diacetylene Cations (HC_4H^+) Tagged with Ar and N_2" *Journal of Physical Chemistry A*, **123 (33)**, 7228-7236, 2019.

Copyright 2019 American Chemical Society. Supporting information (SI), published along with the article, is reproduced in Section 3.6. The publication in its original form is provided in the Appendix (page 209).

Article begins here

Abstract

Electronic spectra of mass-selected HC_4H^+-Ar_n (n=1-3) and HC_4H^+-$(N_2)_n$ (n=1-2) complexes are measured over the 290-530 nm range using resonance-enhanced photodissociation spectroscopy in a tandem mass spectrometer. Vibronic transitions in the visible region are compared with previous experimental and theoretical results for the $\tilde{A}^2\Pi_u \leftarrow \tilde{X}^2\Pi_g$ band system of HC_4H^+. Hole burning experiments confirm that transitions over the 290-340 nm range involve the diacetylene cation (HC_4H^+). Based on previous experiments and comparison with spectra of isoelectronic molecules the peaks are assigned to the $2^2\Pi_u \leftarrow \tilde{X}^2\Pi_g$ band system, with the origin transition for HC_4H^+-Ar occurring at 29723 cm^{-1}. The main progression has a spacing of 906 cm^{-1} and is assigned to the symmetric C-C stretch vibrational mode (ν_3). Assignment of additional bands is complicated by spectral congestion, the possible presence of energetically close-lying electronic states, vibronic coupling effects, and by the fact that HC_4H^+ possibly becomes non-linear in the $2^2\Pi_u$ state.

3.1 Introduction

Small reactive hydrocarbon molecules have been detected in extraterrestrial environments and are believed to contribute to the formation of benzene and larger molecules, including polycyclic aromatic hydrocarbons.[13,14,52,130,131,175,313–315] Hydrocarbon cations, formed through photoionization by cosmic rays or ultraviolet (UV) stellar light, may also play a chemical role by participating in ion-molecule interactions and dissociation processes.[45,162,316]

The diacetylene radical cation (HC_4H^+) is one of the smallest products from acetylene ion-molecule reactions, presumably generated through formation of the $(HCCH)_2^+$ dimer cation followed by H_2 loss.[135,136,151,152,179,180,317–319] It can also be generated from ionization of neutral HC_4H, which is believed to form in extraterrestrial environments through the reaction of acetylene with the ethynyl radical (C_2H).[320] Therefore, HC_4H^+ is expected to exist in environments where acetylene and diacetylene molecules are abundant and exposed to strong UV radiation.[192] The diacetylene cation may play a part in the chemistry of proto-planetary nebulae and has been included in atmospheric models of Titan.[321] It was

once considered as a carrier of diffuse interstellar bands, although this hypothesis was later discounted based on laboratory spectra.[103,170,321–324]

In 1951, Schüler recorded emission spectra of organic vapors in a discharge tube,[166] and the so-called "T" spectrum was later assigned by Callomon[167] to the $\tilde{A}^2\Pi_u \leftarrow \tilde{X}^2\Pi_g$ band system of HC_4H^+, with the origin transition located at 19724.5 cm^{-1}. Strong vibronic transitions were attributed to the C-C stretch (ν_3) progression and even quanta of the doubly degenerate bending mode (ν_7), which gains intensity through Fermi resonance with ν_3. Since then, many theoretical and spectroscopic investigations have focused on the $\tilde{A}^2\Pi_u$ state, which arises from the promotion of an electron from the second highest occupied molecular orbital (HOMO-1, π_u) to the HOMO (π_g).[164,169,171–173,325–327]

Much less is known about the higher excited states of HC_4H^+ which arise from promotion of an electron from the HOMO to the lowest unoccupied molecular orbital (LUMO) giving a dominant electronic configuration $...1(\pi_u)^4 1(\pi_g)^2 2(\pi_u)^1$ associated with five non-Koopmans' states ($^4\Pi_u$, $^2\Pi_u$, $^2\Phi_u$, $^2\Pi_u$, $^2\Pi_u$). Electronic transitions from the ground $^2\Pi_g$ state to the three $^2\Pi_u$ states are spin and dipole allowed and therefore should be observable. Based on previous calculations, two of the $^2\Pi_u$ states and the $^2\Phi_u$ state are predicted to have similar energies, whereas the third $^2\Pi_u$ state is predicted to lie significantly higher in energy.[173] Because the energetic ordering of the states is unclear, it is useful to adopt the notation used in ref. 173 to describe states above $\tilde{A}^2\Pi_u$. Namely, the electronic states are labeled as $n^S\Gamma$, where n is the state energetic order of a given symmetry, S is the spin multiplicity and Γ is the symmetry of the state. With this nomenclature the five lowest doublet excited states are $\tilde{A}^2\Pi_u$, $2^2\Pi_u$, $1^2\Phi_u$, $3^2\Pi_u$, and $4^2\Pi_u$.

As non-Koopmans' excited states are not usually accessible through photoionization of the neutral diacetylene molecule, photoelectron spectra display a gap of ≈ 4 eV between the $\tilde{A}^2\Pi_u$ state and the next accessible excited state.[165,172,328] Observation of the non-Koopmans' electronic states lying within the gap relies on electronic spectroscopy of the HC_4H^+ cation. The $2^2\Pi_u \leftarrow \tilde{X}^2\Pi_g$ transition of HC_4H^+ was reported to occur at 3.75 eV for HC_4H^+ embedded in an argon matrix,[173] and at 3.69 eV for HC_4H^+ in a neon matrix.[174] Assignment of bands lying above the $2^2\Pi_u \leftarrow \tilde{X}^2\Pi_g$ origin transition in the matrix spectra, which may be due to transitions to higher vibrational states or other electronic states, is problematic due to congestion and relatively poor signal to noise ratio.

The uncertainty regarding the location and assignment of the higher lying states represents a primary motivation for the current study – a more comprehensive understanding of electronic transitions of HC_4H^+ in the UV. As a step in this direction, we have measured

photodissociation action spectra of HC_4H^+-Ar and HC_4H^+-N_2 complexes in a tandem mass spectrometer over the 290-540 nm range. Transitions between 290 and 340 nm are recorded for the first time in the gas phase. To ensure that the measured UV bands are indeed associated with the diacetylene cation, we conducted hole burning experiments, depleting the HC_4H^+-Ar population by pumping the origin of the $\tilde{A}^2\Pi_u \leftarrow \tilde{X}^2\Pi_g$ band system. Interpretation of bands in the UV relies on comparisons with spectra of isoelectronic ions $NCCN^+$ and C_4^- and excited state calculations for HC_4H^+.[171,174,329–334]

3.2 Experimental methods

Electronic spectra of HC_4H^+-Ar_n (n=1-3) and HC_4H^+-$(N_2)_n$ (n=1-2) were recorded using resonance-enhanced photodissociation (REPD) spectroscopy in a custom-built tandem quadrupole-octupole-quadrupole mass spectrometer described previously.[263] A brief overview of the arrangement is provided below. A dilute mixture of Ar or N_2 with acetylene ($\approx 0.7\%$), with a stagnation pressure of 4.5 bar, was expanded into a vacuum via a pulsed valve. The supersonic expansion was bombarded with electrons issuing from twin filaments to generate carbocations and tagged complexes, including HC_4H^+-Ar_n (n=1-3) and HC_4H^+-$(N_2)_n$ (n=1-2). After passing through a skimmer, the charged complexes were mass-selected using a quadrupole mass filter and then directed into an octupole ion guide using an electrostatic quadrupole bender. Here, the ions encountered light from a tunable optical parametric oscillator (OPO, EKSPLA NT342B). Resonant excitation of the HC_4H^+ chromophore induced photodissociation of the tagged complexes. The resulting HC_4H^+ cations were mass-selected by a second quadrupole mass filter and detected with a microchannel plate. A photodissociation action spectrum was generated by plotting fragment ion intensity as a function of wavelength. The intensity of the photofragment signal was normalized by laser power at each wavelength. The wavelength was calibrated using a wavemeter (High Finesse Ångstrom LSA UVL).

Hole burning (HB) experiments were conducted for HC_4H^+-Ar complexes to confirm that bands between 290 and 350 nm are associated with transitions of the diacetylene cation. A HB light beam (generated by a tunable OPO, Opotek Vibrant 355 LD) directed along the axis of the first quadrupole mass filter was tuned to the $\tilde{A}^2\Pi_u \leftarrow \tilde{X}^2\Pi_g$ band origin (506.4 nm). The HB beam should deplete the population of HC_4H^+-Ar ions in the octupole region but leave the populations of other isobaric ions unaffected. To assess the effect of the HB light

on the intensities of the bands, spectra were recorded with the HB light off and on. A more complete description of the setup is provided in the supporting information (SI).

3.3 Results and discussion

3.3.1 Calculated properties

Quantum chemical calculations were used to evaluate the ground and excited state electronic structures of the diacetylene radical cation. The equilibrium geometry and harmonic vibrational frequencies of ground state HC_4H^+ were determined at the CCSD/cc-pCVTZ level of theory, employing the Psi4 1.1 program suite.[289] The HC_4H^+ molecule in its ground $\tilde{X}^2\Pi_g$ electronic state was calculated to be linear and centrosymmetric with the dominant electronic configuration $...5(\sigma_g)^2 4(\sigma_u)^2 1(\pi_u)^4 1(\pi_g)^3$. Vibrational frequencies of HC_4H^+ in the $\tilde{X}^2\Pi_g$ state, provided in Table 3.1, agree with results of previous theoretical investigations.[163,164]

Table 3.1 Calculated harmonic vibrational frequencies (cm^{-1}) of HC_4H^+ in the $\tilde{X}^2\Pi_g$ and $\tilde{A}^2\Pi_u$ states. All frequencies are unscaled.

Mode	Description	$\tilde{X}^2\Pi_g$ †	$\tilde{A}^2\Pi_u$ ‡
ν_1, σ_g	C–H symm. stretch	3390	3395
ν_2, σ_g	C≡C symm. stretch	2283	2144
ν_3, σ_g	C–C symm. stretch	956	846
ν_4, σ_u	C–H antisymm. stretch	3389	3394
ν_5, σ_u	C≡C antisymm. stretch	2015	2040
ν_6, π_g	*trans* H–C_4–H bend	737	653
ν_7, π_g	*trans* C≡C–C≡C bend	477	444
ν_8, π_u	*cis* H–C_4–H bend	786	644
ν_9, π_u	*cis* C≡C–C≡C bend	210	233

†CCSD/cc-pCVTZ
‡EOM-CCSD/cc-pCVTZ

Vertical excitation energies and oscillator strengths calculated at the EOM-CCSD/cc-pCVTZ level predict that the strong $\tilde{A}^2\Pi_u \leftarrow \tilde{X}^2\Pi_g$ transition occurs at 2.62 eV, and involves promotion of an electron from the $1\pi_u$ orbital to the singly occupied HOMO $1\pi_g$ orbital. The equilibrium geometry and harmonic vibrational frequencies of the $\tilde{A}^2\Pi_u$ state were calculated at the EOM-CCSD/cc-pCVTZ level. Our calculations predict a linear geometry

for HC_4H^+ in the $\tilde{A}^2\Pi_u$ state, agreeing with previous studies.[335,336] Calculated vibrational frequencies for HC_4H^+ in the $\tilde{A}^2\Pi_u$ state are provided in Table 3.1. The adiabatic excitation energy, including vibrational zero point energy, was determined to be 2.45 eV (Table 3.2), matching the previously measured energy of the $\tilde{A}^2\Pi_u \leftarrow \tilde{X}^2\Pi_g$ origin transition of HC_4H^+ at 19722.6 cm^{-1} (2.45 eV).[337]

The $2^2\Pi_u$, $1^2\Phi_u$, and $3^2\Pi_u$ states were predicted to have vertical excitation energies of 3.93, 4.53, and 5.21 eV, respectively, and correspond to HOMO → LUMO electronic excitations. As noted above, the three electronic states have the same dominant electronic configuration. These excited states were previously studied by Zhang *et al.*[338] using the CASSCF/CASPT2 approach, where the third excited state was assigned as a $^2\Pi_u$ state. The alternative assignment of the third doublet state to $1^2\Phi_u$ (as described in Table 3.2) accords with the calculations in ref. 173, and is consistent with the low predicted oscillator strength for the transition from the ground state.

Table 3.2 Adiabatic (underlined) and vertical excitation energies, and oscillator strengths (f) for HC_4H^+ calculated in this work and from ref. 338. Energies (eV) are relative to the ground ($\tilde{X}^2\Pi_g$) electronic state. Experimental energies for HC_4H^+-Ar are also included.

State	Energy		f^a
	Calc	Exp	
$\tilde{A}^2\Pi_u$	2.62[a], <u>2.45</u>[b]	2.45[c]	3.08x10^{-2}
$2^2\Pi_u$	3.93[a]	3.69[c]	2.48x10^{-2}
$1^2\Phi_u$	4.53[a]		8.98x10^{-6}
$3^2\Pi_u$	5.21[a]		2.17x10^{-2}

[a]CASSCF/CASPT2/cc-pVTZ (from ref. 338)
[b]EOM-CCSD/cc-pCVTZ (this work)
[c]Experimental value for HC_4H^+-Ar (this work)

Understanding spectra arising from transitions to these excited states is complicated by Renner-Teller (RT) interactions. The RT effect is apparently weak for the $\tilde{X}^2\Pi_g$ and $\tilde{A}^2\Pi_u$ states, which split into linear/linear pairs.[336] However, the effects of RT interactions on higher states of HC_4H^+ are unknown. To explore the importance of RT interactions for the $2^2\Pi_u$ state of HC_4H^+, quantum mechanical calculations were conducted using the complete active space self consistent field (CASSCF) method with the the cc-pVTZ basis set in the ORCA suite.[290,339] An active space of 7 electrons and 8 π orbitals was chosen to investigate the $\tilde{X}^2\Pi_g$, $\tilde{A}^2\Pi_u$, and $2^2\Pi_u$ states. First, the geometry of the $\tilde{X}^2\Pi_g$ state was optimized, resulting in a linear structure. The relative energies for each of the two RT components in the

$\tilde{X}^2\Pi_g$, $\tilde{A}^2\Pi_u$, and $2^2\Pi_u$ states were calculated by stepping along the CASSCF ground state normal coordinates for ν_6 (*trans* H–C_4–H bend), ν_7 (*trans* C≡C–C≡C bend), ν_8 (*cis* H–C_4–H bend), and ν_9 (*cis* C≡C–C≡C bend). These potential energy curves and their significance are discussed below.

To understand the interactions between HC_4H^+ and Ar and N_2, the structures and energies of the HC_4H^+-Ar and HC_4H^+-N_2 complexes were calculated using density functional theory (DFT) at the ωB97X-D/aug-cc-pVTZ[340] level using the Gaussian 09 suite.[341] This method accounts for long-range dispersion interactions and is suitable for non-covalently bound complexes.[342] The calculated binding energies account for vibrational zero point energy (within the harmonic approximation) and include counterpoise corrections to address basis set superposition errors.[295] Calculations indicate that Ar and N_2 can attach to HC_4H^+ either end-on or side-on, as shown in Figure 3.1. As shown by Botschwina and Oswald,[343] the non-linear isomer is associated with a $^2A'$ electronic substate arising when the $^2\Pi_g$ state degeneracy is broken through the presence of an off-axis perturber. These two configurations are predicted to have similar binding energies of $\approx 460\,cm^{-1}$ for HC_4H^+-Ar. This agrees with a previous computational study on HC_4H^+-Ar, in which a binding energy of $\approx 500\,cm^{-1}$ was predicted for the linear structure with the non-linear structure being slightly less stable.[343] For HC_4H^+-N_2, the $C_{\infty v}$ linear structure with the N_2 tag positioned along the intermolecular axis (Figure 3.1c) is predicted to be $276\,cm^{-1}$ more stable than the C_s structure (Figure 3.1d). Because the intermolecular bonds in HC_4H^+-Ar and HC_4H^+-N_2 complexes are relatively weak and the HC_4H^+ core is only slightly distorted, the REPD spectra of HC_4H^+-Ar and HC_4H^+-N_2 are expected to resemble closely the absorption spectrum of the bare HC_4H^+ molecule. Optimized structures and calculated energies of complexes with several Ar and N_2 tags are described in the SI.

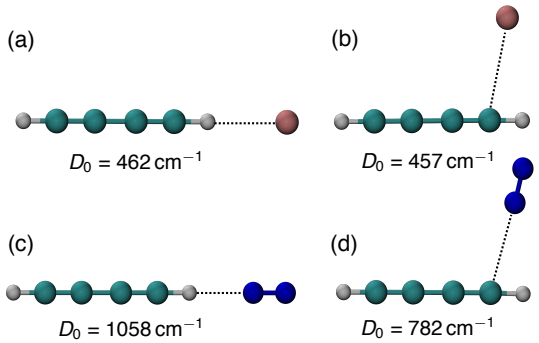

Fig. 3.1 Optimized structures of HC_4H^+ tagged with Ar (a and b) and N_2 (c and d). The calculated dissociation energy (D_0) is listed in each case.

3.3.2 Electronic spectra

Figure 3.2 depicts the electronic spectrum of HC_4H^+-Ar over the visible and UV regions encompassing the $\tilde{A}^2\Pi_u \leftarrow \tilde{X}^2\Pi_g$ and $2^2\Pi_u \leftarrow \tilde{X}^2\Pi_g$ band systems, respectively. Transitions in the UV are approximately ten times weaker than those in the visible region.

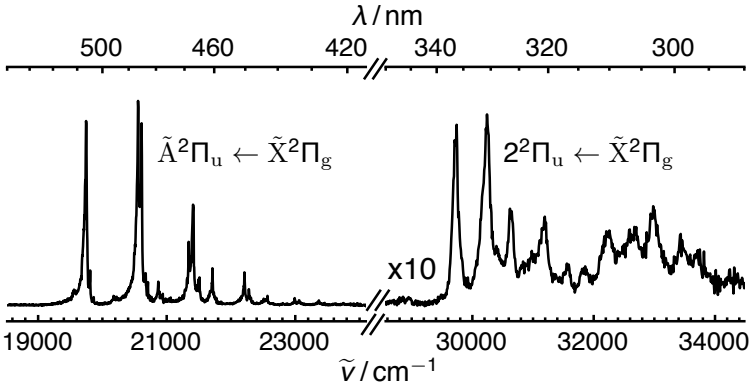

Fig. 3.2 REPD spectra of HC_4H^+-Ar over the 425-530 nm (left) and 290-350 nm (right) ranges obtained by monitoring HC_4H^+ photofragments. The $\tilde{A}^2\Pi_u \leftarrow \tilde{X}^2\Pi_g$ origin transition at 506 nm is estimated to be ≈ 10 times stronger than the $2^2\Pi_u \leftarrow \tilde{X}^2\Pi_g$ origin transition at 336 nm.

The $\tilde{A}^2\Pi_u \leftarrow \tilde{X}^2\Pi_g$ band system (425-530 nm)

We first consider the well-known $\tilde{A}^2\Pi_u \leftarrow \tilde{X}^2\Pi_g$ band system. REPD spectra of HC_4H^+-N_2 and HC_4H^+-Ar complexes over the 425-530 nm range are shown in Figure 3.3 panels a and b, respectively. Because the tagged ions are at low temperature and A_{SO}=-31.1 cm^{-1},[327] the population of the Ω=1/2 spin-orbit component in the ground state should be negligible and transitions should predominately occur from the Ω=3/2 substate with ΔΩ=0 (Hund's case a). Assignments, positions, and spacings of vibronic bands are listed in Table 3.3. Assignments are based on previous studies and comparisons with the simulated spectrum presented in Figure 3.3c.[167,169,171,172] Corresponding spectra for larger HC_4H^+-Ar_n and HC_4H^+-$(N_2)_n$ complexes are provided in the SI.

The spectra of HC_4H^+-Ar and HC_4H^+-N_2 closely resemble the spectrum of the bare HC_4H^+ cation aside from a small blue shift of the bands and the presence of weak additional peaks associated with excitation of intermolecular vibrational modes. The dominant progression in the $\tilde{A}^2\Pi_u \leftarrow \tilde{X}^2\Pi_g$ band system of HC_4H^+ is associated with Fermi polyads arising from the ν_3 C-C stretch vibration interacting with even quanta of the ν_7 C-C bend vibration.[167,169,171,172,325] The $3_0^1/7_0^2$ pair of transitions are observed at $0_0^0 + 809$ and 864 cm^{-1},

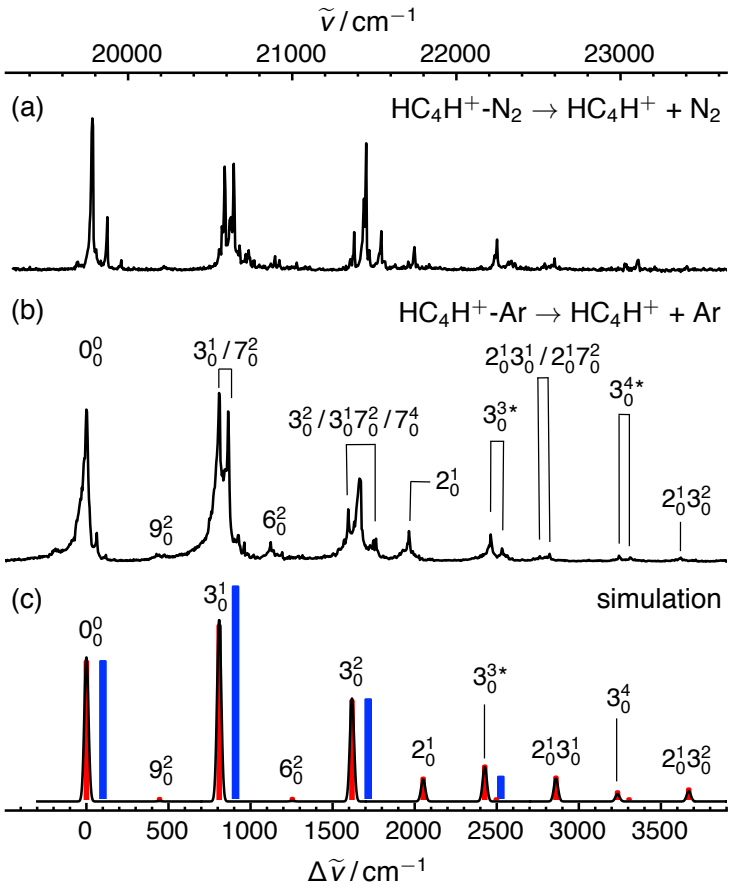

Fig. 3.3 $\tilde{A}^2\Pi_u \leftarrow \tilde{X}^2\Pi_g$ electronic spectra of (a) HC_4H^+-N_2 and (b) HC_4H^+-Ar, obtained by monitoring HC_4H^+ photofragments. (c) Predicted stick spectrum from a Franck-Condon simulation (red sticks) compared to integrated experimental intensities (rectangular blue bars) of the 3_0^n (n=1-3) polyads. Asterisks represent polyads comprised of several transitions that are not individually assigned (see text for details).

respectively, with the 55 cm^{-1} spacing between the two peaks consistent with the 56 cm^{-1} gap measured with rotational resolution using cavity ringdown spectroscopy.[325] Polyads involving ν_3 and ν_7 are observed at higher energies. For example, the $3_0^2/3_0^1 7_0^2/7_0^4$ triad occurs around 1600 cm^{-1} above the origin transition, as indicated in Figure 3.3b. These assignments agree with those in refs. 169 and 172. The groups of bands lying ≈ 2500 and ≈ 3250 cm^{-1} above the origin are assigned to the 3_0^3 and 3_0^4 polyads, respectively. More combinations are possible for higher energy polyads and detailed assignment is frustrated by congestion and low intensity of the bands. Groups of bands, for which individual vibronic transitions are not assigned, are labeled with asterisks in Figure 3.3 and Table 3.3.

The $\tilde{A}^2\Pi_u \leftarrow \tilde{X}^2\Pi_g$ band system was simulated using the PGOPHER program[311] with ground and excited state structures and vibrational frequencies derived at the CCSD/cc-pVTZ

Table 3.3 Band positions and assignments for $\tilde{A}^2\Pi_u \leftarrow \tilde{X}^2\Pi_g$ transitions of HC_4H^+-Ar_n (n=1-3) and HC_4H^+-$(N_2)_n$ (n=1-2) complexes. Asterisks denote polyads involving ν_3 and $2\nu_7$ with possible contributions from several vibronic transitions.

	HC_4H^+-Ar		HC_4H^+-Ar_2		HC_4H^+-Ar_3		HC_4H^+-N_2		HC_4H^+-$(N_2)_2$	
Assignment	$\tilde{\nu}$	$\Delta\tilde{\nu}$	$\tilde{\nu}$	$\Delta\tilde{\nu}$	$\tilde{\nu}$	$\Delta\tilde{\nu}$	$\tilde{\nu}$	$\Delta\tilde{\nu}$	$\tilde{\nu}$	$\Delta\tilde{\nu}$
s_1^0							19694	-88	19758	-59
0_0^0	19746	0	19770	0	19786	0	19782	0	19817	0
s_0^1	19808	56	19841	71			19874	85	19896	79
s_0^2	19865	119					19959	177		
9_0^2	20173	427					20219	437	20275	458
$3_0^1/7_0^2$	20555	809	20581	811	20584	798	20588	806	20639	822
$3_0^1/7_0^2$	20610	864	20636	866			20644	862	20690	873
6_0^2	20869	1123	20874	1104			20896	1114		
8_0^2							20922	1140		
$3_0^1 9_0^2$							21027	1245		
$3_0^2/3_0^1 7_0^2/7_0^4$	21342	1596	21373	1603	31382	1596	21377	1595	21425	1608
$3_0^2/3_0^1 7_0^2/7_0^4$	21410	1664	21419	1649	21455	1669	21451	1669	21499	1682
$3_0^2/3_0^1 7_0^2/7_0^4$	21497	1751	21538	1768	21552	1766	21543	1761	21578	1761
2_0^1	21711	1965	21749	1979	21745	1959	21745	1963	21789	1972
3_0^3*	22209	2463	22 228	2458	22 242	2456	22245	2463	22294	2477
3_0^3*	22278	2532					22337	2555	22364	2547
$2_0^1 3_0^1/2_0^1 7_0^2$	22509	2763					22538	2756	22581	2674
$2_0^1 3_0^1/2_0^1 7_0^2$	22569	2823					22598	2816	22642	2825
3_0^4*	22991	3245	23016	3246			23026	3244	23081	3264
$2_0^1 3_0^2$	23367	3621					23404	3622	23443	3626

and EOM-CCSD/cc-pCVTZ levels, respectively. A good match between the simulated and experimental spectra was found by scaling the calculated harmonic frequencies by 0.957. A simulated stick spectrum of the $\tilde{A}^2\Pi_u \leftarrow \tilde{X}^2\Pi_g$ band system is shown in Figure 3.3c while the corresponding convoluted spectrum (full width at half maximum of 30 cm^{-1}) is shown in black. Bands observed at $0_0^0 + 809$, 1596, 2463, and 3245 cm^{-1} correspond to the predicted positions of the 3_0^1, 3_0^2, 3_0^3, and 3_0^4 transitions, respectively. The simulation does not account for Fermi resonance interactions, in which the 7_0^m transitions borrow a fraction of the 3_0^n transition intensities. Therefore, the predicted 3_0^n transition intensities are more appropriately compared with the sum of the observed intensities for the polyad members. The comparison is

made in Figure 3.3c where the summed experimental intensities are represented as rectangular blue bars and are displaced by $\approx 100\,\mathrm{cm}^{-1}$ from the simulated bands to aid comparison.

The simulation indicates that weak bands at $0_0^0 + 427$, 1123, 1965, and $3245\,\mathrm{cm}^{-1}$ correspond to the 9_0^2, 6_0^2, 2_0^1, and 1_0^1 transitions, respectively, agreeing with previous assignments.[167,171,172,326] Predicted intensities of the 9_0^2 and 2_0^1 transitions match experimental observations, whereas the intensity of the 6_0^2 transition is underestimated. The weak 1_0^1 transition is difficult to distinguish as it overlaps the 3_0^4 polyad transitions. Overall, the good match between theory and experiment suggests that calculations at the CCSD/cc-pCVTZ and EOM-CCSD/cc-pCVTZ levels provide a reasonable description of the $\tilde{X}^2\Pi_g$ and $\tilde{A}^2\Pi_u$ state geometries and frequencies.

3.3.3 Interaction of HC_4H^+ with Ar and N_2

The $\tilde{A}^2\Pi_u \leftarrow \tilde{X}^2\Pi_g$ spectra of HC_4H^+-Ar_n (n=1-3) and HC_4H^+-$(N_2)_n$ (n=1-2) provide information on the interaction of Ar and N_2 with the HC_4H^+ cation. Figure 3.4 shows expanded views of the HC_4H^+-Ar and HC_4H^+-N_2 spectra in the region of the origin transition. In each case, a progression of minor peaks is observed with spacings that are consistent with the expected frequency for the intermolecular stretch vibrational mode (ν_s). For example, weak peaks are observed at $0_0^0 + 56$ and $119\,\mathrm{cm}^{-1}$ for the HC_4H^+-Ar complex that can be assigned to the s_0^1 and s_0^2 transitions, respectively, based on the calculated ground state ν_s frequencies of 61 and $65\,\mathrm{cm}^{-1}$ for the linear and bent structures shown in Figures 3.1a and 3.1b. For HC_4H^+-N_2, corresponding bands appear at $0_0^0 + 85$ and $177\,\mathrm{cm}^{-1}$, respectively, consistent with a predicted intermolecular stretching frequency of $97\,\mathrm{cm}^{-1}$ for the more stable linear structure (see Figure 3.1).

The $\tilde{A}^2\Pi_u \leftarrow \tilde{X}^2\Pi_g$ origin transition of HC_4H^+ occurs at $19722.6\,\mathrm{cm}^{-1}$, implying that the origin transitions of the HC_4H^+-Ar, HC_4H^+-Ar_2, and HC_4H^+-Ar_3 complexes are shifted to higher energy by 23, 47 and $63\,\mathrm{cm}^{-1}$, respectively (Figure 3.5).[337] The almost equal incremental shifts for HC_4H^+-Ar and HC_4H^+-Ar_2 indicate that the first two Ar atoms are attached at equivalent binding sites, consistent, for example, with the Ar atoms preferentially being attached to the two ends of the HC_4H^+ molecule. The $\tilde{A}^2\Pi_u \leftarrow \tilde{X}^2\Pi_g$ origin transitions of the HC_4H^+-N_2 and HC_4H^+-$(N_2)_2$ complexes are blue-shifted by 59 and $94\,\mathrm{cm}^{-1}$, respectively, relative to the origin band of HC_4H^+ (Figure 3.5). The unequal incremental band shifts indicates that either the two N_2 tags are attached at inequivalent

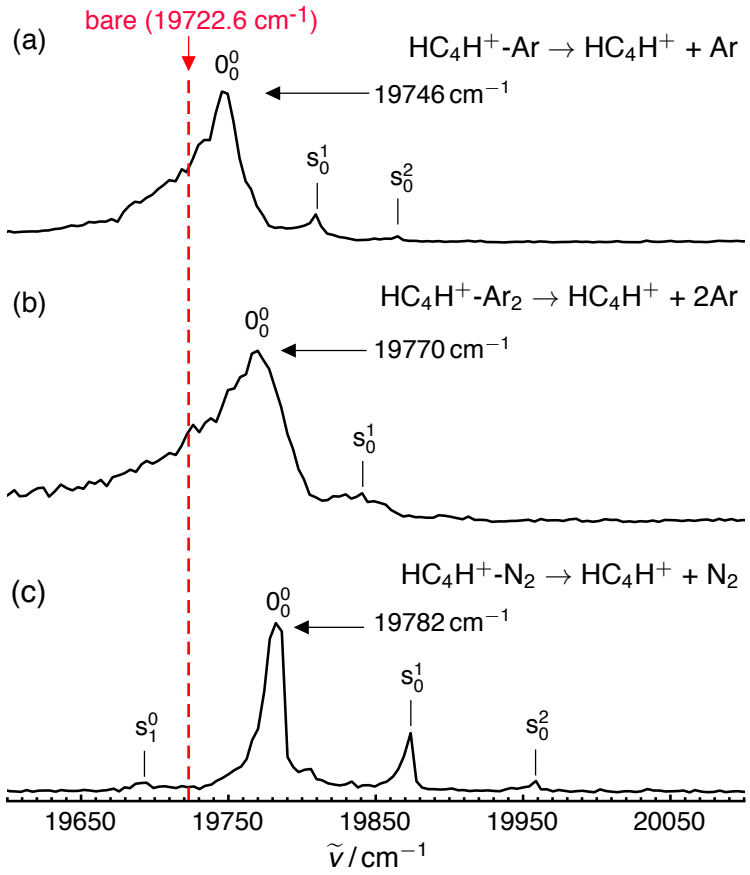

Fig. 3.4 REPD spectra near the $\tilde{A}^2\Pi_u \leftarrow \tilde{X}^2\Pi_g$ origin band for (a) HC_4H^+-Ar, (b) HC_4H^+-Ar_2, and (c) HC_4H^+-N_2. Transitions associated with intermolecular stretching vibrations are labeled. The location of the $\tilde{A}^2\Pi_u \leftarrow \tilde{X}^2\Pi_g$ origin band for bare HC_4H^+ (from ref. 337) is indicated by the dashed red line.

binding sites, or more probably that the first attached N_2 molecule significantly perturbs the HC_4H^+ core.

The blue shift of the $\tilde{A}^2\Pi_u \leftarrow \tilde{X}^2\Pi_g$ origin transition upon complexation with Ar indicates that the intermolecular HC_4H^+-Ar bond is weaker in the excited state than in the ground state. The asymmetric contour of the origin band, which is shaded to lower energy, is further evidence for a decreased intermolecular bond strength in the excited state. Hot bands involving the low energy intermolecular stretch (ν_s) and bend (ν_b) modes, such as s_1^1 and b_1^1, for example, will be shifted slightly to the red of the origin peak if the intermolecular vibrational frequencies are reduced in the excited state.

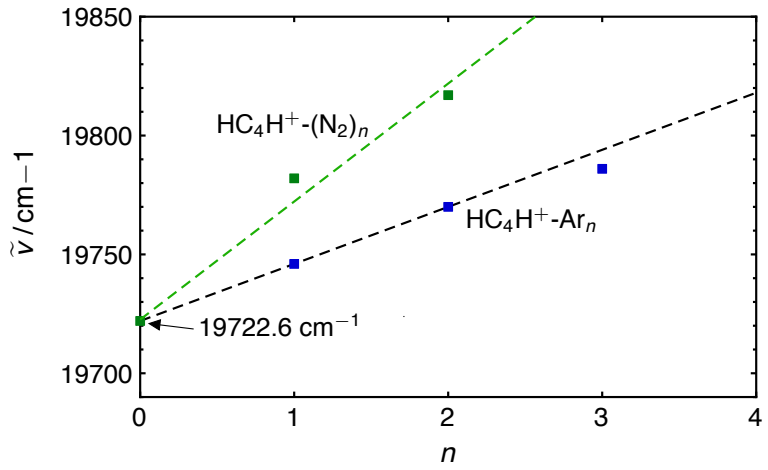

Fig. 3.5 Energies for the $\tilde{A}^2\Pi_u \leftarrow \tilde{X}^2\Pi_g$ origin transitions of HC_4H^+-Ar_n (n=1-3) plotted as a function of n. The wavenumber for the $\tilde{A}^2\Pi_u \leftarrow \tilde{X}^2\Pi_g$ origin transition of HC_4H^+(19722.6 cm^{-1} from ref. 337) is indicated.

Transitions to higher excited states in the 290-345 nm region

The electronic spectrum of HC_4H^+-Ar over the 290-345 nm range, recorded by monitoring HC_4H^+ photofragments, is shown in Figure 3.6. First it was established that all bands over the 290-345 nm range are associated with the diacetylene cation (HC_4H^+) by conducting hole burning (HB) experiments (see Section 3.2 and the SI). A spectrum of the HC_4H^+-N_2 complex was also obtained in this region (available in the SI). However, due to a mass coincidence of HC_4H^+-N_2 and $C_6H_6^+$, which was also formed in the ion source and photodissociated to yield $C_4H_2^+$ in this wavelength range, the spectrum has a poor signal-to-noise ratio.[185,344]

The HC_4H^+-Ar spectrum shown in Figure 3.6 is similar to spectra of HC_4H^+ trapped in rare gas matrices assigned to the $2^2\Pi_u \leftarrow \tilde{X}^2\Pi_g$ excitation,[173,174] although, due to a better signal-to-noise ratio and spectral resolution, additional bands are observed in the present study. Zhang *et al.*[338] predicted the $2^2\Pi_u \leftarrow \tilde{X}^2\Pi_g$ vertical excitation energy to be 3.93 eV, close to the lowest energy band at 29723 cm^{-1} (3.69 eV). The oscillator strength for the $2^2\Pi_u \leftarrow \tilde{X}^2\Pi_g$ transition was calculated to be around half that of the $\tilde{A}^2\Pi_u \leftarrow \tilde{X}^2\Pi_g$ transition (Table 3.2), consistent with the somewhat lower intensity of the UV bands compared to those in the visible (see Figure 3.2). The $2^2\Pi_u \leftarrow \tilde{X}^2\Pi_g$ origin band for HC_4H^+ in a Ne matrix reported in ref. 174 is slightly blue shifted with respect to the HC_4H^+-Ar transition (by $\approx 20\,\text{cm}^{-1}$). The forbidden $1^2\Phi_u \leftarrow \tilde{X}^2\Pi_g$ transition is also predicted to occur in this region, with a vertical excitation energy of 4.53 eV,[338] and may gain intensity via Herzberg-Teller interactions, as appears to occur for HC_6H^+.[345] The $3^2\Pi_u \leftarrow \tilde{X}^2\Pi_g$ vertical excitation energy

for HC_4H^+ is predicted to be 5.21 eV (Table 3.2),[338] suggesting that this transition is unlikely to occur within the 290-350 nm range.

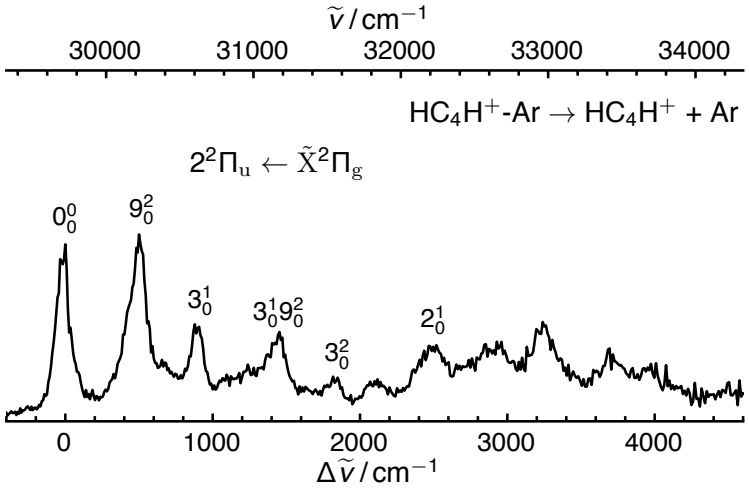

Fig. 3.6 REPD spectrum of HC_4H^+-Ar over the 290-345 nm range, obtained by monitoring HC_4H^+ photofragments. Tentative assignments are indicated. The lower lying peaks are assigned to the $2^2\Pi_u \leftarrow \tilde{X}^2\Pi_g$ system. Peak positions and assignments are given in Table 3.4.

Table 3.4 Band positions (wavenumbers) and assignments for peaks in the $2^2\Pi_u \leftarrow \tilde{X}^2\Pi_g$ system of HC_4H^+-Ar over the 290-345 nm range.

Assignment	$\tilde{\nu}$	$\Delta\tilde{\nu}$	$\tilde{\nu}^\dagger$	$\Delta\tilde{\nu}^\dagger$
0_0^0	29723	0	29753	0
9_0^2	30232	509	30211	459
3_0^1	30629	906		
$3_0^1 9_0^2$	31194	1471	31114	1362
3_0^2	31569	1846		
	32228	2505		
2_0^1	32595	2872		
	32680	2957		
	32981	3258		
	33435	3712		

† Ne matrix peak positions from ref. 174

Band positions and assignments for the HC_4H^+-Ar $2^2\Pi_u \leftarrow \tilde{X}^2\Pi_g$ spectrum are given in Table 3.4. For convenience a selected set of vibrational frequencies for HC_4H^+, $NCCN^+$ and C_4^- are provided in Table 3.5 (an extended set is given in the SI). The strong peak at $0_0^0 + 509\,\text{cm}^{-1}$ was previously assigned in the Ne matrix spectrum to the 9_0^2 (*cis* bending

Table 3.5 Calculated and experimental (underlined) vibrational frequencies (cm^{-1}) of the central σ_g (C-C stretch) and *cis*-bending modes of HC_4H^+, $NCCN^+$, and C_4^- in the $\tilde{X}^2\Pi_g$, $1^2\Pi_u$ ($\tilde{A}^2\Pi_u$ for HC_4H^+), and $2^2\Pi_u$ states.

State	HC_4H^+	$NCCN^+$	C_4^-
	C–C stretch (σ_g, ν_3)	**C–C stretch** (σ_g, ν_2)	**C–C stretch** (σ_g, ν_2)
$\tilde{X}^2\Pi_g$	956[a], 972[b,c]	808[d], 956[e]	893[f], 936[g]
$1^2\Pi_u$	809[a], 846[c], 806[h]	811[i]	750[j], 759[k], 777[l]
$2^2\Pi_u$	906[a]	870[i]	710[m], 755[n]
	C≡C–C≡C bend (π_u, ν_9)	**N≡C–C≡N bend** (π_u, ν_5)	**C≡C–C≡C bend** (π_u, ν_5)
$\tilde{X}^2\Pi_g$	210[a], 200[b],	240[d]	240[f]
$1^2\Pi_u$	214[a], 228[h]	174[i]	223[j], *250*[f]
$2^2\Pi_u$		164[i]	268[m], 271[n]

[a]This work, [b]Ref. 327, [c]Ref. 167, [d]Ref. 329, [e]Ref. 346, [f]Ref. 347, [g]Ref. 348, [h]Ref. 171, [i]Ref. 331, [j]Ref. 349, [k]Ref. 350, [l]Ref. 334 [m]Ref. 332, [n]Ref. 333

mode) transition based on calculated ground state frequencies of HC_4H^+.[174] To some extent this assignment is consistent with data for the isoelectronic ions $NCCN^+$ and C_4^-, for which transitions at 327 and 541 cm^{-1} above the $2^2\Pi_u \leftarrow \tilde{X}^2\Pi_g$ origin band, respectively, were assigned to overtones of the analogous *cis*-bending mode (5_0^2 transition for the linear tetra-atomic molecules – see Table 3.5).[329–331,333,334,351] The bands observed at $0_0^0 + 906\,cm^{-1}$ and $0_0^0 + 1846\,cm^{-1}$ can be assigned to the 3_0^1 and 3_0^2 transitions (C-C stretch vibration), respectively, based on the corresponding spectra of $NCCN^+$ and C_4^-,[331] as the spacings and relative intensities of C-C stretch progression peaks are similar for all three molecules. Assignments for peaks above $0_0^0 + 2000\,cm^{-1}$ are uncertain due to spectral congestion and poor signal. However, the 2_0^1, $2_0^1 9_0^1$, $2_0^1 3_0^1$, 1_0^1, $1_0^1 9_0^2$, and $1_0^1 3_0^1$ transitions should occur in this region.

One problem with the assignment scheme outlined above relates to the exaggerated intensity of the 9_0^2 transition. Whereas for both $NCCN^+$ and C_4^- the corresponding 5_0^2 band is comparatively weak, for HC_4H^+ the 9_0^2 transition has an intensity that is comparable to that of the origin transition. If the assignment for the 9_0^2 band is correct, the ν_9 frequencies in

the $2^2\Pi_u$ and $\tilde{X}^2\Pi_g$ states are similar ($\approx 255\,cm^{-1}$ and $200\,cm^{-1}$,[327] respectively), leading to the expectation of a relatively weak 9_0^2 band – if the molecule remains linear.

An alternative explanation for the vibronic structure in the $2^2\Pi_u \leftarrow \tilde{X}^2\Pi_g$ spectrum is that HC_4H^+ in the $2^2\Pi_u$ state is non-linear, in which case one would expect strong transitions to excited bending vibrational levels in the upper state. As a first step towards exploring this possibility, bending potential energy curves were calculated using the approach employed for $NCCN^+$ in ref. 329 (CASSCF/cc-pVTZ level of theory) whereby the molecule was progressively distorted along the ν_6 (*trans* H–C_4–H bend), ν_7 (*trans* C≡C-C≡C bend), ν_8 (*cis* C≡C-C≡C bend) and ν_9 (*cis* C≡C-C≡C bend) normal mode coordinates derived for the $\tilde{X}^2\Pi_g$ state. One-dimensional potential energy curves along the four bending coordinates (Q_6, Q_7, Q_8, Q_9) are displayed in Figure 3.7. RT interactions split a degenerate Π electronic state through distortion along a bending coordinate, leading to two substates, each of which can be either linear or bent. The calculated potential energy curves along all four bending normal coordinates are split into linear/linear pairs for the $\tilde{X}^2\Pi_g$ and $\tilde{A}^2\Pi_u$ states, as found for $NCCN^+$.[329] The calculations indicate that RT effects are weak for the $\tilde{X}^2\Pi_g$ and $\tilde{A}^2\Pi_u$ states, consistent with previous studies.[326,327] In contrast, the calculations predict that the $2^2\Pi_u$ state is split into a linear-bent pair for distortion along Q_6 (*trans* H–C_4–H bend, Figure 3.7a), linear-linear pair for distortion along Q_7 (*trans* C≡C-C≡C bend, Figure 3.7c), bent-bent pair for distortion along Q_8 (*cis* H–C_4–H bend, Figure 3.7b), and bent-bent pair for distortion along Q_9 (*cis* C≡C-C≡C bend, Figure 3.7d). The bending potential energy curves shown in Figure 3.7c and d indicate that HC_4H^+ in the $2^2\Pi_u$ state is distorted away from linearity along the Q_8 and Q_9 *cis* bend coordinates with respective barriers to linearity of ≈2100 and $\approx 1400\,cm^{-1}$. Therefore, it seems possible that the strong peak at $0_0^0 + 509\,cm^{-1}$ may be associated with excitation of a single quantum of one of the *cis* bending vibrational modes. It would seem that $509\,cm^{-1}$ is too high for the ν_9 C≡C-C≡C bend vibrational mode given that the predicted barrier to linearity is $\approx 1400\,cm^{-1}$ and the vibrational frequency in the ground state is only $210\,cm^{-1}$ (Table 3.1). Rather, the band may be associated with excitation of a single quantum of the ν_8 *cis* H–C_4–H bend vibrational mode for which the barrier to linearity is $\approx 2100\,cm^{-1}$ and the ground state frequency is $786\,cm^{-1}$ (Table 3.1). Electronic spectra of the $C_4D_4^+$-Ar complex would help decide whether the molecule in the $2^2\Pi_u$ state is indeed distorted along the along ν_8 *cis* H–C_4–H bend coordinate. Ultimately, a more comprehensive understanding of HC_4H^+ transitions in the UV region will require gas-phase spectra with better resolution and signal-to-noise ratio, spectra of isotopically substituted species, and calculations for the $2^2\Pi_u$ excited state incorporating consideration of the Renner-Teller couplings and bending potential energy curves that are likely to be highly anharmonic.

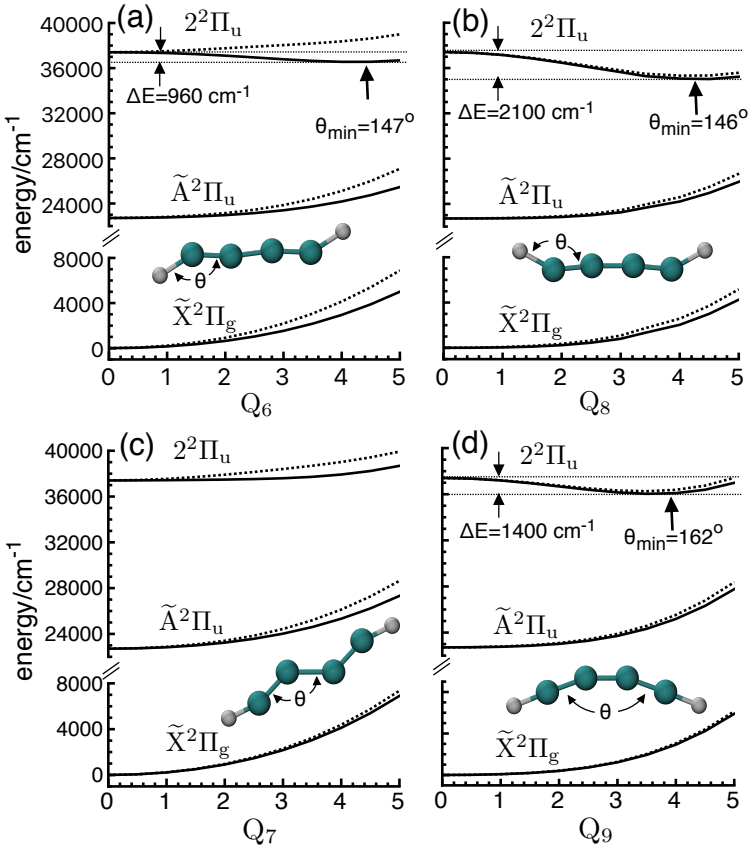

Fig. 3.7 One-dimensional potential energy curves along the bending normal mode coordinates for Renner-Teller components in the $\tilde{X}^2\Pi_g$, $\tilde{A}^2\Pi_u$, and $2^2\Pi_u$ states calculated at the CASSCF/cc-pVTZ level of theory. Potential energy curves along the: (a) Q_6 *trans* H–C_4–H bend coordinate, (b) Q_8 *cis* H–C_4–H bend coordinate, (c) Q_7 *trans* C≡C-C≡C bend coordinate, (d) Q_9 *cis* C≡C-C≡C bend coordinate. Lower and upper Renner-Teller curves for each electronic state are represented by solid and dotted lines, respectively. The dimensionless coordinates Q_i (i=6-9), correspond to the bending normal coordinates for the ground electronic state, with the linear geometry at Q_i=0.

3.4 Conclusions

In summary, electronic spectra of HC_4H^+-Ar_n (n=1-3) and HC_4H^+-$(N_2)_n$ (n=1-2) cation complexes have been recorded over the 290-530 nm range through photodissociation in a tandem mass spectrometer. The $\tilde{A}^2\Pi_u \leftarrow \tilde{X}^2\Pi_g$ electronic spectra of the complexes in the visible region (425-530 nm) are similar to previously recorded spectra,[167,169,171,172] and are matched by simulations based on calculated structural parameters and harmonic vibrational frequencies for the $\tilde{X}^2\Pi_g$ and $\tilde{A}^2\Pi_u$ states at the CCSD/cc-pCVTZ and EOM-CCSD/cc-pCVTZ levels of theory, respectively.

Transitions of HC_4H^+-Ar over the 290-350 nm range previously observed in matrix isolation studies,[173,174] were confirmed to be associated with the diacetylene cation through hole burning experiments. The $2^2\Pi_u \leftarrow \tilde{X}^2\Pi_g$ origin transition was observed at 29723 cm^{-1}, in accordance with previous matrix studies while bands at $0_0^0 + 906$ and 1846 cm^{-1} are tentatively assigned to the 3_0^1 and 3_0^2 transitions, respectively, based on spectra of the isoelectronic systems $NCCN^+$ and $C_4{}^-$. An intense band at $0_0^0 + 509$ cm^{-1} was tentatively assigned to the 9_0^2 transition (overtone of the *cis*-bending mode) on the basis of its frequency, although this assignment does not properly account for its substantial intensity. An alternative explanation, supported by electronic structure calculations, is that HC_4H^+ is distorted along the ν_8 *cis* H–C_4–H bend coordinate and that the band corresponds to excitation of a single quantum of this vibration in the $2^2\Pi_u$ state. Better spectra, spectra of isotopologues, and more reliable calculations that include consideration of Renner-Teller effects are required to understand the transitions of HC_4H^+ in the ultraviolet region.

3.5 Acknowledgments

This research was supported under the Australian Research Council's Discovery Project funding scheme (Project Numbers DP150101427 and DP160100474) as well as by Australian Government Research Training Program Scholarships. U. Jacovella acknowledges support from the Swiss National Science Foundation (P2EZP2_178429).

Article ends here

3.6 Supporting information (SI)

3.6.1 Calculated structures of HC_4H^+-Ar_n (n=1-3) and HC_4H^+-$(N_2)_n$ (n=1-2) complexes

Density functional theory (DFT) calculations at the ωB97X-D/aug-cc-pVTZ level of theory were conducted using the Gaussian 09 suite[341] to predict the ground state binding energies and harmonic vibrational frequencies of the HC_4H^+-Ar_n (n=1-3) and HC_4H^+-$(N_2)_n$ (n=1-2) complexes. The binding energies were corrected for the basis set superposition error (BSSE). Calculated structures, binding energies, and vibrational frequencies are summarized in Figure 3.8 and Table 3.6. Calculated bond lengths of HC_4H^+, HC_4H^+-Ar_n, and HC_4H^+-$(N_2)_n$ (n=1-2) are summarized (Table 3.7) to highlight the effect of the tag (attached end-on) on the geometry of the HC_4H^+ core. The most significant change to HC_4H^+ arising from addition of an Ar atom or N_2 molecule is a slight extension of the neighboring C-H bond (by 0.003 Å for Ar and by 0.008 Å for N_2).

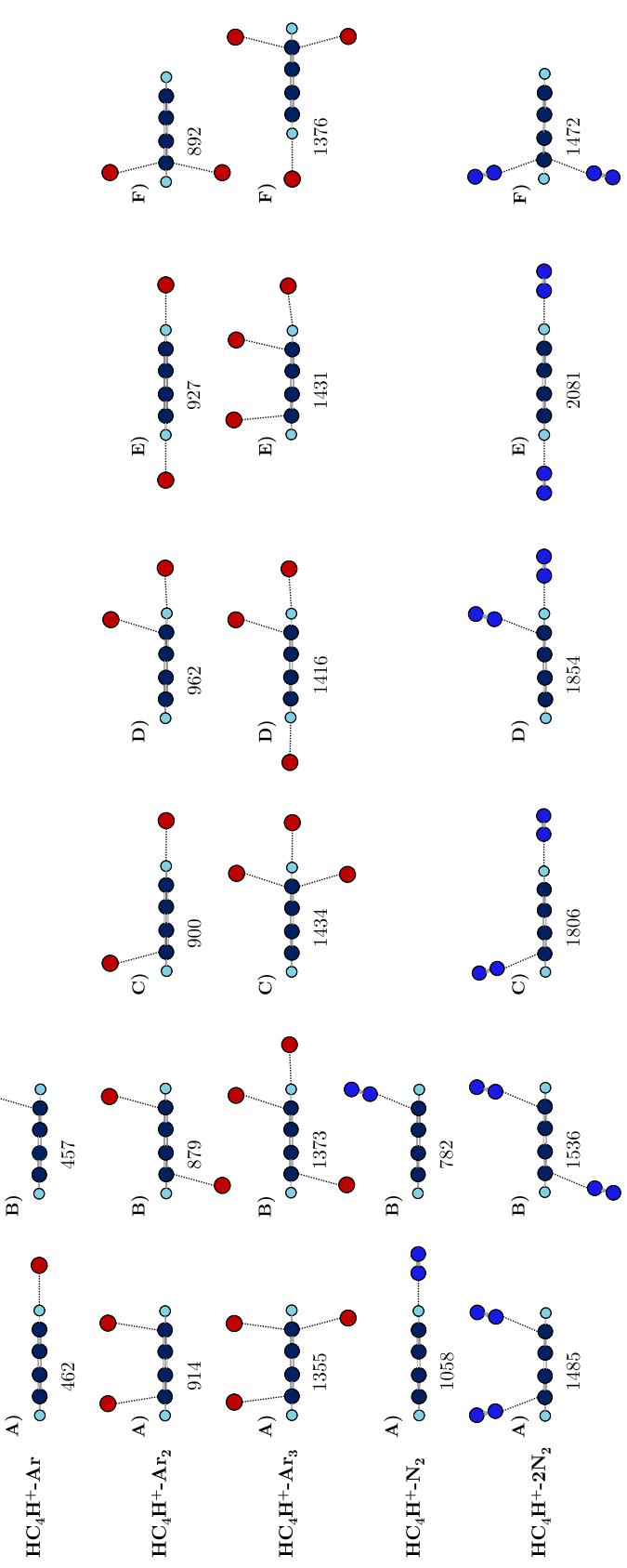

Fig. 3.8 Structures and binding energies (cm^{-1}) for HC_4H^+-Ar_n (n=1-3) and HC_4H^+-$(N_2)_n$ (n=1-2) complexes calculated at the ωb97X-D/aug-cc-pVTZ level of theory. The binding energies account for vibrational zero point energy and include corrections to account for the basis set superposition error (BSSE).

Table 3.6 Harmonic vibrational frequencies (cm^{-1}) of HC_4H^+, HC_4H^+-Ar_n (n=1-3), and HC_4H^+-$(N_2)_n$ (n=1-2) calculated at the ωB97X-D/aug-cc-pVTZ level of theory. Vibrational frequencies are given for the configurations labeled in Figure S1. Two harmonic frequencies are calculated for each bending mode affected by Renner-Teller splitting. All frequencies are unscaled.

Tag	ν_1	ν_2	ν_3	ν_4	ν_5	ν_6	ν_7	ν_8	ν_9	ν_s	ν_s	ν_s	ν_b	ν_s (Ar-Ar)	ν_s (N=N)	ν_s N_2-N_2
(Bare)	3373	2300	967	3366	1946	789/692	515/482	797/703	217/211							
Ar																
(A)	3377	22976	965	3320	1936	786/689	510/481	810/721	217/216	61			31/29			
(B)	3382	2298	965	3375	1940	783/684	508/479	788/694	217/212	65			24			
Ar_2																
(A)	3385	2299	966	3378	1941	783/686	509/481	788/693	222/212	60	59		34, 14	13		
(B)	3385	2299	966	3378	1941	776/685	508/480	779/693	226/216	85	71		21, 18, 13			
(C)	3381	2296	965	3325	1937	789/687	510/483	809/720	223/213	73	60		33, 29, 12			
(D)	3380	2296	965	3327	1938	785/691	510/482	811/717	225/217	73	61		31, 27	21		
(E)	3329	2294	965	3318	1934	807/716	511/484	812/721	221/220	71	45		40/39, 14/13			
(F)	3386	2298	965	3378	1942	777/685	509/481	786/694	227/213	41	85		27, 17, 16			
Ar_3																
(A)	3389	2299	966	3382	1943	777/687	509/479	785/695	222/215	88	76	43	22, 20, 16, 11	14		
(B)	3384	2297	966	3332	1939	782/688	510/482	810/717	228/218	82	64	58	29, 23, 21, 13, 11			
(C)	3335	2295	966	3325	1936	804/713	511/483	809/720	227/221	74	71	45	40, 32, 12, 11	20		
(D)	3383	2296	966	3334	1940	784/691	510/483	806/717	233/218	84	64	39	35, 28, 10	19, 17		
(E)	3383	2297	966	3332	1939	779/688	510/481	806/717	224/217	74	65	61	32, 26, 8	19, 12		
(F)	3386	2296	966	3329	1938	781/687	510/483	808/720	232/217	88	58	41	34, 31, 15, 11, 10			
N_2																
(A)	3378	2293	965	3251	1932	786/689	513/488	870/792	232/229	97			118/116, 43/42		2500	
(B)	3390	2298	965	3378	1941	779/685	509/479	785/695	226/217	98			80, 77, 30		2494	
$(N_2)_2$																
(A)	3396	2300	967	3389	1942	782/689	510/484	787/694	244/213	111	85		87, 80, 74, 72, 32, 19		2500, 2494	14
(B)	3396	2301	967	3389	1943	757/685	510/478	760/694	228/216	94	73		85, 82, 74, 74, 27, 19, 14		2495, 2495	
(C)	3392	2294	966	3267	1935	776/686	512/486	862/788	241/229	95	86		119, 116, 81, 73, 41, 40, 17		2500, 2495	
(D)	3383	2292	965	3273	1935	782/691	511/486	863/783	243/229	95	92		116, 114, 80, 76, 76, 40, 34		2500, 2494	20
(E)	3269	2287	965	3255	1926	869/790	516/494	866/786	249/242	108	76		127/125, 110/109, 54/53, 20/19		2500, 2500	
(F)	3403	2297	966	3383	1943	781/690	512/490	841/697	256/216	106	64		91, 81, 75, 72, 33, 26, 23		2495, 2495	

Table 3.7 Bond lengths (Å) for HC_4H^+, HC_4H^+-Ar_n, and HC_4H^+-$(N_2)_n$ (n=1-2) in the ground $\tilde{X}^2\Pi_g$ state, calculated at the ωB97X-D/aug-cc-pVTZ level of theory.

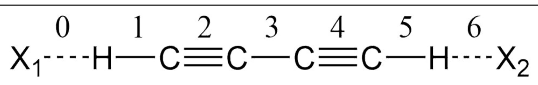

X_1	0	1	2	3	4	5	6	X_2
—	—	1.073	1.225	1.326	1.225	1.073	—	—
Ar	2.554	1.076	1.226	1.326	1.225	1.073	—	—
Ar	2.560	1.076	1.225	1.326	1.225	1.076	2.560	Ar
N_2	2.152	1.081	1.226	1.326	1.224	1.072	—	—
N_2	2.167	1.080	1.226	1.326	1.226	1.080	2.167	N_2

3.6.2 $\tilde{A}^2\Pi_u \leftarrow \tilde{X}^2\Pi_g$ spectra of HC_4H^+-Ar_n (n=1-3) and HC_4H^+-$(N_2)_n$ (n=1-2)

The $\tilde{A}^2\Pi_u \leftarrow \tilde{X}^2\Pi_g$ spectra of HC_4H^+-Ar_n (n=1-3) and HC_4H^+-$(N_2)_n$ (n=1-2), recorded over the 425-515 nm range, are shown in Figure 3.9. The position for the origin transition of bare HC_4H^+ (19 722.6 cm^{-1} - ref. 337) is indicated in the figure by the dotted red line.

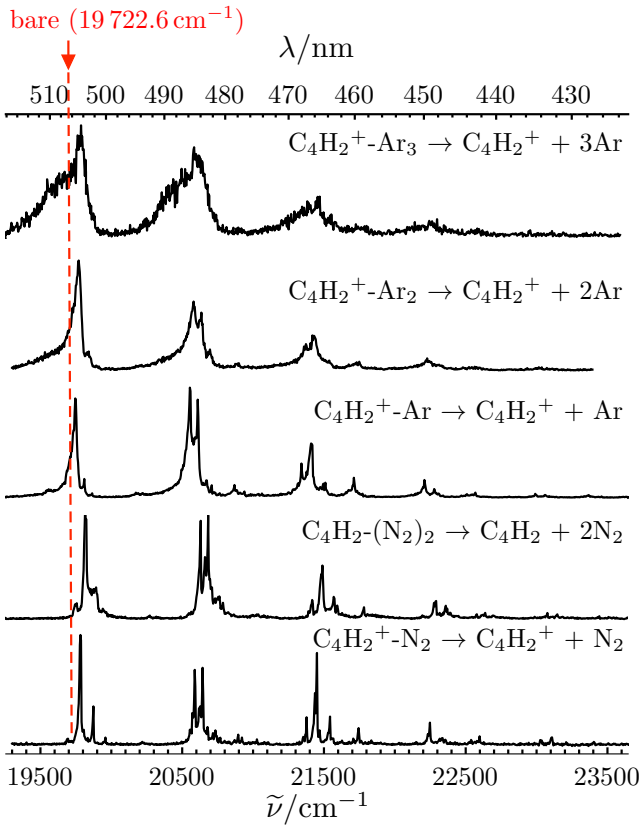

Fig. 3.9 $\tilde{A}^2\Pi_u \leftarrow \tilde{X}^2\Pi_g$ band systems of HC_4H^+-Ar_n (n=1-3) and HC_4H^+-$(N_2)_n$ (n=1-2). The energy of the origin transition of the bare HC_4H^+ cation at 19 722.6 cm^{-1} (ref. 337) is indicated by the red dashed line.

3.6.3 Description of the hole burning experiments

Spectra of HC_4H^+-Ar_n (n=1-3) and HC_4H^+-$(N_2)_n$ (n=1-2) complexes were recorded over the 290-530 nm range using resonance enhanced photodissociation (REPD) spectroscopy by monitoring HC_4H^+ photofragments. Spectra recorded in the visible (420-520 nm) region are similar to previously obtained spectra.[173,174] To test whether bands observed over the

290-350 nm range were also associated with the diacetylene cation we conducted hole burning (HB) experiments for HC_4H^+-Ar ions. Figure 3.10 shows the setup used for hole burning experiments. The experimental approach is similar to that used in the REPD spectroscopy experiments, but with the addition of a second tunable light beam from an optical parametric oscillator (OPO, Opotek Vibrant 355 LD) that passed down the axis of the first quadrupole mass filter (QMF1). The wavelength of this hole burning beam was tuned to the $\tilde{A}^2\Pi_u \leftarrow \tilde{X}^2\Pi_g$ origin band of HC_4H^+-Ar (506.4 nm). A fraction of the HC_4H^+-Ar ion population dissociated following photoexcitation by the HB light, resulting in fewer HC_4H^+-Ar ions reaching the octopole ion guide. In the octopole, the remaining HC_4H^+-Ar ions - and other possible isobaric ions unaffected by HB light - encountered the probe light that was scanned over the 290-350 nm range. To identify which bands corresponded to transitions of HC_4H^+-Ar, a spectrum was recorded with the HB light off and another with the HB light on, as shown in the top right inset of Figure 3.10 in red (HB light off) and blue (HB light on). Because the HC_4H^+-Ar population is reduced when the HB light is on, bands with diminished intensities correspond to transitions of HC_4H^+-Ar. It was found that the intensities of all bands over the 290-350 nm range were uniformly reduced with the HB light on, proving that they are indeed carried by the HC_4H^+-Ar cation.

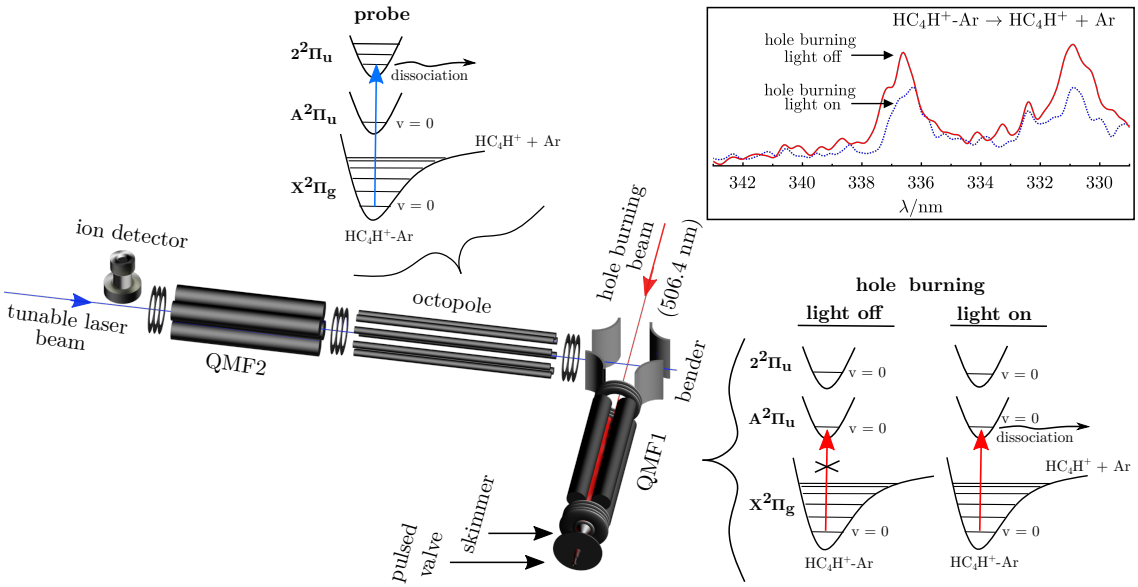

Fig. 3.10 Schematic diagram of the two-laser setup used for hole burning experiments.

3.6.4 The $2^2\Pi_u \leftarrow \tilde{X}^2\Pi_g$ band system of HC_4H^+-Ar and HC_4H^+-N_2

Spectra of HC_4H^+-Ar (Figure 3.11a) and HC_4H^+-N_2 (Figure 3.11b) were recorded over the 295-345 nm range by monitoring the HC_4H^+ photofragment signal. The REPD spectrum of HC_4H^+-N_2 has a relatively poor signal-to-noise ratio. This is because HC_4H^+-N_2 has the same mass as $C_6H_6^+$, which is also formed in the ion source and which also dissociates in the UV region to give $C_4H_2^+$ ions. Band wavenumbers and assignments for the HC_4H^+-N_2 spectrum are provided in Table 3.8.

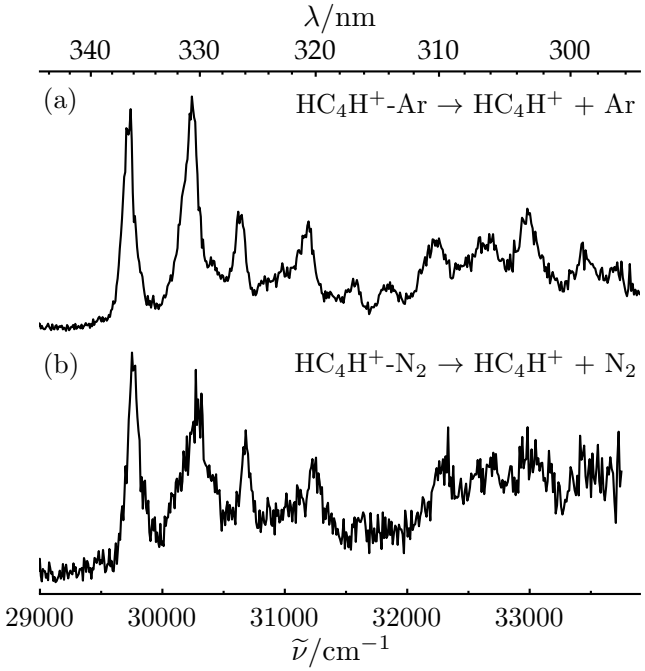

Fig. 3.11 The $2^2\Pi_u \leftarrow \tilde{X}^2\Pi_g$ band system of (a) HC_4H^+-Ar and (b) HC_4H^+-N_2.

Table 3.8 Band positions (cm^{-1}) and assignments for $2^2\Pi_u \leftarrow \tilde{X}^2\Pi_g$ transitions of HC_4H^+-Ar and HC_4H^+-N_2.

	HC_4H^+-Ar		HC_4H^+-N_2	
Assignment	$\widetilde{\nu}$	$\Delta\widetilde{\nu}$	$\widetilde{\nu}$	$\Delta\widetilde{\nu}$
0_0^0	29723	0	29752	0
9_0^2	30232	509	30273	521
3_0^1	30629	906	30681	929
$3_0^1 9_0^2/9_0^4$	31194	1471	31245	1493
3_0^2	31569	1846		
	31829	2106		
2_0^1	32228	2505	32292	2540
	32595	2872	32597	2845
	32680	2957	32703	2951
	32981	3258	32983	3231
	33435	3712		
	33727	4004		

3.6.5 Comparisons with the isoelectronic molecular ions $NCCN^+$ and C_4^-

Previous spectroscopic studies of $NCCN^+$ and C_4^-, which are isoelectronic with HC_4H^+, help understand the spectrum of HC_4H^+ over the 290-350 nm range. The energies of the excited states of HC_4H^+, $NCCN^+$ and C_4^- are provided in Table 3.9 while vibrational frequencies are listed in Table 3.10. Calculations for HC_4H^+ were conducted using the Psi4 1.1 program suite.[289]

Table 3.9 Calculated and experimental excitation energies (eV) for HC_4H^+, $NCCN^+$, and C_4^-. Provided are adiabatic excitation energies (underlined) and vertical excitation energies. Calculations for HC_4H^+ were conducted at the CCSD/cc-pCVTZ and EOM-CCSD/cc-pCVTZ levels. In each case, energies are relative to the energy of the $\tilde{X}^2\Pi_g$ electronic state.

	HC_4H^+	$NCCN^+$	C_4^-
	$\tilde{A}^2\Pi_u$	$\tilde{C}^2\Pi_u$	$\tilde{C}^2\Pi_u$
calculated	2.45[a], 2.67[a]	2.27[b]	2.802[c], 2.91[d]
experimental	2.45[a]	2.11[e]	2.71[f,g]
	$2^2\Pi_u$	$\tilde{D}^2\Pi_u$	$2^2\Pi_u$
calculated	4.00[a]	4.3[b]	3.78[d]
experimental	3.69[a], 3.75[i]	4.16[b]	3.23[e], 3.22[h]
	$3^2\Pi_u$		$3^2\Pi_u$
calculated	4.17[a], 4.84[a], 4.60[j]		
experimental	4.5[i]		3.58[e], 3.56[g]
	$^2\Phi_u$		$^2\Phi_u$
calculated	4.43[i]		5.16[d]
	$^2\Pi_u$		$^2\Pi_u$
calculated	5.40[i], 5.21[j]		

[a]This work, [b]Ref. 329, [c]Ref. 350, [d]Ref. 352, [e]Ref. 330
[f]Ref. 333, [g]Ref. 349, [h]Ref. 334 [i]Ref. 173, [j]Ref. 338

Table 3.10 Selected vibrational frequencies (cm^{-1}) determined for the $\tilde{X}^2\Pi_g$ and lowest two $^2\Pi_u$ excited states of the isoelectronic systems HC_4H^+, $NCCN^+$ and C_4^-. For HC_4H^+ the $1^2\Pi_u$ state corresponds to the $\tilde{A}^2\Pi_u$ state. Calculated and experimental (underlined) values are presented.

State	HC_4H^+	$NCCN^+$	C_4^-
	C≡C stretch	**N≡C stretch**	**C≡C stretch**
	(σ_g, ν_2)	(σ_g, ν_1)	(σ_g, ν_1)
$\tilde{X}^2\Pi_g$	2283[a], 2177[b], 2176.6[c]	2300[d], 2262[e]	2084[f], 2047[g]
$1^2\Pi_u$	1965[a], 1961[h]	2105[i]	1729[j], 1913[k]
$2^2\Pi_u$		2188[i]	2056[j]
	C–C stretch	**C–C stretch**	**C–C stretch**
	(σ_g, ν_3)	(σ_g, ν_2)	(σ_g, ν_2)
$\tilde{X}^2\Pi_g$	956[a], 972[b], 971.5[c]	808[d], 956[e]	893[f], 936[g]
$1^2\Pi_u$	809[a], 846[c], 806[h]	811[i]	750[l], 759[m], 777[k]
$2^2\Pi_u$	906[a]	870[i]	755[n], 710[j]
	C≡C stretch	**N≡C stretch**	**C≡C stretch**
	(σ_u, ν_5)	(σ_u, ν_3)	(σ_u, ν_3)
$\tilde{X}^2\Pi_g$	2015[a], 1827.9[o]	1789[d], 1818[e]	1884[f]
$1^2\Pi_u$	2040[a]		
$2^2\Pi_u$			
	C≡C-C≡C bend	**N≡C–C≡C bend**	**C≡C–C≡C bend**
	(π_g, ν_7)	(π_g, ν_4)	(π_g, ν_4)
$\tilde{X}^2\Pi_g$	438[a], 433[b], 430.3[c]	537[d]	505[f], 396[g]
$1^2\Pi_u$	432[a], 431[h]	351[i]	
$2^2\Pi_u$		607[i]	349[n], 374[j]
	C≡C-C≡C bend	**N≡C–C≡C bend**	**C≡C–C≡C bend**
	(π_u, ν_9)	(π_u, ν_5)	(π_u, ν_5)
$\tilde{X}^2\Pi_g$	210[a], 200[b],	240[d]	240[f]
$f1^2\Pi_u$	214[a], 228[h]	174[i]	223[l], *250*[f]
$2^2\Pi_u$		164[i]	271[n], 268[j]

[a]This work, [b]Ref. 327, [c]Ref. 167, [d]Ref. 329, [e]Ref. 346, [f]Ref. 349, [g]Ref. 348, [h]Ref. 171, [i]Ref. 331, [j]Ref. 334, [k]Ref. 350, [l]Ref. 347 [m]Ref. 332, [n]Ref. 333, [o]Ref. 168

Chapter 4

REPD spectroscopy of $C_4H_4^+$ cations tagged with Ar and N_2

4.1 Introduction

Small carbocations serve as intermediates in reactions occurring in plasmas,[353,354] flames,[355,356] circumstellar and interstellar media,[143,357] and the atmosphere of Titan.[16,358,359] Understanding the reactions in these different environments requires identification of the cations involved. In extraterrestrial environments, $C_4H_4^+$ cations have been proposed to exist where neutral acetylene or larger hydrocarbons encounter ultraviolet (UV) radiation.[148,176,177,188,192,196,360,361] Several $C_4H_4^+$ isomers are predicted to be stable, although the four lowest energy ones, displayed in Figure 4.1 in order of increasing ZPE-corrected electronic energy, are presumed to be the most abundant. Detection of these isomers relies on matching their laboratory spectra with astronomical observations. However, spectroscopic data of $C_4H_4^+$ isomers are limited.

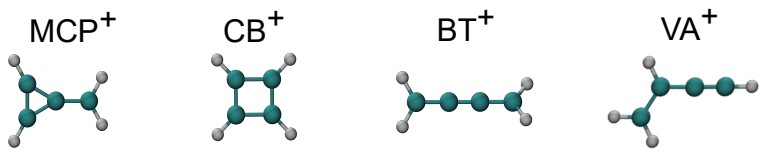

Fig. 4.1 Structures of the lowest energy $C_4H_4^+$ radical cations, methylenecyclopropene (**MCP**$^+$), cyclobutadiene (**CB**$^+$), butatriene (**BT**$^+$), and vinylacetylene (**VA**$^+$).

Electronic transitions of the methylenecyclopropene cation (**MCP**$^+$) and the cyclobutadiene cation (**CB**$^+$) have not been observed, whereas the vinylacetylene cation (**VA**$^+$;

1-but-en-3-yne) and the butatriene cation (**BT**$^+$) are known to exhibit electronic transitions in the visible region of the spectrum.[173,206,207] Nonetheless, these transitions are not yet well characterized. Based on previous neon matrix isolation studies, discussed in Section 4.1.1, **VA**$^+$ and **BT**$^+$ both absorb near 512 nm such that their transitions are difficult to disentangle.[206,207]

In this work, resonance-enhanced photodissociation (REPD) spectra of $C_4H_4^+$-Ar and $C_4H_4^+$-N_2 complexes, generated from a lean C_2H_2/Ar or C_2H_2/N_2 gas mixture, are measured over the 296-550 nm range by monitoring $C_4H_4^+$, $C_4H_3^+$, and $C_4H_2^+$ photofragments. The spectra exhibit band systems commencing at 511 nm and 410 nm, in addition to an intense band below 320 nm. These features are interpreted in the light of previous spectroscopic studies and quantum chemical calculations of the four lowest energy $C_4H_4^+$ isomers. It is shown that the 511 nm system in the REPD spectra arises primarily from the $\tilde{B}^2A''\leftarrow\tilde{X}^2A''$ electronic transition of **VA**$^+$ and that the 410 nm system is due to the $\tilde{D}^2B_3\leftarrow\tilde{X}^2B_2$ transition of **BT**$^+$. The intense hump in the UV region of the spectrum likely arises from electronic transitions of all four $C_4H_4^+$ isomers. The electronic spectra presented here are the first to exhibit clear vibronic structure for **VA**$^+$ and **BT**$^+$ in the gas phase.

This chapter begins with an overview of previous spectroscopic studies of the **VA**$^+$, **BT**$^+$, **CB**$^+$, and **MCP**$^+$ isomers (Section 4.1.1), followed by a description of their formation in the ion source through acetylene ion-molecule reactions and ionization of neutral acetylene clusters (Section 4.1.2). Section 4.2 describes the experimental approach. The electronic spectra are presented and analyzed in Section 4.3, along with calculated pathways to $C_4H_2^+ + H_2$ and $C_4H_3^+ + H$ photofragments from the ground state $C_4H_4^+$ potential energy surface.

4.1.1 Previous spectroscopic studies of $C_4H_4^+$ cations

Information on the structures and energies of the most stable $C_4H_4^+$ isomers have been derived from photoelectron spectroscopy,[199–201,205,362] infrared spectroscopy,[152] and electronic spectroscopy.[206,207] Below, the available spectroscopic data for each of the four isomers are summarized. Energies for the spectroscopically relevant states are provided in Figure 4.2, with solid and dotted arrows corresponding to photoionizing transitions of neutral C_4H_4 and electronic transitions of $C_4H_4^+$ cations, respectively. For simplicity, only excited electronic states within 5 eV of the doublet ground electronic state ($\tilde{X}$) of each $C_4H_4^+$ isomer are displayed. Symmetry classifications for electronic states of **BT**$^+$ (D_{2h}), **CB**$^+$ (D_{2h}), and **MCP**$^+$ (C_{2v}) are based on coordinate systems derived using Mulliken's convention.[363,364]

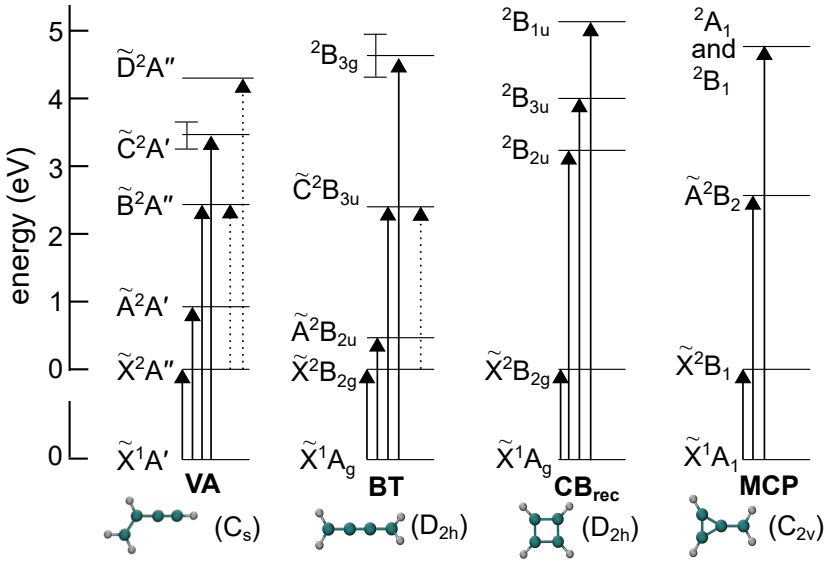

Fig. 4.2 Energy level diagram based on measured ionization energies of neutral C_4H_4 molecules (solid arrows)[199–201,205,362] and excitation energies of $C_4H_4^+$ cations (dotted arrows).[206,207]

The vinylacetylene cation (VA^+)

$\mathbf{VA}^+$ is planar (C_s) in its ground electronic state and is accessible from the closed-shell neutral molecule through removal of an electron from the a″ highest occupied molecular orbital (HOMO). Based on photoelectron spectra, ejection of an electron from the HOMO-1, HOMO-2, and HOMO-3 of the neutral gives rise to the $\tilde{A}^2A'$, $\tilde{B}^2A''$, and $\tilde{C}^2A'$ electronic states lying 1.00, 2.42, and 3.22-3.6 eV above the $\tilde{X}^2A''$ state, respectively (see Fig. 4.2). [201,205]

The first electronic spectrum of $\mathbf{VA}^+$ was recorded for ions in a solid argon matrix over the 250-700 nm range.[173] The $\tilde{B}^2A''\leftarrow\tilde{X}^2A''$ origin transition occurs at 526 nm (2.36 eV) and is accompanied by progressions spaced by 520, 790, and 1320 cm^{-1}. The higher energy HOMO→LUMO transition of $\mathbf{VA}^+$, to an excited electronic state not observable using photoelectron spectroscopy, gives rise to a broad band around 296 nm (4.2 eV). Other contributions to the recorded spectrum, in particular weak bands occurring between 350 and 450 nm (2.76-3.54 eV), were postulated to arise from excitations of an unidentified molecule. In a following study, an absorption spectrum was recorded for ions embedded in a 6 K neon matrix, with the $\tilde{B}^2A''\leftarrow\tilde{X}^2A''$ origin transition observed at 515 nm (2.41 eV).[206] The observed spectrum included matrix site structure artefacts and transitions of HC_4H^+ photofragments as a consequence of the deposited $\mathbf{VA}^+$ ions having sufficient internal energy to dissociate. In the same study, the $\tilde{B}^2A''\leftarrow\tilde{X}^2A''$ origin transition of $\mathbf{VA}^+$ was observed

with rotational resolution in the gas phase at 513 nm (2.42 eV).[206] To date, the higher vibronic transitions within the $\tilde{B}^2A''\leftarrow\tilde{X}^2A''$ band system have not been measured clearly.

The butatriene cation (BT^+)

The linear $\mathbf{BT}^+$ chain isomer is one of the simplest open-shell cumulenic cations.[207,365,366] Ejection of an electron from the HOMO of an odd-type cumulene such as neutral **BT** (with three π bonds) induces a change from planar (D_{2h}) to staggered (D_2) geometry, such that the dihedral angle assumes a value of $\approx$ 26-42° for the cation in its ground electronic state.[207,365,367] The molecular orbitals for these types of cations exhibit so-called "electrohelicity" – the mixing of two overlapping, orthogonal sets of p-orbitals as shown in Figure 4.3.[365,366,368] Electronic states of $\mathbf{BT}^+$ are typically described using molecular term symbols appropriate for the D_{2h} point group (see Fig. 4.2), based on the early photoelectron spectroscopy study of the planar neutral molecule.[369] The photoelectron spectrum of **BT** exhibits bands at 0.68, 2.48, and $\approx$ 4.90 eV above the first ionization band, corresponding to removal of electrons from the HOMO-1, HOMO-2, and HOMO-3 orbitals, respectively. The complex structure of the HOMO-3 ionization band leads to uncertainty in its energy, as indicated by the range shown in Figure 4.2.

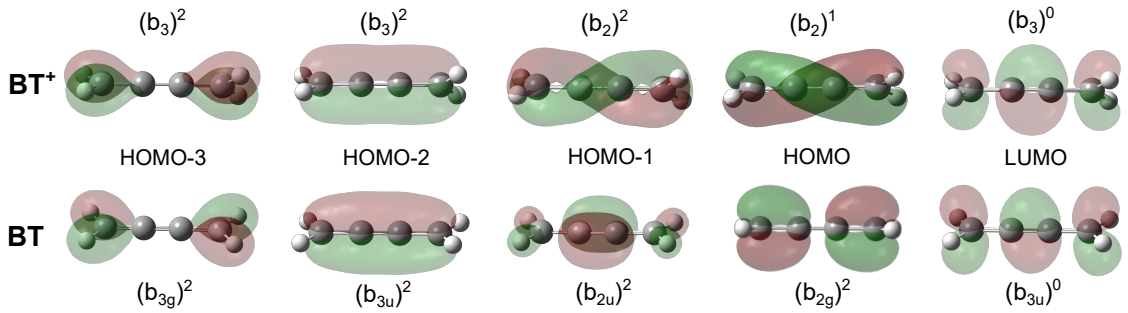

Fig. 4.3 The HOMOs and LUMO of neutral **BT** (D_{2h}) and the $\mathbf{BT}^+$ cation (D_2) as predicted at the CCSD/cc-pVTZ level of theory.

A recent (2015) neon matrix isolation study focused on the $\tilde{C}^2B_{3u}\leftarrow\tilde{X}^2B_{2g}$ electronic transition of $\mathbf{BT}^+$, suspected to occur in the vicinity of 491 nm based on emission observed from a glow discharge of 2-butyne.[370] The absorption spectrum of ions generated from neutral **BT** exhibited transitions of the $\mathbf{VA}^+$ isomer and the diacetylene fragment ion (see Chapter 3) rather than transitions of $\mathbf{BT}^+$, indicating that the experimental conditions favored isomerization of $\mathbf{BT}^+$ to $\mathbf{VA}^+$ and dissociation to $C_4H_2^+ + H_2$.[207] The contribution of $\mathbf{VA}^+$ to the spectrum was reduced by depositing a dilute mixture of **BT** in Ne (1:20000) into the solid Ne matrix and subsequently bombarding it with Ar^+ to ionize. Transitions of $\mathbf{BT}^+$ were

identified by subtracting known $C_4H_2^+$ transitions from the spectrum. The $\tilde{C}^2B_{3u}\leftarrow\tilde{X}^2B_{2g}$ origin transition occurs at 512 nm (2.42 eV), agreeing with the energy difference between the first and third ionization bands in the photoelectron spectrum (see Fig. 4.2). To interpret the $\tilde{C}^2B_{3u}\leftarrow\tilde{X}^2B_{2g}$ absorption spectrum, quantum chemical calculations were conducted at the CASPT2/ANO-L level of theory.[207] The optimized equilibrium geometries for $\mathbf{BT}^+$ in the $\tilde{X}^2B_{2g}$ and $\tilde{C}^2B_{3u}$ electronic states were predicted to be similar, with torsional angles of 39° and 37°, respectively, reflecting the intense origin transition in the spectrum. Based on calculated harmonic vibrational frequencies of $\mathbf{BT}^+$ in the $\tilde{X}^2B_{2g}$ state, bands in the spectrum were assigned to vibronic transitions involving out-of-plane skeletal bending, CH_2 torsional, and C=C stretching vibrational modes with frequencies of 207, 511, and 813 cm^{-1}, respectively. Interestingly, the quantum chemical calculations predict the $\tilde{C}^2B_{3u}\leftarrow\tilde{X}^2B_{2g}$ electronic transition to be the weakest transition (oscillator strength of 0.011) occurring within 5 eV of the $\tilde{X}^2B_{2g}$ state. A higher energy transition, with vertical excitation energy of 4.60 eV and oscillator strength of 0.059, is a promising target for spectroscopic detection of $\mathbf{BT}^+$.

The cyclobutadiene cation ($\mathbf{CB}^+$)

The square $\mathbf{CB}^+$ structure distorts to rectangular ($\mathbf{CB}_{rec}{}^+$) and rhombic ($\mathbf{CB}_{rh}{}^+$) forms that are separated by a low energy barrier.[371] The photoelectron spectrum of the closed-shell neutral **CB** (presumed to be rectangular)[372–375] unveiled three excited electronic states lying 3.26, 3.96, and 5.16 eV above the ground state cation (see Fig. 4.2).[199,362] The spectrum was compared to simulated spectra for ionization to $\mathbf{CB}_{rec}{}^+$, $\mathbf{CB}_{rh}{}^+$, and $\mathbf{CB}_{square}{}^+$, which suggested that the equilibrium geometry of the cation in its ground electronic state ($\tilde{X}^2B_{2g}$) is rectangular rather than rhombic. More recently, calculations of $\mathbf{CB}_{rec}{}^+$ reproduced collision cross sections measured in ion mobility experiments,[180] as well as structure observed in vibrational predissociation spectra of $C_4H_4{}^+$-Ar clusters,[152] supporting a rectangular geometry for $\mathbf{CB}^+$.

An electronic spectrum of $\mathbf{CB}^+$ has not been recorded. Excitation of $\mathbf{CB}_{rec}{}^+$ from the $\tilde{X}^2B_{2g}$ state to the $^2B_{3u}$ state (at 3.96 eV) is dipole-allowed, whereas transitions to the $^2B_{2u}$ and $^2B_{1u}$ states are optically forbidden. Considering the less likely $\mathbf{CB}_{rh}{}^+$ distorted form, two allowed electronic transitions have been predicted at 296 nm (4.19 eV) and 183 nm (6.78 eV).[183]

The methylenecyclopropene cation (MCP$^+$)

The photoelectron spectrum of neutral **MCP** revealed that at least three excited electronic states of the cation lie within 5 eV of the $\tilde{X}^2B_1$ state as shown in Fig. 4.2.[200] Bands lying 2.54 and 4.7 eV above the first ionization band arise from the removal of electrons from the HOMO-1 and HOMO-2 molecular orbitals, respectively, giving rise to $^2B_2$ and $^2B_1$ electronic states.[200,376] To date, no electronic transitions of **MCP**$^+$ have been reported. Although the $\tilde{A}^2B_2 \leftarrow \tilde{X}^2B_1$ transition is electric-dipole forbidden, excitations to the higher lying $^2B_1$ and $^2A_1$ electronic states are allowed and may be promising targets for spectroscopic detection of **MCP**$^+$ depending on their strengths.

Relevance to this work

In summary, based on previous work, electronic transitions of the **VA**$^+$, **BT**$^+$, **CB**$^+$, and **MCP**$^+$ isomers should occur across the visible and UV regions. Band intensities in the REPD spectra measured in this work, over the 296-550 nm range, will depend on the abundance of each isomer and the strengths of its electronic transitions. The REPD spectra are interpreted with the aid of calculated transition energies and oscillator strengths for the four isomers, along with spectral simulations based on calculated Franck-Condon (FC) factors. Ultimately, the REPD spectra may facilitate detection of $C_4H_4^+$ intermediates in remote environments where ion-molecule reactions of acetylene and its cation are similar to those occurring in the ion source. These reactions are described in the following section.

4.1.2 Acetylene reactions leading to $C_4H_4^+$

In this work, $C_4H_4^+$ cations are generated by bombarding an isentropic expansion of C_2H_2 in Ar (or N_2) with electrons. The cations can be formed in the expansion as collisionally stabilized adducts of the $C_2H_2^+ + C_2H_2$ bimolecular reaction, or as fragments of larger carbocations such as $C_6H_6^+$. These reactions can be understood with the help of the energy level diagram shown in Figure 4.4, which was generated based on available experimental and computational data.[178,179,185,377] Stationary points on both reaction surfaces are set to a common $C_6H_6^+$ energy scale (by adding the energy of a C_2H_2 molecule to all points on the $C_4H_4^+$ surface).

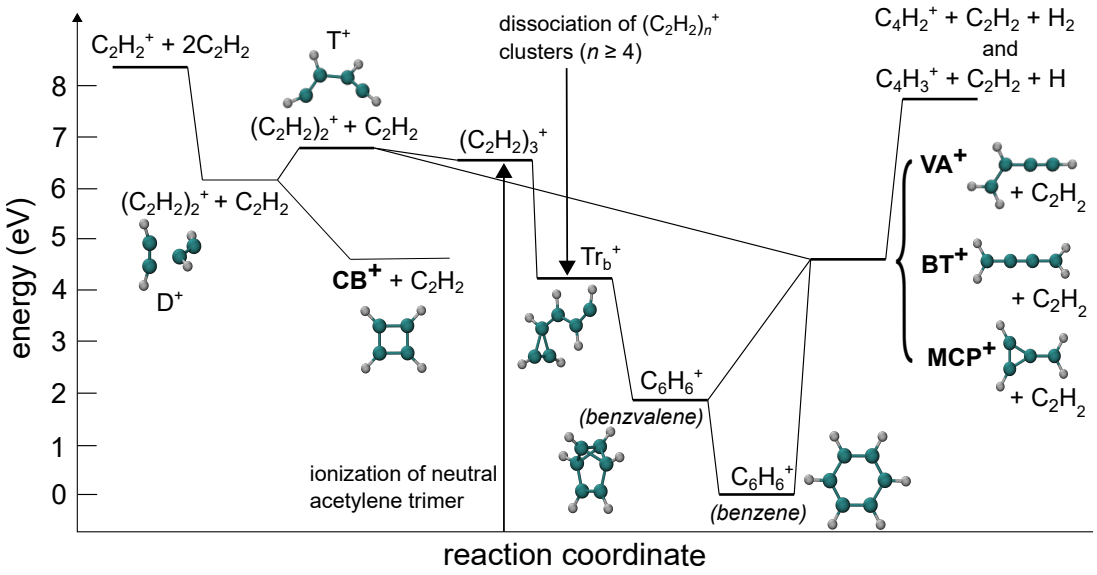

Fig. 4.4 Energy level diagram of stationary points associated with acetylene reactions leading to $C_4H_4^+$ isomers. Energies are based on available thermochemical data.[178,179,185,377,378]

The primary, barrierless reaction of $C_2H_2^+$ and C_2H_2 forms the $(C_2H_2)_2^+$ dimer ion that then accesses the covalent $C_4H_4^+$ potential energy surface:[178,179]

$$C_2H_2^+ + C_2H_2 \rightarrow (C_2H_2)_2^+ \rightarrow C_4H_4^{+*} \tag{4.1}$$

Following formation, the excited $C_4H_4^{+*}$ ions can be stabilized through radiation in low pressure environments or collisions in high pressure environments. Alternatively, they can access two dissociation channels:

$$C_4H_4^{+*} \rightarrow C_4H_3^+ + H \tag{4.2}$$

and

$$C_4H_4^{+*} \rightarrow C_4H_2^+ + H_2 \tag{4.3}$$

The high energy portion of the $C_4H_4^+$ potential energy surface, near the bimolecular entrance channel (eq. 4.1), has been explored experimentally by photoionizing the neutral acetylene dimer, a T-shaped van der Waals complex.[179,185,379–384] Calculations, conducted to understand the geometry of the neutral dimer on the charged potential energy surface, predict that $C_2H_2^+$ and C_2H_2 react to form the dimer ion, D^+ in Figure 4.4.[178] A low energy (< 0.05 eV) barrier leads to $\mathbf{CB}^+$ while a higher energy (≈ 0.5 eV) barrier, T^+, leads to an

intermediate along the pathway to **VA**$^+$, **BT**$^+$, and **MCP**$^+$. Although all four isomers are energetically accessible through the $C_2H_2^+ + C_2H_2$ reaction, calculations suggest that the formation of **CB**$^+$ is the most facile at low energies.[152,180,183] Vibrational predissociation spectroscopy and ion mobility experiments, aimed to characterize the acetylene dimer cation, confirmed that **CB**$^+$ is the predominant $C_4H_4^+$ isomer formed through acetylene ion-molecule reactions.[152,180]

$C_4H_4^+$ cations can also be formed through dissociation of larger carbocations generated through ionization of neutral acetylene clusters, which may occur in low density regions of the supersonic expansion (see Chapter 2). Calculations predict that vertical ionization of the neutral acetylene trimer[155,380,383,385] leads to a $C_4H_4^+$-C_2H_2 complex [$(C_2H_2)_3^+$ in Figure 4.4], a structure that is consistent with the measured infrared spectrum of $(C_2H_2)_3^+$-Ar.[152] The $C_4H_4^+$ "core" has a similar geometry to the T$^+$ transition state (Fig. 4.4) on the $C_4H_4^+$ potential energy surface.[178] If the T$^+$-C_2H_2 complex sheds the C_2H_2 monomer, the T$^+$ fragment either collapses to **CB**$^+$ (through D$^+$) or proceeds *via* an intermediate towards formation of **VA**$^+$, **BT**$^+$, and **MCP**$^+$. Dissociation of larger acetylene cluster ions, such as the tetramer, is predicted to give $C_6H_6^+$ fragments with structures similar to Tr_b^+ in Figure 4.4, that may access the $C_4H_4^+ + C_2H_2$ channel if they retain sufficient internal energies.[377] Evidence from photodissociation studies suggests that the **VA**$^+$ and **MCP**$^+$ isomers are the most likely $C_4H_4^+$ fragments of $C_6H_6^+$, with minor formation of **BT**$^+$.[176,186–188,360,361,386,387] One explanation for the lack of **CB**$^+$ formation is that several $C_6H_6^+$ isomerization barriers lie lower than the dissociation limit ($\approx$ 4.5 eV above the benzene cation), with $C_6H_6^+$ scrambling between acyclic structures ultimately favoring **VA**$^+$ and **MCP**$^+$ production.[189,388–391]

The preference for **VA**$^+$ formation under some experimental conditions may also be due to its high isomerization and dissociation barriers. Because the most stable structures of $C_4H_3^+$ and $C_4H_2^+$ ions are linear, it is believed that $C_4H_4^+$ ions scramble toward linear forms, such as the **VA**$^+$ and **BT**$^+$ isomers, prior to dissociating.[179] Isomerization of **VA**$^+$ is predicted to require $\approx$ 2 eV,[191,392] whereas dissociation to give $C_4H_3^+$ and $C_4H_2^+$ fragments requires $\approx$ 3 eV based on appearance energies and the ionization potential of neutral vinylacetylene.[135,178,179,181,191,201,202,392] Collisional stabilization of intermediates along these dissociation pathways may lead to formation of **VA**$^+$ and **BT**$^+$ in the ion source.

4.2 Experimental and computational methods

REPD spectra of $C_4H_4^+$-Ar and $C_4H_4^+$-N_2 complexes over the 296-550 nm range were recorded in a tandem mass spectrometer. The experimental arrangement has been described in Chapter 2 and only a brief description is given here. The early portion of a pulsed supersonic expansion of a lean acetylene mixture (≈ 0.7 % C_2H_2 in Ar or N_2), with a stagnation pressure of 4.5 bar, was bombarded with electrons to initiate acetylene ion-molecule reactions. The stabilized $C_4H_4^+$ cations were tagged with Ar or N_2 in the expansion. The target $C_4H_4^+$-Ar and $C_4H_4^+$-N_2 cations were mass selected by a quadrupole mass filter (QMF). The ion beam was deflected 90° using an electrostatic quadrupole bender and introduced into an octopole ion guide where it was exposed to light from a tunable optical parametric oscillator (OPO, EKSPLA NT342B). Following resonant photoexcitation, the complexes dissociated to $C_4H_4^+$ (tag loss), $C_4H_2^+$ (H_2 and tag loss), and possibly $C_4H_3^+$ (H and tag loss) fragments, which were mass selected with a second QMF and detected using a microchannel plate. Due to the low signal-to-noise ratio at the onset for $C_4H_2^+$ formation around 410 nm, the mass resolution of the second QMF was reduced slightly to pass $C_4H_2^+$ and $C_4H_3^+$ photofragments. Photodissociation action spectra were obtained by recording the photofragment ion signal (normalized to the laser power) as a function of wavelength (calibrated using an Ångstrom LSA UVL wavemeter).

Quantum chemical calculations were conducted to predict wavelengths for electronic transitions of $C_4H_4^+$ isomers and to understand pathways to $C_4H_2^+ + H_2$ and $C_4H_3^+ + H$ photofragments. Calculations were conducted using the Gaussian 16 suite.[288] Ground state equilibrium geometries and harmonic vibrational frequencies for the **MCP**$^+$, **CB**$_{rec}^+$, **CB**$_{rh}^+$, **BT**$^+$, and **VA**$^+$ structures were calculated at the CCSD/cc-pVTZ level. Electronic transition energies and oscillator strengths were predicted at the EOM-CCSD/cc-pVTZ level using the ground state equilibrium geometries. Franck-Condon (FC) factors and adiabatic excitation energies for the most likely electronic transitions were derived from the calculated geometries and harmonic vibrational frequencies in the ground and excited electronic states using the PGOPHER program.[311] Stationary points on the ground state $C_4H_4^+$ potential energy surface were found by conducting relaxed potential energy surface scans of $C_4H_4^+$ structures along various internal degrees of freedom at the ωB97X-D/aug-cc-pVTZ level of theory. The optimized geometry for each saddle point was verified by its single negative vibrational frequency and by intrinsic reaction coordinate (IRC) calculations.[393] To obtain more reliable energies for all stationary points, single point energies were calculated at the CCSD(T)/aug-cc-pVTZ level and were added to the vibrational zero-point energies obtained

at the ωB97X-D/aug-cc-pVTZ level. The CCSD(T)/aug-cc-pVTZ//ωB97X-D/aug-cc-pVTZ nomenclature is used to refer to this procedure.

To assess the influence of the tag on the $C_4H_4^+$ core, the geometries and harmonic vibrational frequencies of several $C_4H_4^+$-Ar and $C_4H_4^+$-N_2 complexes in the ground electronic state were calculated using density functional theory (DFT) at the ωB97X-D/cc-pVTZ level. Calculated binding energies, used to predict the strength of the intermolecular interaction, account for basis set superposition error.[394]

4.3 Results and discussion

4.3.1 REPD spectra and computational results

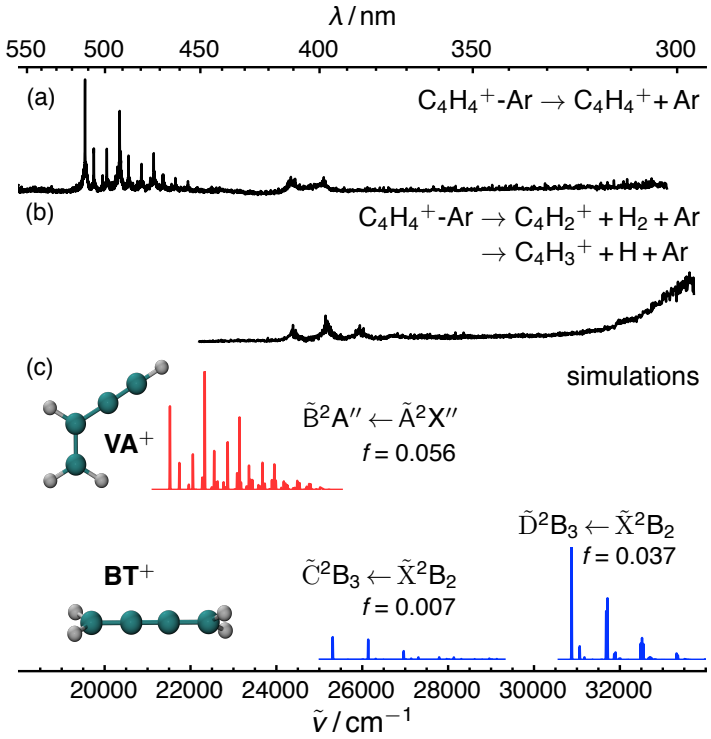

Fig. 4.5 REPD spectra of $C_4H_4^+$-Ar complexes recorded over the 296-550 nm range by monitoring (a) $C_4H_4^+$ and (b) $C_4H_2^+$ and $C_4H_3^+$ photofragments. (c) Simulated spectra and calculated oscillator strengths (f) for the $\tilde{B}^2A''$←$\tilde{X}^2A''$ electronic transition of **VA**$^+$ (red trace) and the $\tilde{C}^2B_3 \leftarrow \tilde{X}^2B_2$ and $\tilde{D}^2B_3 \leftarrow \tilde{X}^2B_2$ electronic transitions of **BT**$^+$ (blue traces), generated from calculations at the EOM-CCSD/cc-pVTZ level of theory. Simulated spectra are plotted so that the origin transitions correspond to the calculated adiabatic excitation energies. Intensities of the simulated spectra are normalized to the strongest electronic transition for each isomer in the visible region.

REPD spectra of $C_4H_4^+$-Ar complexes, recorded over the 296-550 nm range by monitoring $C_4H_4^+$ and $C_4H_2^+$ / $C_4H_3^+$ photofragments, are presented in Figures 4.5a and 4.5b, respectively. The spectrum on the $C_4H_2^+$ / $C_4H_3^+$ (Fig. 4.5b) channel was recorded by reducing the mass resolution of the second QMF, allowing the $C_4H_2^+$ and $C_4H_3^+$ photofragments to be monitored together. A series of narrow bands commences at 511 nm (2.42 eV) and appears only on the $C_4H_4^+$ channel, demonstrating that the $C_4H_4^+$-Ar complexes have enough internal energy to cleave the intermolecular bond, but insufficient energy to sever covalent bonds. A weaker band system is observed around 410 nm (3.02 eV) on both $C_4H_4^+$ and $C_4H_2^+$ / $C_4H_3^+$ channels. An intense, broad band appears on the $C_4H_2^+$ / $C_4H_3^+$ channel at energies above 315 nm (3.94 eV).

To help interpret the REPD spectra, electronic transition energies and oscillator strengths for the four lowest energy $C_4H_4^+$ isomers were calculated at the EOM-CCSD/cc-pVTZ level of theory using ground state equilibrium geometries obtained at the CCSD/cc-pVTZ level. Calculations for the $\mathbf{BT}^+$ cation were conducted using the ground state equilibrium geometry that has D_2 symmetry (see below). The results are summarized in Table 4.1.

All $C_4H_4^+$ isomers, with the exception of $\mathbf{CB}_{\mathrm{rh}}{}^+$, are predicted to have strong electronic transitions occurring between 4.71 and 5.24 eV, such that they all may contribute, depending on abundance, to the structureless band appearing below 315 nm (3.94 eV). The $\tilde{B}^2A''\leftarrow\tilde{X}^2A''$ electronic transition of $\mathbf{VA}^+$ and the $\tilde{C}^2B_3\leftarrow\tilde{X}^2B_2$ and $\tilde{D}^2B_3\leftarrow\tilde{X}^2B_2$ transitions of $\mathbf{BT}^+$ are likely to give rise to the 511 nm (2.42 eV) and 410 nm (3.02 eV) band systems. Because previous calculations, IR vibrational predissociation spectroscopic studies, and ion mobility experiments indicate that the $\mathbf{CB}^+$ isomer should be abundant and is rectangular as opposed to rhombic, the moderately intense $\tilde{B}^2A_1\leftarrow\tilde{X}^2B_2$ electronic transition of $\mathbf{CB}_{\mathrm{rh}}{}^+$ ($f = 0.021$) is unlikely to give rise to the weak 410 nm system.[152,178,180,183] Simulated spectra for the three transitions of $\mathbf{VA}^+$ and $\mathbf{BT}^+$, generated based on calculated FC factors, are displayed in Figure 4.5c and are aligned based on the calculated adiabatic excitation energies. The intensity of each simulated spectrum is normalized to the intensity of the strongest electronic transition for each isomer in the visible region.

Previous studies show that the $\tilde{B}^2A''\leftarrow\tilde{X}^2A''$ transition of $\mathbf{VA}^+$ and the $\tilde{C}^2B_3\leftarrow\tilde{X}^2B_2$ transition of $\mathbf{BT}^+$ overlap in the 440-520 nm region.[207,369,370] Our calculations at the EOM-CCSD/cc-pVTZ level predict that the $\tilde{B}^2A''\leftarrow\tilde{X}^2A''$ adiabatic excitation of $\mathbf{VA}^+$ occurs at 2.67 eV and that the $\tilde{C}^2B_3\leftarrow\tilde{X}^2B_2$ adiabatic excitation of $\mathbf{BT}^+$ occurs at 3.14 eV. The large overestimation of the transition energy for $\mathbf{BT}^+$ is possibly due to inaccurate treatment of static and dynamical electron correlation that has been noted to occur for molecules with highly delocalized electrons.[395–399] The stronger $\tilde{D}^2B_3\leftarrow\tilde{X}^2B_2$ transition ($f = 0.036$) of $\mathbf{BT}^+$

Table 4.1 Vertical (E_{vert}) and adiabatic (E_{adia}) excitation energies and oscillator strengths (f), calculated at the EOM-CCSD/cc-pVTZ level, along with measured E_{adia} (exp) for electronic transitions of the four lowest energy $C_4H_4^+$ isomers (including both distorted geometries of the cyclobutadiene cation **CB**$^+$). Transitions for the **BT**$^+$ isomer were calculated assuming D_2 symmetry. Energies are in eV. For each isomer, 14α represents the electron occupying the highest occupied molecular orbital.

	transition	dominant contribution	E_{vert}	f	E_{adia}	exp
MCP$^+$	$\tilde{A}^2B_2 \leftarrow \tilde{X}^2B_1$	$13\beta \rightarrow 14\beta$	4.40	0		
	$\tilde{B}^2A_2 \leftarrow \tilde{X}^2B_1$	$14\alpha \rightarrow 15\alpha$	5.24	0.009		
	$\tilde{C}^2A_1 \leftarrow \tilde{X}^2B_1$	$12\beta \rightarrow 14\beta$	5.37	0.0005		
	$\tilde{D}^2B_1 \leftarrow \tilde{X}^2B_1$	$11\beta \rightarrow 14\beta$	5.88	0.004		
BT$^+$	$\tilde{A}^2B_2 \leftarrow \tilde{X}^2B_2$	$13\beta \rightarrow 14\beta$	1.92	0		
	$\tilde{B}^2B_3 \leftarrow \tilde{X}^2B_2$	$14\alpha \rightarrow 15\alpha$	2.44	0.015		
	$\tilde{C}^2B_3 \leftarrow \tilde{X}^2B_2$	$12\beta \rightarrow 14\beta$	3.28	0.007	3.14	2.42[a,b]
	$\tilde{D}^2B_3 \leftarrow \tilde{X}^2B_2$	$13\beta \rightarrow 15\beta$	4.04	0.037	3.83	3.02[a]
	$\tilde{E}^2B_3 \leftarrow \tilde{X}^2B_2$	$14\alpha \rightarrow 16\alpha$, $13\alpha \rightarrow 15\alpha$	5.05	0.140		
	$\tilde{F}^2B_2 \leftarrow \tilde{X}^2B_2$	$13\alpha \rightarrow 15\alpha$	5.07	0		
	$\tilde{G}^2B_3 \leftarrow \tilde{X}^2B_2$	$11\beta \rightarrow 14\beta$	6.42	0.08		
CB$_{rec}^+$	$\tilde{A}^2B_{1g} \leftarrow \tilde{X}^2B_{2g}$	$14\alpha \rightarrow 15\alpha$	1.20	0		
	$\tilde{B}^2B_{2u} \leftarrow \tilde{X}^2B_{2g}$	$13\beta \rightarrow 14\beta$	4.64	0		
	$\tilde{C}^2A_u \leftarrow \tilde{X}^2B_{2g}$	$12\beta \rightarrow 15\beta$, $14\alpha \rightarrow 16\alpha$	4.77	0.004		
	$\tilde{D}^2B_{3u} \leftarrow \tilde{X}^2B_{2g}$	$12\beta \rightarrow 14\beta$	5.22	0.103		
CB$_{rh}^+$	$\tilde{A}^2B_1 \leftarrow \tilde{X}^2B_2$	$14\alpha \rightarrow 15\alpha$	2.54	0		
	$\tilde{B}^2A_1 \leftarrow \tilde{X}^2B_2$	$14\alpha \rightarrow 16\alpha$	4.17	0.021		
	$\tilde{C}^2A_2 \leftarrow \tilde{X}^2B_2$	$13\beta \rightarrow 14\beta$	6.14	0.007		
VA$^+$	$\tilde{A}^2A' \leftarrow \tilde{X}^2A''$	$13\beta \rightarrow 14\beta$	1.31	0		
	$\tilde{B}^2A'' \leftarrow \tilde{X}^2A''$	$12\beta \rightarrow 14\beta$	2.90	0.056	2.67	2.42[a,c], 2.36[d]
	$\tilde{C}^2A' \leftarrow \tilde{X}^2A''$	$11\beta \rightarrow 14\beta$	4.69	0.0001		
	$\tilde{D}^2A'' \leftarrow \tilde{X}^2A''$	$14\alpha \rightarrow 15\alpha$	4.72	0.282		

[a]this work, [b]ref. 207, [c]ref. 206, [d]ref. 173

is predicted to occur 0.69 eV above the $\tilde{C}^2B_3 \leftarrow \tilde{X}^2B_2$ transition ($f = 0.007$), coinciding with the bands near 410 nm (3.02 eV). Vibronic structure in the electronic spectra of the two isomers, based on calculated FC factors, are discussed below.

4.3.2 The $\tilde{B}^2A'' \leftarrow \tilde{X}^2A''$ transition of VA^+ (511 nm system)

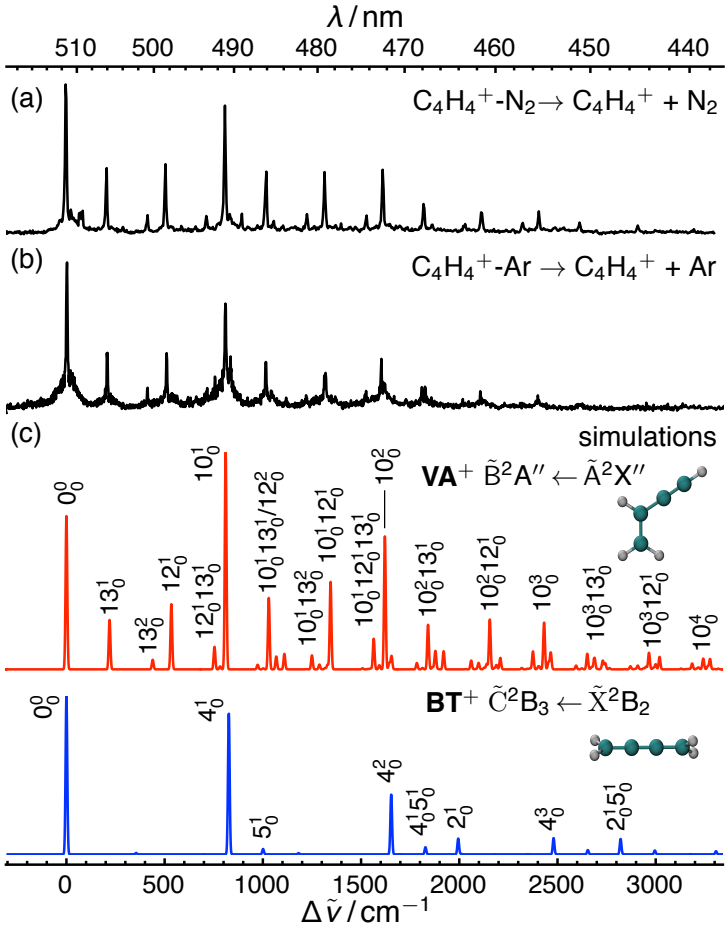

Fig. 4.6 REPD spectra of (a) $C_4H_4^+$-Ar and (b) $C_4H_4^+$-N_2 complexes, recorded over the 436-520 nm range by monitoring $C_4H_4^+$ photofragments. (c) simulated spectra for the $\tilde{B}^2A''\leftarrow\tilde{X}^2A''$ transition of $\mathbf{VA}^+$ (red trace) and the $\tilde{C}^2B_3\leftarrow\tilde{X}^2B_2$ transition of $\mathbf{BT}^+$ (blue trace), shifted by 1977 and 5768 cm^{-1}, respectively, so that the origin transitions coincide with that of the $C_4H_4^+$-Ar complex in (b).

REPD spectra of $C_4H_4^+$-Ar and $C_4H_4^+$-N_2 complexes over the 436-520 nm range are presented in Figure 4.6 panels a and b. To aid in the assignment of bands, simulated spectra of the $\tilde{B}^2A''\leftarrow\tilde{X}^2A''$ transition of $\mathbf{VA}^+$ and the $\tilde{C}^2B_3\leftarrow\tilde{X}^2B_2$ transition of $\mathbf{BT}^+$, shown in Figure 4.6c, are plotted so that the positions and intensities of the origin transitions match those of the 511 nm band in the $C_4H_4^+$-Ar spectrum. These simulations were generated using calculated structures, shown in Figure 4.7, and unscaled harmonic vibrational frequencies (see Tables 4.6 and 4.8) for the isomers in the ground and excited electronic states. The simulated $\tilde{B}^2A''\leftarrow\tilde{X}^2A''$ transition of $\mathbf{VA}^+$ (red trace) reproduces most bands in the REPD spectra whereas the simulated $\tilde{C}^2B_3\leftarrow\tilde{X}^2B_2$ transition of $\mathbf{BT}^+$ (blue trace) matches fewer bands. This indicates that the 511 nm system arises mostly from $\mathbf{VA}^+$. Band assignments

for the $\tilde{B}^2A''\leftarrow\tilde{X}^2A''$ system of $\mathbf{VA}^+$, tabulated in Table 4.2, are based on the simulated spectrum.

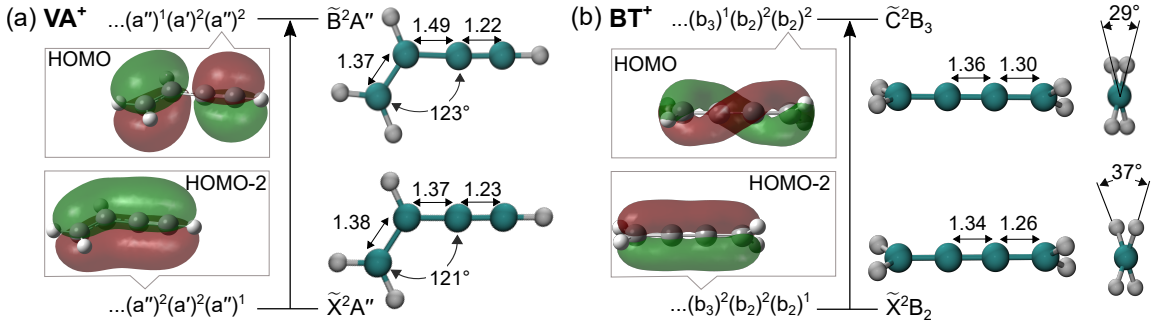

Fig. 4.7 Molecular orbitals and equilibrium geometries relevant to the (a) $\tilde{B}^2A''\leftarrow\tilde{X}^2A''$ transition of the vinylacetylene cation ($\mathbf{VA}^+$) and (b) $\tilde{C}^2B_3\leftarrow\tilde{X}^2B_2$ transition of the butatriene cation ($\mathbf{BT}^+$), calculated at the CCSD/cc-pVTZ and EOM-CCSD/cc-pVTZ levels of theory.

Table 4.2 Assignments, positions, and relative positions of bands for the $\tilde{B}^2A''\leftarrow\tilde{X}^2A''$ band system of $\mathbf{VA}^+$-Ar and $\mathbf{VA}^+$-N_2.

	$\mathbf{VA}^+$-Ar			$\mathbf{VA}^+$-N_2		
band	λ / (nm)	$\tilde{\nu}$ / (cm^{-1})	$\Delta\tilde{\nu}$ / (cm^{-1})	λ / (nm)	$\tilde{\nu}$ / (cm^{-1})	$\Delta\tilde{\nu}$ / (cm^{-1})
0_0^0	511.30	19558	0	511.48	19551	0
13_0^1	506.00	19763	205	506.33	19750	199
13_0^2	500.85	19966	408	500.80	19968	417
12_0^1	498.38	20065	507	498.53	20059	508
$13_0^1 12_0^1$	493.32	20271	713	493.41	20267	716
10_0^1	491.06	20364	806	491.11	20362	811
$13_0^1 10_0^1/12_0^2$	486.14	20570	1012	486.07	20573	1022
$13_0^2 10_0^1/12_0^2 13_0^1$	481.35	20775	1217	481.26	20779	1228
$12_0^1 10_0^1$	479.16	20870	1312	479.18	20869	1318
$13_0^1 12_0^1 10_0^1$	474.38	21080	1522	474.32	21083	1532
10_0^2	472.63	21158	1600	472.48	21165	1614
$13_0^1 10_0^2$	467.86	21374	1816	467.88	21373	1822
$13_0^2 10_0^2$	463.54	21573	2015	463.28	21585	2034
$12_0^1 10_0^2$	461.64	21662	2104	461.55	21666	2115
$13_0^1 12_0^1 10_0^2$				457.08	21878	2327
10_0^3	455.48	21955	2397	455.37	21960	2409
$13_0^1 10_0^3$	450.84	22181	2614	451.12	22167	2616
$12_0^1 10_0^3$				445.18	22463	2912
10_0^4				439.58	22749	3198

There are several obvious progressions in the band system. The progression spaced by $\approx 806\,\mathrm{cm}^{-1}$ is a prominent feature of the REPD spectra, extending for at least three quanta. The spacing is similar to that previously observed in matrix isolation spectra of **VA**$^+$.[173,206] This progression is assigned to ν_{10}, a symmetric (a′) C=C stretching vibrational mode, based on the calculated harmonic vibrational frequency of $811\,\mathrm{cm}^{-1}$ in the $\tilde{\mathrm{B}}^2\mathrm{A}''$ state and the fact that the central C=C bond lengthens as a consequence of the $\pi\rightarrow\pi^*$ transition (indicated by the HOMO-2 and HOMO molecular orbitals displayed in Figure 4.7). Shorter progressions spaced by ≈ 507 and $\approx 200\,\mathrm{cm}^{-1}$ are also observed. Although the $507\,\mathrm{cm}^{-1}$ progression was observed in previous matrix isolation spectra, the $200\,\mathrm{cm}^{-1}$ progression was not apparent due to the width of the bands, contribution of contaminants to the spectra, and presence of matrix site artefacts.[173,201,205–207] Here, the progressions are attributed to the ν_{12} (C_4 skeleton) and ν_{13} (C-C-C) a′ bending vibrational modes (see Figure 4.8), based on the calculated harmonic vibrational frequencies of 534 and $220\,\mathrm{cm}^{-1}$, respectively, in the $\tilde{\mathrm{B}}^2\mathrm{A}''$ state. These progressions build upon the intense progression in ν_{10}, establishing a regular pattern in the spectrum.

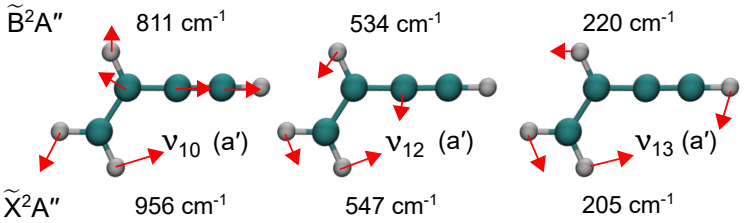

Fig. 4.8 The C-C stretch (ν_{10}), C_4 skeletal bend (ν_{12}), and C-C-C bend (ν_{13}) vibrational normal modes of **VA**$^+$ with corresponding harmonic vibrational frequencies in the $\tilde{\mathrm{X}}^2\mathrm{A}''$ and $\tilde{\mathrm{B}}^2\mathrm{A}''$ states, calculated at the CCSD/cc-pVTZ and EOM-CCSD/cc-pVTZ levels of theory.

The agreement between the simulated and REPD spectra indicates that the (EOM)CCSD/cc-pVTZ calculations adequately describe the geometries and harmonic vibrational frequencies of **VA**$^+$ in the $\tilde{\mathrm{X}}^2\mathrm{A}''$ and $\tilde{\mathrm{B}}^2\mathrm{A}''$ electronic states, and that the Ar and N_2 tags have minor effects on the **VA**$^+$ core. Excitations of intermolecular stretch (ν_s) and bend (ν_b) vibrations give rise to weak features near the origin and 10_0^1 transitions. In the **VA**$^+$-N_2 spectrum (Figure 4.9a), a band $\approx 27\,\mathrm{cm}^{-1}$ above the origin band is assigned to the b_0^1 transition, based on the calculated vibrational frequency ($38\,\mathrm{cm}^{-1}$) for the lowest intermolecular bending mode of the **VA**$^+$-N_2 structure shown in Figure 4.9b. Another weak band, occurring at $0_0^0 + 75\,\mathrm{cm}^{-1}$ likely arises from the s_0^1 transition (a′ intermolecular stretch, ν_s). Similarly, transitions occurring 24 and $86\,\mathrm{cm}^{-1}$ above the 10_0^1 transition are assigned to the $10_0^1 b_0^1$ and $10_0^1 s_0^1$ combination bands, respectively. In the **VA**$^+$-Ar spectrum, weak bands appearing $27\,\mathrm{cm}^{-1}$ above the 0_0^0 and 10_0^1 transitions, shown in Figure 4.10, arise from the b_0^1 and $10_0^1 b_0^1$

transitions, with ν_b being the lowest frequency intermolecular bending vibrational mode. The calculated vibrational frequency for ν_b of 21 cm^{-1}, for the lowest energy $\mathbf{VA}^+$-Ar complex shown in Figure 4.10b, supports these assignments. See Section 4.5.1 in the supporting information (SI) for additional details of calculations on $\mathbf{VA}^+$-Ar and $\mathbf{VA}^+$-N_2 complexes.

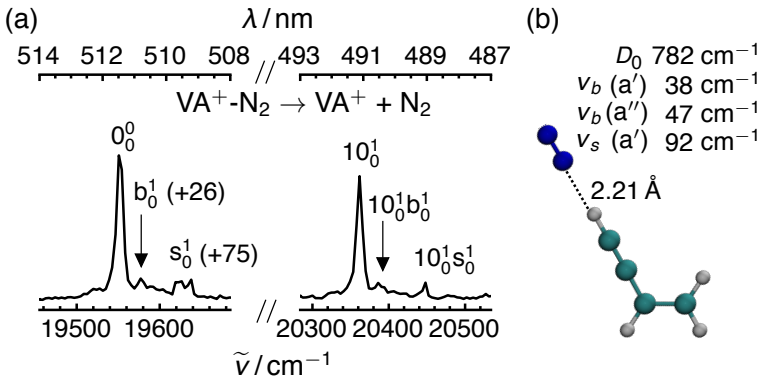

Fig. 4.9 (a) REPD spectrum of $\mathbf{VA}^+$-N_2 over the 508-514 nm and 487-493 nm ranges. (b) Binding energy (D_0) and harmonic vibrational frequencies for intermolecular bending ν_b and stretching ν_s modes of the lowest energy $\mathbf{VA}^+$-N_2 complex, calculated at the ωB97X-D/cc-pVTZ level.

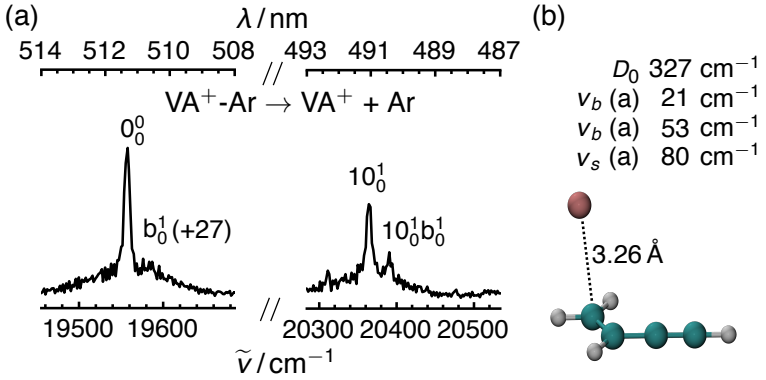

Fig. 4.10 (a) REPD spectrum of $\mathbf{VA}^+$-Ar over the 508-514 nm and 487-493 nm ranges. (b) Binding energy (D_0) and harmonic vibrational frequencies for intermolecular bending ν_b and stretching ν_s modes of the lowest energy $\mathbf{VA}^+$-Ar complex, calculated at the ωB97X-D/cc-pVTZ level.

All bands in the REPD spectra over the 436-520 nm range correspond to the $\tilde{B}^2A''\leftarrow\tilde{X}^2A''$ electronic transition of $\mathbf{VA}^+$ and excitations of intermolecular vibrations of $C_4H_4^+$-Ar and $C_4H_4^+$-N_2 complexes. Bands associated with the weak $\tilde{C}^2B_3\leftarrow\tilde{X}^2B_2$ transition of $\mathbf{BT}^+$ are not evident and are possibly obscured by the strong electronic transition of $\mathbf{VA}^+$. In the previous neon matrix spectrum, the $\tilde{C}^2B_3\leftarrow\tilde{X}^2B_2$ origin transition of $\mathbf{BT}^+$ is observed 118 cm^{-1} above the $\tilde{B}^2A''\leftarrow\tilde{X}^2A''$ origin transition of $\mathbf{VA}^+$.[207] Assuming a similar separation for the tagged

gas-phase cations, the $\tilde{C}^2B_3 \leftarrow \tilde{X}^2B_2$ origin transition of **BT**$^+$ should occur around 508 nm in the REPD spectra, represented by the blue arrow in Figure 4.11.

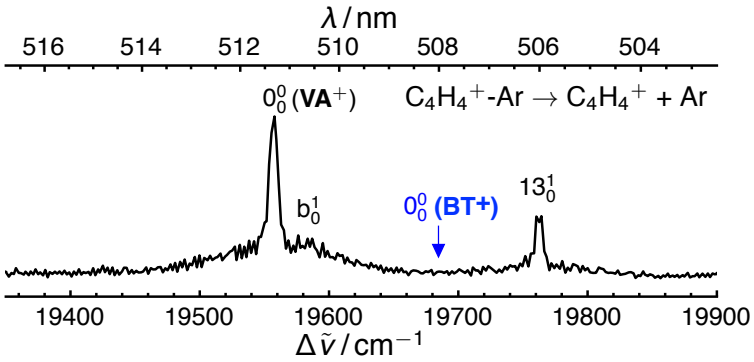

Fig. 4.11 REPD spectrum of $C_4H_4^+$-Ar complexes over the 503-517 nm range, with the expected location of the $\tilde{C}^2B_3 \leftarrow \tilde{X}^2B_2$ origin transition of **BT**$^+$ indicated by the blue arrow.

4.3.3 The $\tilde{D}^2B_3 \leftarrow \tilde{X}^2B_2$ transition of BT$^+$ (410 nm system)

Transitions at 410, 397, and 385 nm in the $C_4H_4^+$-Ar spectrum arise from the $\tilde{D}^2B_3 \leftarrow \tilde{X}^2B_2$ band system of **BT**$^+$. To facilitate assignment of the bands, the REPD spectra of $C_4H_4^+$-Ar complexes, recorded by monitoring the different photofragments (see Fig. 4.5), were summed together to produce the spectrum shown in Figure 4.12a. The spectrum can be compared with the simulated $\tilde{D}^2B_3 \leftarrow \tilde{X}^2B_2$ spectrum, generated using unscaled harmonic vibrational frequencies (see Table 4.8 in the supporting information) and plotted in Figure 4.12b so that the origin transition's position and intensity match those of the 410 nm band in the REPD spectrum. Positions and assignments of bands, based on the simulated spectrum, are tabulated in Table 4.3.

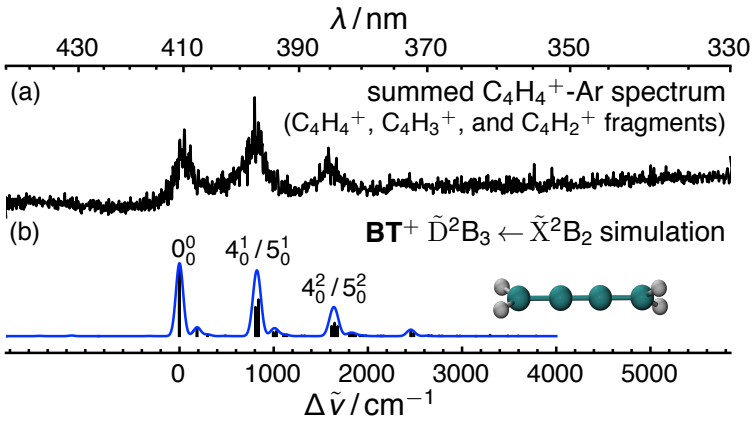

Fig. 4.12 (a) REPD spectrum of $C_4H_4^+$-Ar complexes, generated by summing spectra recorded by monitoring $C_4H_4^+$, $C_4H_3^+$, and $C_4H_2^+$ photofragments (see Fig. 4.5). (b) Simulated $\tilde{D}^2B_3 \leftarrow \tilde{X}^2B_2$ electronic transition of the butatriene radical cation (**BT**$^+$).

Table 4.3 Assignments, positions, and relative positions of bands for the $\tilde{D}^2B_3 \leftarrow \tilde{X}^2B_3$ band system of **BT**$^+$-Ar.

band	λ / (nm)	$\tilde{\nu}$ / (cm^{-1})	$\Delta\tilde{\nu}$ / (cm^{-1})
0_0^0	409.85	24399	0
$4_0^1 / 5_0^1$	397.44	25161	762
$4_0^2 / 5_0^2$	385.24	25958	1559

The bands at 397 nm ($0_0^0 + 762\,\text{cm}^{-1}$) and 385 nm ($0_0^0 + 1559\,\text{cm}^{-1}$) in the REPD spectrum are assigned to the 4_0^1 and 4_0^2 transitions, with their intensities consistent with the predicted lengthening of the C=C bonds (Figure 4.13) and decrease in the ν_4 (a) C=C symmetric stretch vibrational frequency (from 875 to 835 cm^{-1}) from $\tilde{X}^2B_2$ state to $\tilde{D}^2B_3$ state. Transitions associated with the CH_2 twisting vibration (ν_5, a symmetry), which has a calculated harmonic vibrational frequency of 804 cm^{-1} in the $\tilde{D}^2B_3$ state, lend intensity to the 397 and 385 nm bands.

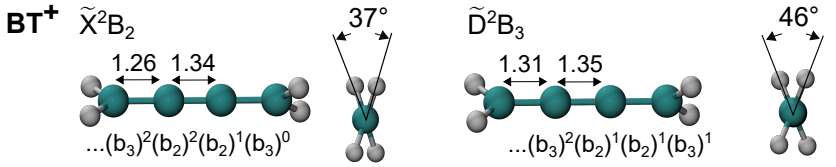

Fig. 4.13 Geometries and dominant electronic configurations for the $\tilde{X}^2B_2$ and $\tilde{D}^2B_3$ (D_2 point group) electronic states of the butatriene radical cation (**BT**$^+$) calculated at the EOM-CCSD/cc-pVTZ level of theory.

4.3.4 Dissociation pathways

The onset for $C_4H_2^+ / C_4H_3^+$ photofragments in the REPD spectrum at ≈ 3.0 eV matches previously measured appearance energies for $C_4H_4^+$ (see Section 4.1.2). Possible dissociation pathways are explored here by calculating stationary points on the ground state $C_4H_4^+$ potential energy surface using the CCSD(T)/aug-cc-pVTZ//ωB97X-D/aug-cc-pVTZ level of theory. A relevant portion of the surface is presented in Figure 4.14, with additional details provided in the supporting information. Energies for the stationary points are relative to the energy of the **BT**$^+$ isomer. Interconversion pathways agree with those previously calculated at different levels of theory, described in Section 4.1.2 and depicted in Figure 4.4.[178,191,202]

The lowest energy dissociation channels correspond to $C_4H_2^+ + H_2$ ([12] in Fig. 4.14) and $C_4H_3^+ + H$ ([14]), with thresholds predicted to lie 2.43 and 2.87 eV above the **BT**$^+$ isomer,

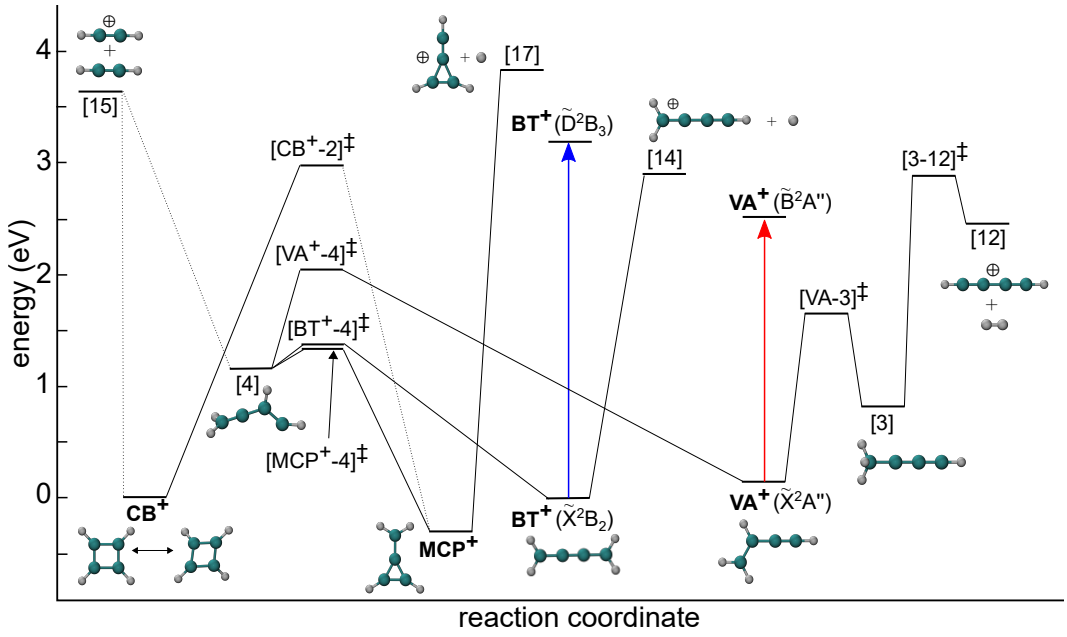

Fig. 4.14 Potential energy surface relevant to the $C_2H_2^+ + C_2H_2$ association reaction, with stationary points calculated at the CCSD(T)/aug-cc-pVTZ//ωB97X-D/aug-cc-pVTZ level of theory. Energies (eV) are relative to **BT**$^+$.

respectively. These channels are accessed through the **BT**$^+$ and **VA**$^+$ chain intermediates to give the linear diacetylene ($C_4H_2^+$) and protonated diacetylene ($C_4H_3^+$) charged fragments, which are the global minima on their respective potential energy surfaces.

Among the four most stable $C_4H_4^+$ isomers, **BT**$^+$ is predicted to most easily sever a C-H bond, through a barrierless pathway, whereas the **VA**$^+$ isomer is the likely intermediate for production of $C_4H_2^+ + H_2$ fragments, involving a barrier ([3-12]†) lying 0.42 eV above the energetic threshold. Because of the low energy interconversion barriers, all $C_4H_4^+$ isomers are able to access the $C_4H_2^+ + H_2$ and $C_4H_3^+ + H$ channels with ≈ 3 eV of internal energy (see Table 4.4), consistent with previously measured appearance energies, kinetic energy release measurements, and available heats of formation.[179,181]

Table 4.4 Dissociation energies (eV), calculated at the CCSD(T)/aug-cc-pVTZ//ωB97X-D/aug-cc-pVTZ level, for the four lowest energy $C_4H_4^+$ isomers.

	$C_4H_2^+ + H_2$	$C_4H_3^+ + H$	$C_2H_2^+ + C_2H_2$
MCP$^+$	3.17	3.19	3.92
BT$^+$	2.85	2.87	3.60
CB$^+$	2.83	2.85	3.58
VA$^+$	2.74	2.76	3.49

4.4 Conclusions

Electronic transitions of $C_4H_4^+$ isomers were investigated using REPD spectroscopy of $C_4H_4^+$-Ar and $C_4H_4^+$-N_2 complexes and quantum chemical calculations at the EOM-CCSD/cc-pVTZ level of theory. The 511 and 410 nm band systems in the REPD spectra were assigned to the $\tilde{B}^2A''\leftarrow\tilde{X}^2A''$ transition of **VA**$^+$ and the $\tilde{D}^2B_3\leftarrow\tilde{X}^2B_2$ transition of **BT**$^+$, respectively. Bands in the spectra were matched by spectral simulations of the two transitions, generated using calculations at the EOM-CCSD/cc-pVTZ level of theory, that aided in the assignment of bands to vibronic transitions. The $\tilde{B}^2A''\leftarrow\tilde{X}^2A''$ electronic spectrum is dominated by a progression in the central C-C stretching vibration spaced by $\approx 806\,cm^{-1}$, with weaker transitions associated with excitation of bending vibrational modes. The $\tilde{D}^2B_3\leftarrow\tilde{X}^2B_2$ transition of **BT**$^+$ spectrum features a short progression in the C=C symmetric stretching vibration, with possible contribution from the CH_2 twisting vibration, spaced by $\approx 760\,cm^{-1}$. The onset for production of $C_4H_2^+$ and $C_4H_3^+$ photofragments at 3.02 eV in the REPD spectrum of $C_4H_4^+$-Ar agrees with calculated ground state dissociation thresholds for **BT**$^+$. Although spectroscopic fingerprints for the **MCP**$^+$ and **CB**$^+$ isomers were not apparent in the REPD spectra, their transitions likely overlap strong electronic transitions of **VA**$^+$ and **BT**$^+$ in the UV, giving rise to the broad band observed in the spectrum above 4 eV.

The spectra measured in this work constitute the first $\tilde{B}^2A''\leftarrow\tilde{X}^2A''$ electronic spectrum of **VA**$^+$ in which the vibronic structure is clearly resolved and the first observation of the $\tilde{D}^2B_3\leftarrow\tilde{X}^2B_2$ transition of **BT**$^+$. These spectra may be useful for the detection of the isomers in remote environments where acetylene ion-molecule reactions occur, including in the interstellar medium and the atmosphere of Titan. Although a kinetic model for $C_4H_4^+$ dissociation was not carried out, owing to the two $C_4H_3^+ + H$ and $C_4H_2^+ + H_2$ dissociation channels being measured together, the calculated stationary points on the ground state $C_4H_4^+$ manifold may prove useful for modeling hydrocarbon chain reactions occurring in extraterrestrial environments, plasmas, and flames. The models are expected to show that **MCP**$^+$ and **CB**$^+$ formation dominates under low energy and pressure conditions, with **VA**$^+$ and **BT**$^+$ production becoming competitive with increased energy and clustering.

4.5 Supporting information (SI)

The following sections provide additional information on the electronic structure calculations of **VA**$^+$-Ar, **VA**$^+$-N_2, and **BT**$^+$-Ar complexes (4.5.1) and of stationary points on the ground state $C_4H_4^+$ potential energy surface (4.5.2).

4.5.1 Electronic structure calculations for VA$^+$-Ar, VA$^+$-N_2, and BT$^+$-Ar

The geometries and harmonic vibrational frequencies of **VA**$^+$, **VA**$^+$-Ar, **VA**$^+$-N_2, **BT**$^+$ and **BT**$^+$-Ar were calculated at the ωB97X-D/cc-pVTZ level to assess the effect of an Ar or N_2 tag on the $C_4H_4^+$ core ion. For the ionic complexes, binding energies were predicted using vibrational zero-point corrected energies of the bare $C_4H_4^+$ cation and the tagged complex, accounting for basis set superposition errors. The similar binding energies for the four predicted **VA**$^+$-Ar complexes, shown in Figure 4.15, suggest that several forms of **VA**$^+$-Ar may be generated in the ion source. For **VA**$^+$-N_2, the end-on configuration (D) is the lowest energy structure, although the similar binding energy for (B) suggests it may also be stabilized in the expansion. For all tagged structures, the geometry (Table 4.5) and harmonic vibrational frequencies (Table 4.6) are similar to those of the core **VA**$^+$ cation, indicating only a mild perturbation by the tag.

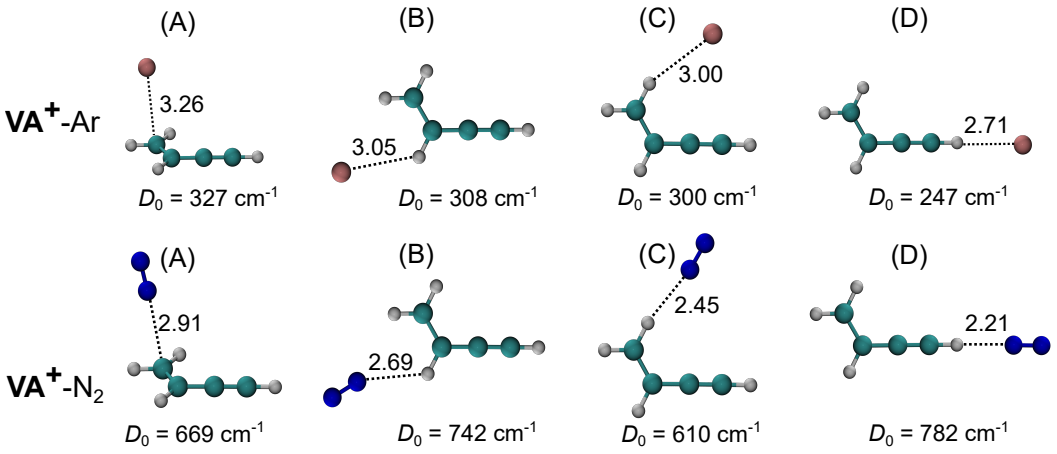

Fig. 4.15 Calculated structures and binding energies (D_0) of **VA**$^+$-Ar and **VA**$^+$-N_2 complexes at the ωB97X-D/cc-pVTZ level of theory. Intermolecular bond lengths are in Å.

Table 4.5 Calculated bond lengths and angles of **VA**$^+$, **VA**$^+$-Ar, and **VA**$^+$-N_2 cations at the ωB97X-D/cc-pVTZ level.

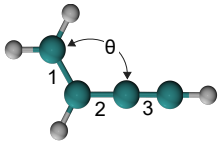

tag	bond length (Å)			θ (deg.)
	1	2	3	
(bare)	1.382	1.372	1.222	120.8
Ar				
(A)	1.383	1.372	1.221	120.8
(B)	1.382	1.372	1.222	120.8
(C)	1.382	1.372	1.222	120.8
(D)	1.382	1.372	1.222	120.8
N_2				
(A)	1.383	1.372	1.221	120.8
(B)	1.383	1.372	1.221	120.9
(C)	1.383	1.372	1.221	120.7
(D)	1.381	1.372	1.223	120.8

Table 4.6 Harmonic vibrational frequencies for $\mathbf{VA}^+$ in the $\widetilde{X}^2A''$ and $\widetilde{B}^2A''$ electronic states, calculated at the EOM-CCSD/cc-pVTZ level of theory with full electron correlation (italicized) and for $\mathbf{VA}^+$, $\mathbf{VA}^+$-Ar, and $\mathbf{VA}^+$-N_2 in their ground electronic states calculated at the ωB97X-D/cc-pVTZ level (normal font). All frequencies are unscaled.

	$H_2CCHCCH^+$			$\mathbf{VA}^+$-Ar				$\mathbf{VA}^+$-N_2			
Mode	$\widetilde{X}^2A''$	$\widetilde{B}^2A''$	$\widetilde{X}^2A''$	(A)	(B)	(C)	(D)	(A)	(B)	(C)	(D)
ν_1	*3409* (a′)	3428 (a′)	3395 (a′)	3397 (a)	3396 (a)	3397 (a)	3362 (a′)	3399 (a)	3397 (a)	3399 (a)	3298 (a′)
ν_2	*3294* (a′)	*3299* (a′)	3279 (a′)	3282 (a)	3279 (a)	3278 (a)	3278 (a′)	3288 (a)	3282 (a)	3272 (a)	3279 (a′)
ν_3	*3225* (a′)	*3232* (a′)	3191 (a′)	3192 (a)	3188 (a)	3191 (a)	3190 (a′)	3194 (a)	3196 (a)	3192 (a)	3191 (a′)
ν_4	*3197* (a′)	*3205* (a′)	3164 (a′)	3167 (a)	3163 (a)	3163 (a)	3163 (a′)	3173 (a)	3166 (a)	3154 (a)	3164 (a′)
ν_5	*2167* (a′)	*2209* (a′)	2153 (a′)	2153 (a)	2153 (a)	2154 (a)	2152 (a′)	2151 (a)	2152 (a)	2154 (a)	2147 (a′)
ν_6	*1513* (a′)	*1655* (a′)	1552 (a′)	1553 (a)	1552 (a)	1552 (a)	1553 (a′)	1554 (a)	1548 (a)	1553 (a)	1552 (a′)
ν_7	*1463* (a′)	*1464* (a′)	1445 (a′)	1446 (a)	1445 (a)	1446 (a)	1446 (a′)	1448 (a)	1439 (a)	1446 (a)	1445 (a′)
ν_8	*1301* (a′)	*1330* (a′)	1288 (a′)	1289 (a)	1289 (a)	1289 (a)	1289 (a′)	1289 (a)	1287 (a)	1292 (a)	1289 (a′)
ν_9	*1153*(a′)	*1110* (a′)	1140 (a′)	1141 (a)	1140 (a)	1141 (a)	1141 (a′)	1142 (a)	1137 (a)	1144 (a)	1140 (a′)
ν_{10}	*956* (a′)	*811* (a′)	947 (a′)	947 (a)	948 (a)	948 (a)	948 (a′)	948 (a)	945 (a)	951 (a)	948 (a′)
ν_{11}	*692* (a′)	*756* (a′)	699 (a′)	701 (a)	700 (a)	700 (a)	708 (a′)	701 (a)	699 (a)	698 (a)	782 (a′)
ν_{12}	*547* (a′)	*534* (a′)	558 (a′)	559 (a)	559 (a)	559 (a)	559 (a′)	560 (a)	558 (a)	561 (a)	560 (a′)
ν_{13}	*205* (a′)	*220* (a′)	211 (a′)	212 (a)	215 (a)	213 (a)	213 (a′)	213 (a)	216 (a)	214 (a)	223 (a′)
ν_{14}	*1105* (a″)	*1053* (a″)	1077 (a″)	1073 (a)	1079 (a)	1079 (a)	1077 (a″)	1078 (a)	1079 (a)	1091 (a)	1076 (a″)
ν_{15}	*938* (a″)	*827* (a″)	902 (a″)	900 (a)	903 (a)	900 (a)	905 (a″)	899 (a)	901 (a)	903 (a)	905 (a″)
ν_{16}	*806*(a″)	*706* (a″)	786 (a″)	786 (a)	788 (a)	787 (a)	792 (a″)	782 (a)	787 (a)	787 (a)	858 (a″)
ν_{17}	*553* (a″)	*391* (a″)	528 (a″)	533 (a)	529 (a)	530 (a)	532 (a″)	547 (a)	526 (a)	535 (a)	539 (a″)
ν_{18}	*294* (a″)	*306* (a″)	282 (a″)	290 (a)	285 (a)	285 (a)	285 (a″)	307 (a)	285 (a)	293 (a)	297 (a″)
ν_s				80 (a)	51 (a)	46 (a)	41 (a′)	124 (a)	75 (a)	79 (a)	92 (a′)
ν_b				21 (a)	32 (a)	34 (a)	19 (a′)	32, 68 (a)	37, 64 (a)	15, 74 (a)	38, 109 (a′)
ν_b				53 (a)	35 (a)	16 (a)	30 (a″)	82, 89 (a)	18, 87 (a)	47, 87 (a)	47, 110 (a″)
$\nu_{s(N\equiv N)}$								2498 (a)	2498 (a)	2498 (a)	2503 (a′)

Two **BT**$^+$-Ar isomers were predicted by calculations at the ωB97X-D/cc-pVTZ level as shown in Figure 4.16. The lower energy planar isomer (A) has a binding energy of 304 cm^{-1}. The less stable isomer (B), with a binding energy of 241 cm^{-1}, has the Ar tag atom above a CH_2 group. Details on the geometries and harmonic vibrational frequencies of the two **BT**$^+$-Ar isomers are provided in Table 4.7 and Table 4.8, respectively.

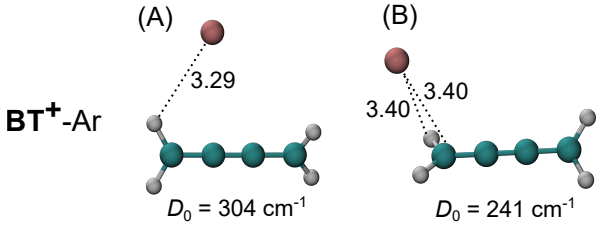

Fig. 4.16 Calculated structures and binding energies (D_0) of **BT**$^+$-Ar complexes at the ωB97X-D/cc-pVTZ level of theory. Intermolecular bond lengths are in Å.

Table 4.7 Calculated bond lengths and dihedral angles of **BT**$^+$ and **BT**$^+$-Ar cations at the ωB97X-D/cc-pVTZ level of theory.

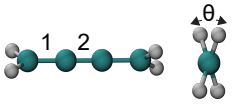

tag	bond length (Å)		θ (deg.)
	1	2	
(bare)	1.322	1.257	39.7
Ar			
(A)	1.322	1.257	39.0
(B)	1.323	1.256	39.0

Table 4.8 Harmonic vibrational frequencies for $\mathbf{BT}^+$ in the $\tilde{X}^2B_2$, $\tilde{B}^2B_3$, $\tilde{C}^2B_3$, and $\tilde{D}^2B_3$ electronic states, calculated at the EOM-CCSD/cc-pVTZ level of theory (italicized) and for $\mathbf{BT}^+$ and $\mathbf{BT}^+$-Ar in their ground electronic states calculated at the ωB97X-D/cc-pVTZ level (normal font). All frequencies are unscaled.

	$\mathbf{BT}^+$			$\mathbf{BT}^+$-Ar		
Mode	$\tilde{X}^2B_2$	$\tilde{C}^2B_3$	$\tilde{D}^2B_3$	$\tilde{X}^2B_2$	(A)	(B)
ν_1	*3141* (a)	*3132* (a)	*3101* (a)	3121 (a)	3122 (a)	3123 (a)
ν_2	*1903* (a)	*1995* (a)	*1932* (a)	1869 (a)	1866 (a)	1876 (a)
ν_3	*1462* (a)	*1436* (a)	*1402* (a)	1434 (a)	1433 (a)	1434 (a)
ν_4	*876* (a)	*827* (a)	*835* (a)	890 (a)	891 (a)	890 (a)
ν_5	*625* (a)	*1001* (a)	*804* (a)	687 (a)	690 (a)	684 (a)
ν_6	*3142* (b_1)	*3130* (b_1)	*3094* (b_1)	3123 (b_1)	3124 (a)	3125 (a)
ν_7	*1550* (b_1)	*1534* (b_1)	*1101* (a)	1576 (b_1)	1578 (a)	1575 (a)
ν_8	*1387* (b_1)	*1398* (b_1)	*1397*(b_1)	1372 (b_1)	1372 (a)	1372 (a)
ν_9	*3247* (b_2)	*3240* (b_2)	*3197* (b_2)	3223 (b_2)	3224 (a)	3224 (a)
ν_{10}	*1029* (b_2)	*977* (b_2)	*920* (b_2)	1012 (b_2)	1011 (a)	1011 (a)
ν_{11}	*977* (b_2)	*827* (b_2)	*828* (b_2)	965 (b_2)	963 (a)	965 (a)
ν_{12}	*481* (b_2)	*414* (b_2)	*350* (b_2)	500 (b_2)	498 (a)	499 (a)
ν_{13}	*210* (b_2)	*178* (b_2)	*94* (b_2)	212 (b_2)	215 (a)	213 (a)
ν_{14}	*3247* (b_3)	*3240* (b_3)	*3197* (b_3)	3223 (b_3)	3224 (a)	3225 (a)
ν_{15}	*1014* (b_3)	*970* (b_3)	*922* (b_3)	1005 (b_3)	1004 (a)	1005 (a)
ν_{16}	*981* (b_3)	*824* (b_3)	*832* (b_3)	964 (b_3)	962 (a)	964 (a)
ν_{17}	*344* (b_3)	*353* (b_3)	*357* (b_3)	372 (b_3)	369 (a)	372 (a)
ν_{18}	*201* (b_3)	*184* (b_3)	*149* (b_3)	203 (b_3)	201 (a)	206 (a)
ν_s					49 (a)	52 (a)
ν_b					34 (a)	74 (a)
ν_b					25 (a)	17 (a)

4.5.2 Calculated stationary points on the ground state $C_4H_4^+$ potential energy surface

Stationary points on the ground state $C_4H_4^+$ potential energy surface were calculated at the ωB97X-D/aug-cc-pVTZ level of theory to help understand the formation of $C_4H_4^+$ isomers from the $C_2H_2^+ + C_2H_2$ bimolecular reaction. The reaction network shown in Figure 4.17 includes isomerization and dissociation pathways with energies relative to the **BT**$^+$ isomer. The **MCP**$^+$, **CB**$^+$, **BT**$^+$, and **VA**$^+$ isomers are the lowest energy structures on the $C_4H_4^+$ potential energy surface. Other minima are labeled [1]-[17] in order of ascending energy (see Fig. 4.18). Structures of transition states are shown in Figure 4.18. A shallow well is predicted for stationary point [9], such that the calculated barrier may be negligible (indicated by the asterisk in Fig. 4.17). Two interconversion barriers exist between the methyleneallene isomer ([4]) and **VA**$^+$. The lower energy pathway (2.00 eV) involves a 2,3-hydrogen shift whereas the higher energy one (2.98 eV) corresponds to a 1,4-hydrogen shift.

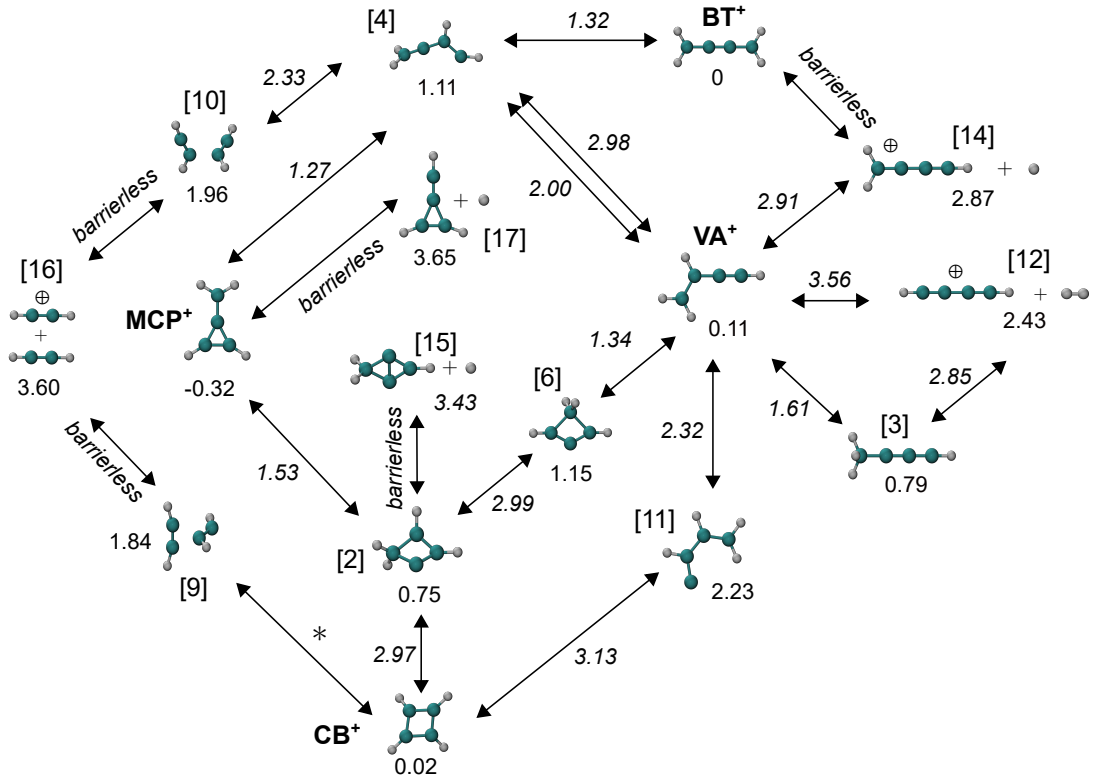

Fig. 4.17 Calculated reaction network for $C_4H_4^+$ formation from acetylene reacting with its radical cation (stationary point [16]) at the CCSD(T)/aug-cc-pVTZ//ωB97X-D/aug-cc-pVTZ. Energies (eV) are relative to the **BT**$^+$ isomer and are italicized for saddle points. See Figure 4.18 for geometries of saddle points.

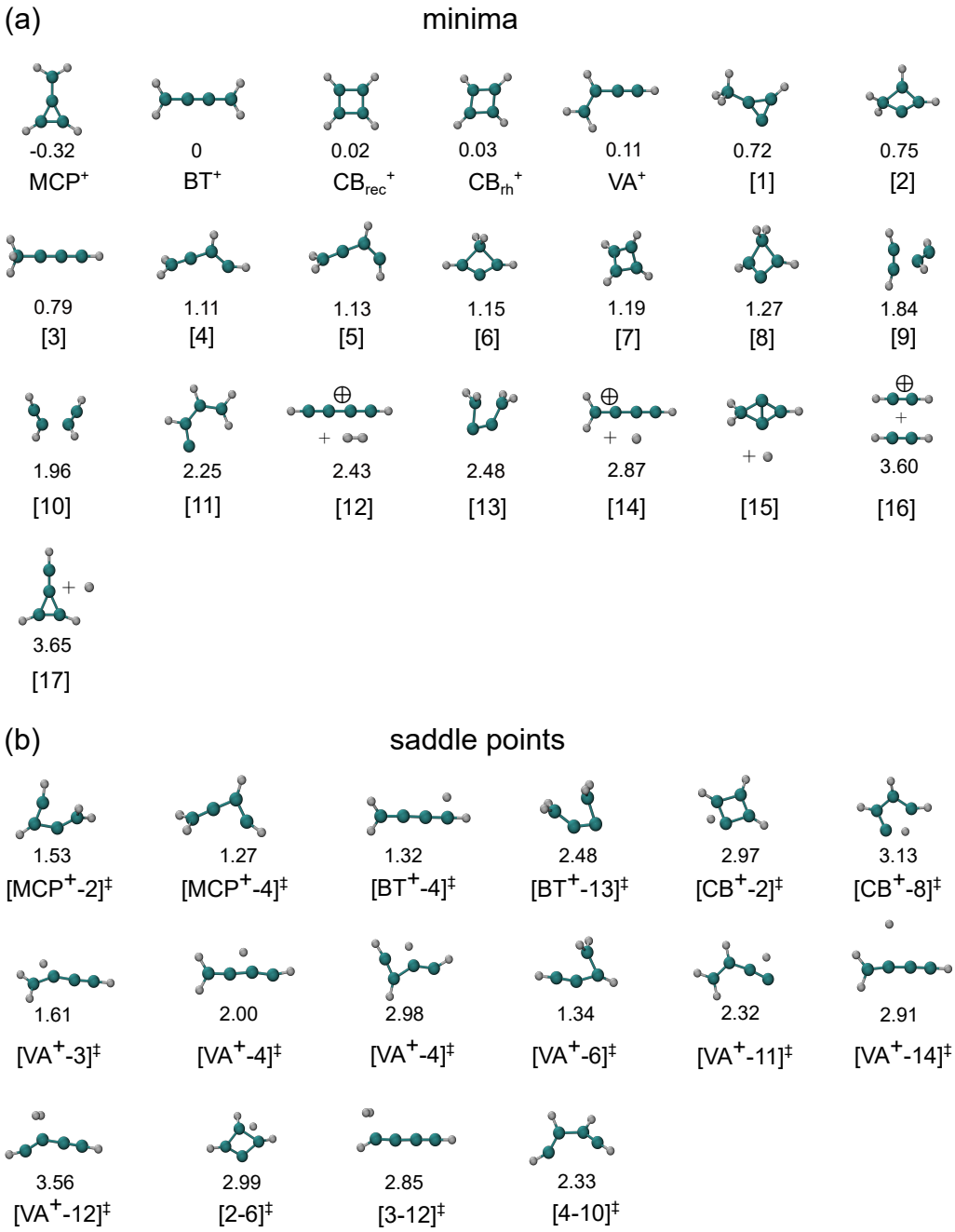

Fig. 4.18 Geometries and energies of stationary points on the ground state $C_4H_4^+$ potential energy surface, calculated at the CCSD(T)/aug-cc-pVTZ//ωB97X-D/aug-cc-pVTZ level.

Chapter 5

Electronic spectrum and photodissociation chemistry of the 1-butyn-3-yl cation ($H_2CCHCCH^+$)

Introduction to Chapter 5

This contents of this chapter have been published and are reprinted with permission from:

> G. Muller, U. Jacovella, K. J. Catani, G. da Silva, E. J. Bieske, "The Electronic Spectrum and Photodissociation Chemistry of the 1-butyn-3-yl cation, $H_3CCHCCH^+$" *Journal of Physical Chemistry A*, **124**, 2366-2371, 2020.

Copyright 2020 American Chemical Society. Supporting information (SI), published along with the article, is reproduced in Section 5.6. The publication in its original form is provided in the Appendix (page 209).

Article begins here

Abstract

The $\tilde{B}^1A' \leftarrow \tilde{X}^1A'$ electronic spectra of the 1-butyn-3-yl cation ($H_3CCHCCH^+$) and the $H_3CCHCCH^+$-Ne and $H_3CCHCCH^+$-Ar complexes are measured using resonance enhanced photodissociation over the 245-285 nm range, with origin transitions occurring at 35936, 35930, and 35928 cm^{-1}, respectively. Vibronic bands are assigned based on quantum chemical calculations and comparison of the spectra with those of the related linear methyl propargyl ($H_3C_4H_2^+$) and propargyl ($H_2C_3H^+$) cations. The photofragment ions are $C_2H_3^+$ (major) and $C_4H_3^+$ (minor), with the preference for $C_2H_3^+$ consistent with master equation simulations for a mechanism that involves rapid electronic deactivation and dissociation on the ground state potential energy surface.

5.1 Introduction

Small carbocations are important in plasmas, combustion processes[356,400] and in extraterrestrial environments.[9,47,81,401,402] There is a growing body of spectroscopic data for small fundamental carbocations in the gas phase, including $C_4H_5^+$,[156,174,225,229,230,403,404] the subject of this paper. $C_4H_5^+$ cations have been detected in Titan's atmosphere using the Ion Neutral Mass Spectrometer,[16] and are suspected to lead to formation of polycyclic aromatic hydrocarbons and tholins that populate the haze layers,[64,405,406] although it is unclear which isomers are present. Laboratory spectroscopic data of $C_4H_5^+$ isomers may facilitate their detection in remote environments. Photoelectron spectroscopy has provided information on two low energy $C_4H_5^+$ structures, the bent 1-butyn-3-yl ($H_3CCHCCH^+$) and linear 2-butyn-1-yl ($H_3C_4H_2^+$) cations (**BT** and **MP** in Figure 5.1),[229,230] with similar spacings between the lower electronic states of the respective cations.[231–233]

The $\tilde{B}^1A' \leftarrow \tilde{X}^1A_1$ electronic transition of the propargyl cation, $H_2C_3H^+$ (**P** in Figure 5.1), corresponding to the promotion of an electron from the second highest occupied molecular orbital (HOMO-1) to the lowest unoccupied molecular orbital (LUMO), was first measured over the 240-268 nm range using neon matrix isolation spectroscopy.[407] The measured spectrum was dominated by a strong progression spaced by 667 cm^{-1} which was assigned to the CCH bending vibration, due to a supposed reduction in symmetry for **P** upon electronic

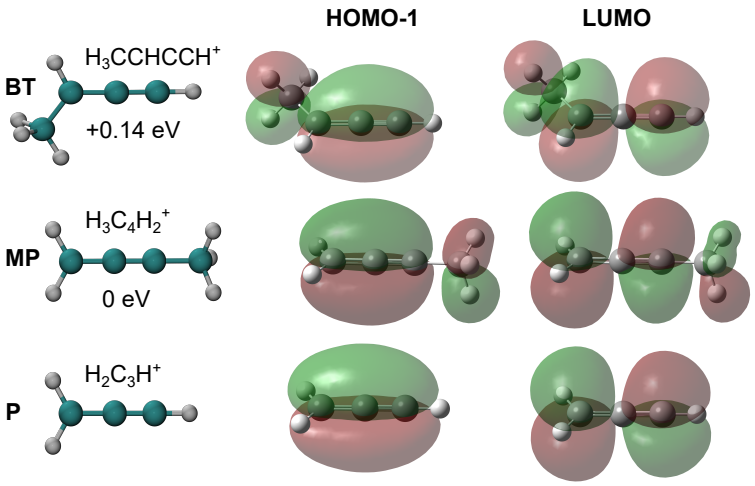

Fig. 5.1 Structures of **BT** ($H_3CCHCCH^+$), **MP** ($H_3C_4H_2^+$), and **P** ($H_2C_3H^+$), calculated at the MP2/aug-cc-pVDZ level of theory. Energies of the $C_4H_5^+$ isomers are relative to that of **MP** and include single point energies at the CCSD(T)/cc-pVTZ level using optimized geometries and vibrational zero-point corrections to energy predicted at the MP2/aug-cc-pVDZ level.

excitation.[407] Later, the spectrum was recorded in the gas phase using resonance enhanced photodissociation (REPD) spectroscopy.[234] Accompanying calculations suggested the $\tilde{B}$ state retains C_{2v} symmetry and the progression was reassigned to the C-C symmetric stretching vibrational mode (ν_5).[234]

Based on the calculated molecular orbitals shown in Figure 5.1, the HOMO-1→LUMO electronic transitions should be similar for **P**, **MP**, and **BT**. In accordance with these expectations, the $\tilde{B}^1A'\leftarrow\tilde{X}^1A'$ electronic transitions of **MP** and **P** occur at similar wavelengths and exhibit comparable progressions in the C-C stretching vibration,[156] demonstrating that the on-axis methyl group has little influence on the propargyl chromophore.

In the current study, REPD spectra of $H_3CCHCCH^+$ and the $H_3CCHCCH^+$-Ne complex were measured to enable comparisons with the spectra of **P** and **MP** and to facilitate possible detection of $H_3CCHCCH^+$ ions in remote environments. Excitation of the $\tilde{B}^1A'\leftarrow\tilde{X}^1A'$ transition of **BT** generates $C_2H_3^+$ and $C_4H_3^+$ photofragments, as is the case for **MP**.[156] To understand the dissociation process and to predict the $C_2H_3^+/C_4H_3^+$ branching ratio, we model the fate of energized **BT** ions using master equation simulations, based on calculated stationary points on the $C_4H_5^+$ ground state potential energy surface. There have been several previous investigations of $C_4H_5^+$ dissociation. Photofragmentation at 193 nm of $C_4H_5^+$ generated from 2-hexyne mainly produced $C_2H_3^+$ photofragments.[222] Collision-induced dissociation of $C_4H_5^+$, presumably the **MP** isomer, also gave nearly exclusively $C_2H_3^+$ fragments, with the dissociation proposed to proceed through a low energy cyclic

isomer.[408] On the other hand, reactive $C^+ + C_3H_5$ collisions, which presumably involve $C_4H_5^+$ intermediates, were found to yield $C_4H_3^+$ products but not $C_2H_3^+$ products.[409] Recently, it was observed that excitation of the $\tilde{B}^1A' \leftarrow \tilde{X}^1A'$ transition of **MP** produced both $C_2H_3^+$ and $C_4H_3^+$ photofragments with a branching ratio of 5:1.[156] Master equation simulations based on a calculated ground state $C_4H_5^+$ potential energy surface suggested the $C_2H_3^+ + C_2H_2$ channel is accessed through a multi-step process, whereas the $C_4H_3^+ + H_2$ fragments are formed through a more direct, albeit higher energy, process.[156] Although the calculations in ref. 156 did not include the **BT** isomer, other calculations predict low energy barriers between **BT** and **MP**,[224] suggesting that both isomers should have similar dissociation mechanisms and play comparable roles in unimolecular reactions of $C_4H_5^+$.

5.2 Methods

5.2.1 Experimental

REPD spectra of $H_3CCHCCH^+$ and $H_3CCHCCH^+$-Ne were recorded through laser excitation of ions in a tandem mass spectrometer. A brief overview of the experimental setup is provided below, while a more complete description is available in ref. 410. $H_3CCHCCH^+$ and $H_3CCHCCH^+$-Ne ions were formed by seeding vapour of liquid 3-bromo-1-butyne (cooled to 0°C) into a pulsed supersonic expansion of argon or neon gas (stagnation pressure ≈ 4 bar) that was bombarded by electrons. The target ions were then mass selected using a quadrupole mass filter and deflected 90° using an electrostatic quadrupole bender into an octupole ion guide where they were exposed to the output light from an optical parametric oscillator (OPO, EKSPLA NT342B). Resonant photoexcitation produced photofragments that were mass selected using a second quadrupole mass filter and detected by a microchannel plate. REPD spectra were obtained by monitoring the photofragment ion yield (normalized with respect to laser power) as a function of wavelength (calibrated using a wavemeter, Ångstrom LSA UVL).

5.2.2 Computational

The structure and energetics of **BT** and other relevant isomers, fragments, and transition states were characterized through quantum chemical calculations using the Gaussian 16 program.[288] The geometry, frequencies, and vibrational zero-point corrected energy for the

electronic ground state of **BT** were calculated at the CCSD/cc-pVTZ level of theory. Vertical excitation energies and oscillator strengths were calculated at the EOM-CCSD/cc-pVTZ level. This level of theory was also used to estimate the equilibrium geometry, frequencies, and vibrational zero-point energy of **BT** in the excited state. Structural and energetic data for the $H_3CCHCCH^+$-Ne and $H_3CCHCCH^+$-Ar complexes are reported in the supporting information (SI).

To explore the dissociation mechanism of **BT**, stationary points on the ground state $C_4H_5^+$ potential energy surface were calculated at the MP2/aug-cc-pVDZ level of theory, building on a previous study of **MP**.[156] Transition states and intermediates were located by scanning along internal coordinates. Intrinsic reaction coordinate (IRC) calculations were used to verify the transition states.[393] Energies of the stationary points were calculated at the CCSD(T)/cc-pVTZ level and include vibrational zero-point energy corrections at the MP2/aug-cc-pVDZ level. The structures, vibrational frequencies, and energies were used to carry out master equation simulations within the Multiwell program.[282,411,412] The modelling procedure follows that used in the earlier study of **MP**, where more details are provided.[156] Rigid-Rotor-Harmonic-Oscillator approximations were used to describe molecular degrees of freedom based on MP2 frequencies and moments of inertia, with the Beyer-Swinehart-Stein-Rabinovitch[413] count method used to determine sums and densities of states. Rice-Ramsperger-Kassel-Marcus (RRKM) theory was used with CCSD(T) energies to obtain microscopic *k(E)* values. Collisional energy transfer is modelled using a single-exponential down model, with average energy transferred in deactivating collisions (ΔE_{down}) set to 200 cm^{-1}, consistent with values derived for organic molecules colliding with Ar at room temperature.[414,415] Note the model is not sensitive to variations in ΔE_{down} given the nearly collisionless environment in the octupole region. For the master equation simulations, the ions were assumed to have a Boltzmann energy distribution corresponding to T=30 K based on previous spectroscopic studies of other molecular ions generated by the source,[416,417] with an additional 4.63 eV of internal energy provided through the absorption of a 268 nm photon.

5.3 Results

5.3.1 REPD spectra

REPD spectra of **BT** over the 245-285 nm range, recorded by monitoring $C_2H_3^+$ and $C_4H_3^+$ photofragments, are shown in Figure 5.2a and b, respectively. The spectra recorded on the $C_2H_3^+$ (+ C_2H_2) and $C_4H_3^+$ (+ H_2) channels have the same structure and relative band intensities, although the $C_2H_3^+$ yield was ≈ 6 times the $C_4H_3^+$ yield across the spectrum. REPD spectra of $H_3CCHCCH^+$-Ne (Fig. 5.2c) are similar to spectra of the bare molecule, whereas significantly broader bands are observed for $H_3CCHCCH^+$-Ar (see SI).

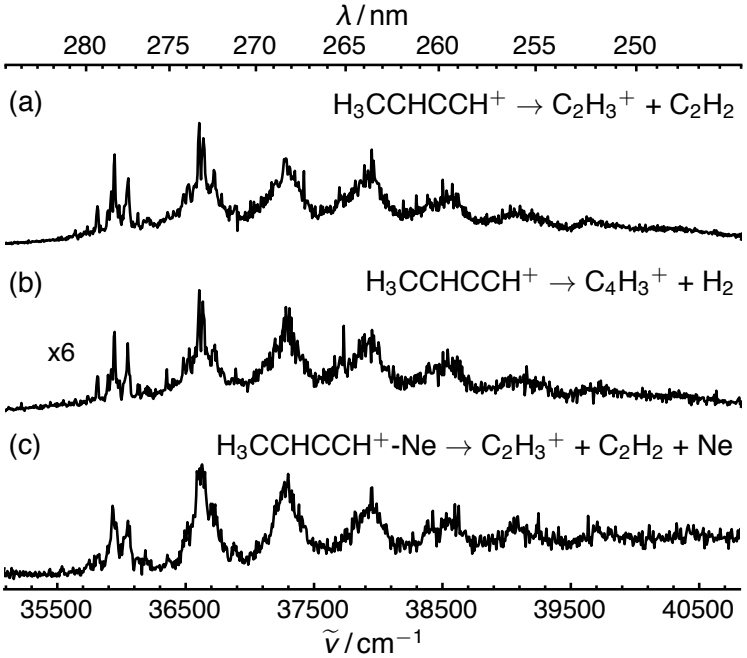

Fig. 5.2 REPD spectra of $H_3CCHCCH^+$ (**BT**), obtained by monitoring (a) $C_2H_3^+$ and (b) $C_4H_3^+$ fragments over the 245-285 nm range; (c) REPD spectrum of $H_3CCHCCH^+$-Ne obtained by monitoring $C_2H_3^+$ fragments.

The observed spectrum of **BT** is associated with the $\tilde{B}^1A' \leftarrow \tilde{X}^1A'$ transition, and occurs in the same spectral region as the corresponding spectra of **P** and **MP**. Its onset around 277 nm is consistent with the calculated adiabatic excitation wavelength of 278 nm (4.46 eV).

5.3.2 Band assignments

Band positions and assignments for the $H_3CCHCCH^+$ and $H_3CCHCCH^+$-Ne spectra are provided in Table 5.1. The spectrum of **BT** is assigned through comparisons with the previously reported spectra of **MP** and **P**.[156,234] For clarity, spectra of the three ions are displayed in Figure 5.3, with the origin transitions adjusted so that they coincide. Spectra of **BT**, **MP**, and **P** all feature a pronounced progression associated with the C-C symmetric stretch vibration. For **BT**, bands at $0_0^0 + 660$, 1320, 1980, and 2640 cm^{-1} are assigned to this progression (11_0^1, 11_0^2, 11_0^3, and 11_0^4 transitions, respectively). The length of the progression, which extends for at least five quanta, is consistent with the predicted substantial elongation of the central C-C bond by 0.10 Å upon electronic excitation (see Figure 5.4). The calculated vibrational frequency for ν_{11} in the $\tilde{B}^1A'$ state, 776 cm^{-1}, matches the experimental progression spacing when scaled by 0.85, a value used to fit the corresponding progression in the **MP** spectrum. The low scaling factor necessary to reconcile the calculated and the observed excited state C-C frequency indicates that the EOM-CCSD/cc-pVTZ calculations overestimate the frequency, as also found for **P** and **MP**.[156,234] For **P**, much better agreement with experiment was found for calculations using the restricted active space self-consistent field (RASSCF) method with the cc-pVTZ basis set. The computational cost of the RASSCF/cc-pVTZ level calculations prevents a similar approach being used for the larger $C_4H_5^+$ systems (**MP** and **BT**).

Table 5.1 Band positions (cm^{-1}), relative band positions ($\Delta\tilde{\nu}/cm^{-1}$), and band assignments for the $\widetilde{B}^1A' \leftarrow \widetilde{X}^1A'$ system of $H_3CCHCCH^+$ and $H_3CCHCCH^+$-Ne.

	$H_3CCHCCH^+$		$H_3CCHCCH^+$-Ne	
Assignment	$\tilde{\nu}$	$\Delta\tilde{\nu}$	$\tilde{\nu}$	$\Delta\tilde{\nu}$
14_1^0	35802	-134		
0_0^0	35936	0	35930	0
14_0^1	36039	103	36051	121
11_0^1	36596	660	36628	698
$11_0^1 14_0^1$	36718	782	36709	779
11_0^2	37270	1334	37298	1368
5_0^1	37721	1785		
11_0^3	37940	2004	37952	2022
11_0^4	38546	2610	38597	2667

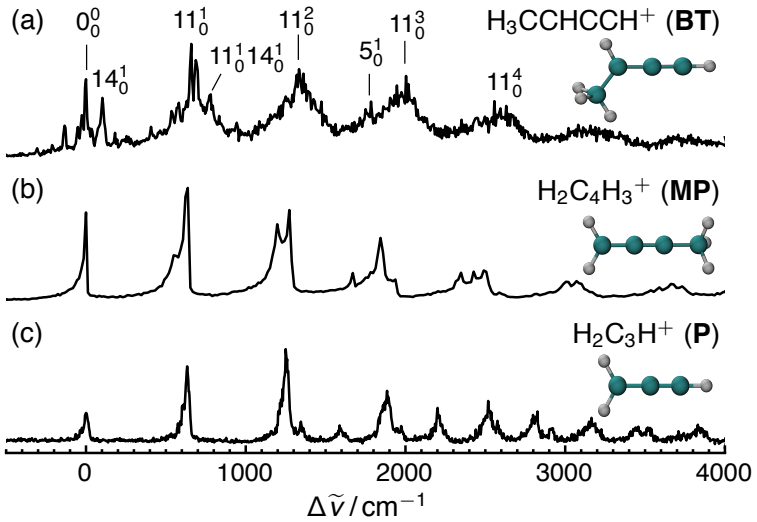

Fig. 5.3 REPD spectra of (a) $H_3CCHCCH^+$ generated by averaging spectra shown in Figs. 5.2a and b, (b) $H_3C_4H_2^+$ taken from ref. 156, and (c) $H_2C_3H^+$-Ne taken from ref. 234. The origin transitions for the spectra have been set to coincide to facilitate comparison.

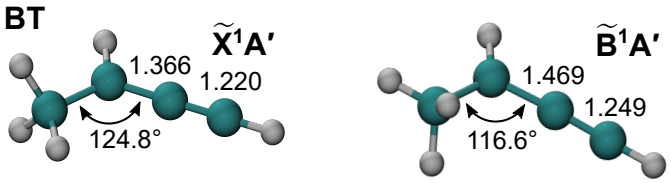

Fig. 5.4 Equilibrium geometries of $H_3CCHCCH^+$(**BT**) in the $\tilde{X}^1A'$ and $\tilde{B}^1A'$ states, calculated at the CCSD/cc-pVTZ and EOM-CCSD/cc-pVTZ levels of theory, respectively.

Spectra of **BT**, **MP**, and **P** all exhibit a band with similar relative intensity between $0_0^0 + 1550$ and 1800 cm^{-1} that arises from excitation of the C≡C stretching vibration (ν_5 for **BT**). The calculated ν_5 vibrational frequency for **BT** in the $\tilde{B}^1A'$ state (1810 cm^{-1}) agrees with the band's position ($0_0^0 + 1785$ cm^{-1}). The band's appreciable intensity is consistent with the predicted increase in the C≡C bond length by 0.03 Å from the ground state to the excited state (Fig. 5.4). This assignment differs from the one advanced in an earlier study of **P**,[234] where the band ($0_0^0 + 1585$ cm^{-1}) was considered to be associated with the out-of-plane CH_2 wag. However, it is clear that the band is unlikely to arise from a wag because the position is not significantly affected by substituting a methyl group for an H atom.

The spectrum of **BT** displays closely spaced vibronic structure at 0_0^0 +103 cm^{-1} and 0_0^0 - 134 cm^{-1} that is not present in the spectra of the other two ions (see Fig. 5.3). Although their assignments are not clear, the bands may be due to transitions involving the lowest frequency a′ mode (ν_{14}), corresponding to bending of the C_4 skeleton. The band at 0_0^0 +103 cm^{-1} can

be tentatively assigned to 14_0^1 based on the calculated ν_{14} vibrational frequency in the $\tilde{B}^1A'$ state (165 cm^{-1}). The band's appreciable intensity is consistent with the reduction in the Me-C-C bending angle from ground to excited state (see Fig. 5.4). The band at 0_0^0 - 134 cm^{-1} may be the 14_1^0 hot band, in-line with a calculated vibrational frequency of 195 cm^{-1} for ν_{14} in the ground state. Its assignment to a hot band is consistent with the band's reduced intensity in the $H_3CCHCCH^+$-Ne spectrum.

5.3.3 Effect of methyl substitution

The presence of an electron-donating methyl group influences the structure of the propargyl chromophore by stabilizing the charge on the carbon to which it is attached, and therefore, depending upon its position, affects conjugation in the molecule. The structural changes can be assessed by comparing the calculated C-C bond lengths for **P**, **BT**, and **MP** (see Fig. 5.5). The bond lengths of **P** reflect its delocalized electronic structure between two resonance forms, $^+C_1$-$C_2{\equiv}C_3$ and $C_1{=}C_2{=}C_3^+$, with a preference for the former form.[226] Replacing an H atom on C_1 with a methyl group, to give **BT**, stabilizes the $^+C_1$-$C_2{\equiv}C_3$ form, consequently increasing the C_1-C_2 bond length. On the other hand, methyl substitution at the C_3 site, to give **MP**, stabilizes the allenyl-type ($C_1{=}C_2{=}C_3^+$) form, with an increase in the C_2-C_3 bond length. These effects may become apparent in higher resolution studies of these fundamental carbocations.

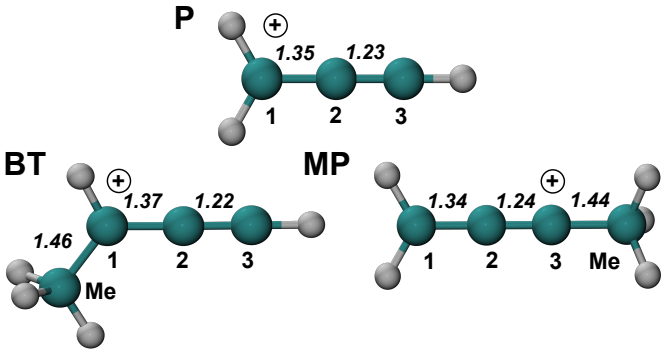

Fig. 5.5 Ground state equilibrium structures of **P**, **BT**, and **MP**, calculated at the CCSD/cc-pVTZ level of theory. Bond lengths (Å) are shown in italic font.

5.3.4 Photodissociation dynamics

Photoexcitation of **BT** over the 245-285 nm range leads to the generation of $C_2H_3^+$ and $C_4H_3^+$ fragments. A $C_2H_3^+ / C_4H_3^+$ branching ratio of ≈ 6:1 was measured while pumping the 11_0^2 transition at 268 nm (4.63 eV), similar to the branching ratio for **MP** (≈ 5:1) for the corresponding transition.[156] For both **MP** and **BT**, the branching ratio over the 230-280 nm range was independent of wavelength. Interestingly, for the $H_3CCHCCH^+$-Ne and $H_3CCHCCH^+$-Ar complexes, the only detected photofragments were $C_2H_3^+$ and $C_4H_3^+$ suggesting that an insignificant fraction of the complexes radiatively relax to the ground state, as these ions would only have sufficient energy to sever the weak intermolecular bond. Therefore, one can assume that nonradiative relaxation, presumably internal conversion, dominates.

We investigated ground state dissociation pathways assuming that dissociation follows internal conversion. A simplified version of the $C_4H_5^+$ potential energy surface is pictured in Figure 5.6 (see SI for more details). The $\tilde{B}^1A'$ state (4.46 eV), accessed through the $\tilde{B}^1A' \leftarrow \tilde{X}^1A'$ transition (arrow), lies above the calculated dissociation thresholds for $C_2H_3^+ + C_2H_2$ (1.93 eV) and $C_4H_3^+ + H_2$ (2.74 eV). The most likely $C_4H_3^+$ fragment is the classical protonated diacetylene structure **[10]**, which can be accessed through two $C_4H_3^+ + H_2$ channels. The lowest energy channel is direct H_2 loss from **BT** through a 2.22 eV barrier **[20]**‡. Calculations suggest that **BT** may access the other $C_4H_3^+ + H_2$ channel through a 1.29 eV interconversion barrier **[24]**‡. Following isomerization to **MP**, H_2 loss can occur through **[9a]**‡, lying 2.29 eV above **BT**. The similar energies of **[20]**‡ and **[9a]**‡ indicate that both $C_4H_3^+ + H_2$ channels are accessible, with the **[9a]**‡ channel slightly more favorable. The $C_2H_3^+ + C_2H_2$ channel, to form the nonclassical protonated acetylene ion and acetylene molecule **[8]**, can also be reached through the initial isomerization step involving **[24]**‡, followed by several additional interconversions prior to dissociating.

The potential energy surface shown in Figure 5.6 was used for RRKM/master equation simulations to predict the $C_2H_3^+ / C_4H_3^+$ branching ratio. Assuming a population of **BT** with a Maxwell-Bolzmann distribution of T=30 K, and given 4.63 eV of internal energy, corresponding to absorption of a 268 nm photon, the model predicts a branching ratio of 1.4:1. Although the model underestimates the measured branching ratio, possibly due to inaccuracies in the calculated energies of points on the $C_4H_5^+$ potential energy surface, it correctly predicts the preference for the $C_2H_3^+ + C_2H_2$ channel.

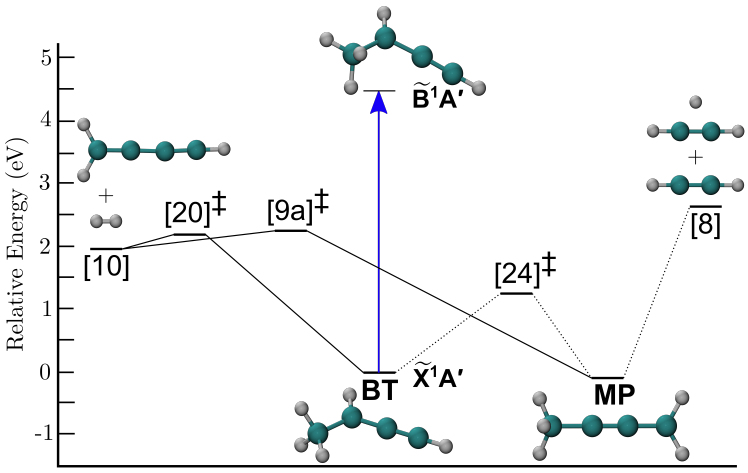

Fig. 5.6 Simplified ground state potential energy surface of $C_4H_5^+$ from calculations at the MP2/aug-cc-pVDZ (geometries and zero point energies) and CCSD(T)/cc-pVTZ (single point energies) levels, with transition states represented by ‡ and dotted lines indicating multistep processes. Energies (zero point added to single point) are relative to the energy of **BT** in its $\tilde{X}^1A'$ state. The $\tilde{B}^1A'$ state energy corresponds to the experimental $\widetilde{B}^1A' \leftarrow \widetilde{X}^1A'$ origin transition (arrow). See SI for details and a more complete potential energy surface.

5.4 Conclusions

In summary, the $\tilde{B}^1A' \leftarrow \tilde{X}^1A'$ band system of $H_3CCHCCH^+$ has been recorded over the 245-285 nm range by monitoring $C_2H_3^+$ and $C_4H_3^+$ photofragments. Bands were assigned through comparison of the spectrum with those of $H_3C_4H_2^+$ and $H_2C_3H^+$ and with the aid of calculated vibrational frequencies. Extended progressions in the $H_3CCHCCH^+$ spectrum, with intervals of $\approx 660\,cm^{-1}$, are attributed to the C-C stretching vibration (ν_{11}). A weak band located around $1800\,cm^{-1}$ above the origin transition is assigned to the 5_0^1 transition, corresponding to an excitation of the symmetric acetylenic (C≡C) stretching mode. Weak bands in the vicinity of the origin transition are tentatively assigned to transitions involving bending of the C_4 skeleton (ν_{14}), which corresponds to the lowest frequency vibrational mode. Minor differences in the calculated structures of $H_3CCHCCH^+$, $H_3C_4H_2^+$, and $H_2C_3H^+$ were rationalized through conjugative effects related to the location of the methyl group. Finally, the dissociation of $H_3CCHCCH^+$ was modeled using master equation simulations based on calculations of the ground state potential energy surface, correctly predicting the preferred generation of $C_2H_3^+$ photofragment ions.

5.5 Acknowledgements

This research was supported under the Australian Research Council's Discovery Project funding scheme (Project Numbers DP150101427 and DP160100474) as well as by Australian Government Research Training Program Scholarships. U. Jacovella acknowledges support from the Swiss National Science Foundation (P2EZP2_178429).

Article ends here

5.6 Supporting information (SI)

5.6.1 Additional spectra

Resonance enhanced photodissociation (REPD) spectra of $H_3CCHCCH^+$, $H_3CCHCCH^+$-Ne, and $H_3CCHCCH^+$-Ar, shown in Figure 5.7, were recorded over the 245-285 nm range by monitoring $C_2H_3^+$ and $C_4H_3^+$ photofragments. As mentioned in the paper, electronically excited $H_3CCHCCH^+$ ions in the $\tilde{B}^1A'$ state yield ≈ 6 times more $C_2H_3^+$ ions than $C_4H_3^+$ ions, and therefore the signal-to-noise ratio for the spectrum in Figure 5.7a is higher than for the spectrum in Figure 5.7b. The signal-to-noise ratio for the spectrum of $H_3CCHCCH^+$-Ne is poor, as the complexes were difficult to generate. Spectra of $H_3CCHCCH^+$-Ar exhibit bands that are broad, possibly due to the presence of multiple $H_3CCHCCH^+$-Ar isomers, which are discussed in the following section.

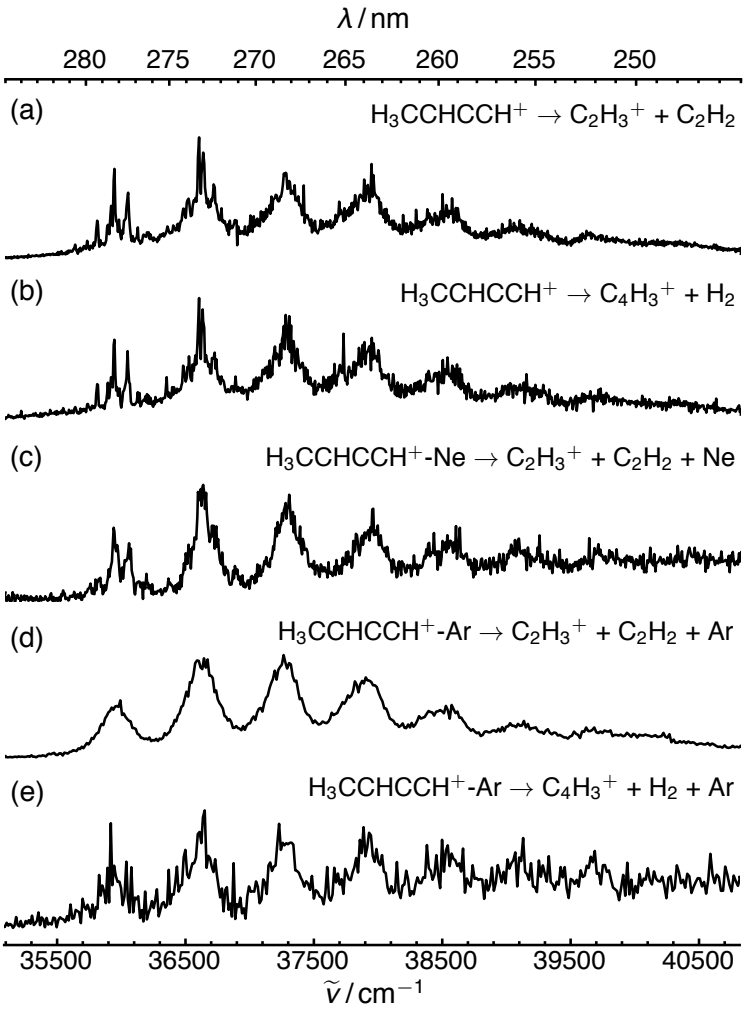

Fig. 5.7 REPD spectra over the 245-285 nm range of (a) $H_3CCHCCH^+$ obtained by monitoring $C_2H_3^+$ fragments, (b) $H_3CCHCCH^+$ obtained by monitoring $C_4H_3^+$ fragments, (c) $H_3CCHCCH^+$-Ne recorded by monitoring $C_2H_3^+$ fragments, (d) $H_3CCHCCH^+$-Ar recorded by monitoring $C_2H_3^+$ fragments, and (e) $H_3CCHCCH^+$-Ar obtained by monitoring $C_4H_3^+$ fragments.

5.6.2 Calculated structures and harmonic vibrational frequencies for $H_3CCHCCH^+$, $H_3CCHCCH^+$-Ne, and $H_3CCHCCH^+$-Ar

As described in the paper, geometries and harmonic vibrational frequencies for $H_3CCHCCH^+$ in the $\tilde{X}^1A'$ and $\tilde{B}^1A'$ electronic states were calculated at the CCSD/cc-pVTZ and EOM-CCSD/cc-pVTZ levels of theory. To investigate the interactions between the rare gas (RG) atoms and $H_3CCHCCH^+$, the geometries, frequencies, and energies of $H_3CCHCCH^+$, $H_3CCHCCH^+$-Ne and $H_3CCHCCH^+$-Ar in the ground state (see Figure 5.8) were calculated at the ωB97X-D/aug-cc-pVTZ level, a level that includes dispersion corrections and which has been used to describe similar non-covalently bound complexes.[156,342] Calculated harmonic vibrational frequencies for $H_3CCHCCH^+$, $H_3CCHCCH^+$-Ar and $H_3CCHCCH^+$-Ne are provided in Tables 5.2 and 5.3. The calculated energies include vibrational zero-point corrections and account for basis set superposition errors.[295]

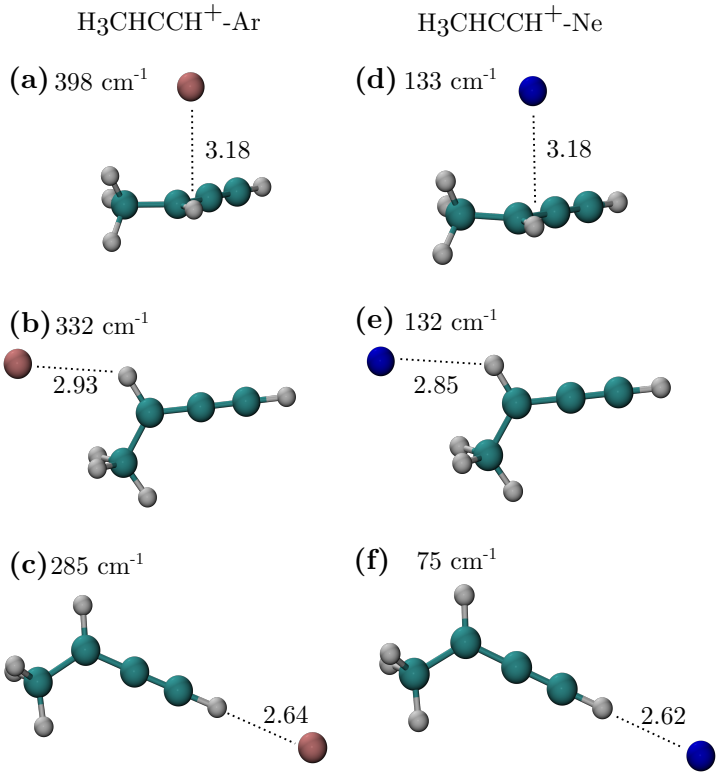

Fig. 5.8 Calculated structures and binding energies (cm^{-1}) of $H_3CCHCCH^+$-Ar and $H_3CCHCCH^+$-Ne at the ωB97X-D/aug-cc-pVTZ level of theory. Binding energies are corrected for basis set superposition errors. For (a) and (e) the indicated bond length corresponds to the distance between the RG atom and the adjacent H atom.

Table 5.2 Harmonic vibrational frequencies (cm^{-1}) of $H_3CCHCCH^+$ in the $\widetilde{X}^1A'$ and $\widetilde{B}^1A'$ states, calculated at the CCSD/cc-pVTZ and EOM-CCSD/cc-pVTZ levels of theory, respectively. All frequencies are unscaled.

Mode	$\widetilde{X}^1A'$	$\widetilde{B}^1A'$
ν_1	*3406*(a′)	*3380* (a′)
ν_2	*3210*(a′)	*3204* (a′)
ν_3	*3169* (a′)	*3224* (a′)
ν_4	*3012* (a′)	*2858* (a′)
ν_5	*2143* (a′)	*1810* (a′)
ν_6	*1524* (a′)	*1459* (a′)
ν_7	*1413* (a′)	*1361* (a′)
ν_8	*1338* (a′)	*1217* (a′)
ν_9	*1209* (a′)	*1164* (a′)
ν_{10}	*1126* (a′)	*1039* (a′)
ν_{11}	*869* (a′)	*776* (a′)
ν_{12}	*656* (a′)	*624* (a′)
ν_{13}	*533* (a′)	*467* (a′)
ν_{14}	*195* (a′)	*163* (a′)
ν_{15}	*3055* (a″)	*2809* (a″)
ν_{16}	*1452* (a″)	*1280* (a″)
ν_{17}	*1079* (a″)	*861* (a″)
ν_{18}	*875* (a″)	*650* (a″)
ν_{19}	*788* (a″)	*457* (a″)
ν_{20}	*253* (a″)	*329* (a″)
ν_{21}	*103* (a″)	*218* (a″)

The calculations predict that the Ne and Ar atoms bind to **BT** at three different sites. The lowest energy conformation involves the RG atom bound side-on and above the C_4 plane of **BT** (Figures 5.8a and d). Less stable configurations have the RG atom bound side-on and in the C_4 plane (Figures 5.8b and e) and the RG attached end-on to the acetylenic hydrogen (Figures 5.8c and 5.8e). The geometry of $H_3CCHCCH^+$ (**BT**) is only slightly affected by the attached Ne or Ar atom.

Table 5.3 Harmonic vibrational frequencies for $H_3CCHCCH^+$, $H_3CCHCCH^+$-Ar and $H_3CCHCCH^+$-Ne in the ground state, calculated at the ωB97X-D/aug-cc-pVTZ level. Columns (a)-(f) correspond to the structures in Figure 5.8. All frequencies are unscaled.

	$H_3CCHCCH^+$	$H_3CCHCCH^+$-Ar			$H_3CCHCCH^+$-Ne		
Mode		(a)	(b)	(c)	(d)	(e)	(f)
ν_1	3401 (a′)	3400 (a)	3399 (a′)	3358(a′)	3398 (a)	3398 (a′)	3395 (a′)
ν_2	2304 (a′)	3202 (a)	3202 (a′)	3201 (a′)	3201 (a)	3202 (a′)	3201 (a′)
ν_3	3150 (a′)	3153 (a)	3152 (a′)	3149 (a′)	3150 (a)	3151 (a′)	3149 (a′)
ν_4	2994 (a′)	2994 (a)	2993 (a′)	2994 (a′)	2994 (a)	2993 (a′)	2992 (a′)
ν_5	2170 (a′)	2172 (a)	2170 (a′)	2164 (a′)	2170 (a)	2170 (a′)	2169 (a′)
ν_6	1517 (a′)	1517 (a)	1519 (a′)	1517 (a′)	1518 (a)	1517 (a′)	1517 (a′)
ν_7	1405 (a′)	1403 (a)	1403 (a′)	1404 (a′)	1404 (a)	1404 (a′)	1404 (a′)
ν_8	1310 (a′)	1312 (a)	1307 (a′)	1311 (a′)	1310 (a)	1308 (a′)	1309 (a′)
ν_9	1211 (a′)	1209 (a)	1211 (a′)	1209 (a′)	1210 (a)	1210 (a′)	1210 (a′)
ν_{10}	1124 (a′)	1123 (a)	1122 (a′)	1124 (a′)	1124 (a)	1124 (a′)	1124 (a′)
ν_{11}	875 (a′)	875 (a)	877 (a′)	875 (a′)	876 (a)	876 (a′)	876 (a′)
ν_{12}	686 (a′)	695 (a)	684 (a′)	704 (a′)	685 (a)	685 (a′)	691 (a′)
ν_{13}	551 (a′)	551 (a)	552 (a′)	551 (a′)	551 (a)	551 (a′)	551 (a′)
ν_{14}	203 (a′)	203 (a)	213 (a′)	205 (a′)	203 (a)	204 (a′)	203 (a′)
ν_{15}	3028 (a″)	3032 (a)	3026 (a″)	3028 (a″)	3028 (a)	3027 (a″)	3026 (a″)
ν_{16}	1423 (a″)	1425 (a)	1424 (a″)	1424 (a″)	1423 (a)	1422 (a″)	1423 (a″)
ν_{17}	1061 (a″)	1066 (a)	1059 (a″)	1061 (a″)	1061 (a)	1059 (a″)	1060 (a″)
ν_{18}	900 (a″)	897 (a)	900 (a″)	916 (a″)	899 (a)	900 (a″)	906 (a″)
ν_{19}	782 (a″)	793 (a)	783 (a″)	782 (a″)	783 (a)	780 (a″)	781 (a″)
ν_{20}	256 (a″)	269 (a)	259 (a″)	263 (a″)	258 (a)	258 (a″)	260 (a″)
ν_{21}	107 (a″)	104 (a)	191 (a″)	103 (a″)	110 (a)	111 (a″)	103 (a″)
ν_s		121 (a)	75 (a′)	40 (a′)	52 (a)	52 (a′)	33 (a′)
ν_b		32 (a)	38 (a′)	22 (a′)	17 (a)	32 (a′)	17 (a′)
ν_b		59 (a)	43 (a″)	37 (a″)	41 (a)	19 (a″)	28 (a″)

5.6.3 Calculated structures and energies of $C_4H_5^+$ isomers, transition states, and fragments

Structures for stationary points on the ground state $C_4H_5^+$ potential energy surface were calculated at the MP2/aug-cc-pVDZ level of theory (see Figure 5.9). The exception was the classical vinyl cation structure, the $C_2H_3^+$ fragment for stationary point [6b], which was not a minimum at that level of theory (see next paragraph). Cartesian coordinates for all stationary points optimized at the MP2/aug-cc-pVDZ level are provided in Table 5.5. The MP2/aug-cc-pVDZ electronic energy and vibrational zero-point corrections to energy are provided in Table 5.4. The vibrational zero-point corrected energies for the different structures, relative to the energy of the methyl propargyl cation (**MP**), are provided in normal font in Figure 5.9, and were used to generate the potential energy surface shown in Figure 5.10. A more accurate potential energy surface was calculated by obtaining single point energies at the CCSD(T)/cc-pVTZ level, corrected by MP2/aug-cc-pVDZ vibrational zero-point energies. These vibrational zero-point corrected energies, relative to the energy of the methyl propargyl cation (italicized in Figure 5.9), were used to generate the potential energy surface shown in Figure 5.11.

As noted above, the classical vinyl cation geometry ([6b]) could not be optimized at the MP2/aug-cc-pVDZ level. Instead, the MP2/aug-cc-pVDZ energy of [6b] was estimated using the calculated energy of the nonclassical structure ([8]) and a previously calculated energy difference between the two configurations.[418] The previous calculations at the CCSD(T)/cc-pVQZ level of theory predicted that [6b] lies 0.16 eV higher in energy than [8], and that the interconversion barrier ($[6b]^{\ddagger}$) between the forms lies only ≈ 0.005 eV above the energy of the classical structure. The 0.16 eV energy difference between the forms was added to the energy for [8] (2.72 eV above **MP**) calculated in this work at the MP2/aug-cc-pVDZ level, resulting in a predicted relative energy for [6b] of 2.88 eV above **MP** (normal font in Figure 5.9). Because [6b] lies in a shallow potential energy well, only the $[6b]^{\ddagger}$ transition state is presented in the potential energy surfaces in Figures 5.10 and 5.11.

For the more accurate potential energy surface shown in Figure 5.11, the classical vinyl cation structure was optimized at the ωB97X-D/cc-pVDZ level and used for a CCSD(T)/cc-pVTZ single point energy calculation. The ωB97X-D/cc-pVDZ vibrational zero-point energy was added to the CCSD(T)/cc-pVTZ single point energy to predict the relative energy of [6b], italicized in Figure 5.9, that was used to generate the potential energy surface in Figure 5.11. Using this approach, the classical vinyl cation [6b] structure is predicted to lie 0.15 eV higher

in energy than the nonclassical structure [8], consistent with previous predictions at the CCSD(T)/cc-pVQZ level.[418]

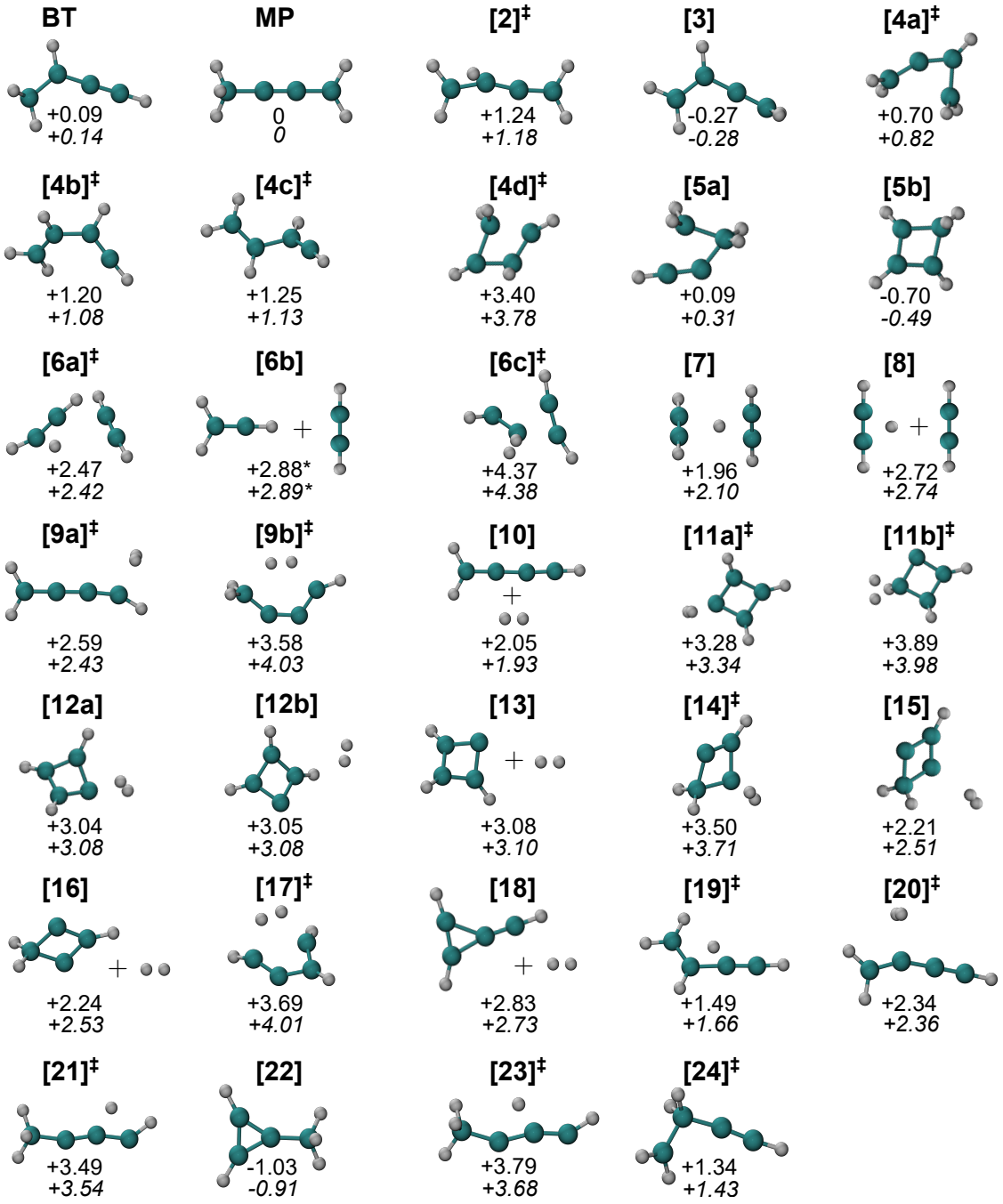

Fig. 5.9 Structures of $C_4H_5^+$ stationary points (see Figures 5.10 and 5.11) calculated at the MP2/aug-cc-pVDZ level (ωB97X-D/cc-pVDZ level for 6b, see text). The MP2/aug-cc-pVDZ vibrational zero-point corrected energy (eV, normal font) and the CCSD(T)/cc-pVTZ single point energy corrected by the MP2/aug-cc-pVDZ vibrational zero-point energy (eV, italicized) are listed below each structure. Energies are relative to the energy of the methyl propargyl cation **MP**.

Table 5.4 Electronic energies and vibrational zero-point energies calculated at the MP2/aug-cc-pVDZ level, along with CCSD(T)/aug-cc-pVTZ single point energies for stationary points on the $C_4H_5^+$ potential energy surface (Figures 5.10 and 5.11, respectively). Cartesian geometric coordinates for the stationary points optimized at the MP2/aug-cc-pVDZ level are given in Table 5.5.

stationary point	MP2/aug-cc-pVDZ electronic energy	CCSD(T)/aug-cc-pVTZ single point energy	MP2/aug-cc-pVDZ vibrational ZPE correction
BT	-154.54121	-154.741545	0.07046
MP	-154.544497	-154.7463852	0.070319
2	-154.496444	-154.7006797	0.0679
3	-154.555975	-154.7579842	0.071749
4a	-154.519939	-154.7175782	0.071603
4b	-154.499456	-154.7056343	0.069216
4c	-154.497578	-154.7041898	0.069484
4d	-154.416923	-154.6050261	0.067742
5a	-154.541006	-154.7353782	0.073262
5b	-154.574321	-154.7693052	0.07518
6a	-154.444422	-154.6480927	0.061047
6b*		-154.6298214	0.060108
6c	-154.378367	-154.5798978	0.064735
7	-154.461293	-154.6580459	0.059032
8	-154.433475	-154.6357081	0.059218
9a	-154.439949	-154.6477236	0.060837
9b	-154.404599	-154.5899434	0.06204
10	-154.454384	-154.6605116	0.055546
11a	-154.416726	-154.6164825	0.063113
11b	-154.396473	-154.5949145	0.065094
12a	-154.423665	-154.6244056	0.061345
12b	-154.423519	-154.6241072	0.061388
13	-154.420402	-154.6215448	0.059422
14	-154.411103	-154.6053456	0.065529
15	-154.455641	-154.64669	0.062703
16	-154.452725	-154.644132	0.060897
17	-154.400309	-154.5904592	0.061909
18	-154.425834	-153.6311458	0.055552
19	-154.485986	-154.6815989	0.066527
20	-154.449471	-154.6508292	0.06134
21	-154.411517	-154.6114124	0.065569

22	-154.585255	-154.7826001	0.073142
23	-154.402187	-154.6081037	0.067171
24	-154.494475	-154.6928404	0.069492

*The classical vinyl cation geometry ([6b]) could not be optimized at the MP2/aug-cc-pVDZ level and was instead optimized at the ωB97X-D/cc-pVDZ level. The vibrational zero-point correction to the energy calculated for the classical vinyl cation at the ωB97X-D/cc-pVDZ level is provided.

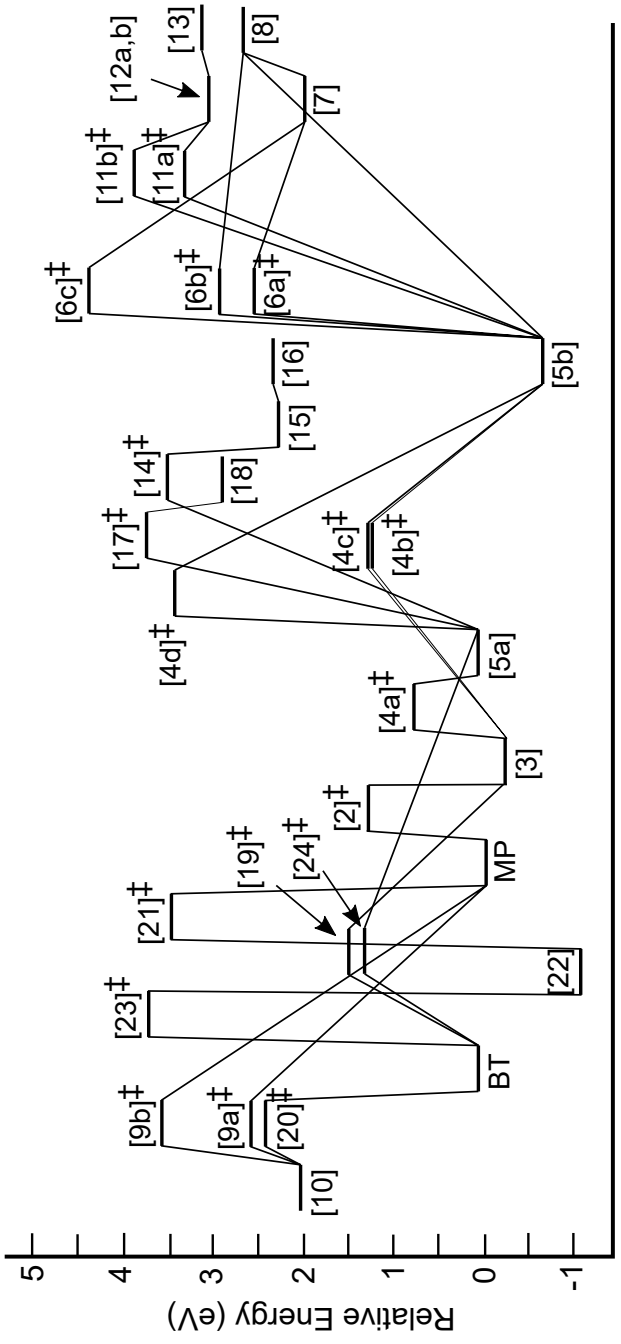

Fig. 5.10 Stationary points on the $C_4H_5^+$ potential energy surface, calculated at the MP2/aug-cc-pVDZ level of theory (ωB97X-D/cc-pVDZ for $[6b]^{\ddagger}$, see text). Low energy dissociation pathways leading to $C_4H_3^+$ (**[10]**) and $C_2H_3^+$ (**[8]** and **[13]**) fragments are included. Energies are relative to the methyl propargyl cation ($H_3C_4H_2^+$, **MP**).

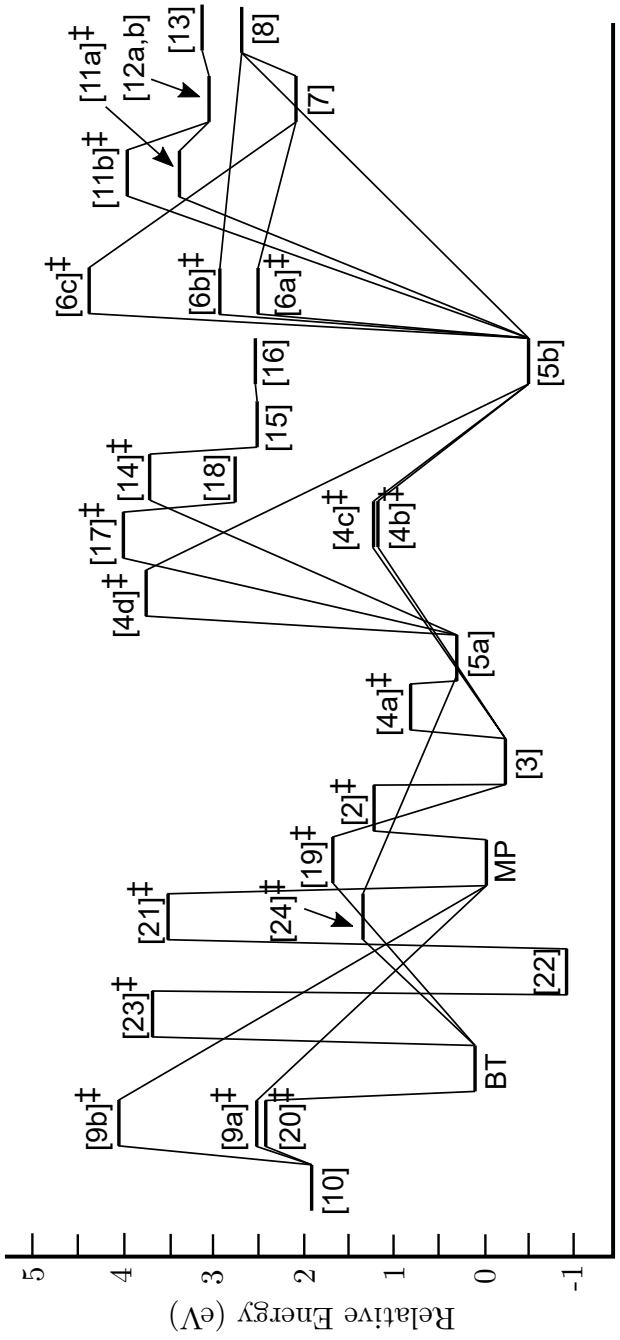

Fig. 5.11 Stationary points on the $C_4H_5^+$ potential energy surface, calculated using geometries at the MP2/aug-cc-pVDZ level of theory (ωB97X-D/cc-pVDZ for $[6b]^{\ddagger}$), single point energies at the CCSD(T)/cc-pVTZ level with vibrational zero-point corrections to energy at the MP2/aug-cc-pVDZ level (ωB97X-D/cc-pVDZ for $[6b]^{\ddagger}$). Low energy dissociation pathways leading to $C_4H_3^+$ (**[10]**) and $C_2H_3^+$ (**[8]** and **[13]**) fragments are included. Energies are relative to the energy of the methyl propargyl cation ($H_3C_4H_2^+$, **MP**).

Table 5.5 Atomic Cartesian coordinates for stationary points calculated at the MP2/aug-cc-pVDZ level of theory, as represented in Figure 5.9. Coordinates for the cation fragments for stationary points [6b], [8], [10], [13], [16], and [18] are provided here. Coordinates for the neutral fragments are given in Table 5.6. The classical vinyl cation geometry ([6b]) was calculated at the ωB97X-D/cc-pVDZ level (see text).

stationary point				
BT	C	-1.452871	0.897091	0
	H	-1.716661	1.53617	0.870409
	H	-2.005952	-0.04711	0
	H	-1.716661	1.53617	-0.870409
	C	0	0.747493	0
	H	0.619499	1.657666	0
	C	0.666696	-0.46825	0
	C	1.286589	-1.542382	0
	H	1.817293	-2.486604	0
MP	C	0.049018	1.976021	0
	H	-0.404896	2.385439	0.914881
	H	-0.404896	2.385439	-0.914881
	H	1.127327	2.243058	0
	C	0	0.534208	0
	C	-0.008562	-0.720008	0
	C	-0.06429	-2.079678	0
	H	-0.087265	-2.638597	0.944315
	H	-0.087265	-2.638597	-0.944315
[2]‡	C	-1.803333	-0.188207	-0.029564
	H	-1.119577	1.185947	0.302875
	H	-2.116269	-0.917886	0.73072
	H	-2.569879	0.297608	-0.645649
	C	-0.494197	0.241412	-0.105077
	C	0.800905	0.202481	0.086163
	C	2.121228	0.290786	0.092867
	H	2.639545	0.896017	-0.659811
	H	2.706132	-0.245798	0.848256
[3]	C	1.673416	-0.441227	-0.000005
	H	0.992059	1.626802	-0.000004
	H	1.368704	-1.492827	-0.000002
	H	2.742964	-0.206857	-0.000007

stationary point				
	C	0.725821	0.565907	-0.000003
	C	-0.60427	0.181332	0.000001
	C	-1.851561	-0.182273	0.000006
	H	-2.382075	-0.334779	0.950234
	H	-2.382089	-0.334767	-0.950217
[4a]‡	C	0.866022	-0.711914	-0.307871
	H	1.6094	1.551936	-0.22394
	H	0.892128	-1.000259	-1.368321
	H	0.922375	-1.488058	0.458691
	C	0.979999	0.708929	0.059272
	C	-0.303853	0.49312	0.28654
	C	-1.430216	-0.258192	0.355637
	H	-1.892757	-0.516133	1.316691
	H	-1.919137	-0.568874	-0.576513
[4b]‡	C	1.433646	-0.682636	-0.379872
	H	1.513896	1.22782	0.107714
	H	-2.62988	0.031827	0.290586
	H	1.981308	-1.53899	-0.777464
	C	0.827607	0.345076	0.082916
	C	-0.582238	0.439941	0.59196
	C	-1.616317	-0.081952	-0.100637
	H	-0.683399	0.978533	1.537065
	H	-1.487454	-0.578622	-1.065208
[4c]‡	C	1.621131	-0.441072	0.722613
	H	1.138794	0.593666	-1.080854
	H	-2.605861	0.281843	-0.119862
	H	2.172729	-0.898481	1.545837
	C	0.857312	-0.007832	-0.206029
	C	-0.610177	-0.35668	0.089784
	C	-1.554087	0.539586	-0.272366
	H	-0.826586	-1.318869	0.554695
	H	-1.314864	1.498174	-0.738416
[4d]‡	C	-0.120682	0.855605	0.047562
	H	2.192502	0.074612	0.293875
	H	-0.194725	1.330972	-0.94721

stationary point				
	H	-0.030329	1.420703	0.980942
	C	1.22739	-0.035745	-0.206009
	C	0.092462	-0.791853	-0.102271
	C	-1.217166	-0.254003	0.02873
	H	-2.121086	-0.338604	-0.580879
	H	-0.221452	-1.064232	1.006188
[5a]	C	-0.079610	0.890372	0
	H	2.359389	-0.038524	0.000012
	H	-0.009192	1.421869	-0.952453
	H	-0.009200	1.421874	0.952442
	C	1.286683	-0.203744	0.000007
	C	0.158546	-0.800912	-0.000016
	C	-1.175160	-0.239623	0.000005
	H	-1.741906	-0.340885	-0.930696
	H	-1.741845	-0.340893	0.930743
[5b]	C	-0.08033	-0.881515	-0.143439
	H	-2.192921	-0.000003	0.270874
	H	1.962881	-0.000016	-0.528935
	H	-0.142661	-1.721716	-0.845866
	C	-1.103665	-0.000007	0.239362
	C	-0.080331	0.88152	-0.143442
	C	1.117744	-0.000001	0.168191
	H	-0.142664	1.721748	-0.845836
	H	1.394855	0.000002	1.22573
$[6a]^{\ddagger}$	C	-0.624928	0.45574	-0.114307
	H	0.17647	1.126547	0.187617
	C	1.400944	0.50311	-2.152647
	H	1.08476	1.245735	-2.870327
	C	-1.486232	-0.362952	-0.542926
	H	-0.714108	-0.696678	-1.332589
	H	-2.483594	-0.794836	-0.470647
	C	1.828173	-0.356861	-1.373681
	H	2.260325	-1.107761	-0.728759
[6b]	C	0	0	-0.586249
(classical H_2CCH^+)	H	0	0.95216	-1.154531

stationary point				
	H	0	-0.95216	-1.154531
	C	0	0	0.676444
	H	0	0	1.767894
[6c]‡	C	1.215158	-0.307866	-0.180567
	H	1.824381	-1.17153	-0.428503
	C	-0.413001	-0.378536	0.296918
	H	-0.466921	-0.943061	1.236827
	C	-1.434937	0.479577	-0.309155
	H	-0.735922	-0.925105	-0.677619
	H	-2.377286	0.23278	0.230526
	C	0.858639	0.867694	0.107243
	H	0.681842	1.895735	0.408941
[7]	C	-1.487507	0.010841	0.618807
	H	-1.526152	-0.029087	-1.699948
	H	1.482012	1.704587	-0.029325
	H	-1.526082	0.029074	1.699956
	C	-1.487469	-0.010843	-0.618802
	C	1.481784	-0.620209	0.010671
	C	1.481786	0.620216	-0.010663
	H	1.482074	-1.70458	0.029334
	H	0.15658	-0.00003	-0.000091
[8]	C	0	0.623976	-0.077111
(nonclassical H_2CCH^+)	H	0	1.713548	-0.065
	C	0	-0.623976	-0.077111
	H	0	-1.713548	-0.065
	H	0	0	1.055335
[9a]‡	C	0.205826	-2.047682	0.041839
	H	-0.671801	-2.705198	0.079425
	H	1.212301	-2.484069	0.030819
	C	0.049968	-0.741039	0.009267
	C	-0.108085	0.559457	-0.021168
	C	-0.156344	1.828745	-0.055566
	H	0.281677	2.821169	-0.090479
	H	-1.712774	2.358888	0.364241
	H	-1.730873	2.337735	-0.429041

stationary point				
[9b]‡	C	-1.589983	-0.184705	-0.000985
	H	-2.139632	-0.00665	-0.939472
	H	-0.399502	1.071248	0.022875
	H	-2.141695	-0.040459	0.942038
	C	-0.542264	-1.032136	-0.015867
	C	0.771225	-1.097167	-0.017764
	C	1.54851	-0.039507	0.000445
	H	2.578636	0.330189	0.005976
	H	0.490296	1.113546	0.020795
[10]	C	-2.000403	0.016334	-0.012556
	H	-3.084979	0.047378	-0.014969
	C	-0.760589	-0.037205	0.022107
	C	0.582599	-0.002529	0.000723
	C	1.88162	0.011089	-0.004556
	H	2.428423	0.966606	-0.005765
	H	2.437198	-0.940118	-0.013575
[11a]‡	C	0.238559	-0.882328	0.146379
	H	2.384245	0.011172	-0.256973
	H	-2.054971	0.0057	0.82068
	H	0.105127	-1.728019	0.829802
	C	1.305759	0.005035	-0.103307
	C	0.215317	0.885682	0.049195
	C	-0.746235	-0.049655	-0.592664
	H	0.058086	1.797229	0.636084
	H	-2.127246	-0.036882	0.016508
[11b]‡	C	0.145245	0.901134	-0.066324
	H	2.242244	-0.064192	0.344275
	H	-2.109107	0.280075	-0.379107
	H	0.073387	1.769674	-0.730148
	C	1.169772	-0.063499	0.144589
	C	0.213892	-0.986204	-0.336587
	C	-0.851319	-0.098362	0.307591
	H	-1.896801	-0.455323	-0.664544
	H	-1.335682	-0.284896	1.269324
[12a]	C	-0.066204	-0.899488	-0.120924

stationary point				
	H	-2.241919	-0.000697	0.030041
	H	2.873223	0.000116	-1.006454
	H	0.236325	-1.798951	-0.665287
	C	-1.161799	-0.000352	-0.133715
	C	-0.066822	0.899549	-0.121122
	C	0.620236	0.000371	0.802295
	H	0.235073	1.799099	-0.665694
	H	2.944833	-0.000053	-0.251812
[12b]	C	0.028674	0.933403	-0.053462
	H	2.20723	0.126374	0.243813
	H	-3.178692	0.283151	-0.357867
	H	-0.294426	1.864235	-0.525925
	C	1.152689	0.068429	-0.041282
	C	0.258776	-1.023468	-0.410491
	C	-0.541726	-0.232078	0.51849
	H	-2.94919	-0.274904	-0.814945
	H	-1.175401	-0.476571	1.375391
[13]	C	0.000018	0.949459	-0.149607
	H	1.804904	-0.182986	0.820316
	H	0.000042	1.900222	-0.688396
	C	0.902127	-0.083999	0.210154
	C	-0.00002	-1.037217	-0.429407
	C	-0.902131	-0.083962	0.210154
	H	-1.804911	-0.182924	0.820314
[14]‡	C	-0.091396	0.539296	0.142197
	H	-2.244184	-0.123539	-0.709482
	H	1.924596	-0.472147	0.224084
	H	-0.133347	0.875756	1.345392
	C	-1.168311	-0.18896	-0.566062
	C	-0.075186	-0.953711	-0.726832
	C	1.148906	-0.094759	-0.452695
	H	-0.071739	-0.01418	1.443137
	H	1.508638	0.400385	-1.360059
[15]	C	0.07813	0.189105	0.757842
	H	2.29433	0.364326	0.00261

stationary point				
	H	-1.824867	0.174385	-0.370636
	H	-1.122264	2.723557	-0.057197
	C	1.238337	0.095942	0.016447
	C	0.245296	-0.543352	-0.697365
	C	-1.056286	-0.487581	0.046508
	H	-0.971602	2.64496	-0.794454
	H	-1.408454	-1.431917	0.479085
[16]	C	0	0.819144	0.087173
	C	0	0	1.198002
	H	0	0	2.287835
	C	0	-0.819144	0.087173
	C	0	0	-1.170258
	H	-0.931111	0	-1.750185
	H	0.931111	0	-1.750185
[17]‡	C	0.57501	0.811012	-0.296947
	H	2.199321	-0.751902	0.229232
	H	0.356502	1.643393	-0.968635
	H	-0.391695	1.214776	1.035696
	C	1.243071	-0.346842	-0.100513
	C	-0.053987	-0.824351	-0.332319
	C	-1.272464	-0.413079	-0.20133
	H	-2.260658	-0.298546	-0.648149
	H	-1.067433	0.70388	1.049983
[18]	C	0.992428	0.689836	-0.000028
	H	1.49929	-1.585278	-0.000009
	H	1.144481	1.768742	0.000091
	C	1.038969	-0.596622	0.000018
	C	-0.396767	-0.147703	-0.000009
	C	-1.625364	-0.000045	0.000004
	H	-2.699372	0.14374	0.000007
[19]‡	C	-1.692464	-0.398344	0.022559
	H	-1.48476	-1.472656	0.000819
	H	0.196777	0.042448	-1.029596
	H	-2.7317	-0.058764	0.044758
	C	-0.677477	0.527235	0.036474

stationary point				
	H	-0.842291	1.607855	-0.018972
	C	0.732625	0.095624	0.076444
	C	1.948521	-0.169938	0.03472
	H	2.994744	-0.446342	-0.018195
[20]‡	C	1.793545	-0.342468	0.000017
	H	0.801543	1.842642	0.391246
	H	1.885005	-1.44004	0.000032
	H	2.68624	0.284345	0.000029
	C	0.550655	0.097674	-0.000026
	H	0.801577	1.842691	-0.391169
	C	-0.809407	-0.010305	-0.000042
	C	-2.043917	-0.125088	0.000007
	H	-3.11962	-0.248513	0.000131
[21]‡	C	1.938692	0.048595	0.009114
	H	2.188976	0.02013	-1.078841
	H	2.477759	-0.79168	0.474778
	H	2.241445	1.031367	0.402479
	C	0.516762	-0.156184	0.028152
	H	-1.401058	1.046113	0.003766
	C	-0.762164	-0.000221	0.003835
	C	-2.108564	-0.183402	-0.006351
	H	-3.015475	0.441342	-0.01068
[22]	C	1.602521	-0.000001	-0.006194
	H	1.91427	0.000012	1.054269
	H	1.990541	0.909658	-0.482864
	H	1.990547	-0.909673	-0.482838
	C	0.127971	-0.000006	-0.012274
	H	-1.642103	1.625985	0.00252
	C	-1.082834	0.689335	0.001434
	C	-1.082847	-0.689329	0.001431
	H	-1.642123	-1.625974	0.002527
[23]‡	C	-1.893353	0.080721	-0.004289
	H	-2.52901	-0.758016	-0.324055
	H	-2.11269	0.996982	-0.577457
	H	-2.120516	0.281718	1.067101

stationary point				
	C	-0.491457	-0.328329	-0.02395
	H	0.264125	1.011028	-0.021496
	C	0.837722	-0.014704	-0.005129
	C	2.120687	-0.073648	0.006435
	H	3.056497	0.484048	0.017505
[24]‡	C	-1.47013	-0.576754	0.024578
	H	2.884713	-0.583356	0.093604
	H	-2.339054	-0.710715	0.685556
	H	-1.185193	-1.413428	-0.627503
	C	1.861273	-0.245334	0.051087
	C	0.724929	0.227031	-0.031899
	C	-0.688676	0.639564	-0.019662
	H	-0.957666	1.386833	0.738988
	H	-0.967183	1.053622	-1.035273

Table 5.6 Atomic Cartesian coordinates for acetylene (neutral fragment for stationary points [6b] and [8]) and H_2 (neutral fragment for stationary points [10], [13], [16], [18]), calculated at the MP2/aug-cc-pVDZ level of theory. Structures and energies, relative to the energy of the **MP** ion, are provided in Figure 5.9.

stationary point				
[6b], [8]	C	0	0	0.615744
	H	0	0	1.690997
	C	0	0	-0.615744
	H	0	0	-1.690997
[10], [13], [16], [18]	H	0	0	0.377466
	H	0	0	-0.377466

Chapter 6

REPD spectroscopy of $C_6H_4^+$ isomers tagged with Ar and N_2

6.1 Introduction

This chapter focuses on the electronic spectroscopy of open-shell $C_6H_4^+$ cations generated in an ionized pulsed expansion of a lean C_2H_2 / Ar or C_2H_2 / N_2 gas mixture. The electronic spectra may help identify $C_6H_4^+$ intermediates involved in acetylene ion-molecule reactions occurring in plasmas,[140,419–427] acetylene-rich flames,[428–430] the interstellar medium (ISM),[20,45,58] and the atmosphere of Titan, one of Saturn's moons.[80] The studies also reveal how excited $C_6H_4^+$ ions dissipate excess energy through fragmentation, which is believed to be a fundamental driving force for hydrocarbon growth.[275] Comparison of the laboratory REPD spectra with astronomical spectra may facilitate detection of $C_6H_4^+$ isomers, including those which may be fragments of larger cations such as benzene,[155,159,186,192,244,252,257,387,402,431,432] or ionized forms of neutral molecules that exist in harsh environments exposed to high energy light.[8,237,238]

A description of the formation, dissociation, and spectroscopy of $C_6H_4^+$ isomers was summarized in Chapter 1. Further details are presented in the following section, followed by an overview of the experimental approach, predictions of quantum chemical calculations, and presentation and interpretation of the measured REPD spectra.

6.1.1 Formation and dissociation of $C_6H_4^+$ cations

Ion-molecule reactions of acetylene plasmas leading to $C_6H_4^+$ depend on the energy and pressure, which influence whether the intermediates are stabilized and if they react further with acetylene, C_2H_2.[433] Excited collision complexes, formed through association reactions along the growth pathway, may be collisionally or radiatively stabilized before forming reaction products. In low temperature, low pressure environments such as the ISM, the excited intermediates can be stabilized through emission of IR radiation or dissociate if an exothermic unimolecular pathway is available.[434] With high internal energies, emission of more than one infrared photon may be necessary to stabilize the intermediate.[433] Also, with increasing internal energy, additional exit channels may become available.[277,435] Consequently, fragmentation of the intermediate becomes competitive at higher energies.

In this work, $C_2H_2^+$ precursor ions are probably produced through Penning ionization by metastable Ar atoms (see Chapter 2).[150,436] For simplicity, the reactions discussed below leading to $C_6H_4^+$ are assumed to involve $C_2H_2^+$ in the $X^2\Pi_u$ and A^2A_g electronic states, the latter of which may internally convert to high lying vibrational levels of the $X^2\Pi_u$ state before reacting.

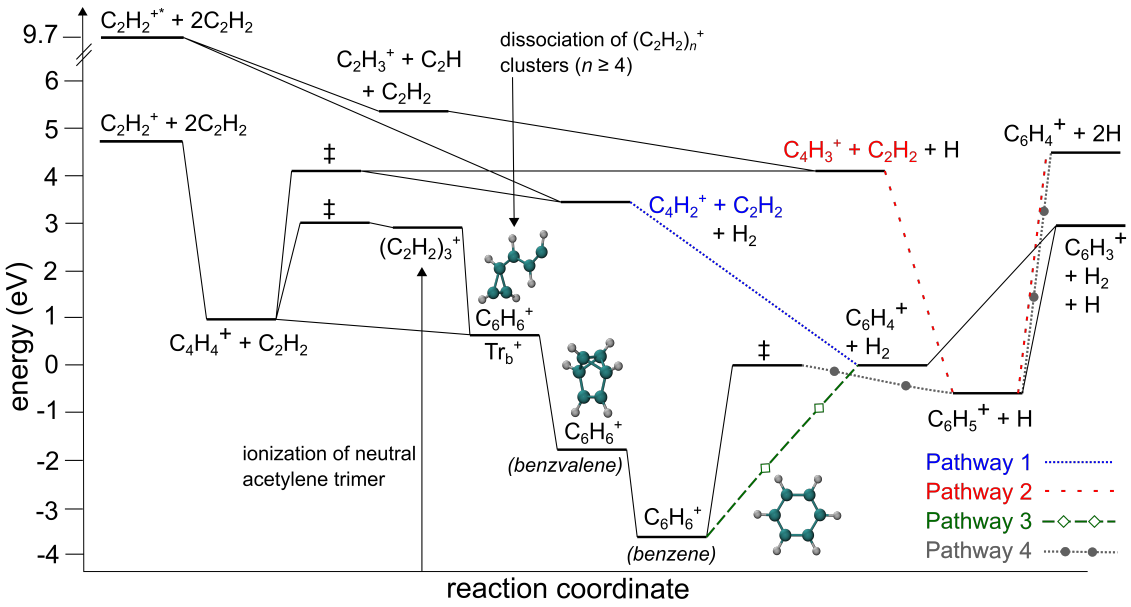

Fig. 6.1 Simplified energy level diagram, generated using available thermochemical data, highlighting four main acetylene ion-molecule reactions leading to $C_6H_4^+$. Energies of stationary points are on a common $C_6H_6^+$ energy scale and are relative to the $C_6H_4^+ + H_2$ energy. Saddle points are indicated by ‡.

Four main pathways leading to $C_6H_4^+$ are summarized in the energy level diagram shown in Figure 6.1, which was produced using available thermochemical data and computational predictions.[155,178,179,185,377,378,387,421,431,437–439] Because at least three acetylene monomers are necessary to generate $C_6H_4^+$, stationary points are set to a common $C_6H_6^+$ energy scale. Possible structures for the intermediates involved are given in Figure 6.2.

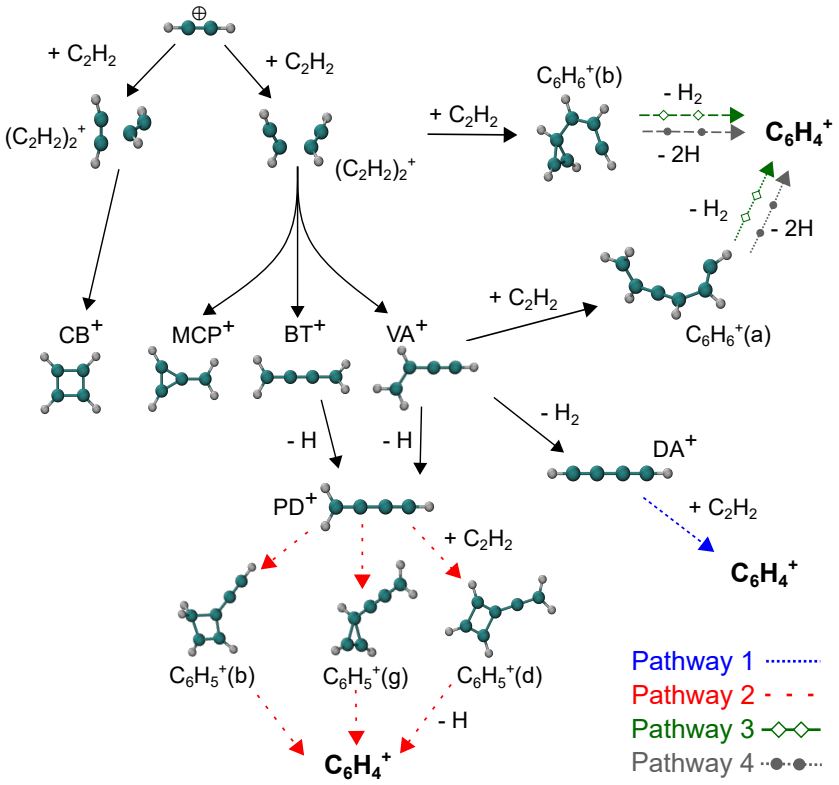

Fig. 6.2 Flow chart of likely $C_4H_4^+$, $C_4H_2^+$, $C_4H_3^+$, $C_6H_5^+$, and $C_6H_6^+$ intermediates along acetylene ion-molecule reaction pathways leading to $C_6H_4^+$. See Figure 6.1 for relative energies.

All pathways to $C_6H_4^+$ rely upon the initial acetylene ion-molecule reaction, introduced in Chapter 1 as equation 1.19 and reproduced here:

$$C_2H_2^+ + C_2H_2 \rightarrow (C_2H_2)_2^+ \rightarrow C_4H_4^+ \tag{6.1}$$

According to computational[178,183] and experimental[152,179,180] investigations, the reaction proceeds through a dimer complex, $(C_2H_2)_2^+$, that enters the covalent $C_4H_4^+$ potential energy surface. Secondary and tertiary reactions involving $C_4H_4^+$ intermediates lead to $C_6H_4^+$ cations.

Some $C_4H_4^+$ ions, generated in the ion source used in this work, have been described in Chapter 4. The REPD spectra of tagged $C_4H_4^+$ ions exhibit transitions due to butatriene

(BT^+) and vinylacetylene (VA^+), whose structures are shown in Figure 6.2. To explain their formation through the initial bimolecular reaction (eq. 6.1) and their fragmentation to $C_4H_2^+ + H_2$ and $C_4H_3^+ + H$, stationary points on the ground state $C_4H_4^+$ potential energy surface were calculated. The reaction was predicted to proceed through two different $(C_2H_2)_2^+$ complexes, with one collapsing to the four-membered ring, cyclobutadiene (CB^+), and the other to an intermediate leading to the methylenecyclopropene (MCP^+), BT^+, and VA^+ isomers (see Figure 6.2). Although the route to CB^+ is expected to be favored under low temperature and pressure conditions, pathways to other $C_4H_4^+$ isomers are likely to prevail in high energy and pressure domains. Secondary and tertiary reactions involving linear $C_4H_4^+$ isomers, particularly VA^+, are believed to play important roles in hydrocarbon growth, possibly through $C_6H_4^+$ intermediates.[183,188,249,250] These reactions are grouped and defined here as Pathways 1-4, as shown in Figures 6.1 and 6.2.

Pathways 1 and 2 occur following dissociation of the excited $C_4H_4^+$ cations to linear $C_4H_3^+$ (protonated diacetylene; PD^+) and $C_4H_2^+$ (diacetylene; DA^+), shown in Fig. 6.2, that subsequently react with another acetylene molecule:[135,136,176,207,246,419,420,422,440,441]

Pathway 1

$$C_4H_4^+ \rightarrow C_4H_2^+ + H_2 \tag{6.2}$$

$$C_4H_2^+ + C_2H_2 \rightarrow C_6H_4^+ \tag{6.3}$$

and

Pathway 2

$$C_4H_4^+ \rightarrow C_4H_3^+ + H \tag{6.4}$$

$$C_4H_3^+ + C_2H_2 \rightarrow C_6H_5^+ + H \tag{6.5}$$

$$C_6H_5^+ \rightarrow C_6H_4^+ + H \tag{6.6}$$

Pathway 1 is thermodynamically favorable and possibly occurs in the ISM and atmosphere of Titan, with the possibility that the resulting $C_6H_4^+$ cations fragment to $C_6H_3^+ + H$.[20,45,58,80,420,422] Because the $C_6H_4^+$ potential energy surface remains relatively unexplored, it is unclear which structures may be stabilized along this pathway. In the case of low-lying $C_6H_4^+$ isomerization barriers, it could be assumed that a large fraction of the ions

relaxes to the lowest energy forms, such as the fully cyclic *meta*- and *ortho*-benzyne cations ($\mathbf{A}^+$ and $\mathbf{F}^+$ in Figure 6.3).[151,256]

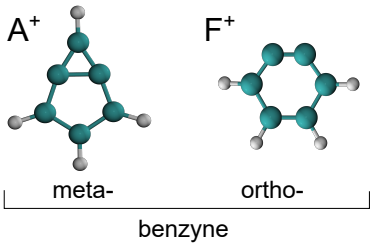

Fig. 6.3 Geometries of the lowest energy benzyne cations.

In higher energy environments, including circumstellar envelopes, flames, and electron impact ionization sources such as that used in this study, Pathway 2 becomes competitive. This is evidenced by results of mass spectrometric studies where the energy of the ionizing electrons was varied.[421,441] With relatively low electron impact energy of 14 eV, pulsed ion cyclotron resonance mass spectrometry revealed that the growth of $C_6H_4^+$ from sequential ion-molecule reactions correlated only with the decay of $C_4H_2^+$ but *not* with $C_4H_3^+$.[441] These results are consistent with $C_4H_3^+$ cations, having low excess internal energy, reacting with acetylene to generate $C_6H_5^+$ intermediates (eq. 6.5) which are then unable to cleave a C-H bond (eq. 6.6) as this overall reaction is slightly endothermic (see Fig. 6.1).[439] Pathway 2 has been presumed to dominate when electron energies are between 16.3 and 18.0 eV, considering that the acetylene cation precursor is in its A^2A_g excited electronic state ($C_2H_2^{+*}$ in Fig. 6.1), which provides an alternative route to $C_4H_3^+$ and with greater internal energy:[421,422,442,443]

$$C_2H_2^{+*} + C_2H_2 \rightarrow C_2H_3^+ + C_2H \tag{6.7}$$

$$C_2H_3^+ + C_2H_2 \rightarrow C_4H_3^+ + H_2 \tag{6.8}$$

At even higher energies, acetylene dissociatively ionizes to C_2H^+ (≈ 18 eV), CH^+ (≈ 22 eV), H^+ (≈ 22 eV), C_2^+ (≈ 24 eV), and C^+ (≈ 25 eV), with the former two fragments reacting with acetylene to form $C_2H_3^+$ intermediates that may then produce $C_6H_4^+$ through eqs. 6.7, 6.8 and Pathway 2.[421,444,445] Beyond 34 eV, acetylene is expected to doubly ionize and dissociate to the same fragments, such that Pathway 2 is still a likely contributor to $C_6H_4^+$.[446–449]

The $C_6H_4^+$ structures produced through Pathway 2 may be inferred from the $C_6H_5^+$ intermediates generated by $C_4H_3^+$ reacting with acetylene (eq. 6.5). Although the reactivity of $C_4H_3^+$ reportedly does not depend on its structure,[140] we consider the lowest energy, linear protonated diacetylene isomer (PD^+ in Fig. 6.2) for simplicity. Quantum chemical calculations predict the association of PD^+ with acetylene produces three initial $C_6H_5^+$ adducts with three- and four-membered rings (see Figure 6.2).[439] At high internal energies, dissociation of the $C_6H_5^+$ adducts may occur rapidly, with H loss resulting in $C_6H_4^+$ isomers that retain the carbon backbone, such as the propargyl cyclopropene and ethynyl cyclobutadiene cations $\mathbf{C}^+$ and $\mathbf{K}^+$ shown in Figure 6.4. These $C_6H_4^+$ isomers have been predicted to lie low in energy on the $C_6H_4^+$ potential energy surface.[151,256]

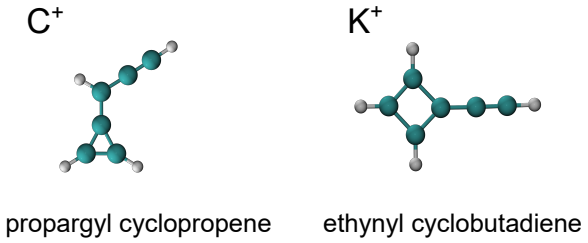

Fig. 6.4 Geometries of possible $C_6H_4^+$ fragments of $C_6H_5^+$ adducts along the $C_4H_3^+ + C_2H_2$ route (Pathway 2).

Pathways 3 and 4 rely on formation of $C_6H_6^+$ cations, which occurs through acetylene addition to (probably linear) $C_4H_4^{+*}$:[140,249,250]

$$C_4H_4^{+*} + C_2H_2 \rightarrow C_6H_6^+ \tag{6.9}$$

This process is unlikely to occur in cold extraterrestrial environments, but may be important at higher pressure and acetylene densities, such as in the ion source used in this work, in which a fraction of $C_4H_4^{+*}$ cations may be collisionally stabilized.[140] Sequential condensation reactions lead to ionized acetylene clusters $[(C_2H_2)_n^+, n = 3, 4, 5, ...]$ that typically give rise to peaks in electron impact ionization mass spectra (see Figure 1.6 in Chapter 1).[148,152,180]

Excited $C_6H_6^{+*}$ cations, once formed, can access two dissociation channels: [155,216,244,387,431]

Pathway 3

$$C_6H_6^+ \rightarrow C_6H_4^+ + H_2 \tag{6.10}$$

and

Pathway 4

$$C_6H_6^+ \rightarrow C_6H_5^+ + H \tag{6.11}$$

$$C_6H_5^+ \rightarrow C_6H_4^+ + H \tag{6.12}$$

The H_2 and H loss channels (eqs. 6.10 and 6.11, respectively) are expected to be competitive at threshold due to similar measured appearance energies of $C_6H_4^+$ and $C_6H_5^+$ from the benzene cation (see Fig. 6.1).[387,431] The structures of the resulting $C_6H_4^+$ fragments depend on the $C_6H_6^+$ intermediates and their internal energies.

The immediate $C_6H_6^+$ structures generated from $C_4H_4^{+*}$ are likely acyclic, based on the previously calculated geometries of intermediates along the $C_4H_4^+ + C_2H_2$ fragmentation pathway of the benzene cation.[390] Because several $C_6H_6^+$ isomerization barriers, including for ring-opening steps, have been calculated to lie below the lowest dissociation limit, scrambling is likely to occur before fragmentation.[189,388–390] The pathway to $C_4H_4^+$ fragments, specifically the vinylacetylene cation (VA^+), has been calculated to be barrierless, and involves an acyclic intermediate shown in Figures 6.2 and 6.5 as $C_6H_6^+$(a). The $C_6H_6^+$(a) isomer, or another acyclic one, may be the initial adduct formed through barrierless *association* of VA^{+*} with acetylene. If the energized adduct dissociates into $C_6H_4^+ + H_2$ (Pathway 3) or $C_6H_5^+ + H$ (Pathway 4), $C_6H_4^+$ chains such as the 1-hexene-3,5-diyne cation, shown as $\mathbf{G}^+$ in Figure 6.5, are likely to be formed. Interestingly, isomer $\mathbf{G}^+$ was spectroscopically identified in an acetylene-helium discharge expansion, as well in a Ne matrix produced using the acyclic $C_6H_6^+$ isomers 1,4- and 1,5-hexadiyne (see Section 6.1.2 for spectroscopic details).[254,256]

Ionization of the early, dense portion of the supersonic expansion is expected to trigger the acetylene ion-molecule reactions described above, although there is a possible contribution of neutral $(C_2H_2)_n$ cluster ionization to $C_6H_4^+$ formation.[152,153,377] Ionization of neutral clusters and dissociation of larger acetylene cluster ions form $C_6H_6^+$ cations with high internal energies.[153,185,377] The relevant portion of the $C_6H_6^+$ potential energy surface has been explored through photoionization of neutral acetylene trimers and tetramers[155,185]

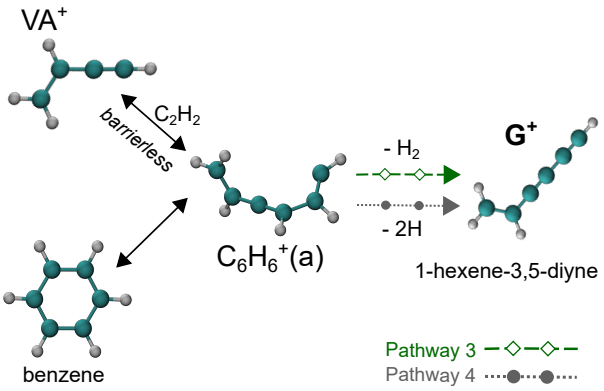

Fig. 6.5 Pathways leading to possible formation of isomer $\mathbf{G}^+$ through a high energy acyclic intermediate, $C_6H_6^+$(a).

complemented by quantum chemical calculations.[185,377] The trimer cation is predicted to be a complex consisting of a $C_4H_4^+$ "core" bound to an acetylene molecule. If collisionally cooled, it may enter the "tightly" bound section of the $C_6H_6^+$ potential energy surface as a vibrationally excited three-membered ring structure,[377] shown in Fig. 6.6 as $C_6H_6^+$(b), with sufficient energy to access the $C_6H_4^+ + H_2$ channel (Pathway 3, see Fig. 6.1). Similarly, the tetramer cation is predicted to consist of an acetylene monomer attached to a covalent $C_6H_6^+$ core, shown as $C_6H_6^+$(c) in Figure 6.6.[185,377] If the tetramer evaporates the neutral monomer, the $C_6H_6^+$(c) fragment may also dissociate to $C_6H_4^+$. Assuming the C-C skeleton remains intact, the $C_6H_4^+$ isomer $\mathbf{C}^+$ may be a favorable fragment of ionized acetylene clusters.

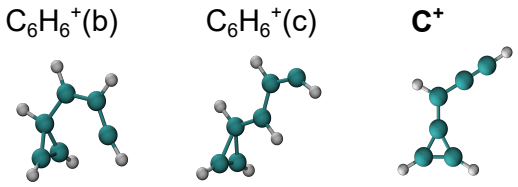

Fig. 6.6 Geometries of two high-energy $C_6H_6^+$ isomers, $C_6H_6^+$(b) and $C_6H_6^+$(c), and a $C_6H_4^+$ isomer, the propargyl cyclopropene cation ($\mathbf{C}^+$), with a similar carbon backbone.

In summary, the formation and stabilization of $C_6H_4^+$ isomers formed through acetylene ion-molecule reactions depend on the internal energies of the precursor ions and $C_6H_4^+$ isomerization barriers and relaxation mechanisms, including collisional stabilization. Although relative energies of several $C_6H_4^+$ isomers have been previously calculated,[151,159,255,256,261,450] there is little information about interconversion and fragmentation pathways. Previous studies show that collision-induced dissociation occurs during the deposition of $C_6H_4^+$ ions into a solid Ne matrix, resulting in formation of HC_6H^+, HC_4H^+, and $HC_6H_2^+$ fragments giving

rise to their characteristic bands in the recorded electronic spectrum.[256] In another study, photolysis of Mg^+-$C_6H_4F_2$ complexes was proposed to initiate a sequential dissociation pathway, first forming $C_6H_4^+$ fragments, believed to be the cyclic *ortho*-benzyne isomer ($\mathbf{F}^+$ in Figure 6.3), that further decompose to yield diacetylene (HC_4H^+) cations.[258] The dissociation energy of $\mathbf{F}^+$ was experimentally determined to have a lower bound of 1.70 eV and upper bound of 2.35 eV, with calculations at the B3LYP/aug-cc-pVTZ level predicting the $C_4H_2^+ + C_2H_2$ threshold lies at 2.56 eV.[258,451] It is unclear whether $C_4H_2^+ + C_2H_2$ is formed directly from $\mathbf{F}^+$ through a reverse Diels-Alder mechanism or if isomerization plays a role.

6.1.2 Previous spectroscopic studies of $C_6H_4^+$ cations

Previously recorded electronic spectra of $C_6H_4^+$ cations are limited to those for isomers $\mathbf{G}^+$, $\mathbf{I}^+$, $\mathbf{J}^+$, and $\mathbf{C}^+$ depicted in Figure 6.7.[254–256,450,450] Table 6.1 summarizes the previously recorded transitions.

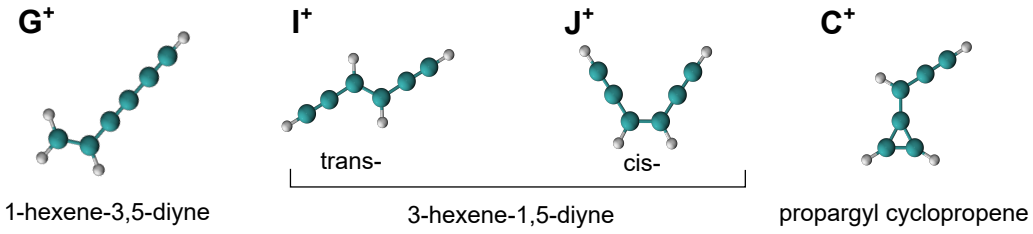

Fig. 6.7 $C_6H_4^+$ isomers previously studied through electronic spectroscopy.

Table 6.1 Electronic transitions and corresponding wavelengths (nm) for $C_6H_4^+$ isomers, obtained through cavity ringdown and matrix isolation spectroscopy experiments.

isomer	transition	band	wavelength (nm) gas phase / Ne matrix
$\mathbf{J}^+$	$^2A_2 \leftarrow \tilde{X}^2B_1$	0_0^0	- - - / 622.0[a]
$\mathbf{G}^+$	$^2A'' \leftarrow \tilde{X}^2A''$	0_0^0	604.41[b] / 608.8[a,b]
$\mathbf{G}^+$	$^2A'' \leftarrow \tilde{X}^2A''$	12_0^1	580.93[c] / 585.3[b,c]
$\mathbf{I}^+$	$^2B_g \leftarrow \tilde{X}^2A_u$	0_0^0	580.07[d] / 585.5[a,b]
$\mathbf{J}^+$	$^2A_2 \leftarrow \tilde{X}^2B_1$	0_0^0	- - - / 385.1[a]
$\mathbf{G}^+$	$^2A'' \leftarrow \tilde{X}^2A''$	0_0^0	- - - / 372.8[a]
$\mathbf{I}^+$	$^2B_g \leftarrow \tilde{X}^2A_u$	0_0^0	- - - / 373.0[a]
$\mathbf{C}^+$	$^2A'' \leftarrow \tilde{X}^2A''$	0_0^0	- - - / 417.0[a]

[a]ref. 256, [b]ref. 450, [c]ref. 254, [d]ref. 255

The first electronic spectrum of $C_6H_4^+$ was recorded for ions in an acetylene-helium plasma expansion using cavity ringdown spectroscopy.[450] By analyzing the rotationally resolved band at 604 nm, the cation was confirmed to be the 1-hexene-1,3-diyne isomer, $\mathbf{G}^+$ in Fig. 6.7, with the band corresponding to the origin of a $^2A'' \leftarrow \tilde{X}^2A''$ transition. Additional transitions within the band system were recorded by trapping the $C_6H_4^+$ ions in a Ne matrix and monitoring absorption, with the origin band observed at 609 nm (see Table 6.1). Most attention was given to a band occurring at 585 nm, initially assigned to the 12_0^1 transition (ν_{12}, in-plane bending vibrational mode), as it exhibited a large intensity that could not be explained. Spectra recorded using different precursors showed that the intensity of the 585 nm band changed with respect to that of the origin transition, signaling a contribution from another isomer. In a subsequent study using cavity ringdown spectroscopy, the 12_0^1 transition of $\mathbf{G}^+$ was confirmed to overlap an $^2B_g \leftarrow \tilde{X}^2A_u$ origin transition of the *trans*-3-hexene-1,5-diyne isomer ($\mathbf{I}^+$ in Figure 6.7).[254,255]

The most comprehensive spectroscopic study of $C_6H_4^+$ isomers involved measuring absorption spectra in Ne matrices and interpreting the spectra using predictions from quantum chemical calculations.[256] In addition to the overlapping band systems of isomers $\mathbf{G}^+$ and $\mathbf{I}^+$ occurring in the visible region, higher energy transitions associated with the two isomers were observed around 373 nm that were also difficult to disentangle. Spectra were recorded using different precursors and were then subtracted from one another after scaling the 609 and 585 nm band intensities for $\mathbf{G}^+$ and $\mathbf{I}^+$, respectively. Based on changes in its intensity, the 373 nm band was assigned to overlapping $^2A'' \leftarrow \tilde{X}^2A''$ and $^2B_g \leftarrow \tilde{X}^2A_u$ origin transitions of $\mathbf{G}^+$ and $\mathbf{I}^+$. Bands at 366 and 359 nm were assigned to vibronic transitions within the band system of $\mathbf{G}^+$, and bands at 367, 360, 353, 347, and 341 nm were attributed to an extended progression in the symmetric in-plane bending vibration of the central C_4 skeleton (ν_8) of $\mathbf{I}^+$. Interestingly, the calculated geometry of $\mathbf{I}^+$ in its excited electronic state was distorted from C_{2h} symmetry along the central HCCH dihedral angle, suggesting that a progression in the twisting vibrational mode (ν_{13}) should have appreciable intensity in the spectrum. However, this progression was not apparent in the measured spectrum.

The Ne matrix spectra also included electronic transitions of the *cis*-3-hexene-1,5-diyne and propargyl cyclopropene cations, shown in Figure 6.7 as isomers $\mathbf{J}^+$ and $\mathbf{C}^+$, respectively. Weak bands at 622 and 385 nm were assigned to two different origin transitions of $\mathbf{J}^+$, based on calculated energies and oscillator strengths. Vibronic progressions within the two band systems were not evident. A band system commencing at 417 nm was tentatively assigned to a $^2A'' \leftarrow \tilde{X}^2A''$ transition of $\mathbf{C}^+$ based on agreement with a simulated spectrum generated using quantum chemical calculations. A low intensity band at 423 nm was not assigned.

Calculations predicted that a transition of isomer $\mathbf{F}^+$ (*o*-benzyne; see Fig. 6.3) occurs nearby, based on a planar equilibrium geometry for the ground electronic state. However, a recent photoelectron spectroscopy investigation confirmed the geometry of $\mathbf{F}^+$ to be twisted (C_2 symmetry, $\tilde{X}^2A$).[261] Energies of excited electronic states of isomer $\mathbf{F}^+$ were only predicted up to 2.22 eV (556 nm) above the $\tilde{X}^2A$ state; understanding of higher-lying electronic states requires further computational investigation.

In the current study, REPD spectra of C_6H_4-Ar and $C_6H_4^+$-N_2 complexes were measured over the 265-700 nm range by monitoring $C_6H_4^+$ and $C_4H_2^+$ photofragments. The spectra are interpreted based on previous spectroscopic studies, hole burning experiments, and electronic structure calculations of relevant isomers in their ground and excited electronic states. To help understand which $C_6H_4^+$ isomers are formed through acetylene ion-molecule reactions in the ion source, and to predict their dissociation energies and mechanisms, stationary points related to reaction Pathways 1-4 and the ground state $C_6H_4^+$ potential energy surface were calculated.

6.2 Experimental methods

Electronic spectra of $C_6H_4^+$-Ar and $C_6H_4^+$-N_2 complexes were recorded using resonance enhanced photodissociation (REPD) spectroscopy over the 265-700 nm range. The experimental apparatus is described in Chapter 2.[263] In this work, a pulsed supersonic expansion of $\approx 0.7\%$ C_2H_2 in Ar (or N_2), with a stagnation pressure of 4.5 bar, was bombarded with electrons to form $C_6H_4^+$ isomers and the $C_6H_4^+$-Ar and $C_6H_4^+$-N_2 complexes. The complexes were mass-selected using a quadrupole mass filter (QMF) and then deflected 90° using an electrostatic quadrupole bender into an octupole ion guide. There, the molecular beam was radially focused and exposed to output light from a tunable optical parametric oscillator (OPO, EKSPLA 342B). Dissociation following resonant photoexcitation of the complexes resulted in $C_6H_4^+$ (tag loss) and $C_4H_2^+$ (C_2H_2 and tag loss) fragments that were mass-selected using a second QMF and detected with a microchannel plate. REPD spectra were generated by plotting photofragment ion yield (normalized to laser power) as a function of wavelength (calibrated using an Ångstrom LSA UVL wavemeter).

As described above, several different $C_6H_4^+$ isomers are expected to form from acetylene ion-molecule reactions. Hole burning (HB) experiments were conducted to help ascertain whether particular bands arise from a single isomer. These HB experiments, described in Chapter 2, involved measuring REPD spectra using the setup described above, but with the

addition of a second OPO (OPOTEK Vibrant 355 LD) that provided the HB light. The HB beam, directed along the axis of the first QMF toward the ion source, was tuned to a wavelength resonant with a strong vibronic transition of an Ar-tagged $C_6H_4^+$ isomer. The complex absorbing the HB light dissociates prior to reaching the octupole, resulting in diminished intensities of bands associated with the selected $C_6H_4^+$ isomer in the REPD spectrum.

6.3 Computational methods

To predict $C_6H_4^+$ structures that are generated in the ion source, stationary points along reaction Pathways 1-4 and the ground state $C_6H_4^+$ potential energy surface were calculated at the ωB97X-D/aug-cc-pVTZ level. Ground state dissociation pathways leading to $C_4H_2^+ + C_2H_2$, $C_6H_2^+ + H_2$, and $C_6H_3^+ + H$ fragments were also investigated. Saddle points were identified by scanning the potential energy surface along bond lengths, angles, and torsions. The optimized geometry for each saddle point was inspected for its single negative frequency and further evaluated through intrinsic reaction coordinate (IRC) calculations.[393] To obtain more accurate energies, single point energies of all optimized geometries were calculated using the coupled-cluster singles, doubles, and perturbative triples method CCSD(T). The CCSD(T)/cc-pVTZ energies were then added to the vibrational zero-point energies calculated at the ωB97X-D/aug-cc-pVTZ level. The CCSD(T)/cc-pVTZ//ωB97X-D/aug-cc-pVTZ nomenclature is used to refer to this computational approach.

To help assign bands to vibronic transitions of $C_6H_4^+$ ions, vertical excitation energies and oscillator strengths for the twelve lowest-energy isomers were calculated using time-dependent density functional theory (TD-DFT) at the ωB97X-D/aug-cc-pVTZ level. Strong electronic transitions were further investigated by calculating excited state equilibrium geometries and harmonic vibrational frequencies, which were used with the corresponding ground state parameters to simulate spectra employing the PGOPHER program.[311] Excited state harmonic vibrational frequencies for all spectral simulations were scaled by 0.957, based on the recommended factor for ground state calculations at the ωB97X-D/aug-cc-pVTZ level.[452]

Ground state equilibrium geometries and harmonic vibrational frequencies for $C_6H_4^+$-Ar and $C_6H_4^+$-N_2 complexes, calculated at the ωB97X-D/aug-cc-pVTZ level, indicate the Ar or N_2 ligands only slightly perturb the geometries and vibrational frequencies of the bare $C_6H_4^+$ ions. Intermolecular bond dissociation energies were calculated, accounting for basis set superposition errors (BSSE) and vibrational zero-point corrected energies of the ionic

complexes, the bare $C_6H_4^+$ ions, and the tags. Structural and energetic data of ground state $C_6H_4^+$-Ar and $C_6H_4^+$-N_2 complexes are provided in the supporting information (SI).

6.4 Results and discussion

6.4.1 Ground state $C_6H_4^+$ potential energy surface and Pathways 1-4

Stationary points associated with reactions along Pathways 1-4 have been calculated to better understand $C_6H_4^+$ formation through acetylene-ion molecule reactions. These calculations are used to interpret the REPD spectra, as the detection of isomers depends on their abundance and the strengths of their electronic transitions.

Calculated stationary points for the lower energy Pathways 1 and 3 are shown in the energy level diagram of Figure 6.8. A simplified version of the ground state $C_6H_4^+$ potential energy surface is embedded within the large brackets. More than seventy covalently bound $C_6H_4^+$ structures were investigated through DFT calculations of the ground state $C_6H_4^+$ potential energy surface (see Figs. 6.15-6.17 in the SI), with the twelve lowest energy structures depicted in Figure 6.8 as $\mathbf{A}^+$ - $\mathbf{L}^+$. Higher-lying points on the $C_6H_4^+$ surface are labeled [n] with n corresponding to the energetic rank (ascending) of the point relative to the global minimum, isomer $\mathbf{A}^+$. The equilibrium geometries calculated in this work for isomers $\mathbf{A}^+$ - $\mathbf{L}^+$ agree with those reported in previous studies (see Figure 6.19 in the SI), aside from the propadienylidene cyclopropene isomer, $\mathbf{D}^+$, which has not been previously considered.[151,256,261]

Ground state calculations predict the $C_4H_2^+ + C_2H_2$ entrance channel of Pathway 1 lies 3.29 eV above $C_6H_4^+$ isomer $\mathbf{A}^+$, with the reaction likely proceeding through a vibrationally excited open-chain $C_6H_4^+$ intermediate, shown in Figure 6.8 as stationary point [47]. Because the interconversion barriers extending from the intermediate are relatively low, several different $C_6H_4^+$ structures are accessible and may be kinetically stabilized, depending on the dissociation and collisional stabilization in the expansion. Based on the lowest calculated $C_6H_3^+ + H$ dissociation limit, 3.18 eV above isomer $\mathbf{A}^+$ (see [64] in Fig. 6.8), it is likely that although a portion of the $C_6H_4^+$ isomers dissociate following reactions in Pathway 1, most of the $C_6H_4^+$ isomers remain intact, consistent with previous experimental observations where ≈ 5 % of the ions detected through Pathway 1 were $C_6H_3^+$ fragments of $C_6H_4^+$.[422] Assuming collisional stabilization is the dominant relaxation mechanism for $C_6H_4^+$ cations generated in the ion source through Pathway 1, the lower energy isomers, particularly the global minimum ($\mathbf{A}^+$), are most likely to occur.

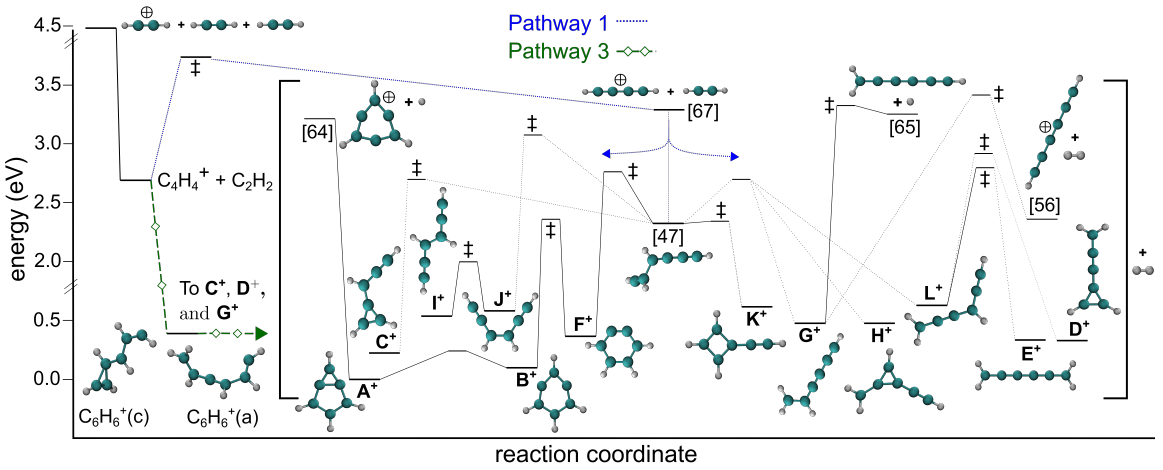

Fig. 6.8 Simplified energy level diagram including calculated stationary points along Pathway 1 (blue dotted lines) and Pathway 3 (green dashed lines with hollow diamonds), with points on the $C_6H_4^+$ potential energy surface embedded within the large brackets. Dotted lines connecting the lowest twelve $C_6H_4^+$ isomers, $\mathbf{A}^+$ - $\mathbf{L}^+$, represent multi-step processes involving intermediates (see Section 6.6.1). Saddle points are indicated by ‡. Energies of all points, calculated at the CCSD(T)/cc-pVTZ//ωB97X-D/aug-cc-pVTZ level, are relative to the energy of $\mathbf{A}^+ + H_2$.

Two $C_6H_6^+$ intermediates were considered for Pathway 3, the first being the acyclic isomer $C_6H_6^+$(a), possibly formed through association of the vinylacetylene cation with neutral acetylene (see Fig. 6.5), and the second being the three-membered ring structure $C_6H_6^+$(c), predicted to result from dissociation of larger acetylene cluster ions (see Fig. 6.6).[377] For both isomers, H-atom shifts are likely necessary to lose H_2, and a number of rearrangements are possible. Not considering other competitive relaxation pathways, these intermediates can easily isomerize and then fragment to $C_6H_4^+$ isomers $\mathbf{C}^+$, $\mathbf{D}^+$, and $\mathbf{G}^+$ (see Figure 6.23 for a possible pathway to $\mathbf{D}^+$).

The stationary points on the $C_6H_4^+$ potential energy surface, embedded within the large brackets in Figure 6.8, help understand the fate of the various isomers following photoexcitation. This is useful for assigning bands to particular isomers in the REPD spectra, as fragmentation may occur following internal conversion of photoexcited $C_6H_4^+$ cations to the ground state manifold. Interestingly, accessing the lowest $C_6H_3^+ + H$ threshold ([64]; 3.18 eV) requires cyclization through isomer $\mathbf{A}^+$, whereas accessing the lowest energy $C_4H_2^+ + C_2H_2$ channel ([67]; 3.29 eV) requires ring-opening through intermediate [47]. Both of these dissociation pathways are barrierless. This suggests that the $C_4H_3^+$ / $C_4H_2^+$ branching ratios should vary for each isomer at near-threshold energies, as fully cyclic $C_6H_4^+$ isomers may prefer the $C_6H_3^+ + H$ channel over the $C_4H_2^+ + C_2H_2$ channel whereas other structures more easily dissociate to $C_4H_2^+ + C_2H_2$.

Stationary points calculated at the CCSD(T)/cc-pVTZ//ωB97X-D/aug-cc-pVTZ level, related to higher-energy reactions along Pathways 2 and 4 that proceed through $C_6H_5^+$ intermediates, are shown in the energy level diagram in Figure 6.9. All energies are relative to the $\mathbf{A}^+ + H_2$ energy, as in Figure 6.8. As previously mentioned, pathways involving dissociation of $C_6H_5^+$ to $C_6H_4^+$ (Pathways 3 and 4) are energetically feasible if the $C_2H_2^+$ precursor is vibrationally hot or electronically excited (see Fig. 6.1), which are likely scenarios in the ion source used in this work.[421,422,442,443]

Calculations predict five different $C_6H_5^+$ adducts, labeled in Figure 6.9 as $C_6H_5^+$(a-d) and (g), occur from the association of $C_4H_3^+$ (protonated diacetylene, PD^+) with acetylene. The $C_6H_4^+$ fragment isomers $\mathbf{D}^+$, $\mathbf{C}^+$, $\mathbf{G}^+$, and $\mathbf{H}^+$, are easily reached through direct, barrierless dissociation of the excited $C_6H_5^+$ adducts. It is noted that the pathway to $\mathbf{E}^+$ from $C_6H_5^+$(c), may require rearrangement on the $C_6H_5^+$ surface to facilitate a change in conjugation to the staggered cumulene fragment.[365]

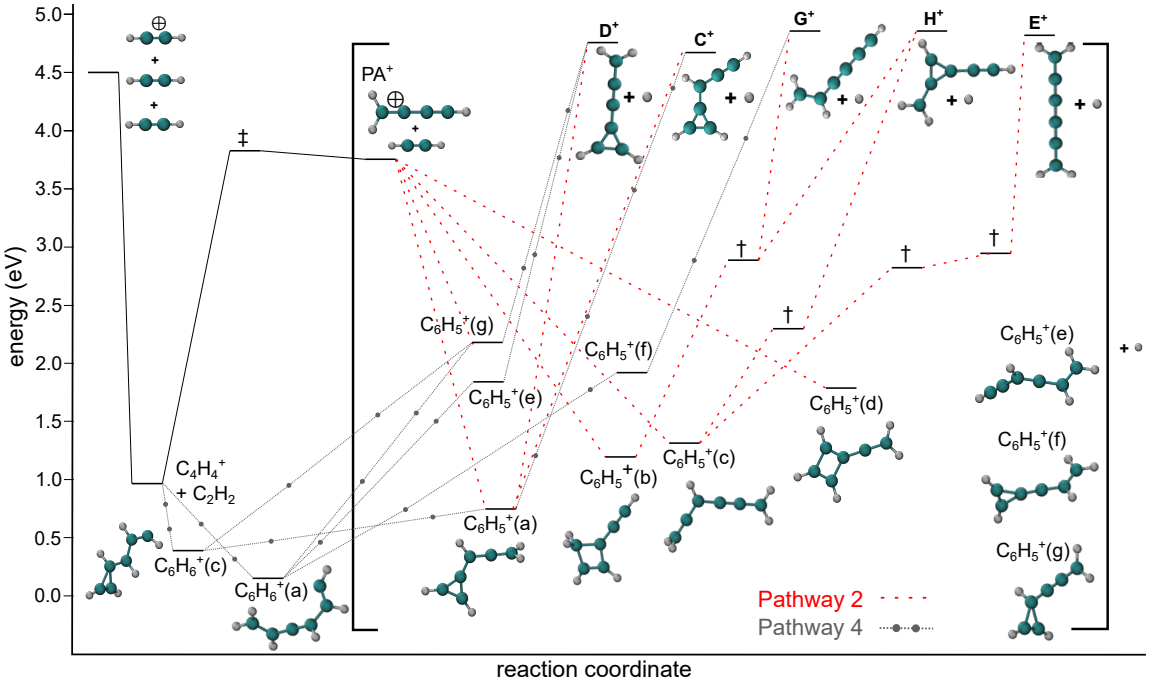

Fig. 6.9 Simplified energy level diagram including calculated stationary points along Pathway 2 (red dashed lines) and Pathway 4 (gray dotted lines with filled circles), with points on the $C_6H_5^+$ potential energy surface embedded within the large brackets. Primary $C_6H_5^+$ isomers are displayed and other higher energy intermediates along dissociation routes are indicated by †. Saddle points are indicated by ‡. Energies of all points are calculated at the CCSD(T)/cc-pVTZ//ωB97X-D/aug-cc-pVTZ level and are relative to $\mathbf{A}^+ + H_2$ for consistency with Figs. 6.1 and 6.8.

6.4.2 REPD spectra

REPD spectra of $C_6H_4^+$-Ar complexes, recorded over the 265-700 nm range by monitoring $C_6H_4^+$ and $C_4H_2^+$ photofragments, are shown in Figures 6.10a and 6.10b, respectively. The spectra are divided into three spectral regions, Region 1 (526-700 nm), Region 2 (375-460 nm), and Region 3 (265-375 nm) that are discussed separately in the following sections. Mass coincidence between $C_6H_4^+$-N_2 and $C_8H_8^+$ ions, which both produce $C_6H_4^+$ photofragments following photoexcitation, complicated measurement of the $C_6H_4^+$-N_2 spectrum at wavelengths below 410 nm, and therefore the spectrum is only presented and discussed in Region 1.

The bare $C_6H_4^+$ ion (tag loss) is the predominant fragment observed from $C_6H_4^+$-Ar and $C_6H_4^+$-N_2 over the 400-700 nm range, with weak $C_4H_2^+$ signal in this region arising from multi-photon processes as confirmed through power dependence measurements. The onset for $C_4H_2^+$ formation (C_2H_2 and tag loss) from single-photon absorption occurs around 426 nm (2.91 eV), with the $C_4H_2^+$ channel dominating at higher energies.

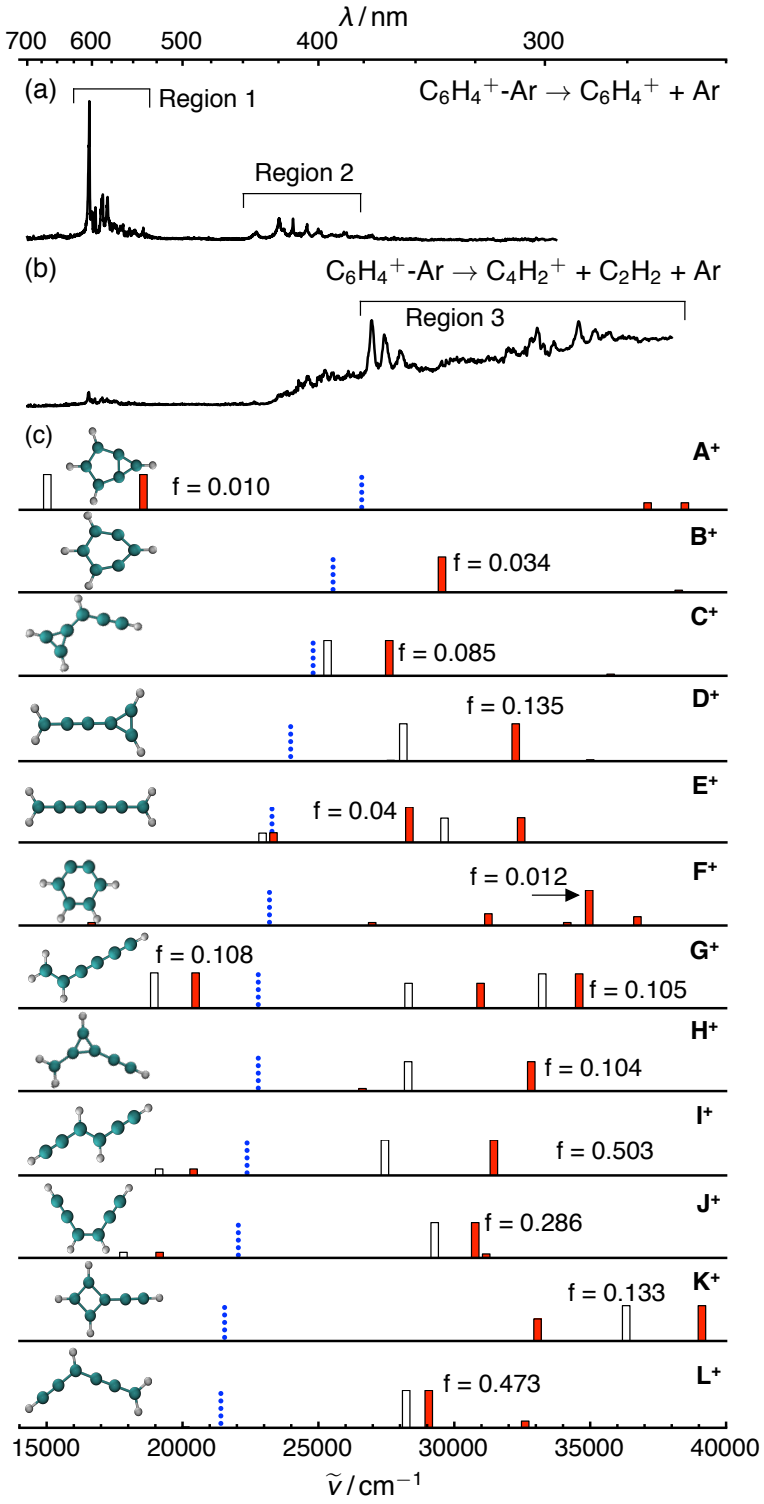

Fig. 6.10 REPD spectra of $C_6H_4^+$-Ar complexes recorded over the 265-700 nm range by monitoring (a) $C_6H_4^+$ and (b) $C_4H_2^+$ photofragments. (c) Predicted vertical (solid bars) and adiabatic (hollow bars) electronic transitions calculated at the TD-DFT ωB97X-D/aug-cc-pVTZ level for isomers $\mathbf{A}^+$ - $\mathbf{L}^+$. Transition energies are unscaled. Intensities are normalized to that of the strongest transition within the range. An adiabatic transition is only displayed if the optimized geometry of the relevant excited electronic state was calculated to have all real vibrational frequencies. Dotted lines correspond to the calculated $C_4H_2^+ + C_2H_2$ dissociation threshold for each isomer.

Spectroscopic identification of $C_6H_4^+$ isomers

Previous band assignments (see Section 6.1.2), quantum chemical calculations, and hole burning experiments are used to identify the $C_6H_4^+$ isomers giving rise to bands in the REPD spectra. Excitation energies and oscillator strengths for electronic transitions over the 200-700 nm range for the twelve lowest energy isomers $\mathbf{A}^+$ - $\mathbf{L}^+$ are depicted in Figure 6.10c. The red bars represent vertical excitation energies and the hollow bars represent adiabatic excitation energies, included only for transitions in which the optimized excited state possessed all real vibrational frequencies. The calculated intensities are normalized to the intensity of the strongest electronic transition for each isomer. The predicted energies and oscillator strengths using TD-DFT are consistent with those previously calculated at other levels of theory, although the energetic ordering of electronic states varies for some isomers.[151,256,261] To help characterize and ensure the correct assignment of the electronic states, molecular orbital information is tabulated in Table 6.5.

TD-DFT calculations predict electronic transitions of isomers $\mathbf{I}^+$, $\mathbf{L}^+$, and $\mathbf{J}^+$ are the strongest among those of the twelve isomers shown in Figure 6.10c, suggesting their bands may be apparent in the REPD spectra even if relatively low quantities of the isomers are stabilized in the ion source. Conversely, the transitions of the benzyne cations, isomers $\mathbf{A}^+$, $\mathbf{B}^+$, and $\mathbf{F}^+$, have the weakest electronic transitions, indicating a substantial population of these ions would be necessary for their bands to be prominent in the spectra. The transitions of isomers $\mathbf{C}^+$, $\mathbf{D}^+$, $\mathbf{K}^+$, $\mathbf{G}^+$, and $\mathbf{H}^+$ are predicted to have intermediate oscillator strengths. Given that the current calculations predict the generation of these isomers is favorable along Pathways 1-4, their transitions may give rise to observable bands.

Region 1. 526-700 nm (1.77 - 2.36 eV)

The spectrum in Region 1 (Figure 6.11c,d) exhibits a series of relatively narrow bands, commencing with an intense band at 604 nm. Excitation of the $C_6H_4^+$-Ar and $C_6H_4^+$-N_2 complexes over this region (1.77-2.36 eV) predominantly generates $C_6H_4^+$ (+ tag) photofragments, with minor $C_4H_2^+$ (+ C_2H_2 + tag) production resulting from multi-photon absorption. The observed photofragments are consistent with the calculated $C_4H_2^+ + C_2H_2$ dissociation energies for isomers $\mathbf{A}^+$ - $\mathbf{L}^+$ (Fig. 6.10c), for which the lowest energy threshold is 2.64 eV. Bands in Region 1 are assigned to the $\tilde{B}^2A'' \leftarrow \tilde{X}^2A''$ and $\tilde{C}^2B_g \leftarrow \tilde{X}^2A_u$ electronic transitions of isomers $\mathbf{G}^+$ and $\mathbf{I}^+$, respectively, based on previous spectroscopic studies, TD-DFT calculations, and HB experiments. The positions and assignments of transitions for $C_6H_4^+$-Ar and $C_6H_4^+$-N_2 in Region 1 are provided in Table 6.2.

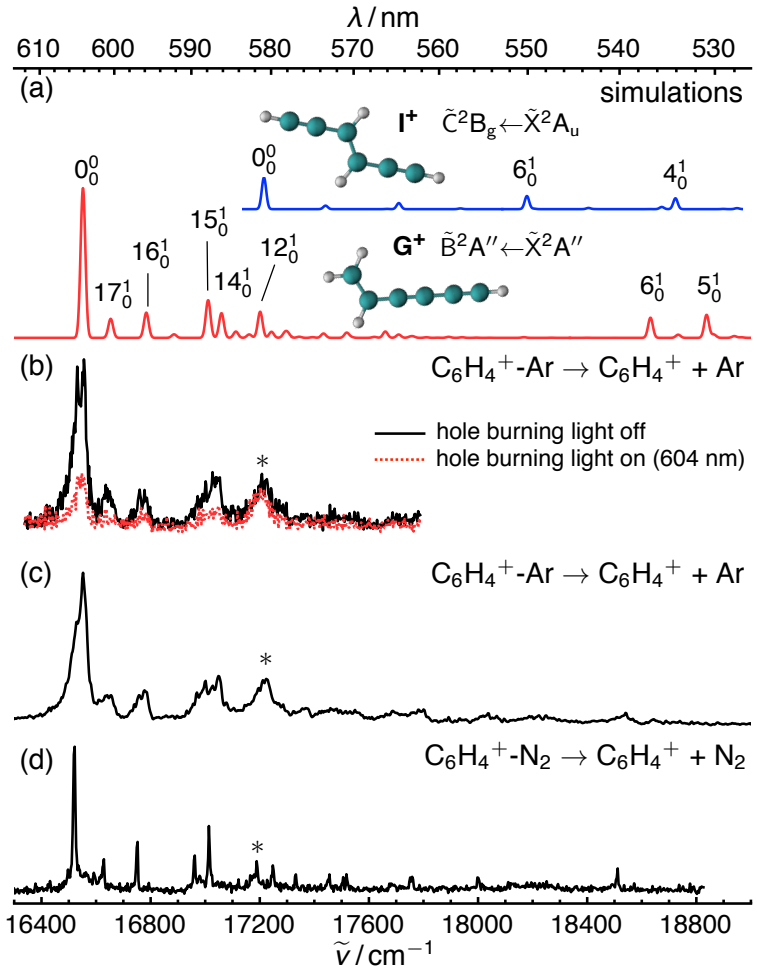

Fig. 6.11 (a) Simulated spectra of the $\tilde{B}^2A'' \leftarrow \tilde{X}^2A''$ transition of isomer $\mathbf{G}^+$ (red trace) and the $\tilde{C}^2B_g \leftarrow \tilde{X}^2A_u$ transition of $\mathbf{I}^+$ (blue trace), generated using TD-DFT calculations at the ωB97X-D/aug-cc-pVTZ level. Excited state vibrational frequencies of both isomers are scaled by 0.957. (b) REPD spectra of $C_6H_4^+$-Ar complexes, recorded in the absence of HB light (black solid trace) and with the HB light tuned to 604 nm (red dotted trace). REPD spectra of (c) $C_6H_4^+$-Ar and (d) $C_6H_4^+$-N_2 complexes recorded by monitoring $C_6H_4^+$ photofragments. The transition of isomer $\mathbf{I}^+$ is indicated by an asterisk.

As described above, the 604 nm band was previously measured in the gas phase using cavity ringdown spectroscopy and assigned to the $\tilde{B}^2A'' \leftarrow \tilde{X}^2A''$ origin transition of isomer $\mathbf{G}^+$ based on *ab initio* calculations and rotational analysis of the spectrum.[254,450] Additional transitions within the band system were recorded in a 6 K neon matrix, with the 12_0^1 transition exhibiting a larger intensity than expected. It was later confirmed, using cavity ringdown spectroscopy, that the 12_0^1 transition of isomer $\mathbf{G}^+$ at 580.93 nm occurs near the $\tilde{C}^2B_g \leftarrow \tilde{X}^2A_u$ origin transition of isomer $\mathbf{I}^+$ at 580.07 nm (see Table 6.1).[255] More recently, vibronic transitions of the two isomers were disentangled by recording several matrix isolation spectra

using different precursors and observing the changes in relative band intensities.[256] The bands were confirmed to belong to vibronic transitions within the $\tilde{B}^2A'' \leftarrow \tilde{X}^2A''$ and $\tilde{C}^2B_g \leftarrow \tilde{X}^2A_u$ band systems of $\mathbf{G}^+$ and $\mathbf{I}^+$ based on calculations at the EOMIP-CCSD/cc-pVDZ level of theory.

Table 6.2 Assignments, positions, and relative positions of bands in REPD spectra of $C_6H_4^+$-Ar and $C_6H_4^+$-N_2 complexes over the 526-700 nm range.

			$C_6H_4^+$-Ar			$C_6H_4^+$-N_2		
isomer	transition	band	λ / nm	$\tilde{\nu}$ / cm^{-1}	$\Delta\tilde{\nu}$ / cm^{-1}	λ / nm	$\tilde{\nu}$ / cm^{-1}	$\Delta\tilde{\nu}$ / cm^{-1}
$\mathbf{G}^+$	$\tilde{B}^2A'' \leftarrow \tilde{X}^2A''$	0_0^0	604.16	16552	0	605.25	16522	0
		17_0^1	600.82	16644	92	601.36	16629	107
		16_0^1	596.02	16778	226	596.94	16752	230
		15_0^1	588.17	17002	450	589.55	16962	440
		14_0^1	586.48	17051	499	587.79	17013	491
		$12_0^1/16_0^1 15_0^1$	581.50	17197	645	582.58	17165	643
		$16_0^1 14_0^1$				579.78	17248	726
		$15_0^1 14_0^1$				572.90	17455	933
		14_0^2	569.83	17549	997	570.84	17518	996
		14_0^3	554.35	18039	1487	555.62	17998	1476
		6_0^1	539.37	18540	1998	540.19	18512	1990
$\mathbf{I}^+$	$\tilde{C}^2B_g \leftarrow \tilde{X}^2A_u$	0_0^0	580.62	17223	0	581.77	17189	0

The first and most intense band in Region 1 of the REPD spectrum occurs at 16552 cm^{-1} (604.16 nm) for $C_6H_4^+$-Ar and 16522 cm^{-1} (605.25 nm) for $C_6H_4^+$-N_2, consistent with the previously measured $\tilde{B}^2A'' \leftarrow \tilde{X}^2A''$ origin transition of isomer $\mathbf{G}^+$ at 16545 cm^{-1} (604.41 nm) in the gas phase.[254,450] The shifts in the origin transitions of the complexes from that of the bare cation are due to the different intermolecular binding energies for the complexes in the ground and excited electronic states (see Chapter 2). The large relative intensity of the origin band suggests that the electronic transition induces minor changes in the geometry of $\mathbf{G}^+$, as predicted by the calculations (see Fig. 6.30 in the SI) which were used to generate the simulated $\tilde{B}^2A'' \leftarrow \tilde{X}^2A''$ spectrum shown in Figure 6.11a (red trace). The simulated spectrum is shifted to align its origin with the 604 nm band in the $C_6H_4^+$-Ar spectrum. Close resemblance between the simulated and REPD spectra demonstrates that the TD-DFT calculations adequately describe the ground and excited electronic states of isomer $\mathbf{G}^+$ and that the bands at $0_0^0 + 226$, $+450$, $+499$, $+645$, and $+1990$ cm^{-1} (596, 588, 586, 582, and 539 nm) arise from the 16_0^1, 15_0^1, 14_0^1, 12_0^1, and 6_0^1 vibronic transitions, respectively, agreeing with the previous assignments made in the neon matrix spectroscopy studies.[254,256,450] The

weak band appearing at $0_0^0 + 92\,\mathrm{cm}^{-1}$ (601 nm), not apparent in previous spectra, corresponds to the 17_0^1 transition involving the lowest frequency a′ bending mode.

To ascertain whether all bands observed in Region 1 arise from transitions of $\mathbf{G}^+$, HB experiments were conducted for $C_6H_4^+$-Ar complexes by tuning the HB light to 604 nm, resonant with the $\tilde{B}^2A'' \leftarrow \tilde{X}^2A''$ origin transition. The Ar-tagged complexes of $\mathbf{G}^+$ photodissociate following exposure to the HB light and the fragments are filtered prior to reaching the electrostatic quadrupole bender. This results in a diminished population of $\mathbf{G}^+$ complexes in the octupole where the molecular beam is exposed to the probe light. The REPD spectra of $C_6H_4^+$-Ar shown in Figure 6.11b were recorded with the HB light on (black solid trace) and off (red dotted trace). The peak at 581 nm appears unaffected by the HB light, signaling that it is due to an isomer other than $\mathbf{G}^+$, presumably $\mathbf{I}^+$ on the basis of previous spectra.[255,256]

TD-DFT calculations predict that the $\tilde{C}^2B_g \leftarrow \tilde{X}^2A_u$ origin transition of isomer $\mathbf{I}^+$ occurs at 519 nm (2.39 eV), agreeing with its appearance at 581 nm (2.13 eV) in the REPD spectrum. Vibronic transitions within the band system are predicted to be much weaker than the origin band based on the simulated spectrum shown in Figure 6.11 (shifted so its origin transition aligns with the 581 nm band in the $C_6H_4^+$-Ar spectrum). This is consistent with the appearance of only weak bands at wavelengths below 581 nm in the REPD spectra and previously measured matrix isolation spectra.[256]

The low intensity of the 581 nm band relative to the 604 nm band indicates that fewer $\mathbf{I}^+$ ions are formed in the ion source than $\mathbf{G}^+$ ions, as the two electronic transitions are predicted to have similar strengths ($f = 0.09$ for the $\tilde{C}^2B_g \leftarrow \tilde{X}^2A_u$ transition of isomer $\mathbf{I}^+$ and $f = 0.11$ for the $\tilde{B}^2A'' \leftarrow \tilde{X}^2A''$ transition of isomer $\mathbf{G}^+$). The predominance of $\mathbf{G}^+$ is rationalized by quantum chemical calculations that predict it lies lower in energy than $\mathbf{I}^+$, and that $\mathbf{G}^+$ is easily formed through acetylene ion-molecule reactions. Along Pathway 1 (Fig. 6.8), the interconversion barriers from intermediate [47] to isomer $\mathbf{G}^+$ are lower than those leading to $\mathbf{I}^+$. In addition, isomer $\mathbf{G}^+$ is predicted to be a direct fragment of the larger $C_6H_6^+$(a) and $C_6H_5^+$(b) intermediates along Pathways 2-4 (Figs. 6.8 and 6.9) whereas interconversion (on the $C_6H_6^+$, $C_6H_5^+$, or $C_6H_4^+$ potential energy surfaces) is necessary to form $\mathbf{I}^+$.

Region 2. 375-460 nm (2.70 - 3.31 eV)

Excitation of $C_6H_4^+$-Ar complexes with light over the 375-460 nm range (Region 2) produces both $C_6H_4^+$ and C4H2+ charged photofragments. Broad bands at 440, 425, and 422 nm and sharper bands at 416, 407, and 400 nm predominantly appear on the $C_6H_4^+$ (+ Ar) channel shown in Figure 6.12c. REPD spectra recorded on both channels ($C_6H_4^+$ and $C_4H_2^+$) were summed together to produce the spectrum shown in Figure 6.12d.

The three sharper bands were previously recorded in a 6 K neon matrix and tentatively ascribed to the $\tilde{B}^2A'' \leftarrow \tilde{X}^2A''$ transition of isomer $\mathbf{C}^+$, based on Franck-Condon factors calculated at the EOMIP-CCSD/cc-pVDZ level.[256] Although the bands coincided with predicted transitions for isomer $\mathbf{C}^+$, it remained unclear whether transitions of the *o*-benzyne cation, isomer $\mathbf{F}^+$, contributed to the bands. Calculations conducted in this work support assignment of the sharper bands at 416, 407, and 400 nm to the $\tilde{B}^2A'' \leftarrow \tilde{X}^2A''$ transition of isomer $\mathbf{C}^+$ as opposed to the nearby $\tilde{F}^2B \leftarrow \tilde{X}^2A$ transition of isomer $\mathbf{F}^+$ which is ≈ 20 times weaker (see Table 6.5 in the SI). The predicted adiabatic excitation energy of 3.14 eV for the $\tilde{B}^2A'' \leftarrow \tilde{X}^2A''$ transition of $\mathbf{C}^+$ corresponds to the energy of the origin band occurring at 416 nm (2.98 eV). As well, the calculated 3.07 eV dissociation energy for the $\mathbf{C}^+$ isomer (see blue dashed arrow in Fig. 6.12d) is consistent with the fact that the three bands appear predominantly on the $C_6H_4^+$ channel (Fig. 6.12c), which indicates that the internal energy of photoexcited $C_6H_4^+$-Ar complexes is not sufficient to generate $C_4H_2^+$ ($+ C_2H_2 + Ar$) fragments.

Based on TD-DFT calculations, the $\tilde{B}^2A'' \leftarrow \tilde{X}^2A''$ electronic transition of $\mathbf{C}^+$ primarily involves promotion of an electron from the HOMO-2 to the HOMO, displayed in Figure 6.13, which induces a 0.11 Å elongation of the C=C bond on the propargyl chain and a 0.04 Å shortening of the adjacent C-C bond connecting the propargyl group to the ring. The band at $0_0^0 + 539\,cm^{-1}$ (407 nm) can be assigned to the 15_0^1 transition while the broad band centered at $0_0^0 + 935\,cm^{-1}$(400 nm) is probably a composite of the 13_0^1, 12_0^1, and 10_0^1 transitions (see relevant vibrational normal modes in Fig. 6.14), based on comparison of the simulated and experimental spectra (Fig. 6.12). These assignments are tabulated in Table 6.3.

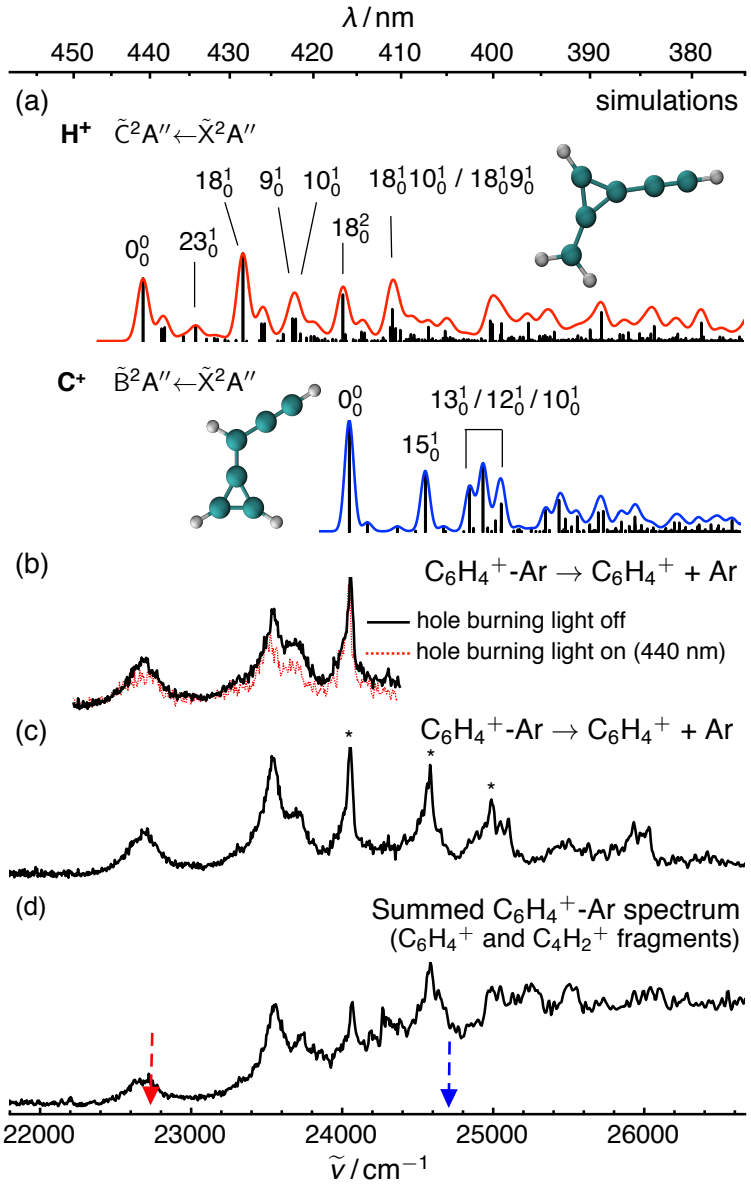

Fig. 6.12 (a) Simulated $\tilde{C}^2A'' \leftarrow \tilde{X}^2A''$ and $\tilde{B}^2A'' \leftarrow \tilde{X}^2A''$ spectra for isomers $\mathbf{H}^+$ and $\mathbf{C}^+$, based on calculations at the PBE1PBE/aug-cc-pVTZ and ωB97X-D/aug-cc-pVTZ levels, respectively. Excited state harmonic vibrational frequencies of both isomers are uniformly scaled by 0.957. (b) REPD spectra of $C_6H_4^+$-Ar complexes, obtained by monitoring $C_6H_4^+$ photofragment signal with the hole burning light off (black traces) and hole burning light on and tuned to 440 nm (red traces). (c) REPD spectrum of $C_6H_4^+$-Ar complexes recorded by monitoring $C_6H_4^+$ photofragments with transitions of $\mathbf{C}^+$ indicated by asterisks. (d) REPD spectrum of $C_6H_4^+$-Ar complexes generated by summing spectra shown in Figs. 6.10a and b. Arrows at 22745 and 24761 cm^{-1} represent calculated $C_4H_2^+ + C_2H_2$ dissociation limits for isomers $\mathbf{H}^+$ and $\mathbf{C}^+$, respectively [CCSD(T)/cc−pVTZ//ωB97X−D/aug−cc−pVTZ level].

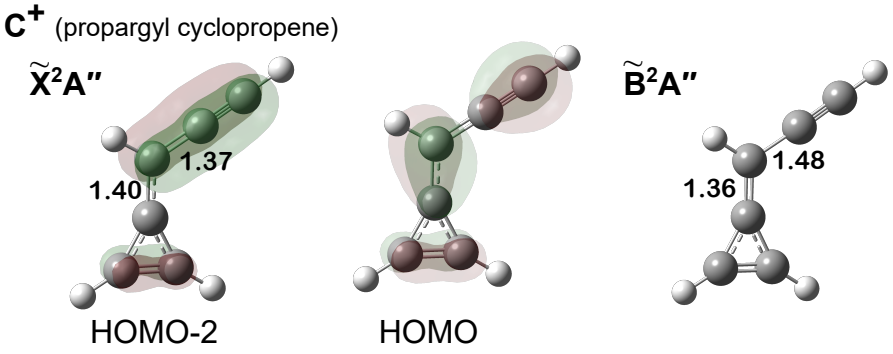

Fig. 6.13 Equilibrium geometries of isomer $\mathbf{C}^+$ in the $\tilde{X}^2A''$ (left) and $\tilde{B}^2A''$ (right) electronic states, calculated at the ωB97X-D/aug-cc-pVTZ level of theory, with bond lengths (Å) for spectroscopically relevant C-C bonds and the HOMO-2 and HOMO of the $\tilde{X}^2A''$ state shown.

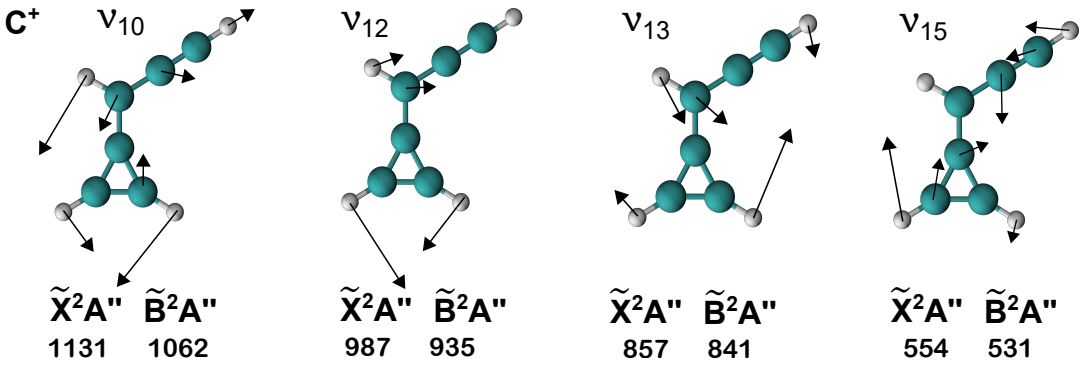

Fig. 6.14 Vibrational normal modes of $C_6H_4^+$ isomer $\mathbf{C}^+$ that include some degree of C-C stretching vibrational motion. Harmonic vibrational frequencies (cm^{-1}) are given for the $\tilde{X}^2A''$ and $\tilde{B}^2A''$ electronic states at the ωB97X-D/aug-cc-pVTZ level of theory.

Table 6.3 Assignments, positions, and relative positions of bands in the REPD spectrum of $C_6H_4^+$-Ar complexes over the 375-460 nm range.

isomer	transition	band	λ / nm	$\tilde{\nu}$ / cm^{-1}	$\Delta\tilde{\nu}$ / cm^{-1}
$\mathbf{H}^+$	$\tilde{C}^2A'' \leftarrow \tilde{X}^2A''$	0_0^0	440.39	22707	0
		18_0^1	424.92	23534	827
		$9_0^1/10_0^1$	421.83	23706	999
$\mathbf{C}^+$	$\tilde{B}^2A'' \leftarrow \tilde{X}^2A''$	0_0^0	415.75	24053	0
		15_0^1	406.80	24582	529
		$13_0^1/12_0^1/10_0^1$	400.19	24988	935

Three broad bands appear at 440, 425, and 422 nm in the REPD spectrum, one of which may correspond with the 423 nm band that was previously recorded in a 6 K neon matrix and could not be assigned.[174] To investigate whether the three bands arise from one isomer, HB experiments were conducted with the HB light tuned to 440 nm. The effect of HB light on the band intensities was assessed by recording REPD spectra, shown in Figure 6.12b, with the HB light off (black solid trace) and then on (red dotted trace). Reduced intensities of the three bands indicate they arise from transitions of one $C_6H_4^+$ isomer ($\mathbf{H}^+$ as argued below) whereas the unaffected 416 nm band arises from another ($\mathbf{C}^+$).

Considering the calculated energies and pathways to formation, the bands at 440, 425, and 422 nm correspond to the $\tilde{C}^2A \leftarrow \tilde{X}^2A''$ transition of isomer $\mathbf{H}^+$. This isomer should have a similar abundance in the ion source as isomer $\mathbf{G}^+$ (Figs. 6.8 and 6.9), and its $\tilde{C}^2A \leftarrow \tilde{X}^2A''$ transition is predicted to have comparable intensity to the $\tilde{B}^2A'' \leftarrow \tilde{X}^2A''$ transition of $\mathbf{G}^+$ whose origin occurs at 604 nm in Region 1. In addition, the calculated $C_4H_2^+ + C_2H_2$ dissociation threshold of 2.82 eV (red dashed arrow in Fig. 6.12d) for the $\mathbf{H}^+$ isomer agrees with the onset of $C_4H_2^+$ photofragments around 426 nm (2.91 eV). The vibronic structure in the spectrum of isomer $\mathbf{H}^+$ is discussed below based on calculated FC factors, focusing on the first three bands at 440 ,425, and 422 nm that appear on the $C_6H_4^+$ channel.

The $\tilde{C}^2A'' \leftarrow \tilde{X}^2A''$ origin transition of isomer $\mathbf{H}^+$ at 440 nm is weaker than the bands at 425 nm and 422 nm, signifying that a substantial change in geometry accompanies photoexcitation. TD-DFT calculations predict that the transition primarily involves HOMO→LUMO excitation (orbitals shown in Figure 6.15), which causes a change in conjugation in the three-membered ring. Optimization of the $\tilde{C}^2A''$ state geometry at the ωB97X-D/aug-cc-pVTZ level failed to converge, possibly because of a shallow potential energy surface associated with ring distortion. However, a minimum was found at the PBE1PBE/aug-cc-pVTZ level with a geometry shown in Fig. 6.15. The PBE1PBE calculations predict that the electronic transition causes the two C-C bonds within the ring to lengthen and the C-H bond to bend 45.7° out of plane.

Based on the calculated geometries and vibrational frequencies of the ground and excited states (see Figures 6.16 and 6.31), vibronic transitions associated with the symmetric C-C ring stretch (ν_9), CH_2 rocking (ν_{10}), and the out-of-plane C-H bending (ν_{18}) modes are expected to have appreciable intensities in the REPD spectrum. The 9_0^1 and 10_0^1 transitions are both predicted to occur near $0_0^0 + 1050\,\mathrm{cm}^{-1}$, supporting their assignments to the band at $0_0^0 + 999\,\mathrm{cm}^{-1}$ (422 nm) in the REPD spectrum. A prominent progression in the ν_{18} C-H out-of-plane bending vibration is predicted with a spacing of $691\,\mathrm{cm}^{-1}$. The calculated intensity of the 18_0^1 transition in the simulated spectrum, shown in Figure 6.12a, agrees with

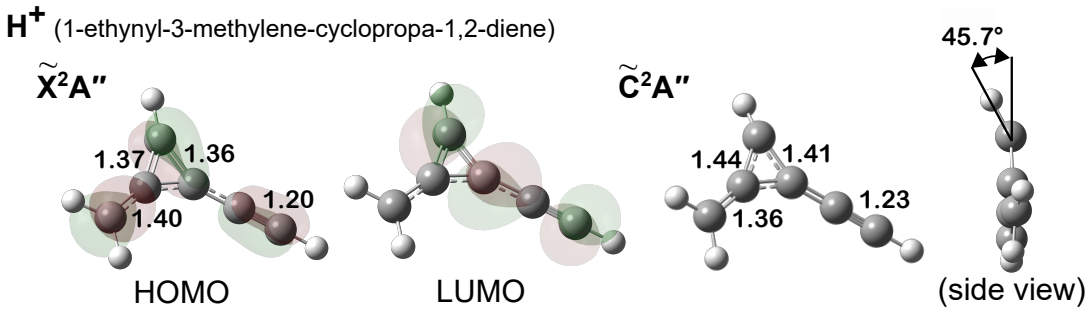

Fig. 6.15 Equilibrium geometries of $C_6H_4^+$ isomer $\mathbf{H}^+$ in its $\tilde{X}^2A''$ and $\tilde{C}^2A''$ electronic states, calculated at the PBE1PBE/aug-cc-pVTZ level of theory, with bond lengths (Å) for spectroscopically relevant C-C bonds and the HOMO and LUMO of the $\tilde{X}^2A''$ state shown.

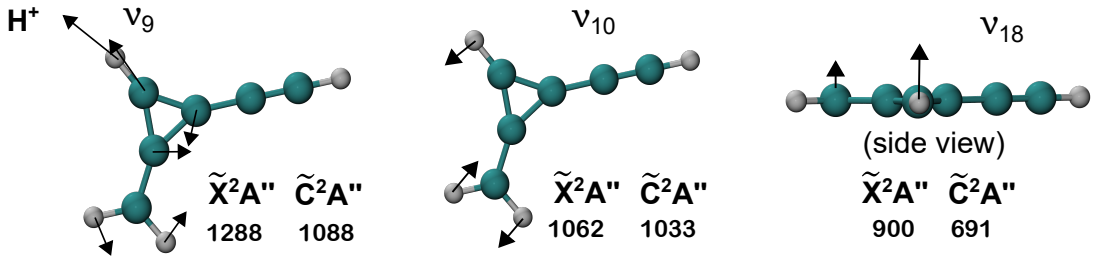

Fig. 6.16 Spectroscopically relevant vibrational normal modes of $C_6H_4^+$ isomer $\mathbf{H}^+$, with harmonic vibrational frequencies (cm^{-1}) for the $\tilde{X}^2A''$ and $\tilde{C}^2A''$ electronic states calculated at the PBE1PBE/aug-cc-pVTZ level of theory.

the intensity of the band at $0_0^0 + 827\,cm^{-1}$ (425 nm) in the REPD spectrum. Assuming the 425 nm band is correctly assigned to the 18_0^1 transition, the calculations underestimate the vibrational frequency for ν_{18} in the $\tilde{C}^2A''$ state by 16 %, which would imply that there is appreciable anharmonicity along the C-H bending coordinate.

Region 3. 265-375 nm (3.31 - 4.68 eV)

Region 3 (265-375 nm) of the REPD spectrum, shown in Figure 6.17b, exhibits four bands near 371 nm followed by several bands below 320 nm that are superimposed on a broad hump that extends for several thousand wavenumbers. The bands below 320 nm were not reported in previous spectroscopic studies of $C_6H_4^+$, and according to the TD-DFT calculations may arise from numerous transitions, including those of isomers $\mathbf{F}^+$, $\mathbf{G}^+$, $\mathbf{D}^+$, and $\mathbf{K}^+$. Confident assignment is currently impossible. Therefore, this section focuses on the 371 nm region. Tentative assignments for these bands are outlined in Table 6.4.

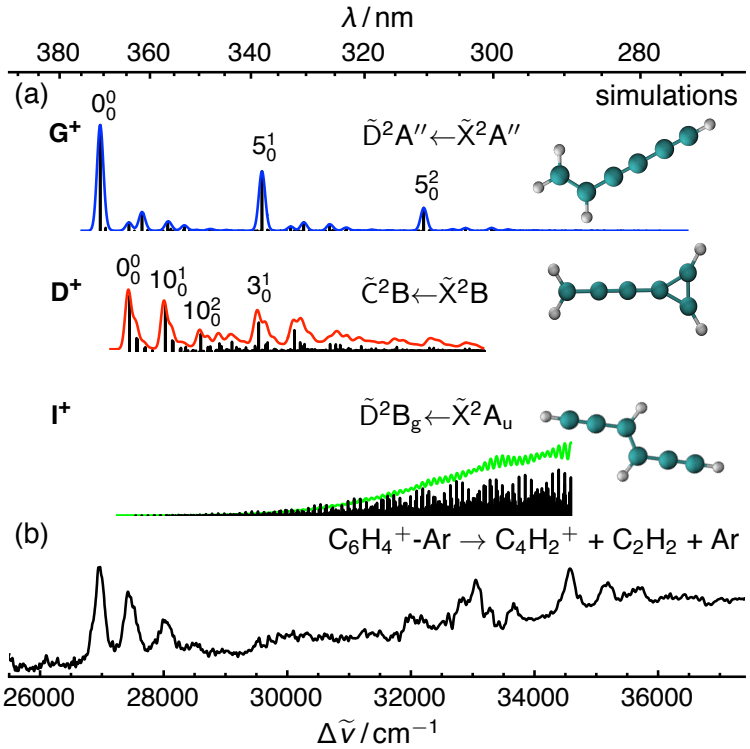

Fig. 6.17 (a) Simulated spectra for the $\tilde{D}^2A'' \leftarrow \tilde{X}^2A''$ transition of $\mathbf{G}^+$ (blue trace), the $\tilde{C}^2B \leftarrow \tilde{X}^2B$ transition of $\mathbf{D}^+$ (red trace), and the $\tilde{D}^2B_g \leftarrow \tilde{X}^2A_u$ transition of $\mathbf{I}^+$ (green trace), generated using TD-DFT calculations at the ωB97X-D/aug-cc-pVTZ level with excited state vibrational frequencies scaled by 0.957. (b) REPD spectra of $C_6H_4^+$-Ar complexes, recorded over the 265-395 nm range by monitoring $C_4H_2^+$ photofragments.

Table 6.4 Tentative assignments (see text), positions, and relative positions for the REPD spectrum of $C_6H_4^+$-Ar complexes over the 265-375 nm range.

isomer	transition	band	λ / nm	$\tilde{\nu}$ / cm^{-1}	$\Delta\tilde{\nu}$ / cm^{-1}
$\mathbf{G}^+$	$\tilde{D}^2A'' \leftarrow \tilde{X}^2A''$	0_0^0	370.75	26972	0
$\mathbf{D}^+$	$\tilde{C}^2B \leftarrow \tilde{X}^2B$	0_0^0	364.62	27426	0
		10_0^1	357.33	27985	559
		10_0^2	350.55	28527	1101

The bands near 371 nm were previously recorded in a 6 K neon matrix and were assigned to the $\mathbf{G}^+$ and $\mathbf{I}^+$ isomers based on calculated electronic transition energies and oscillator strengths.[256] In that study, vibronic transitions of $\mathbf{G}^+$ were distinguished from those of $\mathbf{I}^+$ by recording spectra using various precursors that yielded different relative abundances of the two isomers. Because the changes in the UV band intensities were similar to those observed for the 609 and 585 nm bands, which are known to arise from $\mathbf{G}^+$ and $\mathbf{I}^+$, the

bands at 373, 366, and 359 nm were assigned to vibronic transitions of the two isomers. Photoconversion experiments performed in the study also provided evidence that $\mathbf{I}^+$ absorbs at 373 nm.[256] The intensities of bands at 373 and 585 nm, the latter of which is known to belong to the *trans*-3-hexene-1,5-diyne cation ($\mathbf{I}^+$), increased following exposure of the matrix to 390 nm light. At the same time, the intensities of bands at 385 and 622 nm, corresponding to the *cis* ($\mathbf{J}^+$) conformation of the 3-hexene-1,5-diyne cation, decreased. This *cis*→*trans* photoisomerization was shown to be reversible by exposing the matrix to 375 nm light. Although it is evident that $\mathbf{I}^+$ absorbs at 373 nm, one difficulty is that the calculations conducted in that study predict that the isomer in its $\tilde{D}^2B_g$ electronic state is distorted along the central HCCH dihedral angle, although a progression in the ν_{13} twisting vibrational mode is not prominent in the neon matrix spectrum.

Our TD-DFT calculations agree that the $\tilde{D}^2B_g \leftarrow \tilde{X}^2A_u$ transition of $\mathbf{I}^+$ should appear near 371 nm in the REPD spectrum with an intensity 5 times that of the $\tilde{C}^2B_g \leftarrow \tilde{X}^2A_u$ transition whose origin appears at 581 nm (Region 1). In line with previous calculations accompanying the Ne matrix study,[256] the optimized geometry for the $\tilde{D}^2B_g$ state at the ωB97X-D/aug-cc-pVDZ level is such that $\mathbf{I}^+$ lowers its symmetry from C_{2h} to C_2 upon photoexcitation and has a HCCH dihedral angle of 150° as shown in Figure 6.18. Inspection of the molecular orbitals of isomer $\mathbf{I}^+$ indicates that the $\tilde{D}^2B_g \leftarrow \tilde{X}^2A_u$ (HOMO→LUMO) transition is a $\pi \rightarrow \pi^*$ transition that induces elongation of the central C-C bond (note that TD-DFT calculations predict a similar situation for the *cis* conformer, $\mathbf{J}^+$). The simulated spectrum, generated with C_2 symmetry constraints, is shown in Figure 6.17a with its origin band set to the calculated adiabatic excitation energy (363 nm), although the transition is likely to occur at a wavelength longer than 371 nm based on the neon matrix study.[256] An extended progression in ν_{13}, the HCCH torsional mode, is predicted with a maximum at $0_0^0 + 990\,\mathrm{cm}^{-1}$ (13_0^{10}). Other progressions ($5_0^1 13_0^n$, $9_0^1 13_0^n$, $10_0^1 13_0^n$, $11_0^1 13_0^n$) overlap and give rise to a broad hump that extends for several thousand wavenumbers. This may correspond to the underlying hump in the REPD spectrum upon which the 371, 365, 357, and 351 nm bands are superimposed. The presence of a broad $\tilde{D}^2B_g \leftarrow \tilde{X}^2A_u$ electronic transition of $\mathbf{I}^+$ underneath the resolved bands agrees with previous conclusions of the neon matrix study that $\mathbf{I}^+$ contributes to their intensities.[256] Interestingly, this broad band is not evident at shorter wavelengths in the previous neon matrix spectrum, possibly as a result of *trans*→*cis* photoconversion. Transitions of the *cis* conformer ($\mathbf{J}^+$), observed in the neon matrix spectrum, are not apparent in the REPD spectrum. Ultimately, the peaks at 371, 365, 357, and 351 nm atop the hump must be assigned to another carrier rather than $\mathbf{I}^+$ or $\mathbf{J}^+$.

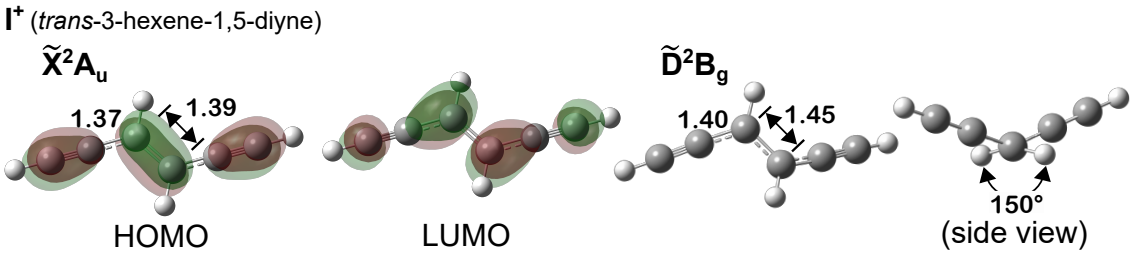

Fig. 6.18 Equilibrium geometries of isomer $\mathbf{I}^+$ in the $\tilde{X}^2A_u$ (left) and $\tilde{D}^2B_g$ (right) electronic states, calculated at the ωB97X-D/aug-cc-pVTZ level of theory, with bond lengths (Å) for spectroscopically relevant C-C bonds and the HOMO and LUMO of the $\tilde{X}^2A_u$ state shown.

On the basis of available evidence, the 371 nm system possibly arises from isomer $\mathbf{G}^+$.[256] TD-DFT calculations predict that the $\tilde{D}^2A'' \leftarrow \tilde{X}^2A''$ adiabatic electronic transition of $\mathbf{G}^+$ occurs at 351 nm (3.53 eV), with an oscillator strength approximately 70% that of the isomer's $\tilde{B}^2A'' \leftarrow \tilde{X}^2A''$ transition in Region 1. The simulated spectrum, represented by the blue trace in Figure 6.17a, is set to align its origin band with the 371 nm (3.34 eV) band in the REPD spectrum based on the assignment made in the previous matrix isolation study.[256] Aside from the origin transition, the 5_0^1 transition, involving an a′ C-C stretching vibration, is the only transition predicted to have appreciable intensity. However, no clear band is apparent in the REPD spectrum near its predicted wavelength of 337 nm ($0_0^0 + 2736\,\mathrm{cm}^{-1}$). The bands at 365 and 357 nm in the REPD spectrum are also not predicted by spectral simulations for $\mathbf{G}^+$, suggesting that either the calculations poorly characterize this transition or that another isomer gives rise to bands in this region of the spectrum. Due to the restricted wavelength range of the HB light source, HB experiments could not be conducted to ascertain whether the 371, 365, 357, and 351 nm bands arise from the same isomer.

Another isomer possibly associated with one or more of the 371, 365, 357, and 351 nm bands is the propadienylidene cyclopropene cation ($\mathbf{D}^+$), an isomer not considered in previous spectroscopic studies. The likely formation of $\mathbf{D}^+$ and its detectability are supported by its relatively low calculated energy (Fig. 6.8) and the reasonably large oscillator strength ($f = 0.135$) of the $\tilde{C}^2B \leftarrow \tilde{X}^2B$ transition (HOMO→LUMO excitation). The calculated adiabatic excitation energy of 3.49 eV coincides with bands occurring between 371-355 nm (3.34-3.50 eV). A short progression in ν_{10}, the lowest frequency C-C stretching vibration, is predicted to arise due to a 0.04 Å shortening of the central C-C bond connecting the ring to the propargylic chain. The predicted spacings and intensities of the 0_0^0, 10_0^1 ($0_0^0 + 577\,\mathrm{cm}^{-1}$), and 10_0^2 ($0_0^0 + 1164\,\mathrm{cm}^{-1}$) transitions, shown in red in Figure 6.17d, match the bands observed in the REPD spectrum at 365 nm, 357 nm ($0_0^0 + 599\,\mathrm{cm}^{-1}$) and 351 nm ($0_0^0 + 1101\,\mathrm{cm}^{-1}$). The

3_0^1 transition, involving the symmetric C≡C stretch of the propargylic chain, is predicted to occur at 339 nm ($0_0^0 + 2185\,cm^{-1}$) although no clear band is apparent in the REPD spectrum.

6.5 Conclusions

In summary, REPD spectra of Ar- and N_2-tagged $C_6H_4^+$ cations, generated through ion-molecule reactions of acetylene, have been recorded over the 265-700 nm range by monitoring $C_6H_4^+$ and $C_4H_2^+$ photofragments. Quantum chemical calculations for isomer energies and interconversion barriers were conducted to predict which isomers were likely to be generated in the ion source. The $C_4H_2^+ + C_2H_2$ reaction can form several isomers through low interconversion barriers on the $C_6H_4^+$ potential energy surface. At higher energies, other pathways to $C_6H_4^+$ are accessible, including the association reaction between protonated diacetylene ($C_4H_3^+$) and C_2H_2 to generate $C_6H_5^+$ adducts that have sufficient internal energy to cleave a C-H bond. Additional possible sources of $C_6H_4^+$ include the formation and fragmentation of energized $C_6H_6^+$ cations. The calculated ground state dissociation thresholds for $C_6H_4^+$ isomers agree with the detection of $C_4H_2^+ + C_2H_2 + Ar$ photofragments following photoexcitation of $C_6H_4^+$-Ar complexes at wavelengths below 426 nm (2.91 eV).

Electronic transitions were assigned based on previous spectroscopic studies,[206,255,256] hole burning experiments, ground state DFT calculations, and excited state TD-DFT calculations for the twelve lowest energy isomers. The spectra were considered over three distinct ranges, Region 1 (526-700 nm), Region 2 (375-460 nm), and Region 3 (265-375 nm). In Region 1, the REPD spectra are similar to previously recorded spectra of $C_6H_4^+$ ions embedded in Ar and Ne matrices.[206,255,256] The $\tilde{B}^2A''\leftarrow\tilde{X}^2A''$ electronic transition of the 1-hexene-3,5-diyne cation ($\mathbf{G}^+$), commencing at 604 nm, is matched by spectral simulations generated from TD-DFT calculations. A weak band appearing $92\,cm^{-1}$ above the $\tilde{B}^2A''\leftarrow\tilde{X}^2A''$ origin transition, not apparent in previous spectra, has been assigned to the 17_0^1 transition based on the spectral simulations. Hole burning experiments confirmed that the $\tilde{C}^2B_g\leftarrow\tilde{X}^2A_u$ electronic transition of the *trans*-3-hexene-1,5-diyne cation ($\mathbf{I}^+$) contributes intensity to the weak 581 nm band.

The $\tilde{B}^2A''\leftarrow\tilde{X}^2A''$ electronic transition of the propargyl cyclopropene cation ($\mathbf{C}^+$) gives rise to sharp bands at 416, 407, and 400 nm in Region 2 of the $C_6H_4^+$-Ar spectrum. The bands are reproduced by spectral simulations, which support the tentative assignments made for these bands in the previous neon matrix study.[256] The REPD spectrum in this region also exhibits three broad bands at 440, 425, and 422 nm, one of which may correspond to a

band at 423 nm in the Ne matrix that could not be assigned.[256] Hole burning experiments confirmed that the three bands arise from a single isomer. The bands were assigned to the $\tilde{C}^2A''\leftarrow\tilde{X}^2A''$ electronic transition of the 1-ethynyl-3-methylene-cyclopropa-1,2-diene cation ($\mathbf{H}^+$) based on the calculated energies and agreement with spectral simulations.

Region 3 of the REPD spectrum exhibits several bands appearing atop a broad hump. The first three bands at 371, 365, and 357 nm were previously observed in the neon matrix spectrum and assigned to transitions of the $\mathbf{G}^+$ and $\mathbf{I}^+$ isomers.[256] In light of the ground state and TD-DFT calculations conducted in this work, a third isomer, the propadienylidene cyclopropene cation ($\mathbf{D}^+$), may also contribute to these bands. Our calculations support the previous assignment of the 371 nm band (373 nm in the neon matrix spectrum) to the $\tilde{D}^2A''\leftarrow\tilde{X}^2A''$ origin transition of $\mathbf{G}^+$.[256] The 365 and 357 nm bands are tentatively reassigned to the $\tilde{C}^2B\leftarrow\tilde{X}^2B$ electronic transition of $\mathbf{D}^+$ and the underlying band is postulated to be due to the $\tilde{D}^2B_g\leftarrow\tilde{X}^2A_u$ electronic transition of $\mathbf{I}^+$, which calculations predict undergoes a reduction in symmetry from lower to upper state. Although these tentative assignments in Region 3 differ from those made in the previous work,[256] they support the conclusion that the $\mathbf{G}^+$ and $\mathbf{I}^+$ isomers contribute to the 371, 365, and 357 nm bands. Ultimately, better spectra and hole burning experiments are necessary to assign the transitions in Region 3.

The recorded gas-phase spectra of $C_6H_4{}^+$ cations may be compared with astronomical spectra to facilitate their detection in remote environments. It is hoped that the measured spectra and calculated transition energies and oscillator strengths guide future sophisticated investigations, in particular with regard to transitions in Region 3 that are difficult to interpret using the available resources. Ion mobility mass spectrometry coupled with laser spectroscopy, for instance, would enable direct observation of different $C_6H_4{}^+$ isomers that can then be separated and individually probed to record isomer-selected electronic spectra.

6.6 Supporting information (SI)

This section includes additional computational data related to the interpretation of measured REPD spectra. It is organized as follows: supporting information for ground state calculations (Section 6.6.1), electronic transition properties (6.6.2), and harmonic vibrational frequencies and bond lengths for relevant isomers in the ground and excited electronic states (6.6.3).

6.6.1 Additional information on ground state calculations

Optimized ground state geometries of the twelve lowest energy $C_6H_4^+$ isomers

A previous computational investigation compared the relative energies of several $C_6H_4^+$ isomers predicted at different levels of theory. Figure 6.19 compares the equilibrium geometries calculated in this study at the ωB97X-D/aug-cc-pVTZ level with geometries calculated at higher levels of theory, including the CCSD(T)/cc-pVTZ level which was judged to be reliable.[151] For isomer $\mathbf{F}^+$, the geometry is compared to the geometry calculated at the CASPT2(9,10)/cc-pVDZ level.[261]

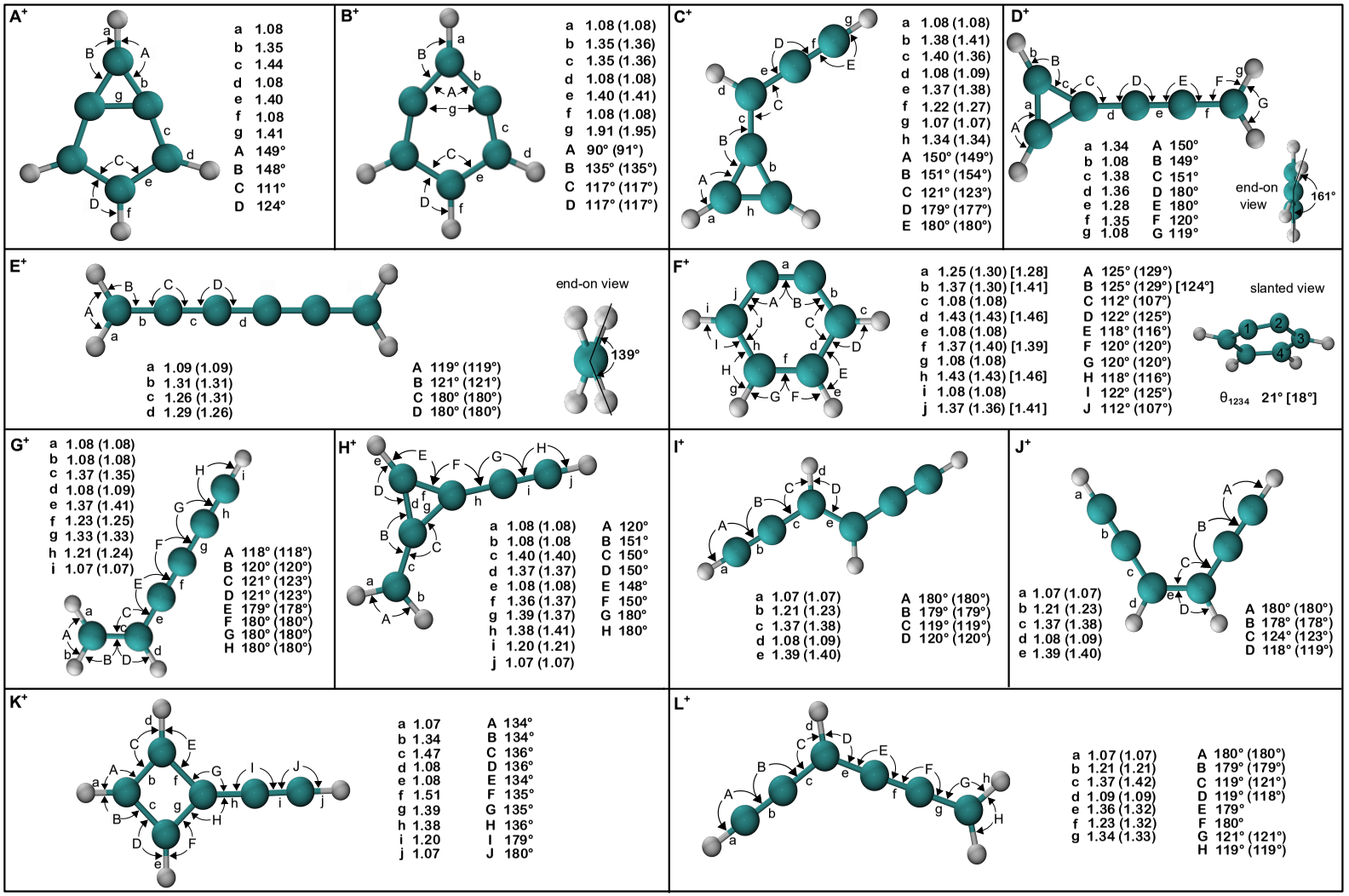

Fig. 6.19 Bond lengths (Å) and angles (degrees) for $C_6H_4^+$ isomers $\mathbf{A}^+$-$\mathbf{L}^+$ calculated at the ωB97X-D/aug-cc-pVTZ level, the (CCST(T)/cc-pVTZ level) from ref. 151, and the [CASPT2(9,10)/cc-pVDZ level] from 261.

Calculated stationary points on the ground state $C_6H_4^+$ potential energy surface

To predict the stability of low-energy $C_6H_4^+$ isomers and their dissociation energies and mechanisms, stationary points on the ground state $C_6H_4^+$ potential energy surface were calculated at the CCSD(T)/cc-pVTZ//ωB97X-D/aug-cc-pVTZ level of theory. Several low energy isomerization and dissociation pathways are shown in Figure 6.20. Geometries and energies associated with stationary points are provided in Figures 6.21 and 6.22.

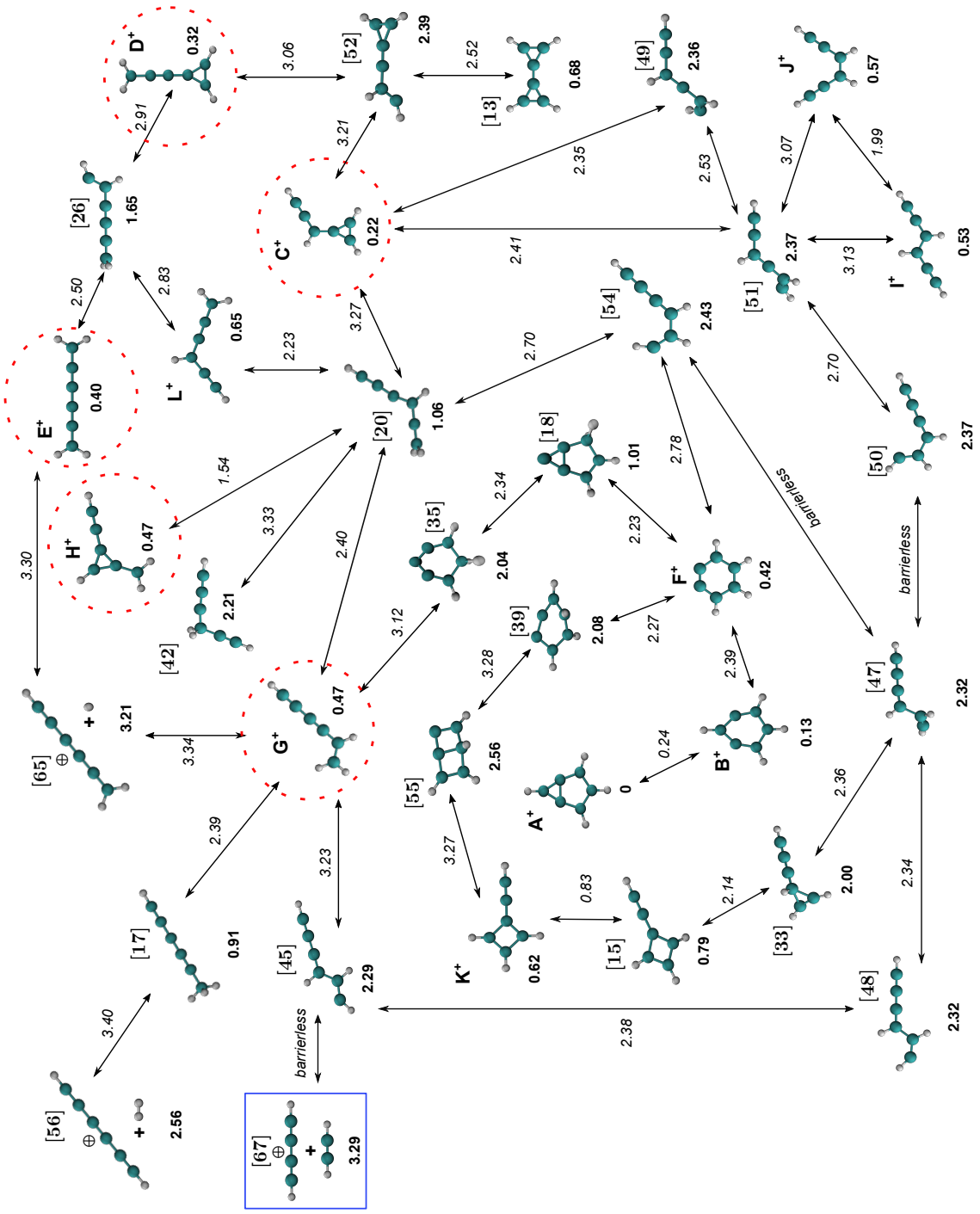

Fig. 6.20 Energies and geometries associated with stationary points on the ground state $C_6H_4^+$ potential energy surface, calculated at the CCSD(T)/cc-pVTZ//ωB97X-D/aug-cc-pVTZ level of theory. Energies (saddle points in italics and minima in bolded font) are relative to the $C_6H_4^+$ global minimum, isomer **A+**. Stationary point [67] (boxed) is the entry point for Pathway 1. Isomers encircled by dotted red lines are calculated to be favorable through Pathway 2. See complementary Figures 6.21 and 6.22.

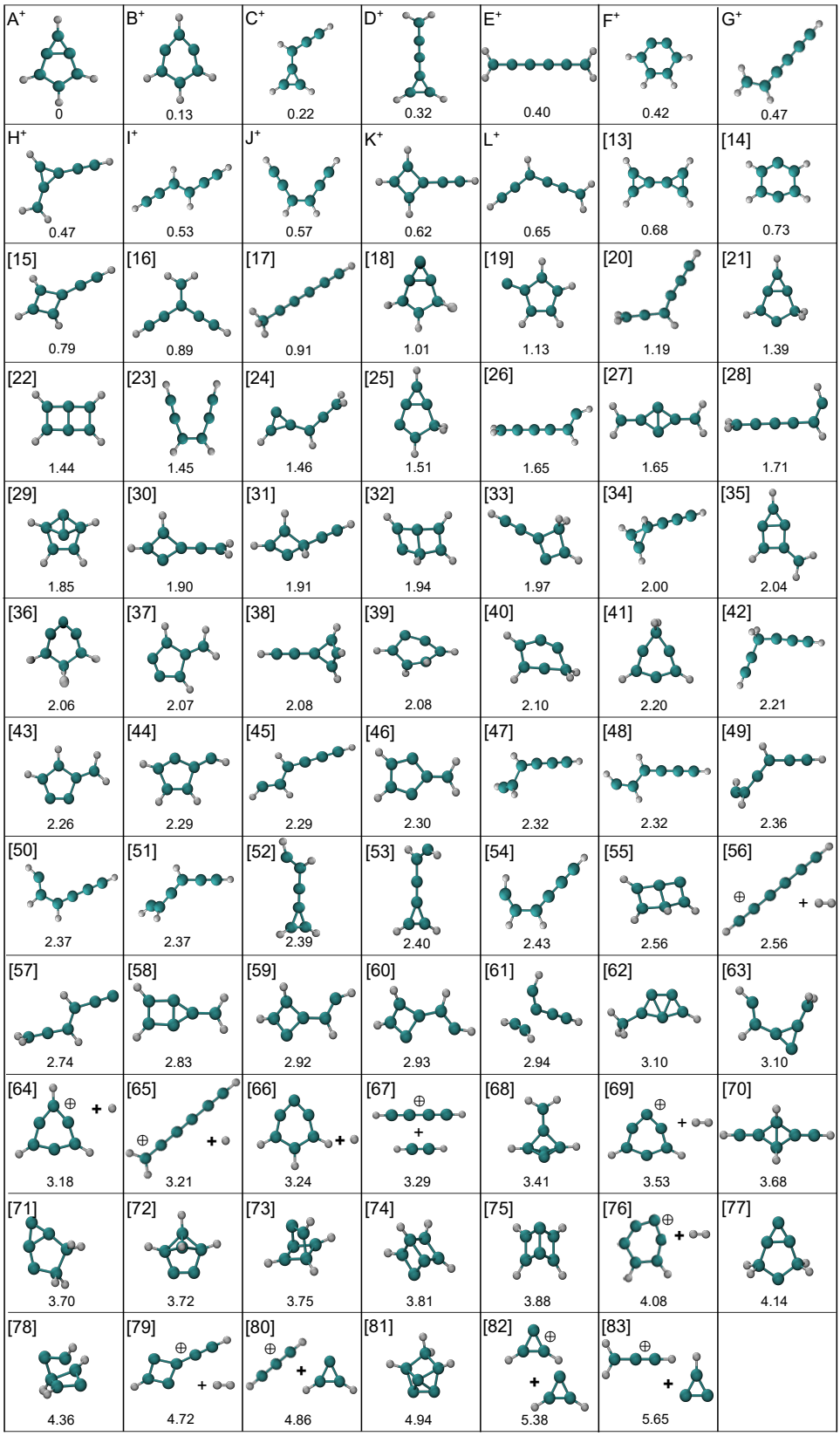

Fig. 6.21 Calculated structures and energies (eV), relative to the global minimum $\mathbf{A}^+$, of minima on the $C_6H_4^+$ potential energy surface. Structures were calculated at the ωB97X-D/aug-cc-pVTZ level and energies were derived from CCSD(T)/cc-pVTZ single point energies and ωB97X-D/aug-cc-pVTZ vibrational zero point energies.

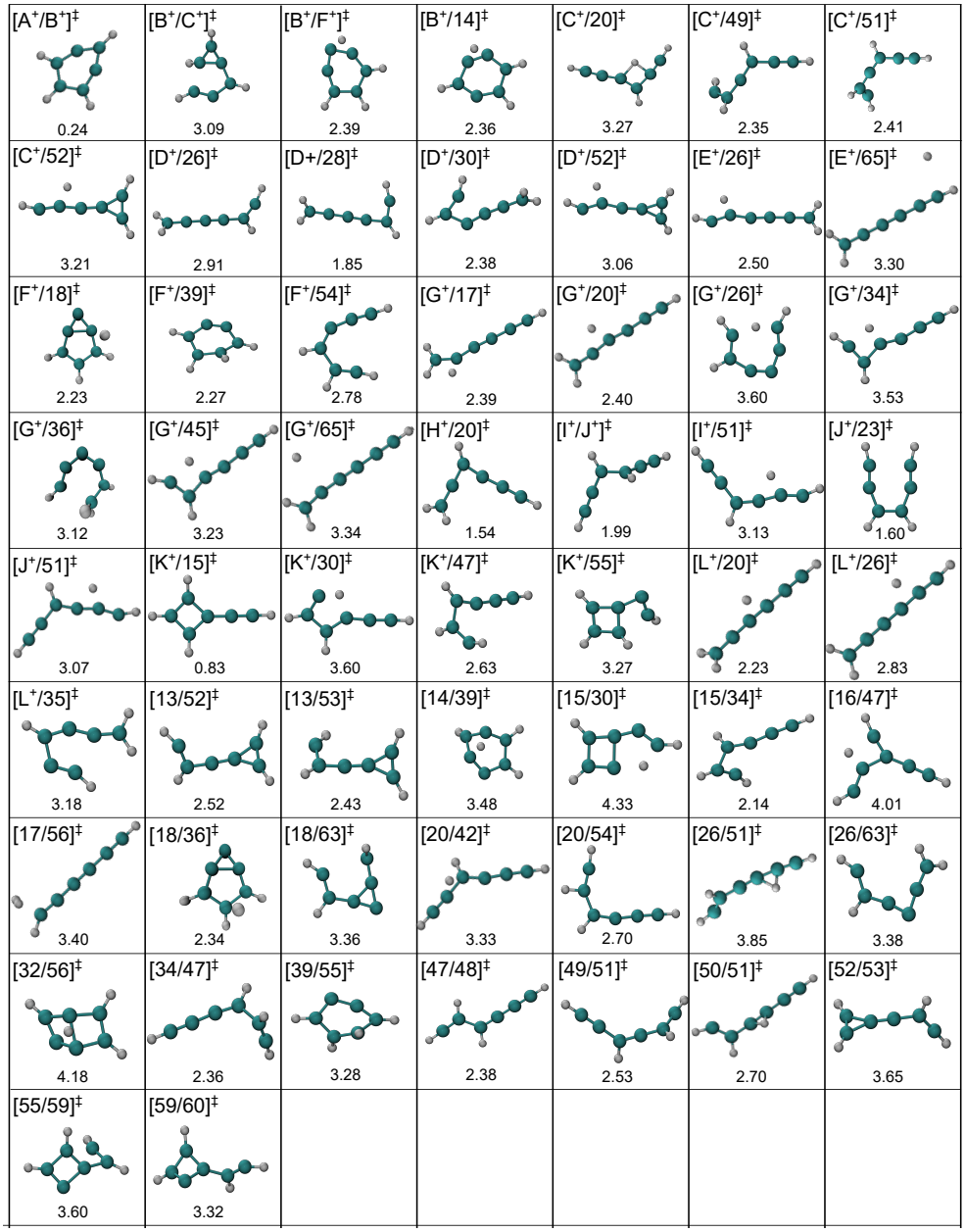

Fig. 6.22 Calculated structures and energies (eV), relative to the global minimum $\mathbf{A}^+$, of saddle points on the $C_6H_4^+$ potential energy surface. Structures were calculated at the ωB97X-D/aug-cc-pVTZ level and energies were derived from CCSD(T)/cc-pVTZ single point energies and ωB97X-D/aug-cc-pVTZ vibrational zero point energies.

Additional calculations related to Pathway 3

The $C_4H_4^+$ intermediate, formed from the association of $C_2H_2^+$ with C_2H_2, can transfer excess energy to Ar atoms leading to collisional stabilization. Subsequent reaction with C_2H_2 results in formation of excited $C_6H_6^{+*}$ ions, which are predicted by calculations to have three-membered rings or be acyclic. One possible mechanism to form isomer $\mathbf{D}^+ + H_2$ from a high-energy $C_6H_6^+$ adduct is shown in Figure 6.23.

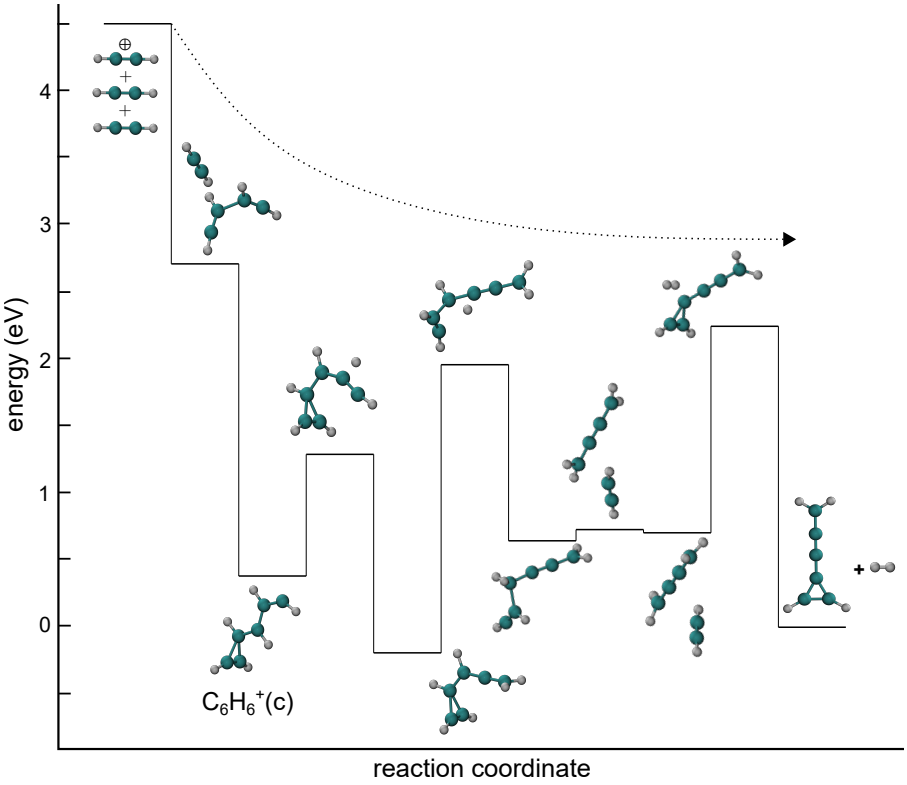

Fig. 6.23 Possible acetylene ion-molecule reaction pathway, involving a high energy $C_6H_6^+$ isomer $C_6H_6^+$(c), to $C_6H_4^+$ isomer $\mathbf{D}^+ + H_2$, calculated at the CCSD(T)/cc-pVTZ//ωB97X-D/aug-cc-pVTZ level of theory.

Other dissociation channels

Regardless of the $C_6H_4^+$ structure, the lowest energy $C_6H_2^+ + H_2$ formation pathway is predicted to proceed through a common intermediate, the methyl chain isomer, $H_3C_6H^+$ (isomer [17] in 6.21), that is accessible from $\mathbf{G}^+$ through 1,2-hydrogen transfer. The dissociation barrier, represented by $[17/56]^\dagger$ in Figure 6.20, lies 3.40 eV above the global minimum, indicating that the $C_6H_2^+ + H_2$ channel is less favorable than the $C_4H_2^+ + C_2H_2$

channel lying at 3.29 eV. Although no bands were observed in REPD spectra recorded by monitoring $C_6H_2^+$ photofragments over the 410-350 nm range, it is likely that the $C_6H_2^+ + H_2$ channel becomes more favorable at higher energy.

Several low energy $C_6H_3^+ + H$ formation pathways are predicted, owing to the stability of several cyclic and linear $C_6H_3^+$ isomers that lie within ≈ 0.17 eV of one another.[453] The lowest energy mechanism is barrierless, requiring 3.18 eV, and involves the formation of the cyclic $C_6H_3^+$ global minimum ([64] in Fig. 6.8) through H loss from *m*-benzyne isomers $\mathbf{A}^+$ and $\mathbf{B}^+$. Another barrierless pathway, lying slightly higher in energy (3.21 eV), involves H loss from isomer $\mathbf{G}^+$ to form the linear protonated triacetylene cation ($H_2C_6H^+$; [65] in Fig. 6.8). Based on the calculated energies, it is possible that $C_6H_3^+ + H + Ar$ photofragments are formed following photoexcitation of $C_6H_4^+$-Ar complexes over the 373-440 nm range. At higher energies, the $C_4H_2^+ + C_2H_2 + Ar$ channel is dominant and $C_6H_3^+ + H + Ar$ formation is less likely.

Geometries and binding energies of $C_6H_4^+$-Ar and $C_6H_4^+$-N_2 complexes

Calculations of $C_6H_4^+$-Ar and $C_6H_4^+$-N_2 complexes were conducted at the ωB97X-D/aug-cc-pVTZ level to understand the interaction between the Ar or N_2 tag with the $C_6H_4^+$ chromophore. The geometries and binding energies, accounting for basis set superposition errors (BSSE), for several complexes are provided in Figures 6.24-6.27. The ωB97X-D/aug-cc-pVTZ level of theory includes dispersion corrections and has been previously used to characterize non-covalent interactions involving small carbocations.[454–456]

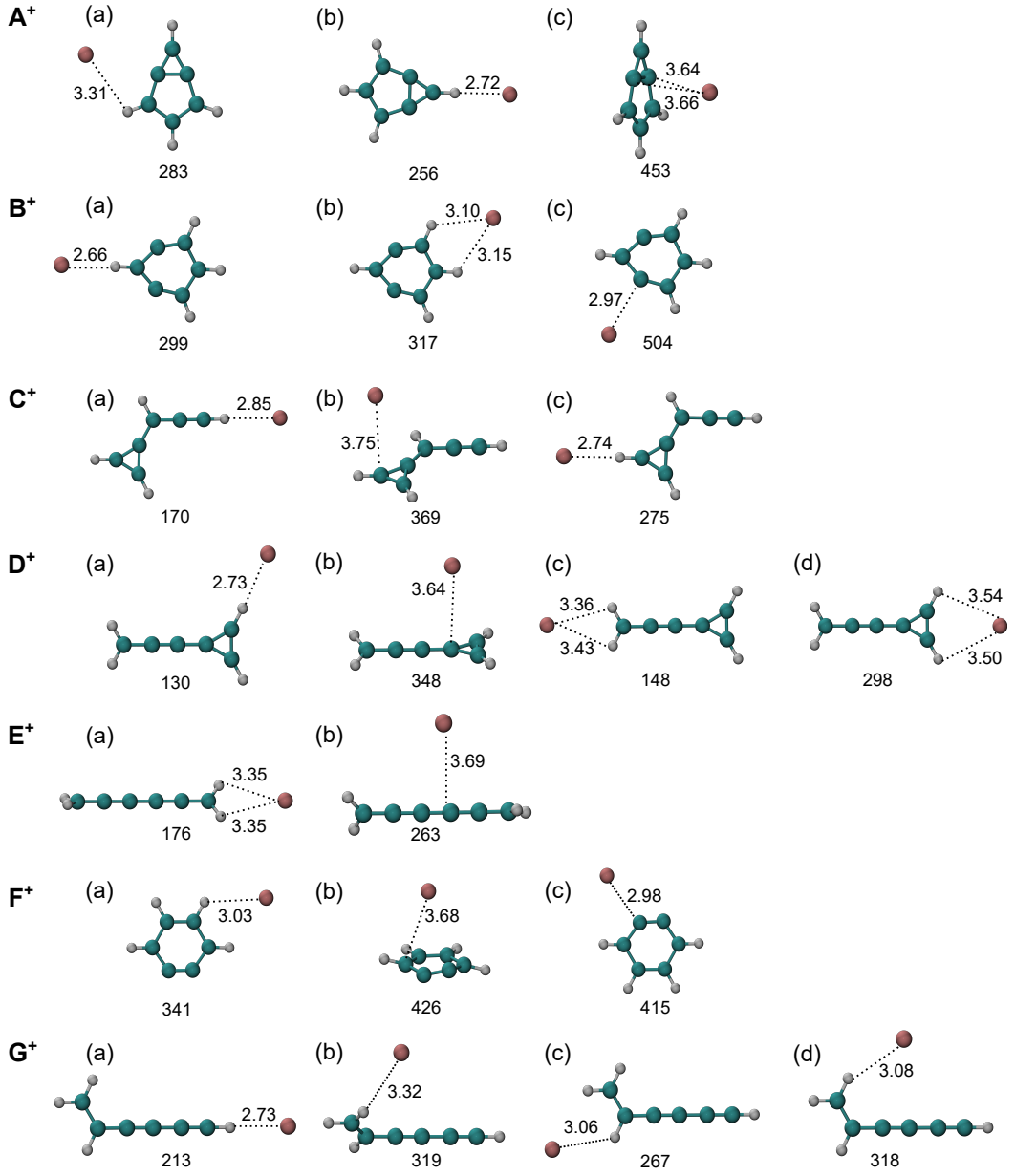

Fig. 6.24 Structures and binding energies (cm^{-1}) of Ar-tagged complexes of isomers $\mathbf{A}^+$-$\mathbf{G}^+$, calculated at the ωB97X-D/aug-cc-pVTZ level of theory. Binding energies include vibrational zero point energies and corrections that account for basis set superposition errors (BSSE).

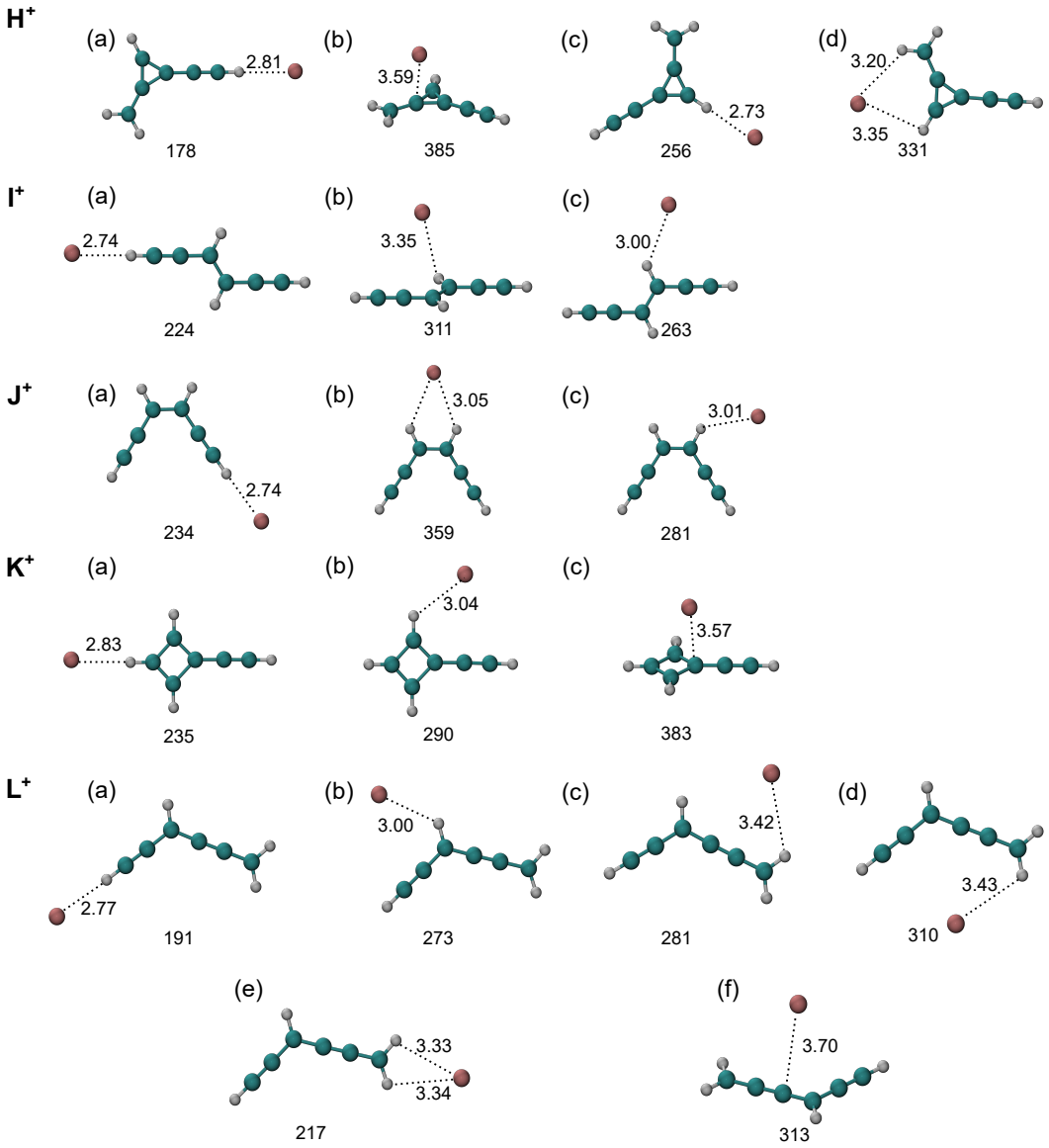

Fig. 6.25 Structures and binding energies (cm^{-1}) of Ar-tagged complexes of isomers $\mathbf{H}^+$-$\mathbf{L}^+$ calculated at the ωB97X-D/aug-cc-pVTZ level of theory. Binding energies include vibrational zero point energies and corrections that account for basis set superposition errors (BSSE).

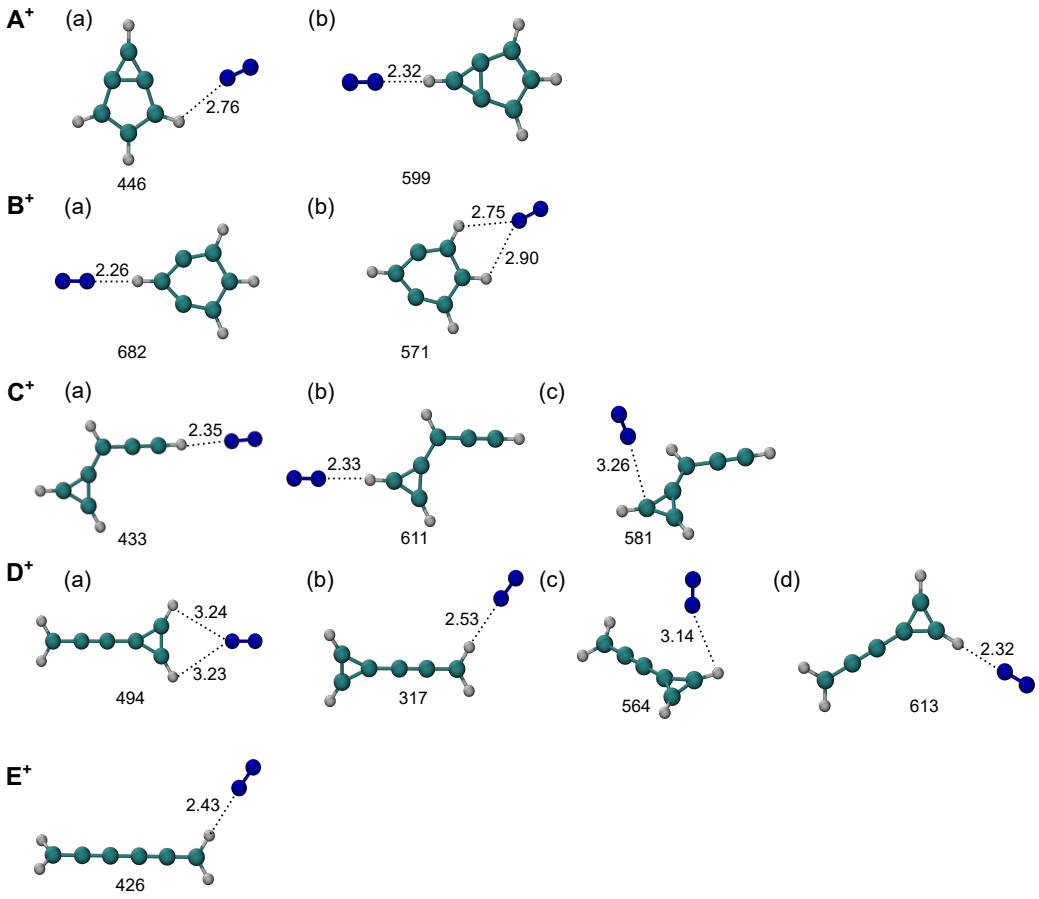

Fig. 6.26 Structures and binding energies (cm^{-1}) of N_2-tagged complexes of isomers $\mathbf{A}^+$-$\mathbf{E}^+$ calculated at the ωB97X-D/aug-cc-pVTZ level of theory. Binding energies include vibrational zero point energies and corrections that account for basis set superposition errors (BSSE).

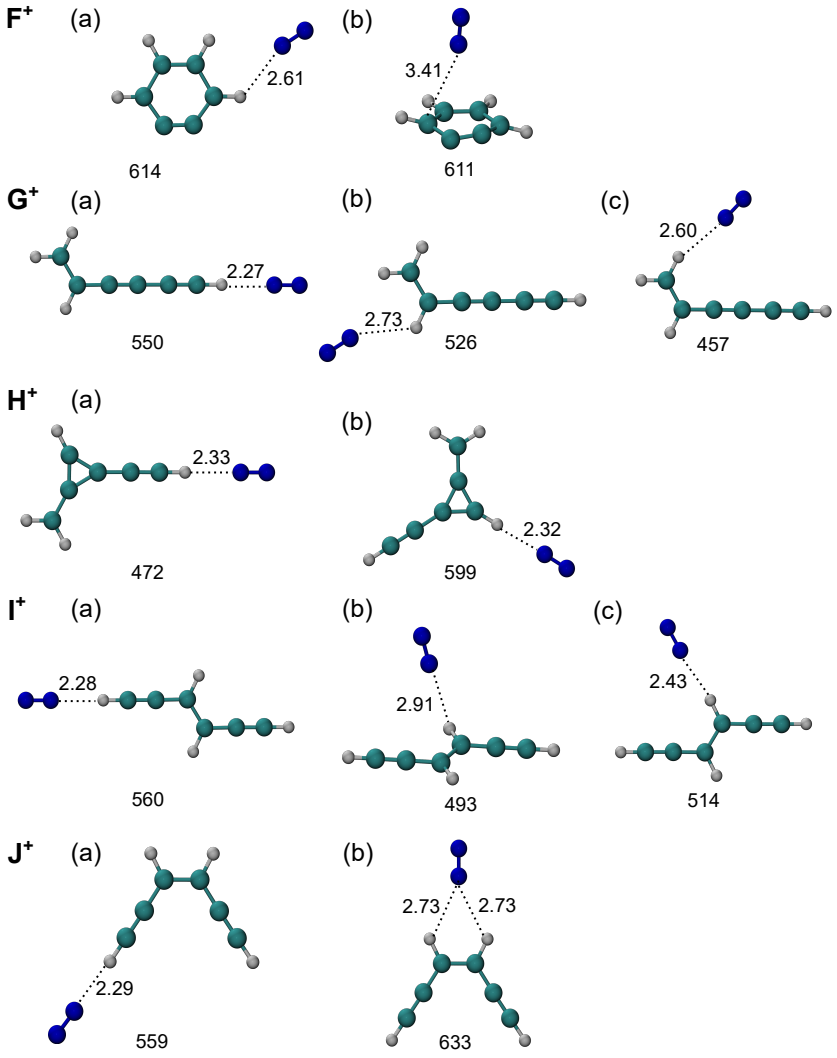

Fig. 6.27 Structures and binding energies (cm^{-1}) of N_2-tagged complexes of isomers $\mathbf{F}^+$-$\mathbf{J}^+$ calculated at the ωB97X-D/aug-cc-pVTZ level of theory. Binding energies include vibrational zero point energies and corrections that account for basis set superposition errors (BSSE).

6.6.2 Electronic transitions and excited state calculations

Energies and oscillator strengths associated with electronic transitions of $C_6H_4^+$ isomers, calculated using TD-DFT at the ωB97X-D/aug-cc-pVTZ level, are consistent with those previously calculated at different levels of theory.[151,256] Electronic states of each $C_6H_4^+$ isomer are described using the $\tilde{X}^2\Gamma$, $\tilde{A}^2\Gamma$, $\tilde{B}^2\Gamma$, ... notation in order of increasing energy, with $\tilde{X}^2\Gamma$ corresponding to the ground electronic state with Γ symmetry. To facilitate comparison

of TD-DFT predictions with those obtained using other approaches, Table 6.5 includes transition energies, oscillator strengths, and molecular orbitals predicted to be involved in electronic transitions. In the table, orbital 20, the highest occupied molecular orbital (HOMO), is singly occupied for all $C_6H_4^+$ radical cations.

Table 6.5 Vertical (E_{vert}) and adiabatic (E_{adia}) excitation energies (eV), oscillator strengths (f), and spin expectation values ($< s^2 >$), calculated at the ωB97X-D/aug-cc-pVTZ level, corresponding to electronic transitions ($f \geq 0.001$) of the twelve lowest energy $C_6H_4^+$ isomers. For all isomers, orbital 20 is the highest occupied molecular orbital (HOMO).

isomer	transition	dominant contribution	E_{vert}	f	$< s^2 >$	E_{adia}	expt.
A$^+$	$\tilde{B}^2B_1 \leftarrow \tilde{X}^2A_2$	$19\beta \rightarrow 20\beta$	2.30	0.010	0.74	1.87	
	$\tilde{C}^2B_1 \leftarrow \tilde{X}^2A_2$	$20\alpha \rightarrow 21\alpha$	4.60	0.002	0.76		
B$^+$	$\tilde{D}^2B_2 \leftarrow \tilde{X}^2A_1$	$20\alpha \rightarrow 21\alpha$	3.67	0.034	0.76		
	$\tilde{G}^2B_1 \leftarrow \tilde{X}^2A_1$	$19\beta \rightarrow 22\beta$	4.75	0.002	1.04		
	$\tilde{I}^2B_1 \leftarrow \tilde{X}^2A_1$	$20\alpha \rightarrow 22\alpha$	5.12	0.003	0.85		
C$^+$	$\tilde{B}^2A'' \leftarrow \tilde{X}^2A''$	$18\beta \rightarrow 20\beta$	3.43	0.085	0.74	3.14	2.98, 2.97[a]
	$\tilde{C}^2A'' \leftarrow \tilde{X}^2A''$	$20\alpha \rightarrow 21\alpha$	4.44	0.004	1.07		
	$\tilde{E}^2A'' \leftarrow \tilde{X}^2A''$	$20\alpha \rightarrow 22\alpha$	5.02	0.286	0.97		
D$^+$	$\tilde{B}^2B \leftarrow \tilde{X}^2B$	$18\beta \rightarrow 20\beta$	3.42	0.003	0.78		
	$\tilde{C}^2B \leftarrow \tilde{X}^2B$	$20\alpha \rightarrow 21\alpha$, $19\alpha \rightarrow 21\alpha$	3.99	0.135	1.20	3.49	3.40
	$\tilde{D}^2A \leftarrow \tilde{X}^2B$	$20\alpha \rightarrow 22\alpha$	4.33	0.005	1.15		
	$\tilde{F}^2B \leftarrow \tilde{X}^2B$	$20\alpha \rightarrow 23\alpha$, $19\beta \rightarrow 22\beta$	5.03	0.003	1.48		
E$^+$	$\tilde{B}^2B_2 \leftarrow \tilde{X}^2B_3$	$20\alpha \rightarrow 21\alpha$	1.63	0.010	0.78		
	$\tilde{D}^2B_2 \leftarrow \tilde{X}^2B_3$	$18\beta \rightarrow 20\beta$, $19\beta \rightarrow 21\beta$	2.89	0.011	1.31	2.82	
	$\tilde{E}^2B_2 \leftarrow \tilde{X}^2B_3$	$20\alpha \rightarrow 22\alpha$	3.51	0.040	0.96		
	$\tilde{G}^2B_2 \leftarrow \tilde{X}^2B_3$	$17\beta \rightarrow 20\beta$	4.02	0.028	1.42	3.65	
	$\tilde{I}^2B_2 \leftarrow \tilde{X}^2B_3$	$19\alpha \rightarrow 22\alpha$	4.91	0.066	1.82		
F$^+$	$\tilde{A}^2B \leftarrow \tilde{X}^2A$	$19\beta \rightarrow 20\beta$	1.07	0.001	0.79		
	$\tilde{B}^2A \leftarrow \tilde{X}^2A$	$18\beta \rightarrow 20\beta$	1.25	0.006	0.77		
	$\tilde{C}^2B \leftarrow \tilde{X}^2A$	$20\alpha \rightarrow 21\alpha$, $18\beta \rightarrow 21\beta$	2.07	0.001	1.99		
	$\tilde{F}^2B \leftarrow \tilde{X}^2A$	$17\beta \rightarrow 20\beta$, $20\alpha \rightarrow 21\alpha$, $18\alpha \rightarrow 21\alpha$	3.88	0.004	1.18		
	$\tilde{G}^2A \leftarrow \tilde{X}^2A$	$19\beta \rightarrow 21\beta$	4.24	0.001	1.08		
	$\tilde{H}^2B \leftarrow \tilde{X}^2A$	$20\alpha \rightarrow 22\alpha$	4.34	0.012	1.38		
	$\tilde{I}^2B \leftarrow \tilde{X}^2A$	$16\beta \rightarrow 20\beta$	4.56	0.003	0.91		
G$^+$	$\tilde{B}^2A'' \leftarrow \tilde{X}^2A''$	$18\beta \rightarrow 20\beta$	2.52	0.108	0.76	2.37	2.05, 2.04[a]
	$\tilde{D}^2A'' \leftarrow \tilde{X}^2A''$	$20\alpha \rightarrow 21\alpha$, $16\beta \rightarrow 20\beta$, $19\alpha \rightarrow 22\alpha$	3.82	0.076	1.30	3.53	3.34, 3.33[a]
	$\tilde{G}^2A'' \leftarrow \tilde{X}^2A''$	$16\beta \rightarrow 20\beta$, $20\alpha \rightarrow 21\alpha$	4.27	0.105	1.18	4.14	
H$^+$	$\tilde{B}^2A'' \leftarrow \tilde{X}^2A''$	$18\beta \rightarrow 20\beta$, $20\alpha \rightarrow 21\alpha$	3.32	0.009	1.76		
	$\tilde{C}^2A''$ (C_1) $\leftarrow \tilde{X}^2A''$	$20\alpha \rightarrow 21\alpha$, $18\beta \rightarrow 20\beta$	4.09	0.104	1.10	3.49*	2.81
	$\tilde{G}^2A'' \leftarrow \tilde{X}^2A''$	$18\alpha \rightarrow 21\alpha$, $18\beta \rightarrow 21\beta$, $20\alpha \rightarrow 21\alpha$	5.04	0.014	1.69		
	$\tilde{I}^2A'' \leftarrow \tilde{X}^2A''$	$18\alpha \rightarrow 21\alpha$, $20\alpha \rightarrow 22\alpha$, $18\beta \rightarrow 21\beta$	5.76	0.125	0.88		
I$^+$	$\tilde{C}^2B_g \leftarrow \tilde{X}^2A_u$	$18\beta \rightarrow 20\beta$, $20\alpha \rightarrow 21\alpha$	2.53	0.092	0.76	2.39	2.14, 2.12[a]
	$\tilde{D}^2B_g$ (C_2) $\leftarrow \tilde{X}^2A_u$	$20\alpha \rightarrow 21\alpha$	3.90	0.503	0.85	3.42	3.32[a]
J$^+$	$\tilde{C}^2A_2 \leftarrow \tilde{X}^2B_1$	$17\beta \rightarrow 20\beta$	2.39	0.045	0.77	2.21	1.99[a]
	$\tilde{D}^2A$ (C_2) $\leftarrow \tilde{X}^2B_1$	$20\alpha \rightarrow 21\alpha$	3.83	0.286	0.84	3.63	3.22[a]
	$\tilde{E}^2B_1 \leftarrow \tilde{X}^2B_1$	$16\beta \rightarrow 20\beta$	3.88	0.032	1.29		
K$^+$	$\tilde{A}^2A' \leftarrow \tilde{X}^2A''$	$20\alpha \rightarrow 21\alpha$, $18\alpha \rightarrow 21\alpha$, $18\beta \rightarrow 20\beta$	1.10	0.005	0.77		
	$\tilde{E}^2A'' \leftarrow \tilde{X}^2A''$	$18\beta \rightarrow 21\beta$, $18\beta \rightarrow 20\beta$	4.08	0.083	1.23		
	$\tilde{G}^2A'' \leftarrow \tilde{X}^2A''$	$18\alpha \rightarrow 21\alpha$	4.83	0.133	1.19	4.51	
L$^+$	$\tilde{C}^2A'' \leftarrow \tilde{X}^2A''$	$17\beta \rightarrow 20\beta$	2.51	0.012	0.74		
	$\tilde{E}^2A'' \leftarrow \tilde{X}^2A''$	$20\alpha \rightarrow 21\alpha$	3.62	0.473	1.01	3.50	
	$\tilde{F}^2A'' \leftarrow \tilde{X}^2A''$	$16\beta \rightarrow 20\beta$, $17\alpha \rightarrow 21\alpha$	4.06	0.085	1.40		

*Calculated at the PBE1PBE/aug-cc-pVTZ level

[a]Energy of origin transition in Ne matrix from ref. 256

6.6.3 Calculated geometries and harmonic vibrational frequencies for isomers C^+, D^+, G^+, H^+, and I^+ in the ground and excited electronic states

Simulated spectra based on calculated Franck-Condon factors aid in assignment of bands in the REPD spectra. The simulations rely on calculated equilibrium structures and harmonic vibrational frequencies in the ground and excited electronic states. These have been calculated at the ωB97X-D/aug-cc-pVTZ level for several $C_6H_4^+$ isomers, with results provided in the figures and tables below. Vibrational modes are numbered according to the Mulliken convention.

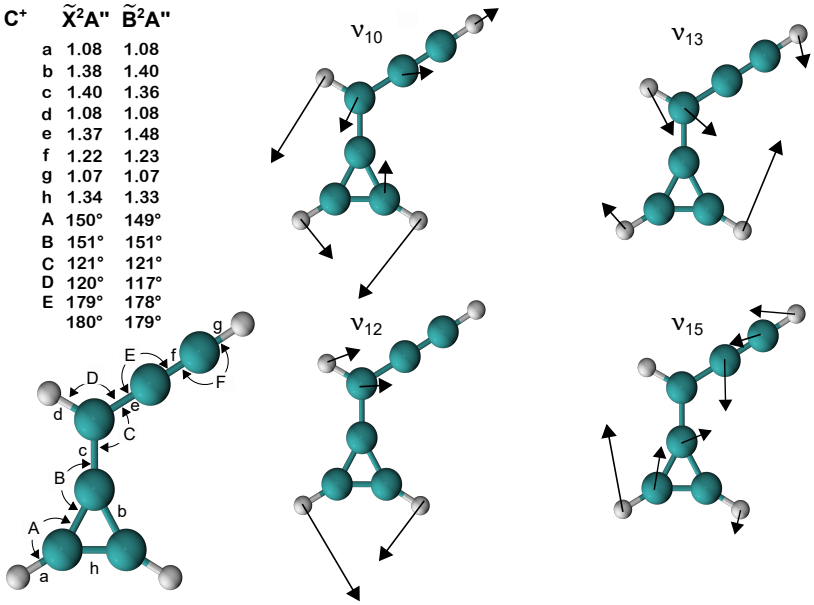

Fig. 6.28 Bond lengths (Å) and angles for the equilibrium geometries of $C_6H_4^+$ isomer $\mathbf{C}^+$ in its $\tilde{X}^2A''$ and $\tilde{B}^2A''$ electronic states, predicted at the ωB97X-D/aug-cc-pVTZ level. Displacement vectors are displayed for the ν_{11}, ν_{12}, ν_{13}, and ν_{15} vibrational modes that are associated with active vibronic transitions in the $\tilde{B}^2A''\leftarrow\tilde{X}^2A''$ band system.

D^+	$\tilde{X}^2B$	$\tilde{C}^2B$
a	1.34	1.32
b	1.08	1.08
c	1.38	1.42
d	1.36	1.32
e	1.28	1.31
f	1.35	1.36
A	150°	151°
B	149°	147°
C	151°	152°
D	180°	180°
E	180°	180°
F	120°	118°

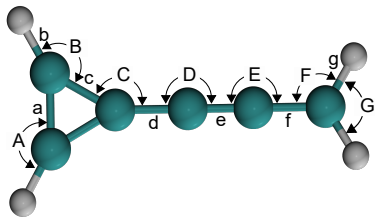

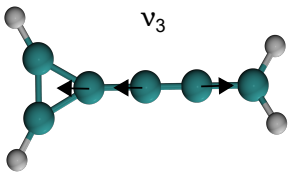

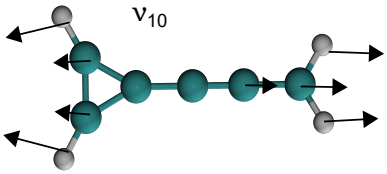

Fig. 6.29 Bond lengths (Å) and angles for the equilibrium geometries of $C_6H_4{}^+$ isomer $\mathbf{D}^+$in its $\tilde{X}^2B$ and $\tilde{C}^2B$ electronic states, predicted at the ωB97X-D/aug-cc-pVTZ level. Displacement vectors are displayed for the ν_3 and ν_{10} vibrational modes that are associated with active vibronic transitions in the $\tilde{C}^2B \leftarrow \tilde{X}^2B$ band system.

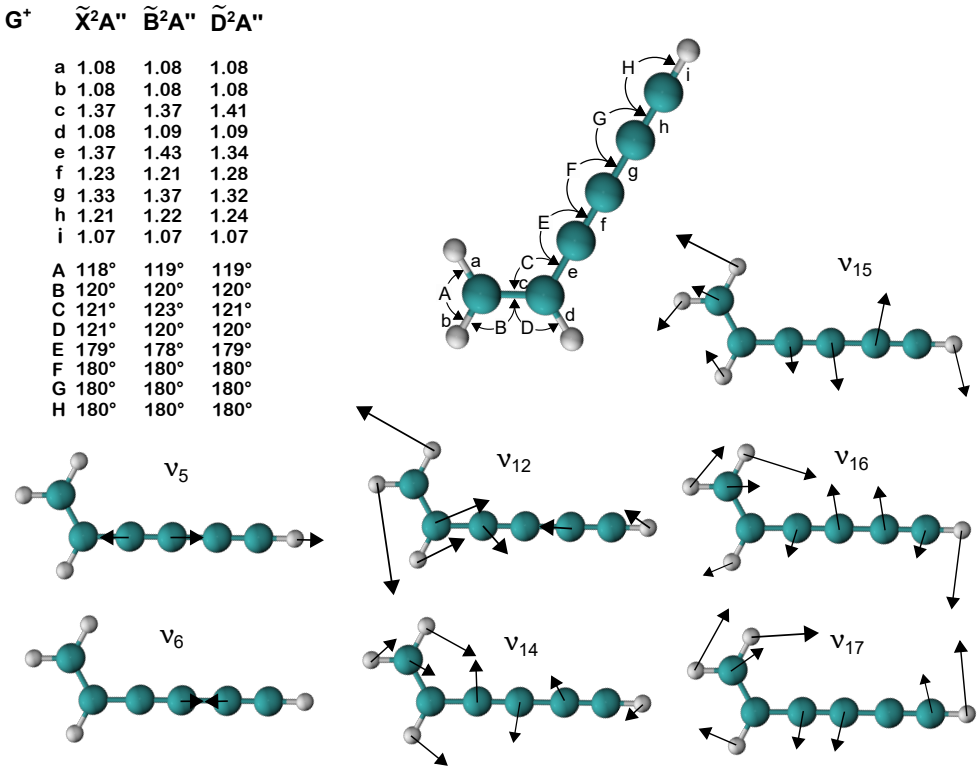

Fig. 6.30 Bond lengths (Å) and angles for the equilibrium geometries of $C_6H_4^+$ isomer $\mathbf{G}^+$ in its $\tilde{X}^2A''$, $\tilde{B}^2A''$, and $\tilde{D}^2A''$ electronic states, predicted at the ωB97X-D/aug-cc-pVTZ level. Displacement vectors are displayed for the ν_5, ν_6, ν_{12}, ν_{14}, ν_{15}, ν_{16}, and ν_{17} vibrational modes that are associated with active vibronic transitions in the REPD spectrum recorded in this work.

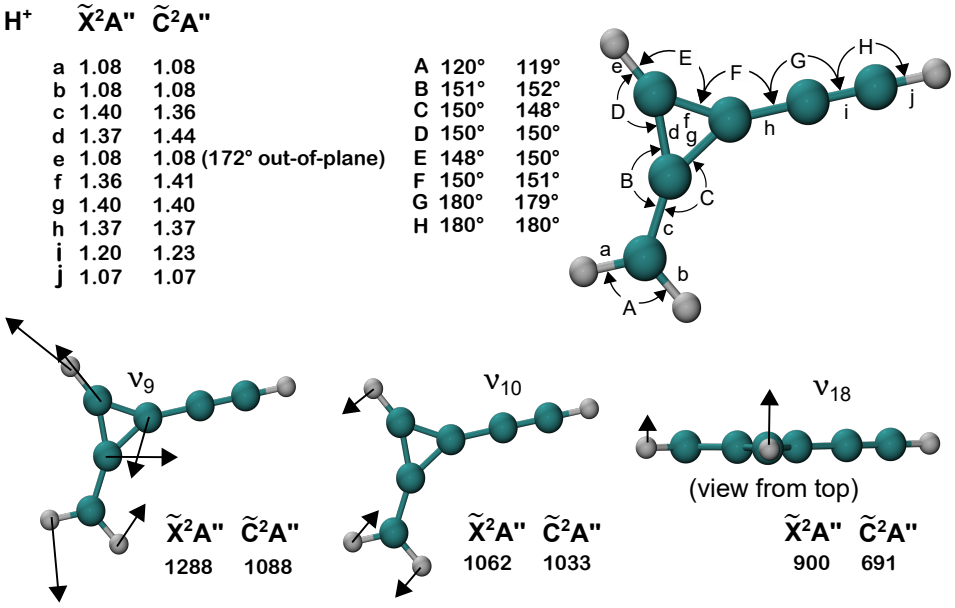

Fig. 6.31 Bond lengths (Å) and angles for the equilibrium geometries of $C_6H_4^+$ isomer $\mathbf{H}^+$ in its $\tilde{X}^2A''$ (C_s) and $\tilde{C}^2A''$ (C_1) electronic states, predicted at the PBE1PBE/aug-cc-pVTZ level. Displacement vectors are shown for the ν_9, ν_{11}, ν_{12}, ν_{14}, ν_{17}, and ν_{20} vibrational modes that are associated with active vibronic transitions in the $\tilde{C}^2A''\leftarrow\tilde{X}^2A''$ band system.

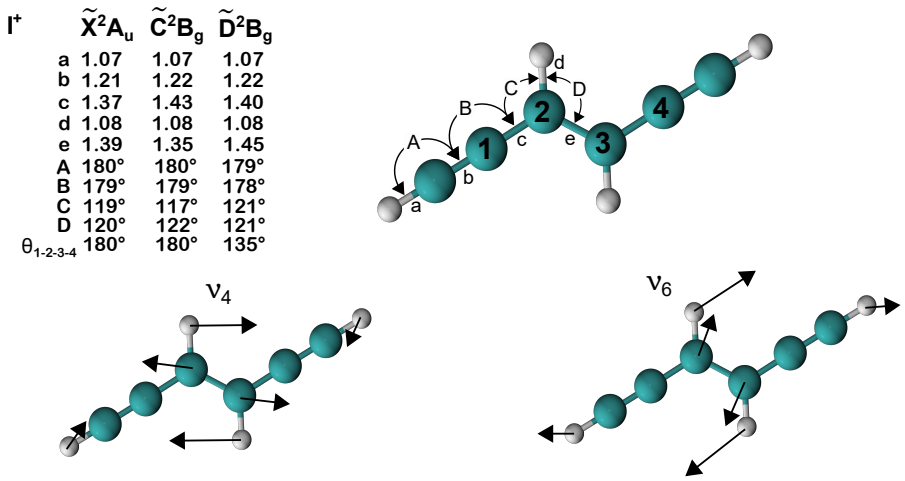

Fig. 6.32 Bond lengths (Å) and angles for the equilibrium geometries of $C_6H_4^+$ isomer $\mathbf{I}^+$ in its $\tilde{X}^2A_u$ (C_{2h}), $\tilde{C}^2B_g$ (C_{2h}), and $\tilde{D}^2B$ (C_2) electronic states, predicted at the ωB97X-D/aug-cc-pVTZ level. Displacement vectors are shown for the ν_4 and ν_6 vibrational modes that are associated with active vibronic transitions in the $\tilde{C}^2B_g\leftarrow\tilde{X}^2A_u$ band system.

Table 6.6 Harmonic vibrational frequencies (cm^{-1}) for $C_6H_4^+$ isomers $\mathbf{A}^+$, $\mathbf{B}^+$, and $\mathbf{C}^+$ in the ground and excited electronic states, calculated at the ωB97X-D/aug-cc-pVTZ level of theory.

	$\mathbf{A}^+$		$\mathbf{B}^+$	$\mathbf{C}^+$	
Mode	$\widetilde{X}^2A_2$	$\widetilde{B}^2B_2$	$\widetilde{X}^2A_2$	$\widetilde{X}^2A''$	$\widetilde{B}^2A''$
ν_1	3269 (a_1)	3267 (a_1)	3241 (a_1)	3423 (a')	3421 (a')
ν_2	3251 (a_1)	3209 (a_1)	3220 (a_1)	3305 (a')	3307 (a')
ν_3	3241 (a_1)	3201 (a_1)	3206 (a_1)	3270 (a')	3271 (a')
ν_4	1822 (a_1)	1767 (a_1)	1784 (a_1)	3208 (a')	3224 (a')
ν_5	1422 (a_1)	1373 (a_1)	1413 (a_1)	2089 (a')	2252 (a')
ν_6	1143 (a_1)	1088 (a_1)	1096 (a_1)	1780 (a')	1741 (a')
ν_7	1048 (a_1)	1037 (a_1)	1059 (a_1)	1473 (a')	1510 (a')
ν_8	970 (a_1)	832 (a_1)	826 (a_1)	1395 (a')	1341 (a')
ν_9	819 (a_1)	676 (a_1)	537 (a_1)	1262 (a')	1207 (a')
ν_{10}	850 (a_2)	802 (a_2)	825 (a_2)	1131 (a')	1062 (a')
ν_{11}	508 (a_2)	603 (a_2)	460 (a_2)	1040 (a')	1022 (a')
ν_{12}	1010 (b_1)	1541 (b_1)	990 (b_1)	987 (a')	935 (a')
ν_{13}	878 (b_1)	963 (b_1)	766 (b_1)	857 (a')	841 (a')
ν_{14}	800 (b_1)	878 (b_1)	617 (b_1)	719 (a')	754 (a')
ν_{15}	492(b_1)	442 (b_1)	542 (b_1)	554 (a')	531 (a')
ν_{16}	261 (b_1)	224 (b_1)	374 (b_1)	346 (a')	337 (a')
ν_{17}	3264(b_2)	3264 (b_2)	3236 (b_2)	130 (a')	127 (a')
ν_{18}	1454(b_2)	2048 (b_2)	1554 (b_2)	1001 (a'')	961 (a'')
ν_{19}	1373(b_2)	1440 (b_2)	1309 (b_2)	861 (a'')	789 (a'')
ν_{20}	1269 (b_2)	1311 (b_2)	1291 (b_2)	770 (a'')	649 (a'')
ν_{21}	1092 (b_2)	1157(b_2)	1118 (b_2)	700 (a'')	509 (a'')
ν_{22}	1041 (b_2)	1103 (b_2)	1059 (b_2)	435 (a'')	421 (a'')
ν_{23}	849 (b_2)	920 (b_2)	927 (b_2)	398 (a'')	409 (a'')
ν_{24}	564 (b_2)	594 (b_2)	526 (b_2)	128 (a'')	158 (a'')

Table 6.7 Harmonic vibrational frequencies (cm^{-1}) for $C_6H_4^+$ isomers $\mathbf{D}^+$, $\mathbf{E}^+$, and $\mathbf{F}^+$ in the ground and excited electronic states, calculated at the ωB97X-D/aug-cc-pVTZ level of theory.

	$\mathbf{D}^+$		$\mathbf{E}^+$		$\mathbf{F}^+$
Mode	$\widetilde{X}^2B$	$\widetilde{C}^2B$	$\widetilde{X}^2B_3$	$\widetilde{D}^2B_1$	$\widetilde{X}^2A$
ν_1	3302 (a)	3303 (a)	3133 (a)	3104 (a)	3235 (a)
ν_2	3158 (a)	3126 (a)	1766 (a)	2272 (a)	3206 (a)
ν_3	2167 (a)	2185 (a)	1604 (a)	1533 (a)	1782 (a)
ν_4	1769 (a)	1732 (a)	1402 (a)	1384 (a)	1517 (a)
ν_5	1486 (a)	1519 (a)	645 (a)	632 (a)	1303 (a)
ν_6	1433 (a)	1594 (a)	600 (a)	655 (a)	1181 (a)
ν_7	1208 (a)	1123 (a)	3232 (b_1)	3102 (b_1)	1082 (a)
ν_8	991 (a)	934 (a)	2044 (b_1)	1992 (b_1)	1025 (a)
ν_9	957 (a)	951 (a)	1450 (b_1)	1422 (b_1)	981 (a)
ν_{10}	621 (a)	603 (a)	1180 (b_1)	1109 (b_1)	896 (a)
ν_{11}	161 (a)	1365 (a)	3230 (b_2)	3192 (b_2)	621 (a)
ν_{12}	3266 (b)	3262 (b)	992 (b_2)	954 (b_2)	529 (a)
ν_{13}	3263 (b)	3217 (b)	969 (b_2)	925 (b_2)	415 (a)
ν_{14}	1228 (b)	1088 (b)	556 (b_2)	480 (b_2)	3223 (b)
ν_{15}	1028(b)	998 (b)	362 (b_2)	348 (b_2)	3203 (b)
ν_{16}	1022 (b)	968 (b)	247 (b_2)	219 (b_2)	1416 (b)
ν_{17}	889 (b)	860 (b)	101 (b_2)	96 (b_2)	1273 (b)
ν_{18}	841 (b)	750 (b)	3230 (b_3)	3192 (b_3)	1228 (b)
ν_{19}	517(b)	443 (b)	991 (b_3)	954 (b_3)	1050 (b)
ν_{20}	507 (b)	426 (b)	968 (b_3)	926 (b_3)	921 (b)
ν_{21}	413 (b)	373 (b)	518 (b_3)	456 (b_3)	761 (b)
ν_{22}	332 (b)	59 (b)	437 (b_3)	451 (b_3)	741 (b)
ν_{23}	127 (b)	160 (b)	261 (b_3)	231 (b_3)	347 (b)
ν_{24}	124 (b)	67 (b)	102 (b_3)	95 (b_3)	212 (b)

Table 6.8 Harmonic vibrational frequencies for $C_6H_4^+$ isomer $\mathbf{G}^+$ in the ground and excited electronic states, calculated at the ωB97X-D/aug-cc-pVTZ and (EOM)CCSD/cc-pVDZ (italicized) levels.

Mode	$\widetilde{X}^2A''$	$\widetilde{B}^2A''$	$\widetilde{D}^2A''$
ν_1	3412, *3418* (a′)	3412, *3414* (a′)	3405 (a′)
ν_2	3278, *3302* (a′)	3282, *3307* (a′)	3279 (a′)
ν_3	3189, *3220* (a′)	3181, (*3211* a′)	3160 (a′)
ν_4	3168, *3183* (a′)	3178, *3188* (a′)	3167 (a′)
ν_5	2303, *2327* (a′)	2347, *2388* (a′)	2736 (a′)
ν_6	2073, *2054* (a′)	2196, *2173* (a′)	1902 (a′)
ν_7	1564, *1554* (a′)	1640, *1656* (a′)	1491 (a′)
ν_8	1460, *1441* (a′)	1453, *1450* (a′)	1426 (a′)
ν_9	1297, *1289* (a′)	1313, *1303* (a′)	1144 (a′)
ν_{10}	1274, *1262* (a′)	1134, *1150* (a′)	1260 (a′)
ν_{11}	1055, *1046* (a′)	1012, *1024* (a′)	1013 (a′)
ν_{12}	720, *710* (a′)	684, *708* (a′)	707 (a′)
ν_{13}	700, *693* (a′)	708, *679* (a′)	545 (a′)
ν_{14}	550, *521* (a′)	540, *531* (a′)	487 (a′)
ν_{15}	481, *466* (a′)	474, *479* (a′)	424 (a′)
ν_{16}	238, *231* (a′)	244, *243* (a′)	216 (a′)
ν_{17}	108, *108* (a′)	102, *106* (a′)	92 (a′)
ν_{18}	1071, *1039* (a″)	1029, *998* (a″)	956 (a″)
ν_{19}	929, *922* (a″)	848, *845* (a″)	772 (a″)
ν_{20}	785, *759* (a″)	680, *696* (a″)	677 (a″)
ν_{21}	632, *613* (a″)	512, *515* (a″)	444 (a″)
ν_{22}	493, *489* (a″)	454, *501* (a″)	354 (a″)
ν_{23}	311, *314* (a″)	310, *310* (a″)	224 (a″)
ν_{24}	138, *137* (a″)	133, *133* (a″)	114 (a″)

Table 6.9 Harmonic vibrational frequencies (cm^{-1}) for $C_6H_4^+$ isomer $\mathbf{H}^+$ in the ground and excited electronic states, calculated at the ωB97X-D/aug-cc-pVTZ and PBE1PBE/aug-cc-pVTZ levels of theory.

	ωB97X-D	PBE1PBE	
Mode	$\widetilde{X}^2A''$	$\widetilde{X}^2A''$ (C_s)	$\widetilde{C}^2A''$ (C_1)
ν_1	3431 (a′)	3429 (a′)	3397 (a)
ν_2	3298 (a′)	3291 (a′)	3278 (a)
ν_3	3280 (a′)	3268 (a′)	3247 (a)
ν_4	3178 (a′)	3172 (a′)	3166 (a)
ν_5	2238 (a′)	2222 (a′)	1975 (a)
ν_6	1794 (a′)	1801 (a′)	1710 (a)
ν_7	1517 (a′)	1516 (a′)	2480 (a)
ν_8	1465 (a′)	1455 (a′)	1457 (a)
ν_9	1296 (a′)	1288 (a′)	1088 (a)
ν_{10}	1071 (a′)	1062 (a′)	1033 (a)
ν_{11}	1038 (a′)	1034 (a′)	955(a)
ν_{12}	888 (a′)	889 (a′)	805 (a)
ν_{13}	734 (a′)	719 (a′)	615 (a)
ν_{14}	713 (a′)	715 (a′)	666 (a)
ν_{15}	554 (a′)	552 (a′)	543 (a)
ν_{16}	327 (a′)	327 (a′)	327 (a)
ν_{17}	138 (a′)	139 (a′)	128 (a)
ν_{18}	907 (a″)	900 (a″)	691 (a)
ν_{19}	853 (a″)	846 (a″)	937 (a)
ν_{20}	832 (a″)	818 (a″)	719 (a)
ν_{21}	607 (a″)	602 (a″)	439 (a)
ν_{22}	375 (a″)	374 (a″)	339 (a)
ν_{23}	277 (a″)	278 (a″)	365 (a)
ν_{24}	180 (a″)	182 (a″)	150 (a)

Table 6.10 Harmonic vibrational frequencies (cm^{-1}) for $C_6H_4^+$ isomer $\mathbf{I}^+$ in the ground and excited electronic states, calculated at the ωB97X-D/aug-cc-pVTZ and (EOM)CCSD/cc-pVDZ (italicized) levels.

Mode	$\widetilde{X}^2A_u$ (C_{2h})	$\widetilde{C}^2B_g$ (C_{2h})	$\widetilde{D}^2B_g$ (C_2)
ν_1	3415, *3417* (a_g)	3215, *3417* (a_g)	3407, *3414* (a)
ν_2	3187, *3209* (a_g)	3197, *3227* (a_g)	3180, *3207* (a)
ν_3	2167, *2150* (a_g)	2148, *2160* (a_g)	1791, *1869* (a)
ν_4	1566, *1571* (a_g)	1581, *1616* (a_g)	2395, *2661* (a)
ν_5	1281, *1282* (a_g)	1316, *1316* (a_g)	1272, *1270* (a)
ν_6	1081, *1075* (a_g)	1011, *1012* (a_g)	1013, *1014* (a)
ν_7	713, *671* (a_g)	732, *703* (a_g)	699, *664* (a)
ν_8	535, *518* (a_g)	518, *513* (a_g)	544, *531* (a)
ν_9	231, *218* (a_g)	237, *234* (a_g)	207, *206* (a)
ν_{10}	899, *898* (a_u)	953, *972* (a_u)	720, *704* (a)
ν_{11}	789, *744* (a_u)	693, *671* (a_u)	738, *720* (a)
ν_{12}	441, *432* (a_u)	514, *514* (a_u)	440, *420* (a)
ν_{13}	99, *99* (a_u)	112, *116* (a_u)	99, *95* (a)
ν_{14}	939, *922* (b_g)	878, *841* (b_g)	721, *673* (b)
ν_{15}	788, *746* (b_g)	686, *665* (b_g)	739, *717* (b)
ν_{16}	319, *318* (b_g)	353, *358* (b_g)	348, *331* (b)
ν_{17}	3412, *3415* (b_u)	3412, *3418* (b_u)	3405, *3410* (b)
ν_{18}	3192 *3214* (b_u)	3200, *3229* (b_u)	3184, *3206* (b)
ν_{19}	2112, *2077* (b_u)	2282, *2304* (b_u)	2095, *2135* (b)
ν_{20}	1315, *1302* (b_u)	1289, *1275* (b_u)	1246, *1243* (b)
ν_{21}	1121, *1114* (b_u)	899, *945* (b_u)	573, *822* (b)
ν_{22}	713, *673* (b_u)	732, *704* (b_u)	696, *644* (b)
ν_{23}	513 *479* (b_u)	506, *491* (b_u)	490, *477* (b)
ν_{24}	124, *120* (b_u)	125, *125* (b_u)	141, *135* (b)

Table 6.11 Harmonic vibrational frequencies (cm^{-1}) for $C_6H_4^+$ isomers $\mathbf{J}^+$, $\mathbf{K}^+$, and $\mathbf{L}^+$ in the ground and excited electronic states, calculated at the ωB97X-D/aug-cc-pVTZ level.

		$\mathbf{J}^+$		$\mathbf{K}^+$	$\mathbf{L}^+$	
Mode	$\widetilde{X}^2B_1$ (C_{2v})	$\widetilde{C}^2A_2$ (C_{2v})	$\widetilde{D}^2A$ (C_2)	$\widetilde{X}^2A''$	$\widetilde{X}^2A''$	$\widetilde{E}^2A''$
ν_1	3416 (a_1)	3412 (a_1)	3427 (a)	3425 (a′)	3416 (a′)	3409 (a′)
ν_2	3199 (a_1)	3226 (a_1)	3155 (a)	3275 (a′)	3250 (a′)	3251 (a′)
ν_3	2170 (a_1)	2166 (a_1)	2125 (a)	3262 (a′)	3163 (a′)	3193 (a′)
ν_4	1528 (a_1)	1607 (a_1)	1360 (a)	3242 (a′)	3146 (a′)	3145 (a′)
ν_5	1239 (a_1)	1214 (a_1)	1144 (a)	2204 (a′)	2243 (a′)	2564 (a′)
ν_6	943 (a_1)	899 (a_1)	856 (a)	1547 (a′)	2128 (a′)	2169 (a′)
ν_7	712 (a_1)	727 (a_1)	751 (a)	1503 (a′)	1534 (a′)	1466 (a′)
ν_8	449 (a_1)	436 (a_1)	420 (a)	1297 (a′)	1449 (a′)	1426 (a′)
ν_9	109 (a_1)	106 (a_1)	100 (a)	1256 (a′)	1305 (a′)	1233 (a′)
ν_{10}	996 (a_2)	1007 (a_2)	777 (a)	1153 (a′)	1105 (a′)	1041 (a′)
ν_{11}	792 (a_2)	696 (a_2)	704 (a)	1082 (a′)	1036 (a′)	1028 (a′)
ν_{12}	467 (a_2)	595 (a_2)	374 (a)	1008 (a′)	886 (a′)	844 (a′)
ν_{13}	173 (a_2)	239 (a_2)	185 (a)	877 (a′)	710 (a′)	735 (a′)
ν_{14}	802 (b_1)	774 (b_1)	749 (b)	740 (a′)	562 (a′)	537 (a′)
ν_{15}	783 (b_1)	687 (b_1)	712 (b)	605 (a′)	362 (a′)	365 (a′)
ν_{16}	322 (b_1)	363 (b_1)	326 (b)	506 (a′)	252 (a′)	242 (a′)
ν_{17}	3413 (b_2)	3414 (b_2)	3425 (b)	168 (a′)	96 (a′)	88 (a′)
ν_{18}	3187 (b_2)	3212 (b_2)	3154 (b)	993 (a″)	1010 (a″)	942 (a″)
ν_{19}	2113 (b_2)	2273 (b_2)	2098 (b)	863 (a″)	869 (a″)	584 (a″)
ν_{20}	1452 (b_2)	1376 (b_2)	1366 (b)	823 (a″)	780 (a″)	698 (a″)
ν_{21}	1094 (b_2)	960 (b_2)	914 (b)	786 (a″)	504 (a″)	388 (a″)
ν_{22}	735 (b_2)	694 (b_2)	753 (b)	535 (a″)	342 (a″)	301 (a″)
ν_{23}	709 (b_2)	725 (b_2)	676 (b)	301 (a″)	200 (a″)	190 (a″)
ν_{24}	237 (b_2)	233 (b_2)	232 (b)	145 (a″)	119 (a″)	1429* (a″)

Chapter 7

Summary and outlook

Electronic spectra of $C_4H_2^+$, $C_4H_4^+$, $C_4H_5^+$, and $C_6H_4^+$ cations have been measured in a custom-built tandem mass spectrometer by photodissociating their messenger-tagged complexes (with Ar, Ne, or N_2) and monitoring photofragment production as a function of wavelength. The spectra were interpreted in the light of calculated transition energies and oscillator strengths, spectral simulations, hole burning experiments, and previous spectroscopic measurements. The spectral data may be useful for detecting $C_4H_2^+$, $C_4H_4^+$, $C_4H_5^+$, and $C_6H_4^+$ cations in remote environments where reactive hydrocarbons exist, including Titan's upper atmosphere and photospheres of asymptotic giant branch stars where the large abundance of C_2H_2 and high flux of far-ultraviolet photons ($91 < \lambda < 240$ nm) are likely to drive ion-molecule reactions.

The spectroscopic experiments were accompanied by quantum chemical calculations of the ground state $C_4H_4^+$, $C_4H_5^+$, and $C_6H_4^+$ potential energy surfaces. Systematic explorations of these surfaces revealed several low-energy minima and saddle points, indicating that multiple isomers can be stabilized and exist in low pressure and temperature environments – consistent with the spectroscopic detection of multiple $C_4H_4^+$ and $C_6H_4^+$ isomers generated in the ionized supersonic expansion of ≈ 0.7 % C_2H_2 in Ar or N_2. The calculated ground state dissociation pathways help rationalize the detection of photofragments: $C_4H_2^+$ and $C_4H_3^+$ from $C_4H_4^+$, $C_2H_3^+$ and $C_4H_3^+$ from $C_4H_5^+$, and $C_4H_2^+$ from $C_6H_4^+$. These calculations are valuable for at least two reasons, i) they provide an estimate of thermodynamical thresholds for dissociation, and ii) they provide information on the reverse reactions, helping to identify ways in which the cations may be synthesized in different environments. The calculated stationary points can be incorporated into chemical models and used for master equation simulations,

such as those carried out in this work to clarify the dissociation of the 1-but-yn-3-yl cation ($H_3CCHCCH^+$) following exposure to 268 nm light.

The studies presented in this work advance our understanding of the electronic structure, formation, and destruction of $C_4H_2^+$, $C_4H_4^+$, $C_4H_5^+$, and $C_6H_4^+$ cations, and it is hoped that future experiments resolve the mysteries that remain. For example, Renner-Teller and Herzberg-Teller interactions involved in higher energy transitions of the diacetylene cation (HC_4H^+) may be teased apart through higher resolution electronic spectroscopy, or two-color photoelectron spectroscopy, accompanied by sophisticated computational approaches. Furthermore, in the future electronic transitions of individual $C_4H_4^+$ and $C_6H_4^+$ isomers may be measured using strategies such as ion-mobility mass spectrometry coupled with laser spectroscopy. Additionally, the isomer responsible for various transitions may be determined using precursors that yield different isomeric abundances.

References

[1] Jones, W.; Lindstedt, R. *Combust. Flame* **1988**, *73*, 233 – 249.

[2] Hucknall, D. *Chemistry of Hydrocarbon Combustion*; Springer Science & Business Media, 2012.

[3] Frenklach, M.; Wang, H. *Symposium (International) on Combustion* **1991**, *23*, 1559 – 1566, Twenty-Third Symposium (International) on Combustion.

[4] Frenklach, M. *Phys. Chem. Chem. Phys.* **2002**, *4*, 2028–2037.

[5] Holland, L.; Ojha, S. *Thin Solid Films* **1979**, *58*, 107–116.

[6] Fink, J.; Müller-Heinzerling, T.; Pflüger, J.; Scheerer, B.; Dischler, B.; Koidl, P.; Bubenzer, A.; Sah, R. *Phys. Rev. B* **1984**, *30*, 4713.

[7] Alman, D. A.; Ruzic, D. N.; Brooks, J. *Phys. Plasmas* **2000**, *7*, 1421–1432.

[8] Frenklach, M.; Feigelson, E. D. *Astrophys. J.* **1989**, *341*, 372–384.

[9] Bohme, D. K. *Chem. Rev.* **1992**, *92*, 1487–1508.

[10] Joblin, C.; Tielens, A.; Cherchneff, I. *European Astronomical Society Publications Series* **2011**, *46*, 177–189.

[11] Chiar, J. E.; Pendleton, Y. J.; Geballe, T. R.; Tielens, A. G. G. M. *Astrophys. J.* **1998**, *507*, 281–286.

[12] Woods, P. M.; Millar, T. J.; Herbst, E.; Zijlstra, A. A. *Astron. Astrophys.* **2003**, *402*, 189–199.

[13] Booke, T. Y.; Tokunaga, A. T.; Weaver, H. A.; Crovisier, J.; Bockelée-Morvan, D.; Crisp, D. *Nature* **1996**, *383*, 606–608.

[14] Kunde, V.; Aikin, A.; Hanel, R.; Jennings, D.; Maguire, W.; Samuelson, R. *Nature* **1981**, *292*, 686–688.

[15] Kim, S. J.; Caldwell, J.; Rivolo, A.; Wagener, R.; Orton, G. S. *Icarus* **1985**, *64*, 233 – 248.

[16] Waite Jr., J. H.; You,; Cravens, T. E.; Coates, A. J.; Crary, F. J.; Magee, B.; Westlake, J. *Science* **2007**, *316*, 870–875.

[17] Avery, L. W.; Broten, N. W.; MacLeod, J. M.; Oka, T.; Kroto, H. W. *Astrophys. J.* **1976**, *205*, L173–L175.

[18] Little, L. T.; Riley, P. W.; Matheson, D. N. *Mon. Not. R. Astron. Soc.* **1977**, *181*, 33P–35P.

[19] Kroto, H.; Kirby, C.; Walton, D.; Avery, L.; Broten, N.; MacLeod, J.; Oka, T. *Astrophys. J.* **1978**, *219*, L133–L137.

[20] Turner, B. E.; Herbst, E.; Terzieva, R. *Astrophys. J. Suppl. Ser.* **2000**, *126*, 427–460.

[21] Sakai, N.; Sakai, T.; Hirota, T.; Yamamoto, S. *Astrophys. J.* **2008**, *672*, 371–381.

[22] Penzias, A. A.; Wilson, R. W. *Astrophys. J.* **1965**, *142*, 419–421.

[23] Dicke, R. H.; Peebles, P. J. E.; Roll, P. G.; Wilkinson, D. T. *Astrophys. J.* **1965**, *142*, 414–419.

[24] Dobbs, C. *Astron. Geophys.* **2013**, *54*, 5.24–5.30.

[25] Nguyen, N. B.; Nunes, F. M.; Thompson, I. J.; Brown, E. F. *Phys. Rev. Lett.* **2012**, *109*, 141101.

[26] Gladstone, G. R. et al. *Science* **2016**, *351*.

[27] Wong, M. L.; Fan, S.; Gao, P.; Liang, M.-C.; Shia, R.-L.; Yung, Y. L.; Kammer, J. A.; Summers, M. E.; Gladstone, G. R.; Young, L. A.; Olkin, C. B.; Ennico, K.; Weaver, H. A.; Stern, S. A. *Icarus* **2017**, *287*, 110 – 115.

[28] Banfield, D.; Gierasch, P.; Bell, M.; Ustinov, E.; Ingersoll, A.; Vasavada, A.; West, R. A.; Belton, M. *Icarus* **1998**, *135*, 230 – 250.

[29] Gillett, F. C.; Forrest, W. J. *Astrophys. J.* **1974**, *187*, L37.

[30] Kim, S. J.; Geballe, T. R. *Icarus* **2005**, *179*, 449–458.

[31] Pollack, J. B.; Rages, K.; Pope, S. K.; Tomasko, M. G.; Romani, P. N.; Atreya, S. K. *J. Geophys. Res. Space Phys.* **1987**, *92*, 15037–15065.

[32] Baines, K. H.; Mickelson, M. E.; Larson, L. E.; Ferguson, D. W. *Icarus* **1995**, *114*, 328 – 340.

[33] Baines, K. H.; Smith, W. *Icarus* **1990**, *85*, 65 – 108.

[34] Bolton, S., et al. *Proc. Int. Astron. Union* **2010**, *6*, 92–100.

[35] Tasker, E. *The Planet Factory: Exoplanets and the Search for a Second Earth*; Bloomsbury Publishing, 2017.

[36] Kuiper, G. P. *Astrophys. J.* **1944**, *100*, 378.

[37] Ali, A.; Sittler Jr, E.; Chornay, D.; Rowe, B.; Puzzarini, C. *Planet. Space Sci.* **2015**, *109*, 46–63.

[38] Raulin, F. *Space Sci. Rev.* **2008**, *135*, 37–48.

[39] Lambert, J.-F.; Sodupe, M.; Ugliengo, P. *Chem. Soc. Rev.* **2012**, *41*, 5373–5374.

[40] Haworth, T. J.; Glover, S. C.; Koepferl, C. M.; Bisbas, T. G.; Dale, J. E. *New Astron. Rev.* **2018**, *82*, 1 – 58.

[41] Cherchneff, I.; Barker, J. R.; Tielens, A. *Astrophys. J.* **1992**, *401*, 269–287.

[42] Frenklach, M.; Clary, D. W.; Gardiner, W. C.; Stein, S. E. *Proc. Combust. Inst.* **1985**, *20*, 887 – 901, Twentieth Symposium (International) on Combustion.

[43] Howe, D. A.; Williams, D. A. *Molecular Astrophysics of Stars and Galaxies*; Clarendon Press, Oxford, UK, 1998; pp 347–370.

[44] Hall, J. L.; Kerzhanovich, V. V.; Jones, J. A.; Cutts, J. A.; Yavrouian, A. A.; Colozza, A.; Lorenz, R. D. *Titan Airship Explorer*, Proceedings, IEEE Aerospace Conference. 2002; pp 1–336.

[45] Schiff, H. I.; Bohme, D. K. *Astrophys. J.* **1979**, *232*, 740–746.

[46] Yamamoto, S. *Introduction to Astrochemistry*; Springer, 2017; pp 91–130.

[47] McEwan, M. J.; Scott, G. B. I.; Adams, N. G.; Babcock, L. M.; Terzieva, R.; Herbst, E. *Astrophys. J.* **1999**, *513*, 287–293.

[48] Adams, N. G.; Smith, D.; Millar, T. J. *Mon. Not. R. Astron. Soc.* **1984**, *211*, 857–865.

[49] Twiddy, N.; Mohebati, A.; Tichý, M. *Int. J. Mass Spectrom. Ion Process.* **1986**, *74*, 251 – 263.

[50] Ervin, K. M.; Armentrout, P. B. *J. Chem. Phys.* **1986**, *84*, 6738–6749.

[51] Gerlich, D. *Chem. Rev.* **1992**, *92*, 1509–1539.

[52] Herbst, E. *Annu. Rev. Phys. Chem.* **1995**, *46*, 27–54.

[53] Elitzur, M.; Watson, W. *Astrophys. J. Lett.* **1978**, *222*, L141–L144.

[54] Elitzur, M.; Watson, W. *Astrophys. J.* **1980**, *236*, 172–181.

[55] Draine, B.; Katz, N. *Astrophys. J.* **1986**, *310*, 392–407.

[56] Gerlich, D.; Horning, S. *Chem. Rev.* **1992**, *92*, 1509–1539.

[57] Barlow, S. E.; Dunn, G. H.; Schauer, M. *Phys. Rev. Lett.* **1984**, *52*, 902–905.

[58] Turner, B. E. *Space Sci. Rev.* **1989**, *51*, 235–337.

[59] Smith, D. *Chem. Rev.* **1992**, *92*, 1473–1485.

[60] Kaiser, R. I.; Nguyen, T. L.; Le, T. N.; Mebel, A. M. *Astrophys. J.* **2001**, *561*, 858–863.

[61] Mebel, A. M.; Kislov, V. V.; Kaiser, R. I. *J. Am. Chem. Soc.* **2008**, *130*, 13618–13629.

[62] Williams, D. A. *Planet. Space Sci.* **1992**, *40*, 1683–1693.

[63] Sakai, N.; Yamamoto, S. *Chem. Rev.* **2013**, *113*, 8981–9015.

[64] Vuitton, V.; Yelle, R.; McEwan, M. *Icarus* **2007**, *191*, 722 – 742.

[65] Heazlewood, B. R.; Softley, T. P. *Ann. Rev. Phys. Chem.* **2015**, *66*, 475–495.

[66] Adams, N. G.; Smith, D.; Clary, D. C. *Astrophys. J.* **1985**, *296*, L31–L34.

[67] Berry, J. L.; Ugelow, M. S.; Tolbert, M. A.; Browne, E. C. *ACS Earth Space Chem.* **2019**, *3*, 202–211.

[68] van Dishoeck, E. F.; Black, J. H., et al. *Astrophys. J.* **1988**, *334*, 771–802.

[69] Kirby, K. P.; Van Dishoeck, E. F. *Advances in Atomic and Molecular Physics*; Elsevier, 1989; Vol. 25; pp 437–476.

[70] van Dishoeck, E. F. *Rate Coefficients in Astrochemistry*; Springer, 1988; pp 49–72.

[71] van Dishoeck, E. F. *Molecular Astrophysics of Stars and Galaxies*; Clarendon Press, Oxford, UK, 1998; pp 53–99.

[72] Atreya, S. K.; Adams, E. Y.; Niemann, H. B.; Demick-Montelara, J. E.; Owen, T. C.; Fulchignoni, M.; Ferri, F.; Wilson, E. H. *Planet. Space Sci.* **2006**, *54*, 1177 – 1187.

[73] Raulin, F. *Nature* **2008**, *454*, 587–589.

[74] Mordaunt, D.; Lambert, I.; Morley, G.; Ashfold, M.; Dixon, R.; Western, C.; Schnieder, L.; Welge, K. *J. Chem. Phys.* **1993**, *98*, 2054–2065.

[75] Wilson, E. H.; Atreya, S. K. *J. Geophys. Res. Planets* **2000**, *105*, 20263–20273.

[76] Zerkle, A. L.; Claire, M. W.; Domagal-Goldman, S. D.; Farquhar, J.; Poulton, S. W. *Nat. Geosci.* **2012**, *5*, 359–363.

[77] Izon, G.; Zerkle, A. L.; Zhelezinskaia, I.; Farquhar, J.; Newton, R. J.; Poulton, S. W.; Eigenbrode, J. L.; Claire, M. W. *Earth Planet. Sci. Lett.* **2015**, *431*, 264 – 273.

[78] Molina-Cuberos, G. J.; López-Moreno, J. J.; Rodrigo, R.; Lara, L. M. *J. Geophys. Res. Planets* **1999**, *104*, 21997–22024.

[79] Molina-Cuberos, G.; López-Moreno, J.; Rodrigo, R.; Lara, L.; O'Brien, K. *Planet. Space Sci.* **1999**, *47*, 1347 – 1354.

[80] Anicich, V. G.; McEwan, M. J. *Planet. Space Sci.* **1997**, *45*, 897–921.

[81] Anicich, V. G.; Wilson, P.; McEwan, M. J. *J. Am. Soc. Mass. Spectr.* **2004**, *15*, 1148 – 1155.

[82] Anicich, V. G.; Wilson, P. F.; McEwan, M. J. *J. Am. Soc. Mass Spectrom.* **2006**, *17*, 544 – 561.

[83] Herbst, E.; Leung, C. M. *Astrophys. J. Suppl. Ser.* **1989**, *69*, 271–300.

[84] Lee, H.-H.; Bettens, R. P. A.; Herbst, E. *Astron. Astrophys. Suppl. Ser.* **1996**, *119*, 111–114.

[85] Glover, S. C. O.; Federrath, C.; Mac Low, M.-M.; Klessen, R. S. *Mon. Not. R. Astron. Soc.* **2010**, *404*, 2–29.

[86] Kalvāns, J. and Shmeld, I., *Astron. Astrophys.* **2010**, *521*, A37.

[87] Glover, S. C. O.; Clark, P. C. *Mon. Not. R. Astron. Soc.* **2012**, *421*, 116–131.

[88] Grassi, T.; Bovino, S.; Schleicher, D. R. G.; Prieto, J.; Seifried, D.; Simoncini, E.; Gianturco, F. A. *Mon. Not. R. Astron. Soc.* **2014**, *439*, 2386–2419.

[89] Pettitt, A. R.; Dobbs, C. L.; Acreman, D. M.; Price, D. J. *Mon. Not. R. Astron. Soc.* **2014**, *444*, 919–941.

[90] Smith, R. J.; Glover, S. C. O.; Clark, P. C.; Klessen, R. S.; Springel, V. *Mon. Not. R. Astron. Soc.* **2014**, *441*, 1628–1645.

[91] Mathews, L. D.; Adams, N. G. *Int. J. Mass Spectrom.* **2011**, *299*, 139 – 144.

[92] Sobel, D. *The Glass Universe: How the Ladies of the Harvard Observatory Took the Measure of the Stars*; Penguin, 2016.

[93] Merrill, P. W. *Publ. Astron. Soc. Pac.* **1934**, *46*, 206.

[94] Heger, M. L. *Lick Obs. Bull.* **1922**, *10*, 146–147.

[95] Hartmann, J. *Astrophys. J.* **1904**, *19*, 268–286.

[96] Swings, P.; Rosenfeld, L. *Astrophys. J.* **1937**, *86*, 483–486.

[97] Merrill, P. W.; Sanford, R. F.; Wilson, O. C.; Burwell, C. G. *Astrophys. J.* **1937**, *86*, 274.

[98] McKellar, A. *Pub. Astron. Soc. Pac.* **1940**, *52*, 187.

[99] Douglas, . E.; Herzberg, G. *Astrophys. J.* **1941**, *94*, 381.

[100] Douglas, A. E. *Nature* **1977**, *269*, 130–132.

[101] Salama, F.; Galazutdinov, G.; Krełowski, J.; Allamandola, L.; Musaev, F. *Astrophys. J.* **1999**, *526*, 265.

[102] Krełowski, J. *Adv. Space Res.* **2002**, *30*, 1395–1407.

[103] Motylewski, T.; Linnartz, H.; Vaizert, O.; Maier, J. P.; Galazutdinov, G. A.; Musaev, F. A.; Krełowski, J.; Walker, G. A. H.; Bohlender, D. A. *Astrophys. J.* **2000**, *531*, 312.

[104] Maier, J. P. *Chem. Soc. Rev.* **1997**, *26*, 21–28.

[105] Bréchignac, P.; Pino, T. *Astron. Astrophys.* **1999**, *343*, L49–L52.

[106] Maier, J. P.; Bohlender, D. A. *Astrophys. J.* **2004**, *602*, 286–290.

[107] Campbell, E. K.; Holz, M.; Gerlich, D.; Maier, J. P. *Nature* **2015**, *523*, 322.

[108] Walker, G. A. H.; Bohlender, D. A.; Maier, J. P.; Campbell, E. K. *Astrophys. J. Lett.* **2015**, *812*, L8.

[109] Walker, G.; Campbell, E.; Maier, J.; Bohlender, D.; Malo, L. *Astrophys. J.* **2016**, *831*, 130.

[110] Cordiner, M. A.; Linnartz, H.; Cox, N. L. J.; Cami, J.; Najarro, F.; Proffitt, C. R.; Lallement, R.; Ehrenfreund, P.; Foing, B. H.; Gull, T. R.; Sarre, P. J.; Charnley, S. B. *Astrophys. J. Lett.* **2019**, *875*, L28.

[111] Jacquinet-Husson, N. et al. *J. Quant. Spectrosc. Ra.* **2008**, *109*, 1043 – 1059.

[112] Rothman, L. et al. *J. Quant. Spectrosc. Ra.* **2005**, *96*, 139 – 204.

[113] Rothman, L. et al. *J. Quant. Spectrosc. Ra.* **2009**, *110*, 533 – 572, HITRAN.

[114] Jr, C. W. B.; Boersma, C.; Ricca, A.; Mattioda, A. L.; Cami, J.; Peeters, E.; de Armas, F. S.; Saborido, G. P.; Hudgins, D. M.; Allamandola, L. J. *Astrophys. J. Suppl. Ser.* **2010**, *189*, 341–351.

[115] Boersma, C.; andA. Ricca, C. W. B. J.; Mattioda, A. L.; Cami, J.; Peeters, E.; de Armas, F. S.; Saborido, G. P.; Hudgins, D. M.; Allamandola, L. J. *Astrophys. J. Suppl. Ser.* **2014**, *211*, 1–12.

[116] Cami, J. *EAS Publ. Ser.* **2011**, *46*, 117–122.

[117] Müller, H. S. P.,; , S.,; Roth, D. A.,; Winnewisser, G., *Astron. Astrophys.* **2001**, *370*, L49–L52.

[118] Müller, H. S.; Schlöder, F.; Stutzki, J.; Winnewisser, G. *J. Mol. Struct.* **2005**, *742*, 215 – 227.

[119] Lovas, F. J. *J. Phys. Chem. Ref. Data* **1992**, *21*, 181–272.

[120] Bailey, J.; Ahlsved, L.; Meadows, V. *Icarus* **2011**, *213*, 218 – 232.

[121] Maier, J. P.; Lakin, N. M.; Walker, G. A. H.; Bohlender, D. A. *Astrophys. J.* **2001**, *553*, 267–273.

[122] Kwok, S. *Astrophys. Space Sci.* **2009**, *319*, 5–21.

[123] Lacy, J. H.; Evans, N. J., II; Achtermann, J. M.; Bruce, D. E.; Arens, J. F.; Carr, J. S. *Astrophys. J.* **1989**, *342*, L43–L46.

[124] Gillett, F. C. *Astrophys. J.* **1975**, *201*, L41–L43.

[125] Singh, S.; McCord, T.; Combe, J.-P.; Rodriguez, S.; Cornet, T.; Le Mouélic, S.; Clark, R.; Maltagliati, L.; Chevrier, V. *Astrophys. J.* **2016**, *828*, 55.

[126] Jeilani, Y. A.; Fearce, C.; Nguyen, M. T. *Phys. Chem. Chem. Phys.* **2015**, *17*, 24294–24303.

[127] Tokunaga, A.; Beck, S.; Geballe, T.; Lacy, J. *Bull. Am. Astr. Soc.* **1980**, *12*, 669.

[128] Curtis, R. A.; Farrar, J. M. *J. Chem. Phys.* **1985**, *83*, 2224–2237.

[129] Martinez Jr, O.; Betts, N. B.; Villano, S. M.; Eyet, N.; Snow, T. P.; Bierbaum, V. M. *Astrophys. J.* **2008**, *686*, 1486.

[130] Shemansky, D. E.; Stewart, A. I. F.; West, R. A.; Esposito, L. W.; Hallett, J. T.; Liu, X. *Science* **2005**, *308*, 978–982.

[131] Lavvas, P.; Coustenis, A.; Vardavas, I. *Planet. Space Sci.* **2008**, *56*, 67 – 99.

[132] Pedersen, J. O. P.; Opansky, B. J.; Leone, S. R. *J. Phys. Chem.* **1993**, *97*, 6822–6829.

[133] Abbas, O.; Schulze-Makuch, D. *Catalyst* **2002**, *518*, 345–348.

[134] Gu, X.; Guo, Y.; Zhang, F.; Mebel, A. M.; Kaiser, R. I. *Faraday Discuss.* **2006**, *133*, 245–275.

[135] Field, F.; Franklin, J.; Lampe, F. *J. Am. Chem. Soc.* **1957**, *79*, 2665–2669.

[136] Rudolph, P. S.; Melton, C. E. *J. Phys. Chem.* **1959**, *63*, 916–918.

[137] Myher, J. J.; Harrison, A. G. *Can. J. Chem.* **1968**, *46*, 1755–1762.

[138] Barlow, S. E.; Dunn, G. H.; Schauer, M. *Phys. Rev. Lett.* **1984**, *52*, 902–905.

[139] Turner, T.; Lee, Y. T. *J. Chem. Phys.* **1984**, *81*, 5638–5643.

[140] Knight, J. S.; Freeman, C. G.; McEwan, M. J.; Anicich, V. G.; Huntress, W. T. *J. Phys. Chem.* **1987**, *91*, 3898–3902.

[141] Hawley, M.; Smith, M. A. *J. Am. Chem. Soc.* **1989**, *111*, 8293–8294.

[142] Hawley, M.; Smith, M. A. *J. Chem. Phys.* **1992**, *96*, 1121–1127.

[143] Glassgold, A.; Omont, A.; Guelin, M. *Astrophys. J.* **1992**, *396*, 115–119.

[144] Coolbaugh, M. T.; Whitney, S. G.; Vaidyanathan, G.; Garvey, J. F. *J. Phys. Chem.* **1992**, *96*, 9139–9144.

[145] Keady, J. J.; Ridgway, S. T. *Astrophys. J.* **1993**, *406*, 199–214.

[146] Le Page, V.; Keheyan, Y.; Bierbaum, V. M.; Snow, T. P. *J. Am. Chem. Soc.* **1997**, *119*, 8373–8374.

[147] Žabka, J.; Dolejšek, Z.; Hrušák, J.; Herman, Z. *Int. J. Mass Spectrom.* **1999**, *185-187*, 195 – 205.

[148] Momoh, P. O.; Abrash, S. A.; Mabrouki, R.; El-Shall, M. S. *J. Am. Chem. Soc.* **2006**, *128*, 12408–12409, PMID: 16984178.

[149] Momoh, P. O.; Xie, E.; Abrash, S. A.; Meot-Ner, M.; El-Shall, M. S. *J. Phys. Chem. A* **2008**, *112*, 6066–6073.

[150] Kočišek, J.; Lengyel, J.; Fárník, M. *J. Chem. Phys.* **2013**, *138*, 124306.

[151] Bera, P. P.; Peverati, R.; Head-Gordon, M.; Lee, T. J. *Phys. Chem. Chem. Phys.* **2015**, *17*, 1859–1869.

[152] Relph, R. A.; Bopp, J. C.; Roscioli, J. R.; Johnson, M. A. *J. Chem. Phys.* **2009**, *131*, 114305–114305.

[153] Fárník, M.; Poterya, V.; Votava, O.; Ončák, M.; Slavíček, P.; Dauster, I.; Buck, U. *J. Phys. Chem. A* **2009**, *113*, 7322–7330.

[154] Douberly, G. E.; Ricks, A. M.; Ticknor, B. W.; McKee, W. C.; v. R Schleyer, P.; Duncan, M. A. *J. Phys. Chem. A* **2008**, *112*, 1897–1906.

[155] Ono, Y.; Ng, C. Y. *J. Am. Chem. Soc.* **1982**, *104*, 4752–4758.

[156] Catani, K. J.; Muller, G.; da Silva, G.; Bieske, E. J. *J. Chem. Phys.* **2017**, *146*, 044307.

[157] Zwier, T. S.; Allen, M. *Icarus* **1996**, *123*, 578 – 583.

[158] Kaiser, R. I.; Balucani, N.; Charkin, D. O.; Mebel, A. M. *Chem. Phys. Lett.* **2003**, *382*, 112 – 119.

[159] van Der Hart, W. J.; Oosterveld, E.; Molenaar-Langeveld, T. A.; Nibbering, N. M. M. *J. Mass. Spectrom.* **1989**, *24*, 59–62.

[160] Dheandhanoo, S.; Forte, L.; Fox, A.; Bohme, D. K. *Can. J. Chem.* **1986**, *64*, 641–648.

[161] Zhou, L.; Zheng, W.; Kaiser, R. I.; Landera, A.; Mebel, A. M.; Liang, M.-C.; Yung, Y. L. *Astrophys. J.* **2010**, *718*, 1243.

[162] Yang, Y.; Li, Z.; Zhao, Y.; Wan, S.; Liu, H.; Huang, X.; Sun, C. *Comput. Theor. Chem.* **2012**, *991*, 66–73.

[163] Gronowski, M.; Kołos, R.; Krełowski, J. *Chem. Phys. Lett.* **2013**, *582*, 56–59.

[164] Ramos, C.; Winter, P. R.; Zwier, T. S.; Pratt, S. T. *J. Chem. Phys.* **2002**, *116*, 4011–4022.

[165] Schwell, M.; Bénilan, Y.; Fray, N.; Gazeau, M.-C.; Es-Sebbar, E.; Gaie-Levrel, F.; Champion, N.; Leach, S. *Mol. Phys.* **2012**, *110*, 2843–2856.

[166] Schüler, H.; Reinebeck, L. *Z. Naturforsch. A* **1951**, *6*, 160–165.

[167] Callomon, J. *Can. J. Phys.* **1956**, *34*, 1046–1074.

[168] Szczepanski, J.; Wang, H.; Jones, B.; Arrington, C. A.; Vala, M. T. *Phys. Chem. Chem. Phys.* **2005**, *7*, 738–742.

[169] Bondybey, V.; English, J. *J. Chem. Phys.* **1979**, *71*, 777–782.

[170] Maier, J.; Chakrabarty, S.; Mazzotti, F.; Rice, C.; Dietsche, R.; Walker, G.; Bohlender, D. *Astrophys. J. Lett.* **2011**, *729*, L20.

[171] Schmidt, T. W.; Pino, T.; van Wijngaarden, J.; Tikhomirov, K.; Güthe, F.; Maier, J. P. *J. Mol. Spectrosc.* **2003**, *222*, 86–92.

[172] Allan, M.; Kloster-Jensen, E.; Maier, J. P. *Chem. Phys.* **1976**, *17*, 11 – 18.

[173] Bally, T.; Tang, W.; Jungen, M. *Chem. Phys. Lett.* **1992**, *190*, 453–459.

[174] Fulara, J.; Grutter, M.; Maier, J. P. *J. Phys. Chem. A* **2007**, *111*, 11831–11836.

[175] Teanby, N.; Irwin, P.; de Kok, R.; Jolly, A.; Bézard, B.; Nixon, C.; Calcutt, S. *Icarus* **2009**, *202*, 620 – 631.

[176] E., K. R.; H., R. D. *J. Mass. Spectrom.* **1985**, *20*, 606–613.

[177] Zhang, M. Y.; Carpenter, B. K.; McLafferty, F. W. *J. Am. Chem. Soc.* **1991**, *113*, 9499–9503.

[178] Hrouda, V.; Roeselova, M.; Bally, T. *J. Phys. Chem. A* **1997**, *101*, 3925–3935.

[179] Ono, Y.; Ng, C. Y. *J. Chem. Phys.* **1982**, *77*, 2947–2955.

[180] Momoh, P. O.; Hamid, A. M.; Abrash, S. A.; El-Shall, M. S. *J. Chem. Phys.* **2011**, *134*, 204315.

[181] Lifshitz, C.; Gibson, D.; Levsen, K.; Dotan, I. *Int. J. Mass Spectrom. and Ion Phys.* **1981**, *40*, 157–165.

[182] Herrebout, D.; Bogaerts, A.; Gijbels, R.; Goedheer, W. J.; Vanhulsel, A. *IEEE Trans. Plasma Sci.* **2003**, *31*, 659–664.

[183] Bera, P. P.; Head-Gordon, M.; Lee, T. J. *Phys. Chem. Chem. Phys.* **2013**, *15*, 2012–2023.

[184] Bandyopadhyay, B.; Stein, T.; Fang, Y.; Kostko, O.; White, A.; Head-Gordon, M.; Ahmed, M. *J. Phys. Chem. A* **2016**, *120*, 5053–5064.

[185] Booze, J. A.; Baer, T. *J. Chem. Phys.* **1993**, *98*, 186–200.

[186] Rosenstock, H.; Larkins, J.; Walker, J. *Int. J. Mass Spectrom. and Ion Phys.* **1973**, *11*, 309 – 328.

[187] Rosenstock, H.; McCulloh, K.; Lossing, F. *Int. J. Mass Spectrom. and Ion Phys.* **1977**, *25*, 327–341.

[188] Ausloos, P. *J. Am. Chem. Soc.* **1981**, *103*, 3931–3932.

[189] Krailler, R. E.; Russell, D. H.; Jarrold, M. F.; Bowers, M. T. *J. Am. Chem. Soc.* **1985**, *107*, 2346–2354.

[190] Booze, J. A.; Baer, T. *J. Chem. Phys.* **1993**, *98*, 186–200.

[191] Koster, G.; Van der Hart, W. *Int. J. Mass Spectrom. Ion Process.* **1997**, *163*, 169–175.

[192] Cernicharo, J.; Heras, A. M.; Tielens, A. G. G. M.; Pardo, J. R.; Herpin, F.; Guélin, M.; Waters, L. B. F. M. *Astrophys. J. Lett.* **2001**, *546*, L123.

[193] Wilson, E. H.; Atreya, S. K. *J. Geophys. Res. Planets* **2003**, *109*.

[194] Stearns, J. A.; Zwier, T. S.; Kraka, E.; Cremer, D. *Phys. Chem. Chem. Phys.* **2006**, *8*, 5317–5327.

[195] Kaiser, R. I.; Parker, D. S.; Mebel, A. M. *Ann. Rev. Phys. Chem.* **2015**, *66*, 43–67, PMID: 25422849.

[196] Zhang, F.; Kim, Y. S.; Kaiser, R. I.; Krishtal, S. P.; Mebel, A. M. *J. Phys. Chem. A* **2009**, *113*, 11167–11173.

[197] Cremer, D.; Kraka, E.; Joo, H.; Stearns, J. A.; Zwier, T. S. *Phys. Chem. Chem. Phys.* **2006**, *8*, 5304–5316.

[198] Mebel, A. M.; KisIov, V. V.; Kaiser, R. I. *J. Chem. Phys.* **2006**, *125*, 133113.

[199] Kohn, D. W.; Chen, P. *J. Am. Chem. Soc.* **1993**, *115*, 2844–2848.

[200] Staley, S. W.; Norden, T. D. *J. Am. Chem. Soc.* **1989**, *111*, 445–449.

[201] Brogli, F.; Heilbronner, E.; Wirz, J.; Kloster-Jensen, E.; Bergman, R. G.; Vollhardt, K. P. C.; Ashe, A. J. *Helvetica Chimica Acta* **1975**, *58*, 2620–2645.

[202] Kharnaior, K. S.; Chandra, A. K.; Lyngdoh, R. D. *Comput. Theor. Chem.* **2017**, *1115*, 158–168.

[203] Holland, D.; Shaw, D.; Sumner, I.; Bowler, M.; Mackie, R.; Shpinkova, L.; Cooper, L.; Rennie, E.; Parker, J.; Johnson, C. *Int. J. Mass Spectrom.* **2002**, *220*, 31–51.

[204] Fournier, J. A.; Shuman, N. S.; Melko, J. J.; Ard, S. G.; Viggiano, A. A. *J. Chem. Phys.* **2013**, *138*, 154201.

[205] Bruckmann, P.; Klessinger, M. *J. Electron Spectrosc.* **1973**, *2*, 341–354.

[206] Araki, M.; Cias, P.; Denisov, A.; Fulara, J.; Maier, J. P. *Can. J. Chem.* **2004**, *82*, 848–853.

[207] Filipkowski, K.; Fulara, J.; Maier, J. P. *J. Mol. Spectrosc.* **2015**, *310*, 45–49.

[208] Chin, C.-H.; Chen, W.-K.; Huang, W.-J.; Lin, Y.-C.; Lee, S.-H. *Icarus* **2013**, *222*, 254 – 262.

[209] Hansen, N.; Klippenstein, S. J.; Taatjes, C. A.; Miller, J. A.; Wang, J.; Cool, T. A.; Yang, B.; Yang, R.; Wei, L.; Huang, C.; Wang, J.; Qi, F.; Law, M. E.; Westmoreland, P. R. *J. Phys. Chem. A* **2006**, *110*, 3670–3678.

[210] Cole, J.; Bittner, J.; Longwell, J.; Howard, J. *Combust. Flame* **1984**, *56*, 51–70.

[211] Parr, A. C.; Elder, F. A. *J. Chem. Phys.* **1968**, *49*, 2659–2664.

[212] Calcote, H. F.; Olson, D. B.; Keil, D. G. *Energy & Fuels* **1988**, *2*, 494–504.

[213] Krishtal, S. P.; Mebel, A. M.; Kaiser, R. I. *J. Phys. Chem. A* **2009**, *113*, 11112–11128.

[214] Kaiser, R. I.; Stranges, D.; Bevsek, H. M.; Lee, Y. T.; Suits, A. G. *J. Chem. Phys.* **1997**, *106*, 4945–4953.

[215] Fahr, A.; Laufer, A. H. *J. Phys. Chem. A* **2005**, *109*, 2534–2539.

[216] Boechat-Roberty, H. M.; Neves, R.; Pilling, S.; Lago, A. F.; De Souza, G. G. B. *Mon. Not. R. Astron. Soc.* **2009**, *394*, 810–817.

[217] Krasnopolsky, V. A. *Icarus* **2009**, *201*, 226–256.

[218] Bourgalais, J.; Spencer, M.; Osborn, D. L.; Goulay, F.; Picard, S. D. L. *J. Phys. Chem. A* **2016**, *120*, 9138–9150.

[219] Capron, M.; Bourgalais, J.; Abhinavam Kailasanathan, R. K.; Osborn, D. L.; Le Picard, S. D.; Goulay, F. *Phys. Chem. Chem. Phys.* **2015**, *17*, 23833–23846.

[220] Loison, J.-C.; Bergeat, A. *Phys. Chem. Chem. Phys.* **2004**, *6*, 5396–5401.

[221] Waite, J. H. et al. *Science* **2005**, *308*, 982–986.

[222] Beussman, D. J.; Erickson, T. A.; Enke, C. G. *J. Am. Soc. Mass Spectrom.* **1996**, *7*, 114–117.

[223] Hehre, W. J.; Devaquet, A. J. P. *J. Am. Chem. Soc.* **1976**, *98*, 4370–4377.

[224] Cunje, A.; Rodriquez, C. F.; Lien, M. H.; Hopkinson, A. C. *J. Org. Chem.* **1996**, *61*, 5212–5220.

[225] Douberly, G. E.; Ricks, A. M.; Ticknor, B. W.; McKee, W. C.; Schleyer, P. v. R.; Duncan, M. A. *J. Phys. Chem. A* **2008**, *112*, 1897–1906.

[226] Apeloig, Y.; M*ü*ller, T. In *Dicoordinated Carbocations*; Rappoport, Z., Stang, P., Eds.; Wiley: Chichester, 1997; Chapter 5.

[227] Dorado, M.; Mo, O.; Yanez, M. *J. Am. Chem. Soc.* **1980**, *102*, 947–950.

[228] van Alem, K.; Lodder, G.; Zuilhof, H. *J. Phys. Chem. A* **2002**, *106*, 10681–10690.

[229] Hrodmarsson, H. R.; Loison, J.-C.; Jacovella, U.; Holland, D. M.; Boyé-Péronne, S.; Gans, B.; Garcia, G. A.; Nahon, L.; Pratt, S. T. *J. Phys. Chem. A* **2019**, *123*, 1521–1528.

[230] Lang, M.; Holzmeier, F.; Hemberger, P.; Fischer, I. *J. Phys. Chem. A* **2015**, *119*, 3995–4000.

[231] Minsek, D. W.; Chen, P. *J. Phys. Chem.* **1990**, *94*, 8399–8401.

[232] Gao, H.; Lu, Z.; Yang, L.; Zhou, J.; Ng, C. Y. *J. Chem. Phys.* **2012**, *137*, 161101.

[233] Garcia, G. A.; Gans, B.; Krüger, J.; Holzmeier, F.; Röder, A.; Lopes, A.; Fittschen, C.; Alcaraz, C.; Loison, J.-C. *Phys. Chem. Chem. Phys.* **2018**, *20*, 8707–8718.

[234] Catani, K. J.; Sanelli, J. A.; Dryza, V.; Gilka, N.; Taylor, P. R.; Bieske, E. J. *J. Chem. Phys.* **2015**, *143*, 184306.

[235] Kiefer, J. H.; Mizerka, L. J.; Patel, M. R.; Wei, H. C. *J. Phys. Chem.* **1985**, *89*, 2013–2019.

[236] Mebel, A. M.; Lin, M. C.; Chakraborty, D.; Park, J.; Lin, S. H.; Lee, Y. T. *J. Chem. Phys.* **2001**, *114*, 8421–8435.

[237] Zhang, F.; Parker, D.; Kim, Y. S.; Kaiser, R. I.; Mebel, A. M. *Astrophys. J.* **2011**, *728*, 141.

[238] Weaver, S. L. W.; Remijan, A. J.; McMahon, R. J.; McCall, B. J. *Astrophys. J. Lett.* **2007**, *671*, L153.

[239] Grützmacher, H.-F.; Lohmann, J. *Justus Liebigs Ann. Chem.* **1967**, *705*, 81–90.

[240] Dewar, M. J. S.; Li, W.-K. *J. Am. Chem. Soc.* **1974**, *96*, 5569–5571.

[241] Dewar, M. J.; Tien, T.-P. *J. Chem. Soc. Chem. Comm.* **1985**, 1243–1244.

[242] Chrostowska, A.; Pfister-Guillouzo, G.; Gracian, F.; Wentrup, C. *Aust. J. Chem.* **2010**, *63*, 1084–1090.

[243] Simon, J. G. G.; Specht, H.; Schweig, A. *Chem. Phys. Lett.* **1992**, *200*, 459–464.

[244] Dannacher, J. *Chem. Phys.* **1978**, *29*, 339–344.

[245] Tseng, C.-M.; Choi, Y.; Huang, C.-L.; Ni, C.-K.; Lee, Y. T.; Lin, M. *J. Phys. Chem. A* **2004**, *108*, 7928–7935.

[246] Miasek, P.; Beauchamp, J. *Int. J. Mass Spectrom. and Ion Phys.* **1974**, *15*, 49 – 66.

[247] Contreras, C. S.; Salama, F. *Astrophys. J., Suppl. Ser.* **2013**, *208*, 6.

[248] Sciamma-O'Brien, E.; Ricketts, C. L.; Salama, F. *Icarus* **2014**, *243*, 325 – 336.

[249] Wagner-Redeker, W.; Illies, A. J.; Kemper, P. R.; Bowers, M. T. *J. Am. Chem. Soc.* **1983**, *105*, 5719–5724.

[250] Anicich, V. G.; Blake, G. A.; Kim, J. K.; McEwan, M. J.; Huntress Jr, W. T. *J. Phys. Chem.* **1984**, *88*, 4608–4617.

[251] Vitvitskii, A. *Theor. Exp. Chem.* **1967**, *2*, 297–302.

[252] Rosenstock, H. M.; Stockbauer, R.; Parr, A. C. *J. Chim. Phys.* **1980**, *77*, 745–750.

[253] Molenaar-Langeveld, T. A.; Fokkens, R. H.; Nibbering, N. M. *J. Mass. Spectrom.* **1986**, *21*, 15–21.

[254] Khoroshev, D.; Araki, M.; Kolek, P.; Birza, P.; Chirokolava, A.; Maier, J. P. *J. Mol. Spectrosc.* **2004**, *227*, 81–89.

[255] Araki, M.; Motylewski, T.; Kolek, P.; Maier, J. P. *Phys. Chem. Chem. Phys.* **2005**, *7*, 2138–2141.

[256] Fulara, J.; Nagy, A.; Filipkowski, K.; Thimmakondu, V. S.; Stanton, J. F.; Maier, J. P. *J. Phys. Chem. A* **2013**, *117*, 13605–13615.

[257] Moini, M.; Leroi, G. E. *J. Phys. Chem.* **1986**, *90*, 4002–4006.

[258] Liu, H.-C.; Wang, C.-S.; Guo, W.; Wu, Y.-D.; Yang, S. *J. Am. Chem. Soc.* **2002**, *124*, 3794–3798.

[259] Hillier, I.; Vincent, M.; Guest, M.; Niessen, W. V. *Chem. Phys. Lett.* **1987**, *134*, 403 – 406.

[260] Li, H.; Huang, M.-B. *Phys. Chem. Chem. Phys.* **2008**, *10*, 5381 – 5387.

[261] Kaiser, D.; Reusch, E.; Hemberger, P.; Bodi, A.; Welz, E.; Engels, B.; Fischer, I. *Phys. Chem. Chem. Phys.* **2018**, *20*, 3988–3996.

[262] Maier, J. P. *J. Phys. Chem. A* **1998**, *102*, 3462–3469.

[263] Wild, D. A.; Bieske, E. J. *Int. Rev. Phys. Chem.* **2003**, *22*, 129–151.

[264] Duncan, M. A. *Int. J. Mass Spectrom.* **2000**, *200*, 545 – 569.

[265] Leckenby, R.; Robbins, E. *Proc. R. Soc. London* **1966**, *291*, 389–412.

[266] Féraud, G.; Dedonder, C.; Jouvet, C.; Inokuchi, Y.; Haino, T.; Sekiya, R.; Ebata, T. *J. Phys. Chem. Lett.* **2014**, *5*, 1236–1240.

[267] Kang, H.; Féraud, G.; Dedonder-Lardeux, C.; Jouvet, C. *J. Phys. Chem. Lett.* **2014**, *5*, 2760–2764.

[268] Snoek, L. C.; Kroemer, R. T.; Simons, J. P. *Phys. Chem. Chem. Phys.* **2002**, *4*, 2130–2139.

[269] Scherzer, W.; Selzle, H.; Schlag, E. *Chem. Phys. Lett.* **1992**, *195*, 11–15.

[270] Wörner, H. J.; Merkt, F. *Handbook of High-resolution Spectroscopy*; Wiley & Sons, UK, 2011; Vol. 1; pp 176–262.

[271] Mulliken, R. S. *J. Chem. Phys.* **1955**, *23*, 1997.

[272] Herzberg, G. *Molecular Spectra and Molecular Structure*; Read Books Ltd, 2013; Vol. 1.

[273] Send, R.; Kuhn, M.; Furche, F. *J. Chem. Theory Comput.* **2011**, *7*, 2376–2386.

[274] Hollas, J. M. *Modern Spectroscopy*; John Wiley & Sons, 2004.

[275] Harris, F.; Beynon, J. *Gas Phase Ion Chemistry Vol. 3, Ions and Light*; Academic Press London, 1984; pp 99–128.

[276] Nishimura, T. *Fundamentals of Mass Spectrometry*; Springer, 2013; pp 29–54.

[277] Maier, J. P.; Thommen, F. *Gas Phase Ion Chemistry Vol. 3, Ions and Light*; Academic Press London, 1984; pp 357–391.

[278] Jortner, J.; Levine, R. D. *Advances in Chemical Physics: Photoselective Chemistry, Part 1, Volume 47*; John Wiley & Sons, 1981.

[279] Schinke, R. *Photodissociation Dynamics: Spectroscopy and Fragmentation of Small Polyatomic Molecules*; Cambridge University Press, 1995.

[280] Glowacki, D. R.; Liang, C.-H.; Morley, C.; Pilling, M. J.; Robertson, S. H. *J. Phys. Chem. A* **2012**, *116*, 9545–9560.

[281] Light, J. C. *J. Chem. Phys.* **1964**, *40*, 3221–3229.

[282] Barker, J. R.; Nguyen, T. L.; Stanton, J. F.; Aieta, C.; Ceotto, M.; Gabas, F.; Kumar, T. J. D.; Li, C. G. L.; Lohr, L. L.; Maranzana, A.; Ortiz, N. F.; Preses, J. M.; Simmie, J. M.; Sonk, J. A.; Stimac, P. J. MultiWell-2013 Software Suite; J.R. Barker, University of Michigan, Ann Arbor, Michigan, USA, 2013, http://aoss.engin.umich.edu/multiwell/.

[283] Bieske, E. J.; Dopfer, O. *Chem. Rev.* **2000**, *100*, 3963–3998.

[284] Duncan, M. A. *Int. Rev. Phys. Chem.* **2003**, *22*, 407–435.

[285] Lisy, J. M. *J. Chem. Phys.* **2006**, *125*, 132302.

[286] Oomens, J.; Pirali, O.; Tielens, A., et al. *Laboratory IR Spectroscopy of PAHs*; 2015.

[287] Navrátil, R.; Jašík, J.; Roithová, J. *J. Mol. Spectrosc.* **2017**, *332*, 52–58.

[288] Frisch, M. J. et al. Gaussian 16 Revision C.01. 2016; Gaussian Inc. Wallingford CT.

[289] Parrish, R. M. et al. *J. Chem. Theory Comput.* **2017**, *13*, 3185–3197.

[290] Neese, F. *Wiley Interdiscip. Rev. Comput. Mol.* **2018**, *8*, e1327.

[291] Møller, C.; Plesset, M. S. *Phys. Rev.* **1934**, *46*, 618.

[292] Watts, J. D.; Gauss, J.; Bartlett, R. J. *J. Chem. Phys.* **1993**, *98*, 8718.

[293] Dreuw, A.; Head-Gordon, M. *Chem. Rev.* **2005**, *105*, 4009–4037.

[294] Grimme, S. *Wiley Interdiscip. Rev. Comput. Mol. Sci.* **2011**, *1*, 211–228.

[295] Boys, S.; Bernardi, F. *Mol. Phys.* **1970**, *19*, 553–566.

[296] Salvador Sedano, P., et al. *Implementation and Application of Basis Set Superposition Error-Correction Schemes to the Theoretical Modeling of Weak Intermolecular Interactions*; Universitat de Girona, 2001.

[297] Casida, M. E.; Huix-Rotllant, M. *Ann. Rev. Phys. Chem.* **2012**, *63*, 287–323.

[298] Santoro, F.; Jacquemin, D. *Wiley Interdiscip. Rev. Comput. Mol. Sci.* **2016**, *6*, 460–486.

[299] Van Caillie, C.; Amos, R. D. *Chem. Phys. Lett.* **1999**, *308*, 249–255.

[300] Furche, F.; Ahlrichs, R. *J. Chem. Phys.* **2002**, *117*, 7433–7447.

[301] Scalmani, G.; Frisch, M. J.; Mennucci, B.; Tomasi, J.; Cammi, R.; Barone, V. *J. Chem. Phys.* **2006**, *124*, 094107.

[302] Emrich, K. *Nuclear Physics A* **1981**, *351*, 379–396.

[303] Emrich, K. *Nuclear Physics A* **1981**, *351*, 397–438.

[304] Sekino, H.; Bartlett, R. J. *Int. J. Quantum Chem.* **1984**, *26*, 255–265.

[305] Krylov, A. I. *Rev. Comp. Chem.* **2017**, *30*, 151–224.

[306] Krylov, A. I. *Annu. Rev. Phys. Chem.* **2008**, *59*, 433–462.

[307] Geertsen, J.; Rittby, M.; Bartlett, R. J. *Chem. Phys. Lett.* **1989**, *164*, 57 – 62.

[308] Stanton, J. F.; Bartlett, R. J. *J. Chem. Phys.* **1993**, *98*, 7029–7039.

[309] Watts, J. D. *Radiation Induced Molecular Phenomena in Nucleic Acids*; Springer, 2008; pp 65–92.

[310] Caricato, M.; Trucks, G. W.; Frisch, M. J.; Wiberg, K. B. *J. Chem. Theory Comput.* **2010**, *7*, 456–466.

[311] Western, C. PGOPHER, a Program for Simulating Rotational Structure. 2010; University of Bristol, http://pgopher.chm.bris.ac.uk.

[312] Duschinsky, F. *Acta Physicochim. URSS* **1937**, *7*, 551.

[313] Winnewisser, G.; Walmsley, C. *Astrophys. Space Sci.* **1979**, *65*, 83–93.

[314] Adams, N. G.; Smith, D. *Astrophys. J.* **1987**, *317*, L25–L27.

[315] Coustenis, A. et al. *Icarus* **2007**, *189*, 35–62.

[316] Gredel, R.; Lepp, S.; Dalgarno, A.; Herbst, E. *Astrophys. J.* **1989**, *347*, 289–293.

[317] Tsuji, M.; Ogawa, T.; Imasaka, T.; Nishimura, Y.; Ishibashi, N. *Bull. Chem. Soc. Jpn.* **1976**, *49*, 53–57.

[318] Koyano, I.; Tanaka, I.; Omura, I. *J. Chem. Phys.* **1964**, *40*, 2734–2735.

[319] Bloch, A. *Advan. Mass Spectom.* **1963**, 48.

[320] Yung, Y. L.; Allen, M.; Pinto, J. P. *Astrophys. J. Suppl. Ser.* **1984**, *55*, 465–506.

[321] Banaszkiewicz, M.; Lara, L.; Rodrigo, R.; López-Moreno, J.; Molina-Cuberos, G. *Icarus* **2000**, *147*, 386–404.

[322] Fonfría, J. P.; Agúndez, M.; Cernicharo, J.; Richter, M. J.; Lacy, J. H. *Astrophys. J.* **2018**, *852*, 80.

[323] Krełowski, J.; Beletsky, Y.; Galazutdinov, G.; Kołos, R.; Gronowski, M.; LoCurto, G. *Astrophys. J. Lett.* **2010**, *714*, L64.

[324] Salama, F.; Galazutdinov, G.; Krełowski, J.; Biennier, L.; Beletsky, Y.; Song, I.-O. *Astrophys. J.* **2011**, *728*, 154.

[325] Raghunandan, R.; Mazzotti, F. J.; Esmail, A. M.; Maier, J. P. *J. Phys. Chem. A* **2011**, *115*, 9365–9369.

[326] Ghosh, A.; Reddy, S. N.; Reddy, S. R.; Mahapatra, S. *J. Phys. Chem. A* **2016**, *120*, 7881–7889.

[327] Jacovella, U.; Merkt, F. *Phys. Chem. Chem. Phys.* **2017**, *19*, 23524–23531.

[328] Baker, C.; Turner, D. W. *Chem. Commun. (London)* **1967**, 797–799.

[329] Riaplov, E.; Wyss, M.; Maier, J. P.; Hochlaf, M.; Rosmus, P. *Int. J. Mass Spectrom.* **2003**, *223*, 107–114.

[330] Fulara, J.; Leutwyler, S.; Maier, J. P.; Spittel, U. *J. Phys. Chem.* **1985**, *89*, 3190–3193.

[331] Rice, C.; Rudnev, V.; Chakrabarty, S.; Maier, J. P. *J. Phys. Chem. A* **2010**, *114*, 1684–1687.

[332] Freivogel, P.; Fulara, J.; Jakobi, M.; Forney, D.; Maier, J. P. *J. Chem. Phys.* **1995**, *103*, 54–59.

[333] Freivogel, P.; Grutter, M.; Forney, D.; Maier, J. P. *J. Chem. Phys.* **1997**, *107*, 22–27.

[334] Tulej, M.; Kirkwood, D. A.; Maccaferri, G.; Dopfer, O.; Maier, J. P. *Chem. Phys.* **1998**, *228*, 293 – 299.

[335] Lecoultre, J.; Maier, J. P.; Rösslein, M. *J. Chem. Phys.* **1988**, *89*, 6081–6085.

[336] Komiha, N.; Rosmus, P.; Maier, J. P. *Mol. Phys.* **2007**, *105*, 893–897.

[337] Kuhn, R.; Maier, J. P.; Ochsner, M. *Mol. Phys.* **1986**, *59*, 441–448.

[338] Zhang, J.; Guo, X.; Cao, Z. *J. Chem. Phys.* **2009**, *131*, 144307.

[339] Neese, F. *Wiley Interdiscip. Rev. Comput. Mol.* **2012**, *2*, 73–78.

[340] Dunning, T. H. *J. Chem. Phys.* **1989**, *90*, 1007–1023.

[341] Frisch, M. J. et al. Gaussian 09 Revision A.1. Gaussian Inc. Wallingford CT 2009.

[342] Chai, J.-D.; Head-Gordon, M. *Phys. Chem. Chem. Phys.* **2008**, *10*, 6615–6620.

[343] Botschwina, P.; Oswald, R. *J. Mol. Spectrosc.* **2003**, *222*, 46 – 56.

[344] Boechat-Roberty, H. M.; Neves, R.; Pilling, S.; Lago, A. F.; De Souza, G. G. B. *Mon. Not. R. Astron. Soc.* **2009**, *394*, 810–817.

[345] Jacovella, U.; Muller, G.; Catani, K. J.; Bartlett, N. *Aust. J. Chem.* **2018**, *72*, 260–266.

[346] Hochlaf, M.; Baer, T.; Qian, X.-M.; Ng, C. Y. *J. Chem. Phys.* **2005**, *123*, 144302.

[347] Zhao, Y.; de Beer, E.; Xu, C.; Taylor, T.; Neumark, D. M. *J. Chem. Phys.* **1996**, *105*, 4905–4919.

[348] Schäfer, M.; Grutter, M.; Fulara, J.; Forney, D.; Freivogel, P.; Maier, J. P. *Chem. Phys. Lett.* **1996**, *260*, 406 – 408.

[349] Zhao, Y.; de Beer, E.; Neumark, D. M. *J. Chem. Phys.* **1996**, *105*, 2575–2582.

[350] Schmatz, S.; Botschwina, P. *Int. J. Mass Spectrom. Ion Process.* **1995**, *149*, 621 – 629.

[351] Zhao, Y.; de Beer, E.; Neumark, D. M. *J. Chem. Phys.* **1996**, *105*, 2575–2582.

[352] Adamowicz, L. *Chem. Phys.* **1991**, *156*, 387 – 394.

[353] Hiraoka, K.; Aoyama, K.; Morise, K. *Can. J. Chem.* **1985**, *63*, 2899–2905.

[354] Savel'ev, A. M.; Starik, A. M. *Tech. Phys.* **2006**, *51*, 444–452.

[355] Fialkov, A.; Homann, K.-H. *Combust. Flame* **2001**, *127*, 2076 – 2090.

[356] Chen, B.; Wang, H.; Wang, Z.; Han, J.; Alquaity, A. B.; Wang, H.; Hansen, N.; Sarathy, S. M. *Combust. Flame* **2019**, *202*, 208 – 218.

[357] Glassgold, A. E.; Mamon, G. A.; Omont, A.; Lucas, R. *Astron. Astrophys.* **1987**, *180*, 183–190.

[358] Keller, C.; Anicich, V.; Cravens, T. *Planetary and Space Science* **1998**, *46*, 1157–1174.

[359] Ali, A.; Sittler, E.; Chornay, D.; Rowe, B.; Puzzarini, C. *Planet. Space Sci.* **2013**, *87*, 96 – 105.

[360] Yim, M. K.; Choe, J. C. *J. Phys. Chem. A* **2011**, *115*, 3087–3094.

[361] Baer, T.; Willett, G. D.; Smith, D.; Phillips, J. S. *J. Chem. Phys.* **1979**, *70*, 4076–4085.

[362] Kreile, J.; Münzel, N.; Schweig, A.; Specht, H. *Chem. Phys. Lett.* **1986**, *124*, 140–146.

[363] Mulliken, R. S. *J. Chem. Phys.* **1955**, *23*, 1997–2011.

[364] Mulliken, R. S. *J. Chem. Phys.* **1956**, *24*, 1118–1118.

[365] Podkopaeva, O. Y.; Chizhov, Y. V. *J. Struct. Chem.* **2006**, *47*, 420–426.

[366] Garner, M. H.; Hoffmann, R.; Rettrup, S.; Solomon, G. C. *ACS Cent. Sci.* **2018**, *4*, 688–700.

[367] Cattarius, C.; Worth, G. A.; Meyer, H.-D.; Cederbaum, L. *J. Chem. Phys.* **2001**, *115*, 2088–2100.

[368] Hendon, C. H.; Tiana, D.; Murray, A. T.; Carbery, D. R.; Walsh, A. *Chemical Science* **2013**, *4*, 4278–4284.

[369] Brogli, F.; Heilbronner, E.; Kloster-Jensen, E.; Schmelzer, A.; Manocha, A.; Pople, J.; Radom, L. *Chem. Phys.* **1974**, *4*, 107–119.

[370] Araki, M.; Uchida, S.; Matsushita, Y.; Tsukiyama, K. *J. Mol. Spectrosc.* **2014**, *297*, 51 – 57.

[371] Roeselová, M.; Bally, T.; Jungwirth, P.; Čársky, P. *Chem. Phys. Lett.* **1995**, *234*, 395–404.

[372] Lauer, G.; Schulte, K. W.; Schweig, A. *J. Am. Chem. Soc.* **1978**, *100*, 4925–4935.

[373] Bally, T.; Masamune, S. *Tetrahedron* **1980**, *36*, 343–370.

[374] Correia, N.; Baker, J. *J. Phys. Chem.* **1985**, *89*, 3861–3863.

[375] Saddique, S.; Worth, G. *Chem. Phys.* **2006**, *329*, 99–108.

[376] Ehara, M.; Nakata, M.; Nakatsuji, H. *Mol. Phys.* **2006**, *104*, 971–982.

[377] Stein, T.; Bandyopadhyay, B.; Troy, T. P.; Fang, Y.; Kostko, O.; Ahmed, M.; Head-Gordon, M. *P. Natl. Acad. Sci.* **2017**, *114*, E4125–E4133.

[378] Ruscic, B.; Pinzon, R. E.; Morton, M. L.; von Laszevski, G.; Bittner, S. J.; Nijsure, S. G.; Amin, K. A.; Minkoff, M.; Wagner, A. F. *J. Phys. Chem. A* **2004**, *108*, 9979–9997.

[379] Takami, M.; Ohshima, Y.; Yamamoto, S.; Matsumoto, Y. *Faraday Discuss. Chem. Soc.* **1988**, *86*, 1–12.

[380] Yu, J.; Su, S.; Bloor, J. E. *J. Phys. Chem.* **1990**, *94*, 5589–5592.

[381] Fraser, G.; Suenram, R.; Lovas, F.; Pine, A.; Hougen, J. T.; Lafferty, W.; Muenter, J. *J. Chem. Phys.* **1988**, *89*, 6028–6045.

[382] Fraser, G. *J. Chem. Phys.* **1989**, *90*, 2097–2108.

[383] Alberts, I. L.; Rowlands, T. W.; Handy, N. C. *J. Chem. Phys.* **1988**, *88*, 3811–3816.

[384] Prichard, D. G.; Nandi, R.; Muenter, J. *J. Chem. Phys.* **1988**, *89*, 115–123.

[385] Prichard, D.; Muenter, J.; Howard, B. *Chem. Phys. Lett.* **1987**, *135*, 9–15.

[386] Rosenstock, H.; Dannacher, J.; Liebman, J. *Radiat. Phys. Chem.* **1982**, *20*, 7–28.

[387] Holland, D.; Shaw, D.; Sumner, I.; Bowler, M.; Mackie, R.; Shpinkova, L.; Cooper, L.; Rennie, E.; Parker, J.; Johnson, C. *Int. J. Mass Spectrom.* **2002**, *220*, 31 – 51.

[388] van der Hartcor, W. *J. Am. Soc. Mass Spectrom.* **1995**, *6*, 513–515.

[389] Van der Hart, W. *J. Am. Soc. Mass Spectrom.* **1996**, *7*, 731–736.

[390] Van der Hart, W. *Int. J. Mass Spectrom.* **1998**, *176*, 23–38.

[391] Keough, T.; Ast, T.; Beynon, J.; Cooks, R. *J. Mass. Spectrom.* **1973**, *7*, 245–247.

[392] Zhang, M. Y.; Wesdemiotis, C.; Marchetti, M.; Danis, P. O.; Ray Jr, J. C.; Carpenter, B. K.; McLafferty, F. W. *J. Am. Chem. Soc.* **1989**, *111*, 8341–8346.

[393] Fukui, K. *Acc. Chem. Res.* **1981**, *14*, 363–368.

[394] Boys, S.; Bernardi, F. *Mol. Phys.* **1970**, *19*, 553.

[395] Niessen, W. V.; Diercksen, G.; Cederbaum, L.; Domcke, W. *Chem. Phys.* **1976**, *18*, 469 – 476.

[396] Pedash, Y. F.; Umanskii, V. *Theor. Exp. Chem.* **1994**, *29*, 342–344.

[397] Pless, V.; Suter, H.; Engels, B. *J. Chem. Phys.* **1994**, *101*, 4042–4048.

[398] Woodcock, H. L.; Schaefer, H. F.; Schreiner, P. R. *J. Phys. Chem. A* **2002**, *106*, 11923–11931.

[399] Massó, H.; Senent, M. L. *J. Phys. Chem. A* **2009**, *113*, 12404–12410.

[400] Hayhurst, A. N.; Jones, H. R. N. *J. Chem. Soc. Faraday Trans. 2* **1987**, *83*, 1–27.

[401] Wilson, E. H.; Atreya, S. K. *J. Geophys. Res. Planets* **2004**, *109*.

[402] Atreya, S. *Science* **2007**, *316*, 843–845.

[403] Dopfer, O.; Roth, D.; Maier, J. P. *Int. J. Mass Spectrom.* **2002**, *218*, 281–297.

[404] Duncan, M. A. *J. Phys. Chem. A* **2012**, *116*, 11477–11491.

[405] Vuitton, V.; Yelle, R.; Lavvas, P. *Phil. Trans. Royal Soc. A Math Phys. Eng. Sci.* **2009**, *367*, 729–741.

[406] Li, A.; Jjunju, F. P. M.; Cooks, R. G. *J. Am. Soc. Mass Spectr.* **2013**, *24*, 1745–1754.

[407] Wyss, M.; Riaplov, E.; Maier, J. P. *J. Chem. Phys.* **2001**, *114*, 10355–10361.

[408] Lalli, P. M.; Corilo, Y. E.; Abdelnur, P. V.; Eberlin, M. N.; Laali, K. K. *Org. Biomol. Chem.* **2010**, *8*, 2580–2585.

[409] Pei, L.; Farrar, J. M. *J. Phys. Chem. A* **2016**, *120*, 6122–6128.

[410] Bieske, E. J. *J. Chem. Soc., Faraday Trans.* **1995**, *91*, 1–12.

[411] Barker, J. R. *Inter. J. Chem. Kinet.* **2001**, *33*, 232–245.

[412] Barker, J. R. *Inter. J. Chem. Kinet.* **2009**, *41*, 748–763.

[413] Stein, S. E.; Rabinovitch, B. S. *J. Chem. Phys* **1973**, *58*, 2438–2445.

[414] Hippler, H.; Troe, J.; Wendelken, H. J. *J. Chem. Phys.* **1983**, *78*, 6709–6717.

[415] Lam, A. K.; Li, C.; Khairallah, G.; Kirk, B. B.; Blanksby, S. J.; Trevitt, A. J.; Wille, U.; O'Hair, R. A.; da Silva, G. *Phys. Chem. Chem. Phys.* **2012**, *14*, 2417–2426.

[416] Dryza, V.; Sanelli, J. A.; Robertson, E. G.; Bieske, E. J. *J. Phys. Chem. A* **2012**, *116*, 4323–4329.

[417] Poad, B. L. J.; Wearne, P. J.; Bieske, E. J.; Buchachenko, A. A.; Bennett, D. I. G.; Kłos, J.; Alexander, M. H. *J. Chem. Phys.* **2008**, *129*, 184306–8.

[418] Psciuk, B. T.; Benderskii, V. A.; Schlegel, H. B. *Theor. Chem. Acc.* **2007**, *118*, 75–80.

[419] Derwish, G.; Galli, A.; Guidoni, A. G.; Volpi, G. G. *J. Am. Chem. Soc.* **1965**, *87*, 1159–1168.

[420] Futrell, J. H.; Tiernan, T. O. *J. Phys. Chem.* **1968**, *72*, 158–164.

[421] Szabo, I.; Derrick, P. *Int. J. Mass Spectrom. Ion Phys.* **1971**, *7*, 55 – 69.

[422] Anicich, V. G.; Huntress, W. T.; McEwan, M. J. *J. Phys. Chem.* **1986**, *90*, 2446–2450.

[423] Fujii, T. *Phys. Rev. E* **1998**, *58*, 6495–6502.

[424] Gielen, J.; Van De Sanden, M.; Schram, D. *Appl. Phys. Lett.* **1996**, *69*, 152–154.

[425] Van de Sanden, M.; Van Hest, M.; De Graaf, A.; Smets, A.; Letourneur, K.; Boogaarts, M.; Schram, D. *Diamond and related materials* **1999**, *8*, 677–681.

[426] Vasile, M.; Smolinsky, G. *Int. J. Mass Spectrom. Ion Phys.* **1977**, *24*, 11–23.

[427] Benedikt, J. *J. Phys. D Appl. Phys.* **2010**, *43*, 043001.

[428] Eraslan, A. N.; Brown, R. C. *Combust. Flame* **1988**, *74*, 19 – 37.

[429] Calcote, H. F.; Jensen, D. E. *Advances in Chemistry Series No. 58*; American Chemical Society, 1967; Chapter 17, pp 291–314.

[430] Larionova, I.; Fialkov, B.; Kalinich, K. Y.; Fialkov, A.; Ospanov, B. *Combustion, Explosion and Shock Waves* **1993**, *29*, 341–344.

[431] Kühlewind, H.; Kiermeier, A.; Neusser, H. J. *J. Chem. Phys.* **1986**, *85*, 4427–4435.

[432] Ohmichi, N.; Malinovich, Y.; Ziesel, J. P.; Lifshitz, C. *J. Phys. Chem.* **1989**, *93*, 2491–2495.

[433] Anicich, V. G.; Sen, A. D.; Huntress Jr, W. T.; McEwan, M. J. *J. Chem. Phys.* **1990**, *93*, 7163–7172.

[434] Bates, D. *Astrophys. J.* **1983**, *267*, L121–L124.

[435] Robinson, P. J.; Holbrook, K. A. *Unimolecular Reactions*; Wiley-Interscience, 1972.

[436] Şahin, Ö.; Tapan, I.; Özmutlu, E. N.; Veenhof, R. *J. Instrum.* **2010**, *5*, P05002.

[437] Ruscic, B.; Pinzon, R. E.; von Laszewski, G.; Kodeboyina, D.; Burcat, A.; Leahy, D.; Montoy, D.; Wagner, A. F. *J. Phys. Conf. Ser.* **2005**, *16*, 561–570.

[438] Ruscic, B.; Bross, D. H. Active Thermochemical Tables (ATcT) values based on ver. 1.122e of the Thermochemical Network, Argonne National Laboratory (2019); available at ATcT.anl.gov. 2019.

[439] Peverati, R.; Bera, P. P.; Lee, T. J.; Head-Gordon, M. *Astrophys. J.* **2016**, *830*, 128.

[440] Munson, M. *J. Phys. Chem.* **1965**, *69*, 572–578.

[441] Brill, F. W.; Eyler, J. R. *J. Phys. Chem.* **1981**, *85*, 1091–1094.

[442] Reutt, J.; Wang, L.; Pollard, J.; Trevor, D.; Lee, Y.; Shirley, D. *J. Chem. Phys.* **1986**, *84*, 3022–3031.

[443] Cha, C.; Weinkauf, R.; Boesl, U. *J. Chem. Phys.* **1995**, *103*, 5224–5235.

[444] Tate, J. T.; Smith, P.; Vaughan, A. *Phys. Rev.* **1935**, *48*, 525.

[445] Plessis, P.; Marmet, P. *Int. J. Mass Spectrom. Ion Proc.* **1986**, *70*, 23 – 44.

[446] Zyubina, T. S.; Dyakov, Y. A.; Lin, S. H.; Bandrauk, A. D.; Mebel, A. M. *J. Chem. Phys.* **2005**, *123*, 134320.

[447] King, S. J.; Price, S. D. *J. Chem. Phys.* **2007**, *127*, 174307.

[448] Alagia, M.; Callegari, C.; Candori, P.; Falcinelli, S.; Pirani, F.; Richter, R.; Stranges, S.; Vecchiocattivi, F. *J. Chem. Phys.* **2012**, *136*, 204302.

[449] Falcinelli, S.; Alagia, M.; Farrar, J. M.; Kalogerakis, K. S.; Pirani, F.; Richter, R.; Schio, L.; Stranges, S.; Rosi, M.; Vecchiocattivi, F. *J. Chem. Phys.* **2016**, *145*, 114308.

[450] Araki, M.; Linnartz, H.; Cias, P.; Denisov, A.; Fulara, J.; Batalov, A.; Shnitko, I.; Maier, J. P. *J. Chem. Phys.* **2003**, *118*, 10561–10565.

[451] Clauberg, H.; Minsek, D. W.; Chen, P. *J. Am. Chem. Soc.* **1992**, *114*, 99–107.

[452] Johnson III, R. D., Ed. *NIST Computational Chemistry Comparison and Benchmark Database, Release 18, October 2016*; NIST Standard Reference Database Number 101; http://cccbdb.nist.gov/.

[453] Peverati, R.; Bera, P. P.; Lee, T. J.; Head-Gordon, M. *J. Phys. Chem. A* **2014**, *118*, 10109–10116.

[454] Catani, K. J.; Muller, G.; Jusko, P.; Theulé, P.; Bieske, E. J.; Jouvet, C. *J. Chem. Phys.* **2017**, *147*, 084302.

[455] Muller, G.; Catani, K. J.; Scholz, M. S.; Jacovella, U.; Bartlett, N. I.; Bieske, E. J. *J. Phys. Chem. A* **2019**, *123*, 7228–7236.

[456] Muller, G.; Jacovella, U.; Catani, K. J.; da Silva, G.; Bieske, E. J. *J. Phys. Chem. A* **2020**,

Appendix : Reproduced publications

Chapters 3 and 5 have been published in the Journal of Physical Chemistry A and were formatted to fit the style of this thesis. Reproductions of the peer-reviewed articles are provided here.

- G. Muller, K. J. Catani, M. S. Scholz, U. Jacovella, N. I. Bartlett, E.J. Bieske, "Electronic Spectra of Diacetylene Cations (HC_4H^+) Tagged with Ar and N_2" *Journal of Physical Chemistry A*, **123 (33)**, 7228-7236, 2019.
- G. Muller, U. Jacovella, K. J. Catani, G. da Silva, E. J. Bieske, "The Electronic Spectrum and Photodissociation Chemistry of the 1-butyn-3-yl cation, $H_3CCHCCH^+$" *Journal of Physical Chemistry A*, **124**, 2366-2371, 2020.

Reproduced publications begin here

THE JOURNAL OF PHYSICAL CHEMISTRY A

Article

Cite This: J. Phys. Chem. A 2019, 123, 7228−7236

pubs.acs.org/JPCA

Electronic Spectra of Diacetylene Cations (HC_4H^+) Tagged with Ar and N_2

Published as part of The Journal of Physical Chemistry virtual special issue "Leo Radom Festschrift".

Giel Muller, Katherine J. Catani, Michael S. Scholz, Ugo Jacovella, Nastasia I. Bartlett, and Evan J. Bieske*

School of Chemistry, University of Melbourne, Parkville, Victoria 3010, Australia

Supporting Information

ABSTRACT: Electronic spectra of mass-selected HC_4H^+−Ar_n (n = 1−3) and HC_4H^+-$(N_2)_n$ (n = 1−2) complexes are measured over the 290−530 nm range using resonance-enhanced photodissociation spectroscopy in a tandem mass spectrometer. Vibronic transitions in the visible region are compared with previous experimental and theoretical results for the $\tilde{A}^2\Pi_u \leftarrow \tilde{X}^2\Pi_g$ band system of HC_4H^+. Hole burning experiments confirm that transitions over the 290−340 nm range involve the diacetylene cation (HC_4H^+). On the basis of previous experiments and comparison with spectra of isoelectronic molecules the peaks are assigned to the $2^2\Pi_u \leftarrow \tilde{X}^2\Pi_g$ band system, with the origin transition for HC_4H^+−Ar occurring at 29723 cm^{-1}. The main progression has a spacing of 906 cm^{-1} and is assigned to the symmetric C−C stretch vibrational mode (ν_3). The assignment of additional bands is complicated by spectral congestion, the possible presence of energetically close-lying electronic states, vibronic coupling effects, and by the fact that HC_4H^+ possibly becomes nonlinear in the $2^2\Pi_u$ state.

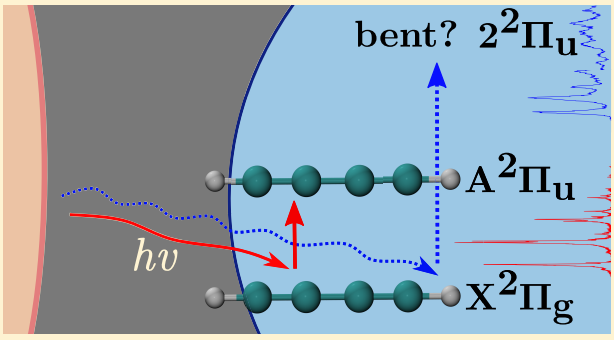

INTRODUCTION

Small reactive hydrocarbon molecules have been detected in extraterrestrial environments and are believed to contribute to the formation of benzene and larger molecules, including polycyclic aromatic hydrocarbons.[1−9] Hydrocarbon cations, formed through photoionization by cosmic rays or ultraviolet (UV) stellar light, may also play a chemical role by participating in ion−molecule interactions and dissociation processes.[10−12]

The diacetylene radical cation (HC_4H^+) is one of the smallest products from acetylene ion−molecule reactions, presumably generated through formation of the $(HCCH)_2^+$ dimer cation followed by H_2 loss.[13−21] It can also be generated from the ionization of neutral HC_4H, which is believed to form in extraterrestrial environments through the reaction of acetylene with the ethynyl radical (C_2H).[22] Therefore, HC_4H^+ is expected to exist in environments where acetylene and diacetylene molecules are abundant and exposed to strong UV radiation.[23] The diacetylene cation may play a part in the chemistry of proto-planetary nebulae and has been included in atmospheric models of Titan.[24] It was once considered as a carrier of diffuse interstellar bands, although this hypothesis was later discounted based on laboratory spectra.[24−29]

In 1951, Schüler recorded emission spectra of organic vapors in a discharge tube,[30] and the so-called "T" spectrum was later assigned by Callomon[31] to the $\tilde{A}^2\Pi_u \leftarrow \tilde{X}^2\Pi_g$ band system of HC_4H^+, with the origin transition located at 19724.5 cm^{-1}. Strong vibronic transitions were attributed to the C−C stretch (ν_3) progression and even quanta of the doubly degenerate bending mode (ν_7), which gains intensity through Fermi resonance with ν_3. Since then, many theoretical and spectroscopic investigations have focused on the $\tilde{A}^2\Pi_u$ state, which arises from the promotion of an electron from the second highest occupied molecular orbital (HOMO−1, π_u) to the HOMO (π_g).[32−39]

Much less is known about the higher excited states of HC_4H^+ which arise from promotion of an electron from the HOMO to the lowest unoccupied molecular orbital (LUMO) giving a dominant electronic configuration ...$1(\pi_u)^4 1(\pi_g)^2 2(\pi_u)^1$ associated with five non-Koopmans' states ($^4\Pi_u$, $^2\Pi_u$, $^2\Phi_u$, $^2\Pi_u$, $^2\Pi_u$). Electronic transitions from the ground $^2\Pi_g$ state to the three $^2\Pi_u$ states are spin and dipole allowed and therefore should be observable. On the basis of previous calculations, two of the $^2\Pi_u$ states and the $^2\Phi_u$ state are predicted to have similar energies, whereas the third $^2\Pi_u$ state is predicted to lie significantly higher in energy.[39] Because the energetic ordering of the states is unclear, it is useful to adopt the notation used in ref 39 to describe states above $\tilde{A}^2\Pi_u$.

Received: June 24, 2019
Revised: July 30, 2019
Published: July 31, 2019

Downloaded via UNIV OF MELBOURNE on December 26, 2019 at 20:56:54 (UTC).
See https://pubs.acs.org/sharingguidelines for options on how to legitimately share published articles.

© 2019 American Chemical Society

DOI: 10.1021/acs.jpca.9b05996
J. Phys. Chem. A 2019, 123, 7228−7236

Namely, the electronic states are labeled as $n^S\Gamma$, where n is the state energetic order of a given symmetry, S is the spin multiplicity, and Γ is the symmetry of the state. With this nomenclature the five lowest doublet excited states are $\tilde{A}^2\Pi_u$, $2^2\Pi_u$, $1^2\Phi_u$, $3^2\Pi_u$, and $4^2\Pi_u$.

As non-Koopmans' excited states are not usually accessible through photoionization of the neutral diacetylene molecule, photoelectron spectra display a gap of ≈4 eV between the $\tilde{A}^2\Pi_u$ state and the next accessible excited state.[37,40,41] Observation of the non-Koopmans' electronic states lying within the gap relies on electronic spectroscopy of the HC_4H^+ cation. The $2^2\Pi_u \leftarrow \tilde{X}^2\Pi_g$ transition of HC_4H^+ was reported to occur at 3.75 eV for HC_4H^+ embedded in an argon matrix,[39] and at 3.69 eV for HC_4H^+ in a neon matrix.[42] The assignment of bands lying above the $2^2\Pi_u \leftarrow \tilde{X}^2\Pi_g$ origin transition in the matrix spectra, which may be due to transitions to higher vibrational states or other electronic states, is problematic due to congestion and relatively poor signal-to-noise ratio.

The uncertainty regarding the location and assignment of the higher lying states represents a primary motivation for the current study—to obtain a more comprehensive understanding of electronic transitions of HC_4H^+ in the UV. As a step in this direction, we have measured the photodissociation action spectra of HC_4H^+–Ar and HC_4H^+–N_2 complexes in a tandem mass spectrometer over the 290–540 nm range. Transitions between 290 and 340 nm are recorded for the first time in the gas phase. To ensure that the measured UV bands are indeed associated with the diacetylene cation, we conducted hole burning experiments, depleting the HC_4H^+–Ar population by pumping the origin of the $\tilde{A}^2\Pi_u \leftarrow \tilde{X}^2\Pi_g$ band system. Interpretation of bands in the UV relies on comparisons with spectra of isoelectronic ions $NCCN^+$ and C_4^- and excited state calculations for HC_4H^+.[36,42−48]

EXPERIMENTAL METHODS

Electronic spectra of HC_4H^+–Ar_n (n = 1–3) and HC_4H^+–$(N_2)_n$ (n = 1–2) were recorded using resonance-enhanced photodissociation (REPD) spectroscopy in a custom-built tandem quadrupole–octupole–quadrupole mass spectrometer described previously.[49] A brief overview of the arrangement is provided below. A dilute mixture of Ar or N_2 with acetylene (≈0.7%), with a stagnation pressure of 4.5 bar, was expanded into a vacuum via a pulsed valve. The supersonic expansion was bombarded with electrons issuing from twin filaments to generate carbocations and tagged complexes, including HC_4H^+–Ar_n (n = 1–3) and HC_4H^+–$(N_2)_n$ (n = 1–2). After passing through a skimmer, the charged complexes were mass-selected using a quadrupole mass filter and then directed into an octupole ion guide using an electrostatic quadrupole bender. Here, the ions encountered light from a tunable optical parametric oscillator (OPO, EKSPLA NT342B). Resonant excitation of the HC_4H^+ chromophore induced photodissociation of the tagged complexes. The resulting HC_4H^+ cations were mass-selected by a second quadrupole mass filter and detected with a microchannel plate. A photodissociation action spectrum was generated by plotting fragment ion intensity as a function of wavelength. The intensity of the photofragment signal was normalized by laser power at each wavelength. The wavelength was calibrated using a wavemeter (High Finesse Ångstrom LSA UVL).

Hole burning (HB) experiments were conducted for HC_4H^+–Ar complexes to confirm that bands between 290 and 350 nm are associated with transitions of the diacetylene cation. A HB light beam (generated by a tunable OPO, Opotek Vibrant 355 LD) directed along the axis of the first quadrupole mass filter was tuned to the $\tilde{A}^2\Pi_u \leftarrow \tilde{X}^2\Pi_g$ band origin (506.4 nm). The HB beam should deplete the population of HC_4H^+–Ar ions in the octupole region but leave the populations of other isobaric ions unaffected. To assess the effect of the HB light on the intensities of the bands, spectra were recorded with the HB light off and on. A more complete description of the setup is provided in the Supporting Information (SI).

RESULTS AND DISCUSSION

Calculated Properties. Quantum chemical calculations were used to evaluate the ground and excited state electronic structures of the diacetylene radical cation. The equilibrium geometry and harmonic vibrational frequencies of ground state HC_4H^+ were determined at the CCSD/cc-pCVTZ level of theory, employing the Psi4 1.1 program suite.[50] The HC_4H^+ molecule in its ground $\tilde{X}^2\Pi_g$ electronic state was calculated to be linear and centrosymmetric with the dominant electronic configuration $...5(\sigma_g)^2 4(\sigma_u)^2 1(\pi_u)^4 1(\pi_g)^3$. Vibrational frequencies of HC_4H^+ in the $\tilde{X}^2\Pi_g$ state, provided in Table 1, agree with results of previous theoretical investigations.[34,51]

Table 1. Calculated Harmonic Vibrational Frequencies (cm^{-1}) of HC_4H^+ in the $\tilde{X}^2\Pi_g$ and $\tilde{A}^2\Pi_u$ States. All frequencies Are Unscaled

mode	description	$\tilde{X}^2\Pi_g$[a]	$\tilde{A}^2\Pi_u$[b]
ν_1, σ_g	C–H symm. stretch	3390	3395
ν_2, σ_g	C≡C symm. stretch	2283	2144
ν_3, σ_g	C–C symm. stretch	956	846
ν_4, σ_u	C–H antisymm. stretch	3389	3394
ν_5, σ_u	C≡C antisymm. stretch	2015	2040
ν_6, π_g	*trans* H–C_4–H bend	737	653
ν_7, π_g	*trans* C≡C–C≡C bend	477	444
ν_8, π_u	*cis* H–C_4–H bend	786	644
ν_9, π_u	*cis* C≡C–C≡C bend	210	233

[a]CCSD/cc-pCVTZ. [b]EOM-CCSD/cc-pCVTZ.

Vertical excitation energies and oscillator strengths calculated at the EOM-CCSD/cc-pCVTZ level predict that the strong $\tilde{A}^2\Pi_u \leftarrow \tilde{X}^2\Pi_g$ transition occurs at 2.62 eV, and involves promotion of an electron from the $1\pi_u$ orbital to the singly occupied HOMO $1\pi_g$ orbital. The equilibrium geometry and harmonic vibrational frequencies of the $\tilde{A}^2\Pi_u$ state were calculated at the EOM-CCSD/cc-pCVTZ level. Our calculations predict a linear geometry for HC_4H^+ in the $\tilde{A}^2\Pi_u$ state, agreeing with previous studies.[52,53] Calculated vibrational frequencies for HC_4H^+ in the $\tilde{A}^2\Pi_u$ state are provided in Table 1. The adiabatic excitation energy, including vibrational zero point energy, was determined to be 2.45 eV (Table 2), matching the previously measured energy of the $\tilde{A}^2\Pi_u \leftarrow \tilde{X}^2\Pi_g$ origin transition of HC_4H^+ at 19722.6 cm^{-1} (2.45 eV).[54]

The $2^2\Pi_u$, $1^2\Phi_u$, and $3^2\Pi_u$ states were predicted to have vertical excitation energies of 3.93, 4.53, and 5.21 eV, respectively, and correspond to HOMO → LUMO electronic excitations. As noted above, the three electronic states have the same dominant electronic configuration. These excited states were previously studied by Zhang et al.[55] using the CASSCF/CASPT2 approach, where the third excited state was assigned as a $^2\Pi_u$ state. The alternative assignment of the third doublet state to $1^2\Phi_u$ (as described in Table 2) accords with the

DOI: 10.1021/acs.jpca.9b05996
J. Phys. Chem. A 2019, 123, 7228–7236

Table 2. Adiabatic (Underlined) and Vertical Excitation Energies, and Oscillator Strengths (f) for HC_4H^+, Calculated in This Work and from Reference 55[a]

state	energy: calculated	energy: experimental	f[b]
$\tilde{A}^2\Pi_u$	2.62[b], <u>2.45</u>[c]	2.45[d]	3.08×10^{-2}
$2^2\Pi_u$	3.93[b]	3.69[d]	2.48×10^{-2}
$1^2\Phi_u$	4.53[b]		8.98×10^{-6}
$3^2\Pi_u$	5.21[b]		2.17×10^{-2}

[a]Energies (eV) are relative to the ground ($\tilde{X}^2\Pi_g$) electronic state. Experimental energies for HC_4H^+–Ar are also included. [b]CASSCF/CASPT2/cc-pVTZ (from ref 55). [c]EOM-CCSD/cc-pCVTZ (this work). [d]Experimental value for HC_4H^+–Ar (this work).

calculations in ref 39, and is consistent with the low predicted oscillator strength for the transition from the ground state.

Understanding spectra arising from transitions to these excited states is complicated by Renner-Teller (RT) interactions. The RT effect is apparently weak for the $\tilde{X}^2\Pi_g$ and $\tilde{A}^2\Pi_u$ states, which split into linear/linear pairs.[53] However, the effects of RT interactions on higher states of HC_4H^+ are unknown. To explore the importance of RT interactions for the $2^2\Pi_u$ state of HC_4H^+, quantum mechanical calculations were conducted using the complete active space self-consistent field (CASSCF) method with the cc-pVTZ basis set in the ORCA suite.[56,57] An active space of seven electrons and eight π orbitals was chosen to investigate the $\tilde{X}^2\Pi_g$, $\tilde{A}^2\Pi_u$, and $2^2\Pi_u$ states. First, the geometry of the $\tilde{X}^2\Pi_g$ state was optimized, resulting in a linear structure. The relative energies for each of the two RT components in the $\tilde{X}^2\Pi_g$, $\tilde{A}^2\Pi_u$, and $2^2\Pi_u$ states were calculated by stepping along the CASSCF ground state normal coordinates for ν_6 (*trans* H–C_4–H bend), ν_7 (*trans* C≡C–C≡C bend), ν_8 (*cis* H–C_4–H bend), and ν_9 (*cis* C≡C–C≡C bend). These potential energy curves and their significance are discussed below.

To understand the interactions between HC_4H^+ and Ar and N_2, the structures and energies of the HC_4H^+–Ar and HC_4H^+–N_2 complexes were calculated using density functional theory (DFT) at the ωB97X-D/aug-cc-pVTZ[58] level using the Gaussian 09 suite.[59] This method accounts for long-range dispersion interactions and is suitable for noncovalently bound complexes.[60] The calculated binding energies account for vibrational zero point energy (within the harmonic approximation) and include counterpoise corrections to address basis set superposition errors.[61] Calculations indicate that Ar and N_2 can attach to HC_4H^+ either end-on or side-on, as shown in Figure 1a,b. As shown by Botschwina and Oswald,[62] the nonlinear isomer is associated with a $^2A'$ electronic substate arising when the $^2\Pi_g$ state degeneracy is broken through the presence of an off-axis perturber. These two configurations are predicted to have similar binding energies of ≈460 cm^{-1} for HC_4H^+–Ar. This agrees with a previous computational study on HC_4H^+–Ar, in which a binding energy of ≈500 cm^{-1} was predicted for the linear structure with the nonlinear structure being slightly less stable.[62] For HC_4H^+–N_2, the $C_{\infty v}$ linear structure with the N_2 tag positioned along the intermolecular axis (Figure 1c) is predicted to be 276 cm^{-1} more stable than the C_s structure (Figure 1d). Because the intermolecular bonds in HC_4H^+–Ar and HC_4H^+–N_2 complexes are relatively weak and the HC_4H^+ core is only slightly distorted, the REPD spectra of HC_4H^+–Ar and HC_4H^+–N_2 are expected to resemble closely the

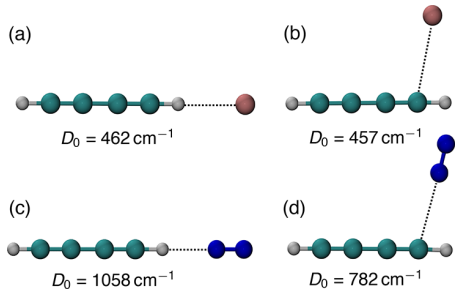

Figure 1. Optimized structures of HC_4H^+ tagged with Ar (a and b) and N_2 (c and d). The calculated dissociation energy (D_0) is listed in each case.

absorption spectrum of the bare HC_4H^+ molecule. Optimized structures and calculated energies of complexes with several Ar and N_2 tags are described in the SI.

Electronic Spectra. Figure 2 depicts the electronic spectrum of HC_4H^+–Ar over the visible and UV regions

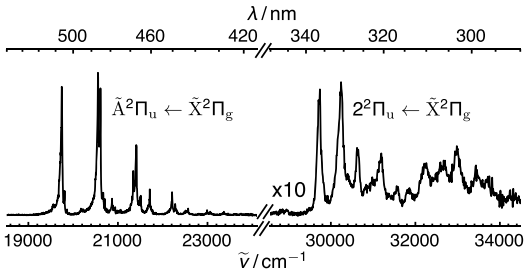

Figure 2. REPD spectra of HC_4H^+–Ar over the 425–530 nm (left) and 290–350 nm (right) ranges obtained by monitoring HC_4H^+ photofragments. The $\tilde{A}^2\Pi_u \leftarrow \tilde{X}^2\Pi_g$ origin transition at 506 nm is estimated to be ≈10 times stronger than the $2^2\Pi_u \leftarrow \tilde{X}^2\Pi_g$ origin transition at 336 nm.

encompassing the $\tilde{A}^2\Pi_u \leftarrow \tilde{X}^2\Pi_g$ and $2^2\Pi_u \leftarrow \tilde{X}^2\Pi_g$ band systems, respectively. Transitions in the UV are approximately 10 times weaker than those in the visible region.

$\tilde{A}^2\Pi_u \leftarrow \tilde{X}^2\Pi_g$ Band System (425–530 nm). We first consider the well-known $\tilde{A}^2\Pi_u \leftarrow \tilde{X}^2\Pi_g$ band system. REPD spectra of HC_4H^+–N_2 and HC_4H^+–Ar complexes over the 425–530 nm range are shown in Figure 3 panels a and b, respectively. Because the tagged ions are at low temperature and A_{SO} = −31.1 cm^{-1},[35] the population of the $\Omega = {}^1/_2$ spin–orbit component in the ground state should be negligible and transitions should predominately occur from the $\Omega = {}^3/_2$ substate with $\Delta\Omega = 0$ (Hund's case a). Assignments, positions, and spacings of vibronic bands are listed in Table 3. Assignments are based on previous studies and comparisons with the simulated spectrum presented in Figure 3c.[31,36−38] Corresponding spectra for larger HC_4H^+–Ar_n and HC_4H^+–$(N_2)_n$ complexes are provided in the SI.

The spectra of HC_4H^+–Ar and HC_4H^+–N_2 closely resemble the spectrum of the bare HC_4H^+ cation aside from a small blue shift of the bands and the presence of weak additional peaks associated with excitation of intermolecular vibrational modes. The dominant progression in the $\tilde{A}^2\Pi_u \leftarrow \tilde{X}^2\Pi_g$ band system of HC_4H^+ is associated with Fermi polyads arising from the ν_3 C–C stretch vibration interacting with even quanta of the ν_7 C–C bend vibration.[31,32,36−38] The $3_0^1/7_0^2$ pair of transitions are observed at 0_0^0 + 809 and 864 cm^{-1}, respectively, with the

DOI: 10.1021/acs.jpca.9b05996
J. Phys. Chem. A 2019, 123, 7228−7236

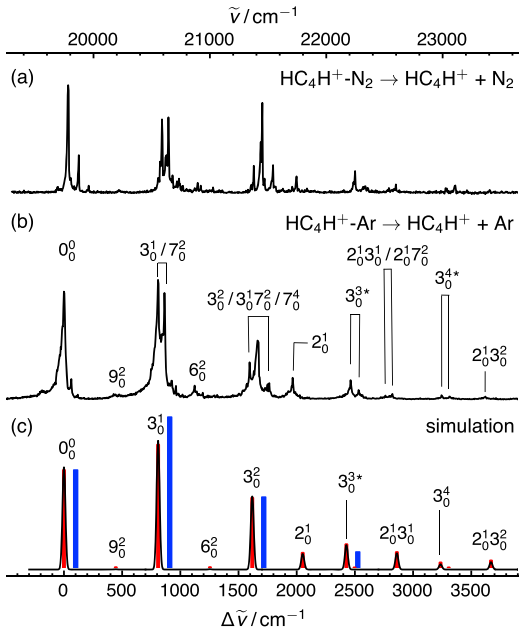

Figure 3. $\tilde{A}^2\Pi_u \leftarrow \tilde{X}^2\Pi_g$ electronic spectra of (a) HC_4H^+–N_2 and (b) HC_4H^+–Ar, obtained by monitoring HC_4H^+ photofragments. (c) Predicted stick spectrum from a Franck–Condon simulation (red sticks) compared to integrated experimental intensities (rectangular blue bars) of the 3_0^n (n = 1–3) polyads. Asterisks represent polyads comprising several transitions that are not individually assigned (see text for details).

55 cm^{-1} spacing between the two peaks consistent with the 56 cm^{-1} gap measured with rotational resolution using cavity ringdown spectroscopy.[32] Polyads involving ν_3 and ν_7 are observed at higher energies. For example, the $3_0^2/3_0^1 7_0^2/7_0^4$ triad occurs around 1600 cm^{-1} above the origin transition, as indicated in Figure 3b. These assignments agree with those in refs 37 and 38. The groups of bands lying at ≈2500 and ≈3250 cm^{-1} above the origin are assigned to the 3_0^3 and 3_0^4 polyads, respectively. More combinations are possible for higher energy polyads, and detailed assignment is frustrated by congestion and low intensity of the bands. Groups of bands, for which individual vibronic transitions are not assigned, are labeled with asterisks in Figure 3 and Table 3.

The $\tilde{A}^2\Pi_u \leftarrow \tilde{X}^2\Pi_g$ band system was simulated using the PGOPHER program[63] with ground and excited state structures and vibrational frequencies derived at the CCSD/cc-pVTZ and EOM-CCSD/cc-pCVTZ levels, respectively. A good match between the simulated and experimental spectra was found by scaling the calculated harmonic frequencies by 0.957. A simulated stick spectrum of the $\tilde{A}^2\Pi_u \leftarrow \tilde{X}^2\Pi_g$ band system is shown in Figure 3c while the corresponding convoluted spectrum (full width at half-maximum of 30 cm^{-1}) is shown in black. Bands observed at 0_0^0 + 809, 1596, 2463, and 3245 cm^{-1} correspond to the predicted positions of the 3_0^1, 3_0^2, 3_0^3, and 3_0^4 transitions, respectively. The simulation does not account for Fermi resonance interactions, in which the 7_0^m transitions borrow a fraction of the 3_0^n transition intensities. Therefore, the predicted 3_0^n transition intensities are more appropriately compared with the sum of the observed intensities for the polyad members. The comparison is made in Figure 3c where the summed experimental intensities are represented as rectangular blue bars and are displaced by ≈100 cm^{-1} from the simulated bands to aid comparison.

The simulation indicates that weak bands at 0_0^0 + 427, 1123, 1965, and 3245 cm^{-1} correspond to the 9_0^2, 6_0^2, 2_0^1, and 1_0^1 transitions, respectively, agreeing with previous assignments.[31,33,36,37] Predicted intensities of the 9_0^2 and 2_0^1 transitions match experimental observations, whereas the intensity of the 6_0^2 transition is underestimated. The weak 1_0^1 transition is difficult to distinguish as it overlaps the 3_0^4 polyad

Table 3. Band Positions (in cm^{-1}) and Assignments for $\tilde{A}^2\Pi_u \leftarrow \tilde{X}^2\Pi_g$ Transitions of HC_4H^+–Ar_n (n = 1–3) and HC_4H^+–$(N_2)_n$ (n = 1–2) Complexes. Asterisks Denote Polyads Involving ν_3 and $2\nu_7$ with Possible Contributions from Several Vibronic Transitions

	HC_4H^+–Ar		HC_4H^+–Ar_2		HC_4H^+–Ar_3		HC_4H^+–N_2		HC_4H^+–$(N_2)_2$	
assignment	$\tilde{\nu}$	$\Delta\tilde{\nu}$	$\tilde{\nu}$	$\Delta\tilde{\nu}$	$\tilde{\nu}$	$\Delta\tilde{\nu}$	$\tilde{\nu}$	$\Delta\tilde{\nu}$	$\tilde{\nu}$	$\Delta\tilde{\nu}$
s_1^0							19694	−88	19758	−59
0_0^0	19746	0	19770	0	19786	0	19782	0	19817	0
S_0^1	19808	56	19841	71			19874	85	19896	79
S_0^2	19865	119					19959	177		
9_0^2	20173	427					20219	437	20275	458
$3_0^1/7_0^2$	20555	809	20581	811	20584	798	20588	806	20639	822
$3_0^1/7_0^2$	20610	864	20636	866			20644	862	20690	873
6_0^2	20869	1123	20874	1104			20896	1114		
8_0^2							20922	1140		
$3_0^1 9_0^2$							21027	1245		
$3_0^2/3_0^1 7_0^2/7_0^4$	21342	1596	21373	1603	31382	1596	21377	1595	21425	1608
$3_0^2/3_0^1 7_0^2/7_0^4$	21410	1664	21419	1649	21455	1669	21451	1669	21499	1682
$3_0^2/3_0^1 7_0^2/7_0^4$	21497	1751	21538	1768	21552	1766	21543	1761	21578	1761
2_0^1	21711	1965	21749	1979	21745	1959	21745	1963	21789	1972
3_0^{3*}	22209	2463	22 228	2458	22 242	2456	22245	2463	22294	2477
3_0^{3*}	22278	2532					22337	2555	22364	2547
$2_0^1 3_0^1/2_0^1 7_0^2$	22509	2763					22538	2756	22581	2674
$2_0^1 3_0^1/2_0^1 7_0^2$	22569	2823					22598	2816	22642	2825
3_0^{4*}	22991	3245	23016	3246			23026	3244	23081	3264
$2_0^1 3_0^2$	23367	3621					23404	3622	23443	3626

DOI: 10.1021/acs.jpca.9b05996
J. Phys. Chem. A 2019, 123, 7228–7236

transitions. Overall, the good match between theory and experiment suggests that calculations at the CCSD/cc-pCVTZ and EOM-CCSD/cc-pCVTZ levels provide a reasonable description of the $\tilde{X}^2\Pi_g$ and $\tilde{A}^2\Pi_u$ state geometries and frequencies.

Interaction of HC_4H^+ with Ar and N_2. The $\tilde{A}^2\Pi_u \leftarrow \tilde{X}^2\Pi_g$ spectra of $HC_4H^+{-}Ar_n$ (n = 1−3) and $HC_4H^+{-}(N_2)_n$ (n = 1−2) provide information on the interaction of Ar and N_2 with the HC_4H^+ cation. Figure 4 shows expanded views of the

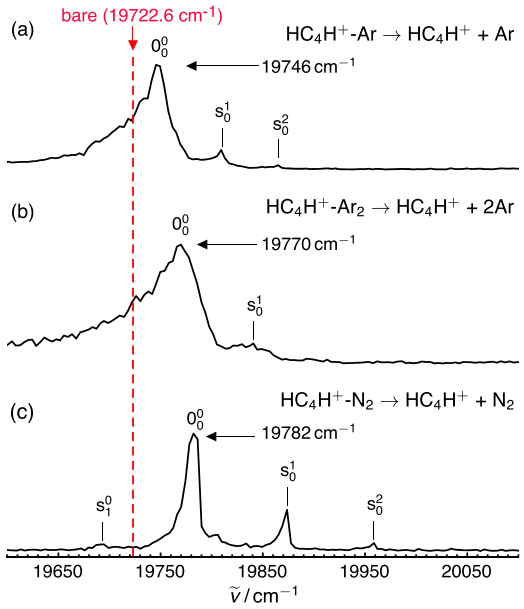

Figure 4. REPD spectra near the $\tilde{A}^2\Pi_u \leftarrow \tilde{X}^2\Pi_g$ origin band for (a) $HC_4H^+{-}Ar$, (b) $HC_4H^+{-}Ar_2$, and (c) $HC_4H^+{-}N_2$. Transitions associated with intermolecular stretching vibrations are indicated. The location of the $\tilde{A}^2\Pi_u \leftarrow \tilde{X}^2\Pi_g$ origin band for bare HC_4H^+ (from ref 54) is indicated by the dashed red line.

$HC_4H^+{-}Ar$ and $HC_4H^+{-}N_2$ spectra in the region of the origin transition. In each case, a progression of minor peaks is observed with spacings that are consistent with the expected frequency for the intermolecular stretch vibrational mode (ν_s). For example, weak peaks are observed at 0_0^0 + 56 and 119 cm^{-1} for the $HC_4H^+{-}Ar$ complex that can be assigned to the s_0^1 and s_0^2 transitions, respectively, based on the calculated ground state ν_s frequencies of 61 and 65 cm^{-1} for the linear and bent structures shown in Figure 1a,b. For $HC_4H^+{-}N_2$, corresponding bands appear at 0_0^0 + 85 and 177 cm^{-1}, respectively, consistent with a predicted intermolecular stretching frequency of 97 cm^{-1} for the more stable linear structure (see Figure 1).

The $\tilde{A}^2\Pi_u \leftarrow \tilde{X}^2\Pi_g$ origin transition of HC_4H^+ occurs at 19722.6 cm^{-1}, implying that the origin transitions of the $HC_4H^+{-}Ar$, $HC_4H^+{-}Ar_2$, and $HC_4H^+{-}Ar_3$ complexes are shifted to higher energy by 23, 47, and 63 cm^{-1}, respectively (Figure 5).[54] The almost equal incremental shifts for $HC_4H^+{-}Ar$ and $HC_4H^+{-}Ar_2$ indicate that the first two Ar atoms are attached at equivalent binding sites, consistent, for example, with the Ar atoms preferentially being attached to the two ends of the HC_4H^+ molecule. The $\tilde{A}^2\Pi_u \leftarrow \tilde{X}^2\Pi_g$ origin transitions of the $HC_4H^+{-}N_2$ and $HC_4H^+{-}(N_2)_2$ complexes are blue-shifted by 59 and 94 cm^{-1}, respectively, relative to the origin band of HC_4H^+ (Figure 5). The unequal incremental band shifts indicate that either the two N_2 tags are attached at

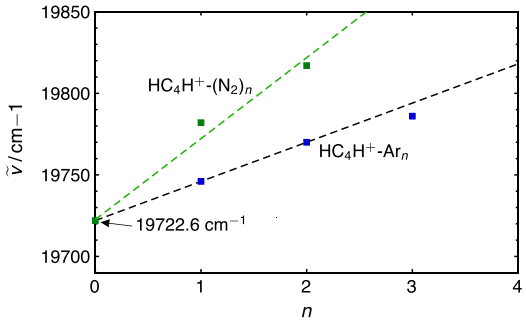

Figure 5. Energies for the $\tilde{A}^2\Pi_u \leftarrow \tilde{X}^2\Pi_g$ origin transitions of $HC_4H^+{-}Ar_n$ (n = 1−3) plotted as a function of n. The wavenumber for the $\tilde{A}^2\Pi_u \leftarrow \tilde{X}^2\Pi_g$ origin transition of HC_4H^+(19722.6 cm^{-1} from ref 54) is indicated.

inequivalent binding sites or more probably that the first attached N_2 molecule significantly perturbs the HC_4H^+ core.

The blue shift of the $\tilde{A}^2\Pi_u \leftarrow \tilde{X}^2\Pi_g$ origin transition upon complexation with Ar indicates that the intermolecular $HC_4H^+{-}Ar$ bond is weaker in the excited state than in the ground state. The asymmetric contour of the origin band, which is shaded to lower energy, is further evidence for a decreased intermolecular bond strength in the excited state. Hot bands involving the low energy intermolecular stretch (ν_s) and bend (ν_b) modes, such as s_1^1 and b_1^1, for example, will be shifted slightly to the red of the origin peak if the intermolecular vibrational frequencies are reduced in the excited state.

Transitions to Higher Excited States in the 290−345 nm Region. The electronic spectrum of $HC_4H^+{-}Ar$ over the 290−345 nm range, recorded by monitoring HC_4H^+ photofragments, is shown in Figure 6. First it was established that all

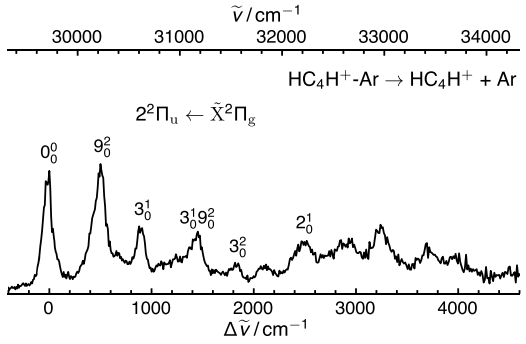

Figure 6. REPD spectrum of $HC_4H^+{-}Ar$ over the 290−345 nm range, obtained by monitoring HC_4H^+ photofragments. Tentative assignments are indicated. The lower lying peaks are assigned to the $2^2\Pi_u \leftarrow \tilde{X}^2\Pi_g$ system. Peak positions and assignments are given in Table 4.

bands over the 290−345 nm range are associated with the diacetylene cation (HC_4H^+) by conducting hole burning (HB) experiments (see Experimental Methods and SI). A spectrum of the $HC_4H^+{-}N_2$ complex was also obtained in this region (available in the SI). However, due to a mass coincidence of $HC_4H^+{-}N_2$ and $C_6H_6^+$, which was also formed in the ion source and photodissociated to yield $C_4H_2^+$ in this wavelength range, the spectrum has a poor signal-to-noise ratio.[64,65]

The $HC_4H^+{-}Ar$ spectrum shown in Figure 6 is similar to spectra of HC_4H^+ trapped in rare gas matrices assigned to the

DOI: 10.1021/acs.jpca.9b05996
J. Phys. Chem. A 2019, 123, 7228−7236

$2^2\Pi_u \leftarrow \tilde{X}^2\Pi_g$ excitation,[39,42] although, due to a better signal-to-noise ratio and spectral resolution, additional bands are observed in the present study. Zhang et al.[55] predicted the $2^2\Pi_u \leftarrow \tilde{X}^2\Pi_g$ vertical excitation energy to be 3.93 eV, close to the lowest energy band at 29723 cm^{-1} (3.69 eV). The oscillator strength for the $2^2\Pi_u \leftarrow \tilde{X}^2\Pi_g$ transition was calculated to be around half that of the $\tilde{A}^2\Pi_u \leftarrow \tilde{X}^2\Pi_g$ transition (Table 2), consistent with the somewhat lower intensity of the UV bands compared to those in the visible (see Figure 2). The $2^2\Pi_u \leftarrow \tilde{X}^2\Pi_g$ origin band for HC_4H^+ in a Ne matrix reported in ref 42 is slightly blue-shifted with respect to the HC_4H^+–Ar transition (by ≈20 cm^{-1}). The forbidden $1^2\Phi_u \leftarrow \tilde{X}^2\Pi_g$ transition is also predicted to occur in this region, with a vertical excitation energy of 4.53 eV,[55] and may gain intensity via Herzberg–Teller interactions, as appears to occur for HC_6H^+.[66] The $3^2\Pi_u \leftarrow \tilde{X}^2\Pi_g$ vertical excitation energy for HC_4H^+ is predicted to be 5.21 eV (Table 2),[55] suggesting that this transition is unlikely to occur within the 290–350 nm range.

Band positions and assignments for the $2^2\Pi_u \leftarrow \tilde{X}^2\Pi_g$ spectrum of HC_4H^+–Ar are given in Table 4. For convenience a selected set of vibrational frequencies for HC_4H^+, $NCCN^+$, and C_4^- are provided in Table 5 (an extended set is given in the SI). The strong peak at 0_0^0 + 509 cm^{-1} was previously assigned in the Ne matrix spectrum to the 9_0^2 (*cis*-bending mode) transition based on calculated ground state frequencies of HC_4H^+.[42] To some extent this assignment is consistent with data for the isoelectronic ions $NCCN^+$ and C_4^-, for which transitions at 327 and 541 cm^{-1} above the $2^2\Pi_u \leftarrow \tilde{X}^2\Pi_g$ origin band, respectively, were assigned to overtones of the analogous *cis*-bending mode (5_0^2 transition for the linear tetra-atomic molecules; see Table 5).[43−45,47,48,70] The bands observed at 0_0^0 + 906 cm^{-1} and 0_0^0 + 1846 cm^{-1} can be assigned to the 3_0^1 and 3_0^2 transitions (C–C stretch vibration), respectively, based on the corresponding spectra of $NCCN^+$ and C_4^-,[45] as the spacings and relative intensities of C–C stretch progression peaks are similar for all three molecules. Assignments for peaks above 0_0^0 + 2000 cm^{-1} are uncertain due to spectral congestion and poor signal. However, the 2_0^1, $2_0^1 9_0^1$, $2_0^1 3_0^1$, 1_0^1, $1_0^1 9_0^2$, and $1_0^1 3_0^1$ transitions should occur in this region.

One problem with the assignment scheme outlined above relates to the exaggerated intensity of the 9_0^2 transition. Whereas for both $NCCN^+$ and C_4^- the corresponding 5_0^2 band is comparatively weak, for HC_4H^+ the 9_0^2 transition has an intensity that is comparable to that of the origin transition. If the assignment for the 9_0^2 band is correct, the ν_9 frequencies in the $2^2\Pi_u$ and $\tilde{X}^2\Pi_g$ states are similar (≈ 255 and 200 cm^{-1},[35] respectively), leading to the expectation of a relatively weak 9_0^2 band, if the molecule remains linear.

An alternative explanation for the vibronic structure in the $2^2\Pi_u \leftarrow \tilde{X}^2\Pi_g$ spectrum is that HC_4H^+ in the $2^2\Pi_u$ state is nonlinear, in which case one would expect strong transitions to excited bending vibrational levels in the upper state. As a first step toward exploring this possibility, bending potential energy curves were calculated using the approach employed for $NCCN^+$ in ref 43 (CASSCF/cc-pVTZ level of theory) whereby the molecule was progressively distorted along the ν_6 (*trans* H–C_4–H bend), ν_7 (*trans* C≡C–C≡C bend), ν_8 (*cis* C≡C–C≡C bend) and ν_9 (*cis* C≡C–C≡C bend) normal mode coordinates derived for the $\tilde{X}^2\Pi_g$ state. One-dimensional potential energy curves along the four bending coordinates (Q_6, Q_7, Q_8, Q_9) are displayed in Figure 7. RT interactions split a degenerate Π electronic state through distortion along a bending coordinate, leading to two substates, each of which can be either linear or bent. The calculated potential energy curves along all four bending normal coordinates are split into linear/linear pairs for the $\tilde{X}^2\Pi_g$ and $\tilde{A}^2\Pi_u$ states, as found for $NCCN^+$.[43] The calculations indicate that RT effects are weak for the $\tilde{X}^2\Pi_g$ and $\tilde{A}^2\Pi_u$ states, consistent with previous studies.[33,35] In contrast, the calculations predict that the $2^2\Pi_u$ state is split into a linear-bent pair for distortion along Q_6 (*trans* H–C_4–H bend, Figure 7a), linear–linear pair for distortion along Q_7 (*trans* C≡C–C≡C bend, Figure 7c), bent–bent pair for distortion along Q_8 (*cis* H–C_4–H bend, Figure 7b), and bent–bent pair for distortion along Q_9 (*cis* C≡C–C≡C bend, Figure 7d). The bending potential energy curves shown in Figure 7 panels c and d indicate that HC_4H^+ in the $2^2\Pi_u$ state is distorted away from linearity along the Q_8 and Q_9 *cis* bend coordinates with respective barriers to linearity of ≈2100 and ≈1400 cm^{-1}. Therefore, it seems possible that the strong peak at 0_0^0 + 509 cm^{-1} may be associated with excitation of a single quantum of one of the *cis* bending vibrational modes. It would seem that 509 cm^{-1} is too high for the ν_9 C≡C–C≡C bend vibrational mode given that the predicted barrier to linearity is ≈1400 cm^{-1} and the vibrational frequency in the ground state is only 210 cm^{-1} (Table 1). Rather, the band may be associated with

Table 4. Band Positions (in cm^{-1}) and Assignments for Peaks in the $2^2\Pi_u \leftarrow \tilde{X}^2\Pi_g$ System of HC_4H^+–Ar over the 290–345 nm Range

assignment	$\tilde{\nu}$	$\Delta\tilde{\nu}$	$\tilde{\nu}^a$	$\Delta\tilde{\nu}^a$
0_0^0	29723	0	29753	0
9_0^2	30232	509	30211	459
3_0^1	30629	906		
$3_0^1 9_0^2$	31194	1471	31114	1362
3_0^2	31569	1846		
	32228	2505		
2_0^1	32595	2872		
	32680	2957		
	32981	3258		
	33435	3712		

[a]Ne matrix peak positions from ref 42.

Table 5. Calculated and Experimental (Underlined) Vibrational Frequencies (cm^{-1}) of the Central σ_g (C–C Stretch) and *cis*-Bending Modes of HC_4H^+, $NCCN^+$, and C_4^- in the $\tilde{X}^2\Pi_g$, $1^2\Pi_u$ ($\tilde{A}^2\Pi_u$ for HC_4H^+), and $2^2\Pi_u$ States

state	HC_4H^+	$NCCN^+$	C_4^-
	C–C stretch (σ_g, ν_3)	C–C stretch (σ_g, ν_2)	C–C stretch (σ_g, ν_2)
$\tilde{X}^2\Pi_g$	956[a], 972[b,c]	808[d], 956[e]	893[f], 936[g]
$1^2\Pi_u$	809[a], 846[c], 806[h]	811[i]	750[j], 759[k], 777[l]
$2^2\Pi_u$	906[a]	870[i]	710[m], 755[n]
	C≡C–C≡C bend (π_u, ν_9)	N≡C–C≡N bend (π_u, ν_5)	C≡C–C≡C bend (π_u, ν_5)
$\tilde{X}^2\Pi_g$	210[a], 200[b],	240[d]	240[f]
$1^2\Pi_u$	214[a], 228[h]	174[i]	223[j], 250[f]
$2^2\Pi_u$		164[i]	268[m], 271[n]

[a]This work. [b]Reference 35. [c]Reference 31. [d]Reference 43. [e]Reference 67. [f]Reference 68. [g]Reference 69. [h]Reference 36. [i]Reference 45. [j]Reference 70. [k]Reference 71. [l]Reference 48. [m]Reference 46. [n]Reference 47.

DOI: 10.1021/acs.jpca.9b05996
J. Phys. Chem. A 2019, 123, 7228−7236

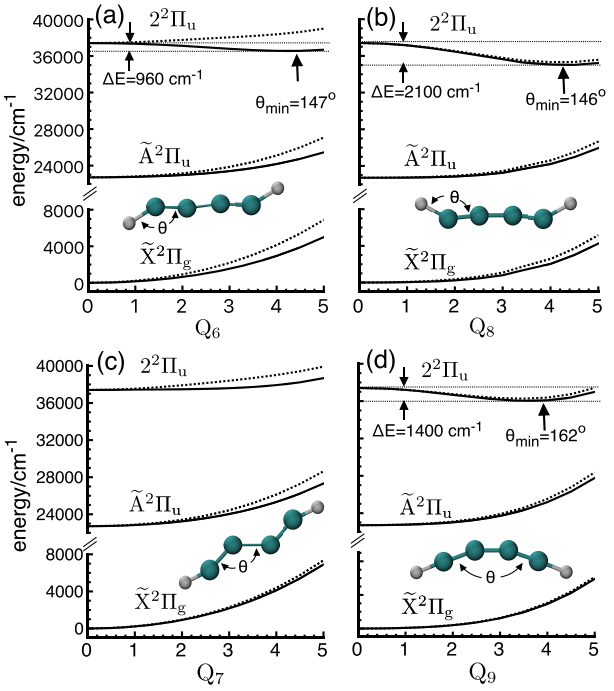

Figure 7. One-dimensional potential energy curves along the bending normal mode coordinates for Renner-Teller components in the $\tilde{X}^2\Pi_g$, $\tilde{A}^2\Pi_u$, and $2^2\Pi_u$ states calculated at the CASSCF/cc-pVTZ level of theory. Potential energy curves along the (a) Q_6 *trans* H−C_4−H bend coordinate, (b) Q_8 *cis* H−C_4−H bend coordinate, (c) Q_7 *trans* C≡C−C≡C bend coordinate, (d) Q_9 *cis* C≡C−C≡C bend coordinate. Lower and upper Renner-Teller curves for each electronic state are represented by solid and dotted lines, respectively. The dimensionless coordinates Q_i (i = 6−9), correspond to the bending normal coordinates for the ground electronic state, with the linear geometry at Q_i = 0.

excitation of a single quantum of the ν_8 *cis* H−C_4−H bend vibrational mode for which the barrier to linearity is ≈2100 cm^{-1} and the ground state frequency is 786 cm^{-1} (Table 1). Electronic spectra of the $C_4D_2^+$−Ar complex would help decide whether the molecule in the $2^2\Pi_u$ state is indeed distorted along the along ν_8 *cis* H−C_4−H bend coordinate. Ultimately, a more comprehensive understanding of HC_4H^+ transitions in the UV region will require gas-phase spectra with better resolution and signal-to-noise ratio, spectra of isotopically substituted species, and calculations for the $2^2\Pi_u$ excited state incorporating consideration of the Renner-Teller couplings and bending potential energy curves that are likely to be highly anharmonic.

CONCLUSIONS

In summary, electronic spectra of HC_4H^+−Ar_n (n = 1−3) and HC_4H^+−$(N_2)_n$ (n = 1−2) cation complexes have been recorded over the 290−530 nm range through photodissociation in a tandem mass spectrometer. The $\tilde{A}^2\Pi_u \leftarrow \tilde{X}^2\Pi_g$ electronic spectra of the complexes in the visible region (425−530 nm) are similar to previously recorded spectra[31,36−38] and are matched by simulations based on calculated structural parameters and harmonic vibrational frequencies for the $\tilde{X}^2\Pi_g$ and $\tilde{A}^2\Pi_u$ states at the CCSD/cc-pCVTZ and EOM-CCSD/cc-pCVTZ levels of theory, respectively.

Transitions of HC_4H^+−Ar over the 290−350 nm range previously observed in matrix isolation studies[39,42] were confirmed to be associated with the diacetylene cation through hole burning experiments. The $2^2\Pi_u \leftarrow \tilde{X}^2\Pi_g$ origin transition was observed at 29723 cm^{-1}, in accordance with previous matrix studies, while bands at 0_0^0 + 906 and 1846 cm^{-1} are tentatively assigned to the 3_0^1 and 3_0^2 transitions, respectively, based on spectra of the isoelectronic systems NCCN$^+$ and C_4^-. An intense band at 0_0^0 + 509 cm^{-1} was tentatively assigned to the 9_0^2 transition (overtone of the *cis*-bending mode) on the basis of its frequency, although this assignment does not properly account for its substantial intensity. An alternative explanation, supported by electronic structure calculations, is that HC_4H^+ is distorted along the ν_8 *cis* H−C_4−H bend coordinate and that the band corresponds to excitation of a single quantum of this vibration in the $2^2\Pi_u$ state. Better spectra, spectra of isotopologues, and more reliable calculations that include consideration of Renner-Teller effects are required to understand the transitions of HC_4H^+ in the ultraviolet region.

ASSOCIATED CONTENT

Supporting Information

The Supporting Information is available free of charge on the ACS Publications website at DOI: 10.1021/acs.jpca.9b05996.

Calculated structures and measured electronic spectra of HC_4H^+−Ar_n (n = 1−3) and HC_4H^+−$(N_2)_n$ (n = 1−2) complexes and a description of the hole burning experiments (PDF)

AUTHOR INFORMATION

Corresponding Author

*E-mail: evanjb@unimelb.edu.au.

ORCID

Giel Muller: 0000-0003-1173-6825
Katherine J. Catani: 0000-0003-1524-596X
Michael S. Scholz: 0000-0003-3290-2722
Evan J. Bieske: 0000-0003-1848-507X

Notes

The authors declare no competing financial interest.

ACKNOWLEDGMENTS

This research was supported under the Australian Research Council's Discovery Project funding scheme (Project Nos. DP15010142 and DP160100474) as well as by Australian Government Research Training Program Scholarships. U. Jacovella acknowledges support from the Swiss National Science Foundation (P2EZP2_178429).

REFERENCES

(1) Brooke, T.; Tokunaga, A.; Weaver, H.; Crovisier, J.; Bockelée-Morvan, D.; Crisp, D. Detection of Acetylene in the Infrared Spectrum of Comet Hyakutake. *Nature* **1996**, *383*, 606−608.
(2) Herbst, E. Chemistry in the Interstellar Medium. *Annu. Rev. Phys. Chem.* **1995**, *46*, 27−54.
(3) Shemansky, D. E.; Stewart, A. I. F.; West, R. A.; Esposito, L. W.; Hallett, J. T.; Liu, X. The Cassini UVIS Stellar Probe of the Titan Atmosphere. *Science* **2005**, *308*, 978−982.
(4) Lavvas, P.; Coustenis, A.; Vardavas, I. Coupling Photochemistry with Haze Formation in Titan's Atmosphere, Part II: Results and Validation with Cassini/Huygens Data. *Planet. Space Sci.* **2008**, *56*, 67−99.

DOI: 10.1021/acs.jpca.9b05996
J. Phys. Chem. A 2019, 123, 7228−7236

(5) Teanby, N.; Irwin, P.; de Kok, R.; Jolly, A.; Bézard, B.; Nixon, C.; Calcutt, S. Titan's Stratospheric C_2N_2, C_3H_4, and C_4H_2 Abundances from Cassini/CIRS Far-Infrared Spectra. *Icarus* **2009**, *202*, 620−631.
(6) Winnewisser, G.; Walmsley, C. M. Carbon Chain Molecules in Interstellar Clouds. *Astrophys. Space Sci.* **1979**, *65*, 83−93.
(7) Adams, N. G.; Smith, D. On the Synthesis of c-C_3H_2 in Interstellar Clouds. *Astrophys. J.* **1987**, *317*, L25−L27.
(8) Kunde, V.; Aikin, A.; Hanel, R.; Jennings, D.; Maguire, W.; Samuelson, R. C_4H_2, HC_3N and C_2N_2 in Titan's Atmosphere. *Nature* **1981**, *292*, 686−688.
(9) Coustenis, A.; Achterberg, R. K.; Conrath, B. J.; Jennings, D. E.; Marten, A.; Gautier, D.; Nixon, C. A.; Flasar, F. M.; Teanby, N. A.; Bézard, B.; et al. The Composition of Titan's Stratosphere from Cassini/CIRS Mid-Infrared Spectra. *Icarus* **2007**, *189*, 35−62.
(10) Gredel, R.; Lepp, S.; Dalgarno, A.; Herbst, E. Cosmic-Ray-Induced Photodissociation and Photoionization Rates of Interstellar Molecules. *Astrophys. J.* **1989**, *347*, 289−293.
(11) Schiff, H. I.; Bohme, D. K. An Ion−Molecule Scheme for the Synthesis of Hydrocarbon-Chain and Organonitrogen Molecules in Dense Interstellar Clouds. *Astrophys. J.* **1979**, *232*, 740−746.
(12) Yang, Y.; Li, Z.; Zhao, Y.; Wan, S.; Liu, H.; Huang, X.; Sun, C. Mechanism for the Formation of Benzene in the Titan's Atmosphere: A Theoretical Study on the Mechanism of Reaction. *Comput. Theor. Chem.* **2012**, *991*, 66−73.
(13) Field, F.; Franklin, J.; Lampe, F. Reactions of Gaseous Ions. II. Acetylene. *J. Am. Chem. Soc.* **1957**, *79*, 2665−2669.
(14) Ono, Y.; Ng, C. Y. A Study of the Unimolecular Decomposition of the $(C_2H_2)_2^+$Complex. *J. Chem. Phys.* **1982**, *77*, 2947−2955.
(15) Relph, R. A.; Bopp, J. C.; Roscioli, J. R.; Johnson, M. A. Structural Characterization of $(C_2H_2)_{1-6}^+$ Cluster Ions by Vibrational Predissociation Spectroscopy. *J. Chem. Phys.* **2009**, *131*, 114305.
(16) Momoh, P. O.; Hamid, A. M.; Abrash, S. A.; El-Shall, M. S. Structure and Hydration of the $C_4H_4^{\bullet+}$Ion Formed by Electron Impact Ionization of Acetylene Clusters. *J. Chem. Phys.* **2011**, *134*, 204315.
(17) Tsuji, M.; Ogawa, T.; Imasaka, T.; Nishimura, Y.; Ishibashi, N. Formation of Diacetylene Ion ($A^2\Pi_u$) by Controlled Electron Impact on Unsaturated Molecules. *Bull. Chem. Soc. Jpn.* **1976**, *49*, 53−57.
(18) Rudolph, P. S.; Melton, C. E. Mass Spectrometric Studies of Ionic Intermediates in the α-Particle Radiolysis of the C_2 Hydrocarbons. I. Acetylene. *J. Phys. Chem.* **1959**, *63*, 916−918.
(19) Koyano, I.; Tanaka, I.; Omura, I. Chemi - Ionization in Photoexcited Acetylene. *J. Chem. Phys.* **1964**, *40*, 2734−2735.
(20) Bloch, A. Mass Spectra of Acetylene Under High Pressure in the Ion Source. *Adv. Mass Spectrom.* **1963**, *2*, 48−50.
(21) Bera, P. P.; Peverati, R.; Head-Gordon, M.; Lee, T. J. Hydrocarbon Growth via Ion−Molecule Reactions: Computational Studies of the Isomers of $C_4H_2^+$, $C_6H_2^+$and $C_6H_4^+$ and Their Formation Paths from Acetylene and its Fragments. *Phys. Chem. Chem. Phys.* **2015**, *17*, 1859−1869.
(22) Yung, Y. L.; Allen, M.; Pinto, J. P. Photochemistry of the Atmosphere of Titan - Comparison Between Model and Observations. *Astrophys. J., Suppl. Ser.* **1984**, *55*, 465−506.
(23) Cernicharo, J.; Heras, A. M.; Tielens, A. G. G. M.; Pardo, J. R.; Herpin, F.; Guélin, M.; Waters, L. B. F. M. Infrared Space Observatory's Discovery of C_4H_2, C_6H_2, and Benzene in CRL 618. *Astrophys. J.* **2001**, *546*, L123.
(24) Banaszkiewicz, M.; Lara, L.; Rodrigo, R.; López-Moreno, J.; Molina-Cuberos, G. A Coupled Model of Titan's Atmosphere and Ionosphere. *Icarus* **2000**, *147*, 386−404.
(25) Fonfría, J. P.; Agúndez, M.; Cernicharo, J.; Richter, M. J.; Lacy, J. H. Carbon Chemistry in IRC+10216: Infrared Detection of Diacetylene. *Astrophys. J.* **2018**, *852*, 80.
(26) Krełowski, J.; Beletsky, Y.; Galazutdinov, G.; Kołos, R.; Gronowski, M.; LoCurto, G. Evidence for Diacetylene Cation as the Carrier of a Diffuse Interstellar Band. *Astrophys. J., Lett.* **2010**, *714*, L64.
(27) Maier, J.; Chakrabarty, S.; Mazzotti, F.; Rice, C.; Dietsche, R.; Walker, G.; Bohlender, D. Assignment of 5069 Å Diffuse Interstellar Band to HC_4H^+: Disagreement with Laboratory Absorption Band. *Astrophys. J., Lett.* **2011**, *729*, L20.
(28) Motylewski, T.; Linnartz, H.; Vaizert, O.; Maier, J. P.; Galazutdinov, G. A.; Musaev, F. A.; Krełowski, J.; Walker, G. A. H.; Bohlender, D. A. Gas-Phase Electronic Spectra of Carbon-Chain Radicals Compared with Diffuse Interstellar Band Observations. *Astrophys. J.* **2000**, *531*, 312.
(29) Salama, F.; Galazutdinov, G.; Krełowski, J.; Biennier, L.; Beletsky, Y.; Song, I.-O. Polycyclic Aromatic Hydrocarbons and the Diffuse Interstellar Bands: A Survey. *Astrophys. J.* **2011**, *728*, 154.
(30) Schüler, H.; Reinebeck, L. Über neue Spektren in der Glimmentladung mit Benzoldampf. *Z. Naturforsch., A: Phys. Sci.* **1951**, *6*, 160−165.
(31) Callomon, J. An Emission Spectrum of the Diacetylene Ion: a Study of Schüler's "T" Spectrum Under High Resolution. *Can. J. Phys.* **1956**, *34*, 1046−1074.
(32) Raghunandan, R.; Mazzotti, F. J.; Esmail, A. M.; Maier, J. P. Renner - Teller and Fermi Resonance Interactions for the ν_3= 1 and ν_7 = 2 Vibronic Levels in the $A^2\Pi_u$ and $X^2\Pi_g$ Electronic States of HC_4H^+. *J. Phys. Chem. A* **2011**, *115*, 9365−9369.
(33) Ghosh, A.; Reddy, S. N.; Reddy, S. R.; Mahapatra, S. Vibronic Coupling in the $\tilde{X}^2\Pi_g$−$\tilde{A}^2\Pi_u$ Band System of Diacetylene Radical Cation. *J. Phys. Chem. A* **2016**, *120*, 7881−7889.
(34) Ramos, C.; Winter, P. R.; Zwier, T. S.; Pratt, S. T. Photoelectron Spectroscopy via the $1^1\Delta_u$ State of Diacetylene. *J. Chem. Phys.* **2002**, *116*, 4011−4022.
(35) Jacovella, U.; Merkt, F. Spin-Orbit Interaction and Renner-Teller Effect in $HCCCCH^+$Studied by High-Resolution Photoelectron Spectroscopy. *Phys. Chem. Chem. Phys.* **2017**, *19*, 23524−23531.
(36) Schmidt, T. W.; Pino, T.; van Wijngaarden, J.; Tikhomirov, K.; Güthe, F.; Maier, J. P. Electronic Photodissociation Spectra of the Ar_n−$C_4H_2^+$ (n = 1−4) Weakly Bound Cationic Complexes. *J. Mol. Spectrosc.* **2003**, *222*, 86−92.
(37) Allan, M.; Kloster-Jensen, E.; Maier, J. P. Emission Spectra of the Radical Cations of Diacetylene ($\tilde{A}^2\Pi_u \rightarrow \tilde{X}^2\Pi_g$), Triacetylene ($\tilde{A}^2\Pi_g \rightarrow \tilde{X}^2\Pi_u$), and Tetraacetylene ($\tilde{A}^2\Pi_u \rightarrow \tilde{X}^2\Pi_g$, 0_0^0), and the Lifetimes of Some Vibronic Levels of the $\tilde{A}$ States. *Chem. Phys.* **1976**, *17*, 11−18.
(38) Bondybey, V.; English, J. Electronic Spectrum of the Diacetylene Radical Cation in Solid Rare Gases. *J. Chem. Phys.* **1979**, *71*, 777−782.
(39) Bally, T.; Tang, W.; Jungen, M. The Electronic Structure of the Radical Cations of Butadiene, Vinylacetylene and Diacetylene: Similarities and Differences. *Chem. Phys. Lett.* **1992**, *190*, 453−459.
(40) Baker, C.; Turner, D. W. Photoelectron Spectra of Acetylene, Diacetylene, and their Deutero-Derivatives. *Chem. Commun. (London)* **1967**, 797−799.
(41) Schwell, M.; Bénilan, Y.; Fray, N.; Gazeau, M.-C.; Es-Sebbar, E.; Gaie-Levrel, F.; Champion, N.; Leach, S. Ionization Photophysics and Rydberg Spectroscopy of Diacetylene. *Mol. Phys.* **2012**, *110*, 2843−2856.
(42) Fulara, J.; Grutter, M.; Maier, J. P. Higher Excited Electronic Transitions of Polyacetylene Cations $HC_{2n}H^+$ n = 2−7 in Neon Matrixes. *J. Phys. Chem. A* **2007**, *111*, 11831−11836.
(43) Riaplov, E.; Wyss, M.; Maier, J. P.; Hochlaf, M.; Rosmus, P. Electronic and Infrared Absorption Spectra of $NCCN^+$. *Int. J. Mass Spectrom.* **2003**, *223*, 107−114.
(44) Fulara, J.; Leutwyler, S.; Maier, J. P.; Spittel, U. Electronic Absorption Spectra of Cyanogen Cation ($N{\equiv}C\text{-}C{\equiv}N^+$), Cyanoacetylene Cation ($H\text{-}C{\equiv}C\text{-}C{\equiv}N^+$), and Methylcyanoacetylene Cation ($CH_3{}^-C{\equiv}C\text{-}C{\equiv}N^+$) in Neon Matrixes. *J. Phys. Chem.* **1985**, *89*, 3190−3193.
(45) Rice, C.; Rudnev, V.; Chakrabarty, S.; Maier, J. P. $D^2\Pi_u$, $C^2\Pi_u \leftarrow X^2\Pi_g$ Electronic Transitions of $NCCN^+$. *J. Phys. Chem. A* **2010**, *114*, 1684−1687.
(46) Freivogel, P.; Fulara, J.; Jakobi, M.; Forney, D.; Maier, J. P. Electronic Absorption Spectra of Linear Carbon Chains in Neon Matrices. II. C_{2n}^-, C_{2n}, and $C_{2n}H$. *J. Chem. Phys.* **1995**, *103*, 54−59.

DOI: 10.1021/acs.jpca.9b05996
J. Phys. Chem. A 2019, 123, 7228−7236

(47) Freivogel, P.; Grutter, M.; Forney, D.; Maier, J. P. Electronic Absorption Spectra of C_4^- and C_6^- Chains in Neon Matrices. *J. Chem. Phys.* **1997**, *107*, 22−27.
(48) Tulej, M.; Kirkwood, D. A.; Maccaferri, G.; Dopfer, O.; Maier, J. P. Electronic Spectra of Linear Carbon Anions. *Chem. Phys.* **1998**, *228*, 293−299.
(49) Wild, D. A.; Bieske, E. J. Infrared Investigations of Negatively Charged Complexes and Clusters. *Int. Rev. Phys. Chem.* **2003**, *22*, 129−151.
(50) Parrish, R. M.; Burns, L. A.; Smith, D. G. A.; Simmonett, A. C.; DePrince, A. E.; Hohenstein, E. G.; Bozkaya, U.; Sokolov, A. Y.; Remigio, R. D.; Richard, R: M.; et al. Psi4 1.1: An Open-Source Electronic Structure Program Emphasizing Automation, Advanced Libraries, and Interoperability. *J. Chem. Theory Comput.* **2017**, *13*, 3185−3197.
(51) Gronowski, M.; Kołos, R.; Krełowski, J. A Theoretical Study on Structure and Spectroscopy of Isomers. *Chem. Phys. Lett.* **2013**, *582*, 56−59.
(52) Lecoultre, J.; Maier, J. P.; Rösslein, M. Geometric Structure of Diacetylene Cation in the $\tilde{X}^2\Pi_g$and $\tilde{A}^2\Pi_u$ Electronic States. *J. Chem. Phys.* **1988**, *89*, 6081−6085.
(53) Komiha, N.; Rosmus, P.; Maier, J. P. Low Lying Quartet States in Diacetylene, Triacetylene and Benzene Radical Cations. *Mol. Phys.* **2007**, *105*, 893−897.
(54) Kuhn, R.; Maier, J. P.; Ochsner, M. Absolute Rotational Assignment of the Origin Band of the $A^2\Pi_u \leftarrow X^2\Pi_g$ Transition of the Diacetylene Cation. *Mol. Phys.* **1986**, *59*, 441−448.
(55) Zhang, J.; Guo, X.; Cao, Z. Electronic Spectra of the Linear Polyyne Cations $HC_{2n}H^+$ (n = 2−8): An Ab Initio Study. *J. Chem. Phys.* **2009**, *131*, 144307.
(56) Neese, F. The ORCA Program System. *Wiley Interdiscip. Rev. Comput. Mol.* **2012**, *2*, 73−78.
(57) Neese, F. Software Update: the ORCA Program System, Version 4.0. *Wiley Interdiscip. Rev. Comput. Mol.* **2018**, *8*, No. e1327.
(58) Dunning, T. H. Gaussian-Basis Sets for Use in Correlated Molecular Calculations. 1. The Atoms Boron Through Neon and Hydrogen. *J. Chem. Phys.* **1989**, *90*, 1007−1023.
(59) Frisch, M. J.; Trucks, G. W.; Schlegel, H. B.; Scuseria, G. E.; Robb, M. A.; Cheeseman, J. R.; Montgomery, J. A., Jr.; Vreven, T.; Kudin, K. N.; Burant, J. C.; Millam, J. M.; Iyengar, S. S.; Tomasi, J.; Barone, V.; Mennucci, B.; Cossi, M.; Scalmani, G.; Rega, N.; Petersson, G. A.; Nakatsuji, H.; Hada, M.; Ehara, M.; Toyota, K.; Fukuda, R.; Hasegawa, J.; Ishida, M.; Nakajima, T.; Honda, Y.; Kitao, O.; Nakai, H.; Klene, M.; Li, X.; Knox, J. E.; Hratchian, H. P.; Cross, J. B.; Bakken, V.; Adamo, C.; Jaramillo, J.; Gomperts, R.; Stratmann, R. E.; Yazyev, O.; Austin, A. J.; Cammi, R.; Pomelli, C.; Ochterski, J. W.; Ayala, P. Y.; Morokuma, K.; Voth, G. A.; Salvador, P.; Dannenberg, J. J.; Zakrzewski, V. G.; Dapprich, S.; Daniels, A. D.; Strain, M. C.; Farkas, O.; Malick, D. K.; Rabuck, A. D.; Raghavachari, K.; Foresman, J. B.; Ortiz, J. V.; Cui, Q.; Baboul, A. G.; Clifford, S.; Cioslowski, J.; Stefanov, B. B.; Liu, G.; Liashenko, A.; Piskorz, P.; Komaromi, I.; Martin, R. L.; Fox, D. J.; Keith, T.; Al-Laham, M. A.; Peng, C. Y.; Nanayakkara, A.; Challacombe, M.; Gill, P. M. W.; Johnson, B.; Chen, W.; Wong, M. W.; Gonzalez, C.; Pople, J. A. *Gaussian 09*, revision A.1; Gaussian, Inc.: Wallingford, CT, 2009.
(60) Chai, J.-D.; Head-Gordon, M. Long-Range Corrected Hybrid Density Functionals with Damped Atom-Atom Dispersion Corrections. *Phys. Chem. Chem. Phys.* **2008**, *10*, 6615−6620.
(61) Boys, S.; Bernardi, F. The Calculation of Small Molecular Interactions by the Differences of Separate Total Energies. Some Procedures with Reduced Errors. *Mol. Phys.* **1970**, *19*, 553−566.
(62) Botschwina, P.; Oswald, R. Complexes of an Argon Atom with Linear Cations: Results of Coupled Cluster Calculations. *J. Mol. Spectrosc.* **2003**, *222*, 46−56.
(63) Western, C. M. *PGOPHER*, version 10.1; University of Bristol: Cantock's Close, Bristol BS8 1TS: United Kingdom, 2018.
(64) Booze, J. A.; Baer, T. The Photoionization and Dissociation Dynamics of Energy-selected Acetylene Dimers, Trimers, and Tetramers. *J. Chem. Phys.* **1993**, *98*, 186−200.
(65) Boechat-Roberty, H. M.; Neves, R.; Pilling, S.; Lago, A. F.; De Souza, G. G. B. Dissociation of the Benzene Molecule by Ultraviolet and Soft X-Rays in Circumstellar Environment. *Mon. Not. R. Astron. Soc.* **2009**, *394*, 810−817.
(66) Jacovella, U.; Muller, G.; Catani, K. J.; Bartlett, N.; Bieske, E. J. Electronic Spectra of the Triacetylene Cation (HC_6H^+) and Protonated Triacetylene ($HC_6H_2^+$) Tagged with Ar. *Aust. J. Chem.* **2019**, *72*, 260−266.
(67) Hochlaf, M.; Baer, T.; Qian, X.-M.; Ng, C. Y. A Vacuum Ultraviolet Pulsed Field Ionization-Photoelectron Study of Cyanogen Cation in the Energy Range of 13.2−15.9 eV. *J. Chem. Phys.* **2005**, *123*, 144302.
(68) Zhao, Y.; de Beer, E.; Xu, C.; Taylor, T.; Neumark, D. M. Spectroscopy and Electron Detachment Dynamics of C_4^-, C_6^-, and C_8^-. *J. Chem. Phys.* **1996**, *105*, 4905−4919.
(69) Schäfer, M.; Grutter, M.; Fulara, J.; Forney, D.; Freivogel, P.; Maier, J. P. Emission Spectrum of Mass-Selected C_4^-: $C^2\Pi_u \rightarrow X^2\Pi_g$ in a Neon Matrix. *Chem. Phys. Lett.* **1996**, *260*, 406−408.
(70) Zhao, Y.; de Beer, E.; Neumark, D. M. Rotationally Resolved Spectrum of the $C^2\Pi_u \leftarrow X^2\Pi_g$ Electronic Transition of C_4^- via Resonant Two-Photon Detachment Spectroscopy. *J. Chem. Phys.* **1996**, *105*, 2575−2582.
(71) Schmatz, S.; Botschwina, P. Large-Scale Coupled Cluster Calculations for the Linear Carbon Anions C_3^-, C_4^-, $C_7^-$and.C_{10}^-. *Int. J. Mass Spectrom. Ion Processes* **1995**, *149*, 621−629.

DOI: 10.1021/acs.jpca.9b05996
J. Phys. Chem. A 2019, 123, 7228−7236

THE JOURNAL OF PHYSICAL CHEMISTRY A

pubs.acs.org/JPCA Article

Electronic Spectrum and Photodissociation Chemistry of the 1-Butyn-3-yl Cation, $H_3CCHCCH^+$

Giel Muller, Ugo Jacovella, Katherine J. Catani, Gabriel da Silva, and Evan J. Bieske*

Cite This: J. Phys. Chem. A 2020, 124, 2366−2371 Read Online

ACCESS | Metrics & More | Article Recommendations | Supporting Information

ABSTRACT: The $\tilde{B}^1A' \leftarrow \tilde{X}^1A'$ electronic spectra of the 1-butyn-3-yl cation ($H_3CCHCCH^+$) and the $H_3CCHCCH^+$-Ne and $H_3CCHCCH^+$-Ar complexes are measured using resonance enhanced photodissociation over the 245−285 nm range, with origin transitions occurring at 35936, 35930, and 35928 cm^{-1}, respectively. Vibronic bands are assigned based on quantum chemical calculations and comparison of the spectra with those of the related linear methyl propargyl ($H_3C_4H_2^+$) and propargyl ($H_2C_3H^+$) cations. The photofragment ions are $C_2H_3^+$ (major) and $C_4H_3^+$ (minor), with the preference for $C_2H_3^+$ consistent with master equation simulations for a mechanism that involves rapid electronic deactivation and dissociation on the ground state potential energy surface.

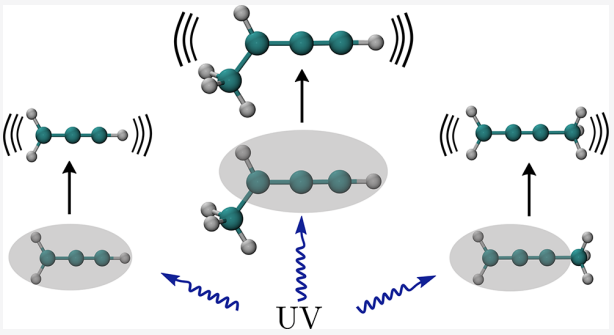

Downloaded via UNIV OF MELBOURNE on May 12, 2020 at 05:40:08 (UTC).
See https://pubs.acs.org/sharingguidelines for options on how to legitimately share published articles.

INTRODUCTION

Small carbocations are important in plasmas, combustion processes,[1,2] and extraterrestrial environments.[3−7] There is a growing body of spectroscopic data for small fundamental carbocations in the gas phase, including $C_4H_5^+$,[8−14] the subject of this paper. $C_4H_5^+$ cations have been detected in Titan's atmosphere using the ion neutral mass spectrometer[15] and are suspected to lead to formation of polycyclic aromatic hydrocarbons and tholins that populate the haze layers,[16−18] although it is unclear which isomers are present. Laboratory spectroscopic data of $C_4H_5^+$ isomers may facilitate their detection in remote environments. Photoelectron spectroscopy has provided information on two low energy $C_4H_5^+$ structures, the bent 1-butyn-3-yl ($H_3CCHCCH^+$) and linear 2-butyn-1-yl ($H_3C_4H_2^+$) cations (**BT** and **MP** in Figure 1),[12,14] with similar spacings between the lower electronic states of the respective cations.[19−21]

The $\tilde{B}^1A' \leftarrow \tilde{X}^1A_1$ electronic transition of the propargyl cation, $H_2C_3H^+$ (**P** in Figure 1), corresponding to the promotion of an electron from the second highest occupied molecular orbital (HOMO−1) to the lowest unoccupied molecular orbital (LUMO), was first measured over the 240−268 nm range using neon matrix isolation spectroscopy.[22] The measured spectrum was dominated by a strong progression spaced by 667 cm^{-1}, which was assigned to the CCH bending vibration, due to a supposed reduction in symmetry for **P** upon electronic excitation.[22] Later, the spectrum was recorded in the gas phase using resonance enhanced photodissociation (REPD) spectroscopy.[23] Accompanying calculations suggested the $\tilde{B}$ state retains C_{2v} symmetry and the progression was reassigned to the C−C symmetric stretching vibrational mode (ν_5).[23]

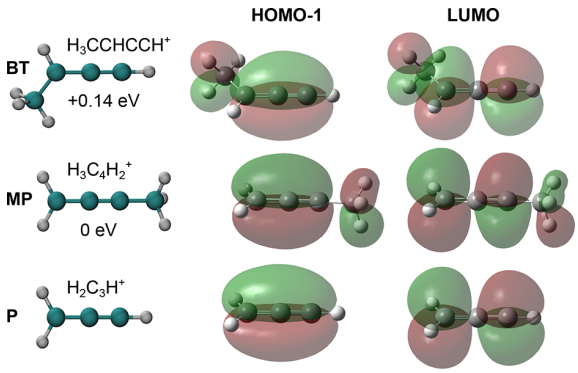

Figure 1. Structures of **BT** ($H_3CCHCCH^+$), **MP** ($H_3C_4H_2^+$), and **P** ($H_2C_3H^+$), calculated at the MP2/aug-cc-pVDZ level of theory. Energies of the $C_4H_5^+$ isomers are relative to that of **MP** and include single-point energies at the CCSD(T)/cc-pVTZ level using optimized geometries and vibrational zero-point corrections to energy predicted at the MP2/aug-cc-pVDZ level.

Received: December 21, 2019
Revised: February 25, 2020
Published: March 2, 2020

ACS Publications © 2020 American Chemical Society

On the basis of the calculated molecular orbitals shown in Figure 1, the HOMO−1 → LUMO electronic transitions should be similar for **P**, **MP**, and **BT**. In accordance with these expectations, the $\tilde{B}^1A' \leftarrow \tilde{X}^1A'$ electronic transitions of **MP** and **P** occur at similar wavelengths and exhibit comparable progressions in the C−C stretching vibration,[13] demonstrating that the on-axis methyl group has little influence on the propargyl chromophore.

In the current study, REPD spectra of $H_3CCHCCH^+$ and the $H_3CCHCCH^+$-Ne complex were measured to enable comparisons with the spectra of **P** and **MP** and to facilitate possible detection of $H_3CCHCCH^+$ ions in remote environments. Excitation of the $\tilde{B}^1A' \leftarrow \tilde{X}^1A'$ transition of **BT** generates $C_2H_3^+$ and $C_4H_3^+$ photofragments, as is the case for **MP**.[13] To understand the dissociation process and to predict the $C_2H_3^+/C_4H_3^+$ branching ratio, we model the fate of energized **BT** ions using master equation simulations, based on calculated stationary points on the $C_4H_5^+$ ground state potential energy surface. There have been several previous investigations of $C_4H_5^+$ dissociation. Photofragmentation at 193 nm of $C_4H_5^+$ generated from 2-hexyne mainly produced $C_2H_3^+$ photofragments.[24] Collision induced dissociation of $C_4H_5^+$, presumably the **MP** isomer, also gave nearly exclusively $C_2H_3^+$ fragments, with the dissociation proposed to proceed through a low energy cyclic isomer.[25] However, reactive $C^+ + C_3H_5$ collisions, which presumably involve $C_4H_5^+$ intermediates, were found to yield $C_4H_3^+$ products but not $C_2H_3^+$ products.[26] Recently, it was observed that excitation of the $\tilde{B}^1A' \leftarrow \tilde{X}^1A'$ transition of **MP** produced both $C_2H_3^+$ and $C_4H_3^+$ photofragments with a branching ratio of 5:1.[13] Master equation simulations based on a calculated ground state $C_4H_5^+$ potential energy surface suggested the $C_2H_3^+ + C_2H_2$ channel is accessed through a multistep process, whereas the $C_4H_3^+ + H_2$ fragments are formed through a more direct, albeit higher energy, process.[13] Although the calculations in ref 13 did not include the **BT** isomer, other calculations predict low energy barriers between **BT** and **MP**,[27] suggesting that both isomers should have similar dissociation mechanisms and play comparable roles in unimolecular reactions of $C_4H_5^+$.

METHODS

Experimental Section. REPD spectra of $H_3CCHCCH^+$ and $H_3CCHCCH^+$-Ne were recorded through laser excitation of ions in a tandem mass spectrometer. A brief overview of the experimental setup is provided below, while a more complete description is available in ref 28. $H_3CCHCCH^+$ and $H_3CCHCCH^+$-Ne ions were formed by seeding vapor of liquid 3-bromo-1-butyne (cooled to 0 °C) into a pulsed supersonic expansion of argon or neon gas (stagnation pressure ≈4 bar) that was bombarded by electrons. The target ions were then mass selected using a quadrupole mass filter and deflected 90° using an electrostatic quadrupole bender into an octupole ion guide where they were exposed to the output light from an optical parametric oscillator (OPO, EKSPLA NT342B). Resonant photoexcitation produced photofragments that were mass selected using a second quadrupole mass filter and detected by a microchannel plate. REPD spectra were obtained by monitoring the photofragment ion yield (normalized with respect to laser power) as a function of wavelength (calibrated using a wavemeter, Ångstrom LSA UVL).

Computational Details. The structure and energetics of **BT** and other relevant isomers, fragments, and transition states were characterized through quantum chemical calculations using the Gaussian 16 program.[29] The geometry, frequencies, and vibrational zero-point corrected energy for the electronic ground state of **BT** were calculated at the CCSD/cc-pVTZ level of theory. Vertical excitation energies and oscillator strengths were calculated at the EOM-CCSD/cc-pVTZ level. This level of theory was also used to estimate the equilibrium geometry, frequencies, and vibrational zero-point energy of **BT** in the excited state. Structural and energetic data for the $H_3CCHCCH^+$-Ne and $H_3CCHCCH^+$-Ar complexes are reported in the Supporting Information.

To explore the dissociation mechanism of **BT**, stationary points on the ground state $C_4H_5^+$ potential energy surface were calculated at the MP2/aug-cc-pVDZ level of theory, building on a previous study of **MP**.[13] Transition states and intermediates were located by scanning along internal coordinates. Intrinsic reaction coordinate (IRC) calculations were used to verify the transition states.[30] Energies of the stationary points were calculated at the CCSD(T)/cc-pVTZ level and include vibrational zero-point energy corrections at the MP2/aug-cc-pVDZ level. The structures, vibrational frequencies, and energies were used to carry out master equation simulations within the Multiwell program.[31−33] The modeling procedure follows that used in the earlier study of **MP**, where more details are provided.[13] Rigid-rotor-harmonic-oscillator approximations were used to describe molecular degrees of freedom based on MP2 frequencies and moments of inertia, with the Beyer−Swinehart−Stein−Rabinovitch[34] count method used to determine sums and densities of states. Rice−Ramsperger−Kassel−Marcus (RRKM) theory was used with CCSD(T) energies to obtain microscopic $k(E)$ values. Collisional energy transfer is modeled using a single-exponential down model, with average energy transferred in deactivating collisions (ΔE_{down}) set to 200 cm^{-1}, consistent with values derived for organic molecules colliding with Ar at room temperature.[35,36] Note the model is not sensitive to variations in ΔE_{down} given the nearly collisionless environment in the octupole region. For the master equation simulations, the ions were assumed to have a Boltzmann energy distribution corresponding to T = 30 K based on previous spectroscopic studies of other molecular ions generated by the source,[37,38] with an additional 4.63 eV of internal energy provided through the absorption of a 268 nm photon.

RESULTS

REPD Spectra. REPD spectra of **BT** over the 245−285 nm range, recorded by monitoring $C_2H_3^+$ and $C_4H_3^+$ photofragments, are shown in Figure 2a,b, respectively. The spectra recorded on the $C_2H_3^+$ ($+C_2H_2$) and $C_4H_3^+$ ($+H_2$) channels have the same structure and relative band intensities, although the $C_2H_3^+$ yield was ≈6 times the $C_4H_3^+$ yield across the spectrum. REPD spectra of $H_3CCHCCH^+$-Ne (Figure 2c) are similar to spectra of the bare molecule, whereas significantly broader bands are observed for $H_3CCHCCH^+$-Ar (see the Supporting Information).

The observed spectrum of **BT** is associated with the $\tilde{B}^1A' \leftarrow \tilde{X}^1A'$ transition, and occurs in the same spectral region as the corresponding spectra of **P** and **MP**. Its onset around 277 nm is consistent with the calculated adiabatic excitation wavelength of 278 nm (4.46 eV).

Band Assignments. Band positions and assignments for the $H_3CCHCCH^+$ and $H_3CCHCCH^+$-Ne spectra are provided in Table 1. The spectrum of **BT** is assigned through

https://dx.doi.org/10.1021/acs.jpca.9b11810
J. Phys. Chem. A 2020, 124, 2366−2371

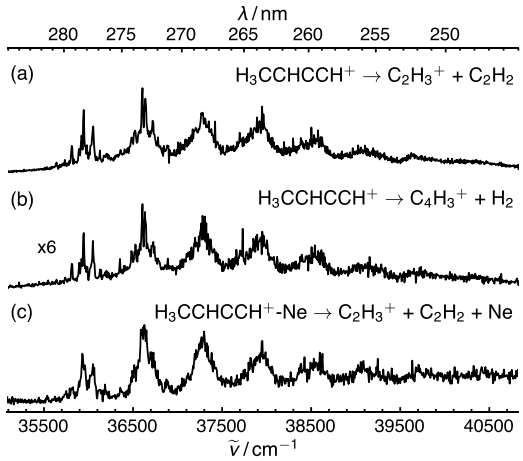

Figure 2. REPD spectra of $H_3CCHCCH^+$ (**BT**), obtained by monitoring (a) $C_2H_3^+$ and (b) $C_4H_3^+$ fragments over the 245−285 nm range. (c) REPD spectrum of $H_3CCHCCH^+$-Ne obtained by monitoring $C_2H_3^+$ fragments.

Table 1. Band Positions (cm^{-1}), Relative Band Positions ($\Delta\tilde{\nu}/cm^{-1}$), and Band Assignments for the $\tilde{B}^1A' \leftarrow \tilde{X}^1A'$ System of $H_3CCHCCH^+$ and $H_3CCHCCH^+$-Ne

	$H_3CCHCCH^+$		$H_3CCHCCH^+$-Ne	
assignment	$\tilde{\nu}$	$\Delta\tilde{\nu}$	$\tilde{\nu}$	$\Delta\tilde{\nu}$
14_1^0	35802	−134		
0_0^0	35936	0	35930	0
14_0^1	36039	103	36051	121
11_0^1	36596	660	36628	698
$11_0^1 14_0^1$	36718	782	36709	779
11_0^2	37270	1334	37298	1368
5_0^1	37721	1785		
11_0^3	37940	2004	37952	2022
11_0^4	38546	2610	38597	2667

comparisons with the previously reported spectra of **MP** and **P**.[13,23] For clarity, spectra of the three ions are displayed in Figure 3, with the origin transitions adjusted so that they coincide. Spectra of **BT**, **MP**, and **P** all feature a pronounced progression associated with the C−C symmetric stretch vibration. For **BT**, bands at 0_0^0 + 660, 1320, 1980, and 2640 cm^{-1} are assigned to this progression (11_0^1, 11_0^2, 11_0^3, and 11_0^4 transitions, respectively). The length of the progression, which extends for at least five quanta, is consistent with the predicted substantial elongation of the central C−C bond by 0.10 Å upon electronic excitation (see Figure 4). The calculated

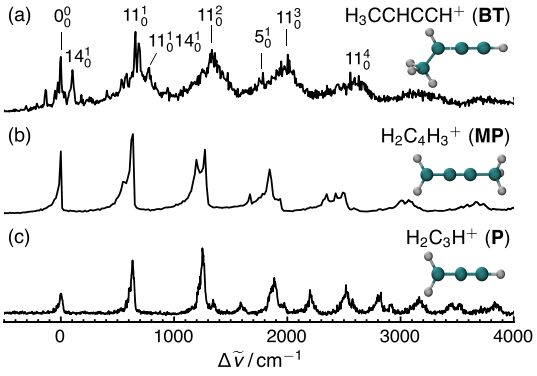

Figure 3. REPD spectra of (a) $H_3CCHCCH^+$ generated by averaging spectra shown in Figure 2a,b, (b) $H_3C_4H_2^+$ (reproduced from ref 13, with the permission of AIP publishing https://doi.org/10.1063/1.4974338), and (c) $H_2C_3H^+$-Ne (reproduced from ref 23, with the permission of AIP publishing http://dx.doi.org/10.1063/1.4935169). The origin transitions for the spectra have been set to coincide to facilitate comparison.

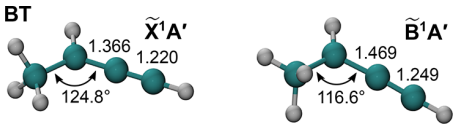

Figure 4. Equilibrium geometries of $H_3CCHCCH^+$ (**BT**) in the $\tilde{X}^1A'$ and $\tilde{B}^1A'$ states, calculated at the CCSD/cc-pVTZ and EOM-CCSD/cc-pVTZ levels of theory, respectively.

vibrational frequency for ν_{11} in the $\tilde{B}^1A'$ state, 776 cm^{-1}, matches the experimental progression spacing when scaled by 0.85, a value used to fit the corresponding progression in the **MP** spectrum. The low scaling factor necessary to reconcile the calculated and the observed excited state C−C frequency indicates that the EOM-CCSD/cc-pVTZ calculations overestimate the frequency, as also found for **P** and **MP**.[13,23] For **P**, much better agreement with experiment was found for calculations using the restricted active space self-consistent field (RASSCF) method with the cc-pVTZ basis set. The computational cost of the RASSCF/cc-pVTZ level calculations prevents a similar approach being used for the larger $C_4H_5^+$ systems (**MP** and **BT**).

Spectra of **BT**, **MP**, and **P** all exhibit a band with similar relative intensity between 0_0^0 + 1550 and 1800 cm^{-1} that arises from excitation of the C≡C stretching vibration (ν_5 for **BT**). The calculated ν_5 vibrational frequency for **BT** in the $\tilde{B}^1A'$ state (1810 cm^{-1}) agrees with the band's position (0_0^0 + 1785 cm^{-1}). The band's appreciable intensity is consistent with the predicted increase in the C≡C bond length by 0.03 Å from the ground state to the excited state (Figure 4). This assignment differs from the one advanced in an earlier study of **P**,[23] where the band (0_0^0 + 1585 cm^{-1}) was considered to be associated with the out-of-plane CH_2 wag. However, it is clear that the band is unlikely to arise from a wag because the position is not significantly affected by substituting a methyl group for an H atom.

The spectrum of **BT** displays closely spaced vibronic structure at 0_0^0 + 103 cm^{-1} and 0_0^0 − 134 cm^{-1} that is not present in the spectra of the other two ions (see Figure 3). Although their assignments are not clear, the bands may be due to transitions involving the lowest frequency a′ mode (ν_{14}), corresponding to bending of the C_4 skeleton. The band at 0_0^0 + 103 cm^{-1} can be tentatively assigned to 14_0^1 on the basis of the calculated ν_{14} vibrational frequency in the $\tilde{B}^1A'$ state (165 cm^{-1}). The band's appreciable intensity is consistent with the reduction in the Me−C−C bending angle from the ground to excited state (see Figure 4). The band at 0_0^0 − 134 cm^{-1} may be the 14_1^0 hot band, in-line with a calculated vibrational frequency of 195 cm^{-1} for ν_{14} in the ground state. Its assignment to a hot band is consistent with the band's reduced intensity in the $H_3CCHCCH^+$-Ne spectrum.

Effect of Methyl Substitution. The presence of an electron-donating methyl group influences the structure of the propargyl chromophore by stabilizing the charge on the carbon

https://dx.doi.org/10.1021/acs.jpca.9b11810
J. Phys. Chem. A 2020, 124, 2366−2371

to which it is attached and, therefore, depending upon its position, affects conjugation in the molecule. The structural changes can be assessed by comparing the calculated C—C bond lengths for **P**, **BT**, and **MP** (see Figure 5). The bond

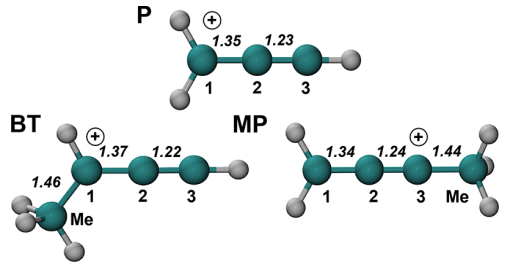

Figure 5. Ground state equilibrium structures of **P**, **BT**, and **MP**, calculated at the CCSD/cc-pVTZ level of theory. Bond lengths (Å) are shown in italic font.

lengths of **P** reflect its delocalized electronic structure between two resonance forms, $^{+}C_1—C_2{\equiv}C_3$ and $C_1{=}C_2{=}C_3^{+}$, with a preference for the former form.[39] Replacing an H atom on C_1 with a methyl group, to give **BT**, stabilizes the $^{+}C_1—C_2{\equiv}C_3$ form, consequently increasing the $C_1—C_2$ bond length. However, methyl substitution at the C_3 site, to give **MP**, stabilizes the allenyl-type ($C_1{=}C_2{=}C_3^{+}$) form, with an increase in the $C_2—C_3$ bond length. These effects may become apparent in higher resolution studies of these fundamental carbocations.

Photodissociation Dynamics. Photoexcitation of **BT** over the 245−285 nm range leads to the generation of $C_2H_3^{+}$ and $C_4H_3^{+}$ fragments. A $C_2H_3^{+}/C_4H_3^{+}$ branching ratio of ≈6:1 was measured while pumping the 11_0^2 transition at 268 nm (4.63 eV), similar to the branching ratio for **MP** (≈5:1) for the corresponding transition.[13] For both **MP** and **BT**, the branching ratio over the 230−280 nm range was independent of wavelength. Interestingly, for the $H_3CCHCCH^{+}$-Ne and $H_3CCHCCH^{+}$-Ar complexes, the only detected photofragments were $C_2H_3^{+}$ and $C_4H_3^{+}$, suggesting that an insignificant fraction of the complexes radiatively relax to the ground state, as these ions would only have sufficient energy to sever the weak intermolecular bond. Therefore, one can assume that nonradiative relaxation, presumably internal conversion, dominates.

We investigated ground state dissociation pathways assuming that dissociation follows internal conversion. A simplified version of the $C_4H_5^{+}$ potential energy surface is pictured in Figure 6 (see the Supporting Information for more details). The $\tilde{B}^1A'$ state (4.46 eV), accessed through the $\tilde{B}^1A' \leftarrow \tilde{X}^1A'$ transition (arrow), lies above the calculated dissociation thresholds for $C_2H_3^{+} + C_2H_2$ (1.93 eV) and $C_4H_3^{+} + H_2$ (2.74 eV). The most likely $C_4H_3^{+}$ fragment is the classical protonated diacetylene structure [**10**], which can be accessed through two $C_4H_3^{+} + H_2$ channels. The lowest energy channel is direct H_2 loss from **BT** through a 2.22 eV barrier [**20**]‡. Calculations suggest that **BT** may access the other $C_4H_3^{+} + H_2$ channel through a 1.29 eV interconversion barrier [**24**]‡. Following isomerization to **MP**, H_2 loss can occur through [**9a**]‡, lying 2.29 eV above **BT**. The similar energies of [**20**]‡ and [**9a**]‡ indicate that both $C_4H_3^{+} + H_2$ channels are accessible, with the [**9a**]‡ channel slightly more favorable. The $C_2H_3^{+} + C_2H_2$ channel, to form the nonclassical protonated acetylene ion and acetylene molecule [**8**], can also be reached

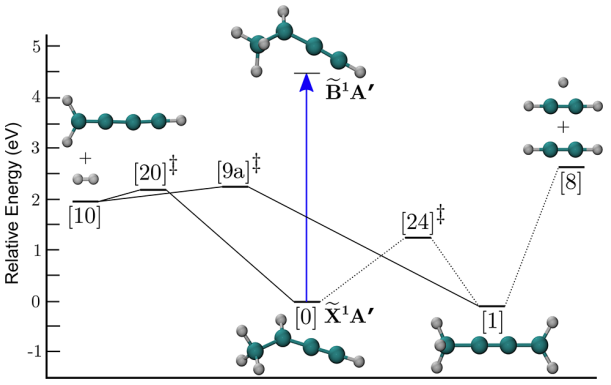

Figure 6. Simplified ground state potential energy surface of $C_4H_5^{+}$ from calculations at the MP2/aug-cc-pVDZ (geometries and zero-point energies) and CCSD(T)/cc-pVTZ (single-point energies) levels, with transition states represented by ‡ and dotted lines indicating multistep processes. Energies (zero point added to single point) are relative to the energy of **BT** in its $\tilde{X}^1A'$ state. The $\tilde{B}^1A'$ state energy corresponds to the experimental $\tilde{B}^1A' \leftarrow \tilde{X}^1A'$ origin transition (arrow). See the Supporting Information for details and a more complete potential energy surface.

through the initial isomerization step involving [**24**]‡, followed by several additional interconversions prior to dissociating.

The potential energy surface shown in Figure 6 was used for RRKM/master equation simulations to predict the $C_2H_3^{+}/C_4H_3^{+}$ branching ratio. Assuming a population of **BT** with a Maxwell−Bolzmann distribution of T = 30 K, and given 4.63 eV of internal energy, corresponding to absorption of a 268 nm photon, the model predicts a branching ratio of 1.4:1. Although the model overestimates the measured branching ratio, possibly due to inaccuracies in the calculated energies of points on the $C_4H_5^{+}$ potential energy surface, it correctly predicts the preference for the $C_2H_3^{+} + C_2H_2$ channel.

CONCLUSIONS

In summary, the $\tilde{B}^1A' \leftarrow \tilde{X}^1A'$ band system of $H_3CCHCCH^{+}$ has been recorded over the 245−285 nm range by monitoring $C_2H_3^{+}$ and $C_4H_3^{+}$ photofragments. Bands were assigned through comparison of the spectrum with those of $H_3C_4H_2^{+}$ and $H_2C_3H^{+}$ and with the aid of calculated vibrational frequencies. Extended progressions in the $H_3CCHCCH^{+}$ spectrum, with intervals of ≈660 cm^{-1}, are attributed to the C−C stretching vibration (ν_{11}). A weak band located around 1800 cm^{-1} above the origin transition is assigned to the 5_0^1 transition, corresponding to an excitation of the symmetric acetylenic (C≡C) stretching mode. Weak bands in the vicinity of the origin transition are tentatively assigned to transitions involving bending of the C_4 skeleton (ν_{14}), which corresponds to the lowest frequency vibrational mode. Minor differences in the calculated structures of $H_3CCHCCH^{+}$, $H_3C_4H_2^{+}$, and $H_2C_3H^{+}$ were rationalized through conjugative effects related to the location of the methyl group. Finally, the dissociation of $H_3CCHCCH^{+}$ was modeled using master equation simulations based on calculations of the ground state potential energy surface, correctly predicting the preferred generation of $C_2H_3^{+}$ photofragment ions.

https://dx.doi.org/10.1021/acs.jpca.9b11810
J. Phys. Chem. A 2020, 124, 2366−2371

■ ASSOCIATED CONTENT

Supporting Information

The Supporting Information is available free of charge at https://pubs.acs.org/doi/10.1021/acs.jpca.9b11810.

(a) Measured electronic spectra of $H_3CCHCCH^+$, $H_3CCHCCH^+$-Ne, and $H_3CCHCCH^+$-Ar; (b) calculated structures and harmonic vibrational frequencies for $H_3CCHCCH^+$, $H_3CCHCCH^+$-Ne, and $H_3CCHCCH^+$-Ar; (c) calculated structures and energies for $C_4H_5^+$ isomers, transition states, and fragments and stationary points and Cartesian coordinates (PDF)

■ AUTHOR INFORMATION

Corresponding Author

Evan J. Bieske − *School of Chemistry, The University of Melbourne, Melbourne, Victoria, Australia 3010;* orcid.org/0000-0003-1848-507X; Email: evanjb@unimelb.edu.au

Authors

Giel Muller − *School of Chemistry, The University of Melbourne, Melbourne, Victoria, Australia 3010;* orcid.org/0000-0003-1173-6825

Ugo Jacovella − *School of Chemistry, The University of Melbourne, Melbourne, Victoria, Australia 3010*

Katherine J. Catani − *School of Chemistry, The University of Melbourne, Melbourne, Victoria, Australia 3010;* orcid.org/0000-0003-1524-596X

Gabriel da Silva − *Department of Chemical Engineering, The University of Melbourne, Melbourne, Victoria, Australia 3010;* orcid.org/0000-0003-4284-4474

Complete contact information is available at: https://pubs.acs.org/10.1021/acs.jpca.9b11810

Notes

The authors declare no competing financial interest.

■ ACKNOWLEDGMENTS

This research was supported under the Australian Research Council's Discovery Project funding scheme (Project Numbers DP15010142 and DP160100474) as well as by Australian Government Research Training Program Scholarships. U. Jacovella acknowledges support from the Swiss National Science Foundation (P2EZP2_178429).

■ REFERENCES

(1) Hayhurst, A. N.; Jones, H. R. N. Ions and Soot in Flames. *J. Chem. Soc., Faraday Trans. 2* **1987**, *83*, 1−27.

(2) Chen, B.; Wang, H.; Wang, Z.; Han, J.; Alquaity, A. B.; Wang, H.; Hansen, N.; Sarathy, S. M. Ion Chemistry in Premixed Rich Methane Flames. *Combust. Flame* **2019**, *202*, 208−218.

(3) Bohme, D. K. PAH and Fullerene Ions and Ion/Molecule Reactions in Interstellar and Circumstellar Chemistry. *Chem. Rev.* **1992**, *92*, 1487−1508.

(4) McEwan, M. J.; Scott, G. B. I.; Adams, N. G.; Babcock, L. M.; Terzieva, R.; Herbst, E. New H and H_2 Reactions with Small Hydrocarbon Ions and Their Roles in Benzene Synthesis in Dense Interstellar Clouds. *Astrophys. J.* **1999**, *513*, 287−293.

(5) Wilson, E. H.; Atreya, S. K. Current State of Modeling the Photochemistry of Titan's Mutually Dependent Atmosphere and Ionosphere. *J. Geophys. Res.* **2004**, *109*. DOI: 10.1029/2003JE002181

(6) Anicich, V. G.; Wilson, P.; McEwan, M. J. A SIFT Ion−molecule Study of Some Reactions in Titan's Atmosphere. Reactions of N^+, N_2^+, and HCN^+ with CH_4, C_2H_2, and C_2H_4. *J. Am. Soc. Mass Spectrom.* **2004**, *15*, 1148−1155.

(7) Atreya, S. Titan's Organic Factory. *Science* **2007**, *316*, 843−845.

(8) Dopfer, O.; Roth, D.; Maier, J. P. Interaction of $C_3H_3^+$ Isomers with Molecular Nitrogen: IR Spectra of $C_3H_3^+$−$(N_2)_n$ Clusters (n = 1−6. *Int. J. Mass Spectrom.* **2002**, *218*, 281−297.

(9) Fulara, J.; Grutter, M.; Maier, J. P. Higher Excited Electronic Transitions of Polyacetylene Cations $HC_{2n}H^+$ *n* 2−7 in Neon Matrixes. *J. Phys. Chem. A* **2007**, *111*, 11831−11836.

(10) Douberly, G. E.; Ricks, A. M.; Ticknor, B. W.; McKee, W. C.; Schleyer, P. v. R.; Duncan, M. A. Infrared Photodissociation Spectroscopy of Protonated Acetylene and its Clusters. *J. Phys. Chem. A* **2008**, *112*, 1897−1906.

(11) Duncan, M. A. Infrared Laser Spectroscopy of Mass-Selected Carbocations. *J. Phys. Chem. A* **2012**, *116*, 11477−11491.

(12) Lang, M.; Holzmeier, F.; Hemberger, P.; Fischer, I. Threshold Photoelectron Spectra of Combustion Relevant C_4H_5 and C_4H_7 Isomers. *J. Phys. Chem. A* **2015**, *119*, 3995−4000.

(13) Catani, K. J.; Muller, G.; da Silva, G.; Bieske, E. J. Electronic Spectrum and Photodissociation Chemistry of the Linear Methyl Propargyl Cation $H_2C_4H_3^+$. *J. Chem. Phys.* **2017**, *146*, No. 044307.

(14) Hrodmarsson, H. R.; Loison, J.-C.; Jacovella, U.; Holland, D. M. P.; Boyé-Péronne, S.; Gans, B.; Garcia, G. A.; Nahon, L.; Pratt, S. T. Valence-Shell Photoionization of C_4H_5: The 2-Butyn-1-yl Radical. *J. Phys. Chem. A* **2019**, *123*, 1521−1528.

(15) Waite, J. H., Jr.; Young, D. T.; Cravens, T. E.; Coates, A. J.; Crary, F. J.; Magee, B.; Westlake, J. The Process of Tholin Formation in Titan's Upper Atmosphere. *Science* **2007**, *316*, 870−875.

(16) Vuitton, V.; Yelle, R.; McEwan, M. Ion Chemistry and N-containing Molecules in Titan's Upper Atmosphere. *Icarus* **2007**, *191*, 722−742.

(17) Vuitton, V.; Yelle, R.; Lavvas, P. Composition and Chemistry of Titan's Thermosphere and Ionosphere. *Philos. Trans. R. Soc., A* **2009**, *367*, 729−741.

(18) Li, A.; Jjunju, F. P. M.; Cooks, R. G. Nucleophilic Addition of Nitrogen to Aryl Cations: Mimicking Titan Chemistry. *J. Am. Soc. Mass Spectrom.* **2013**, *24*, 1745−1754.

(19) Minsek, D. W.; Chen, P. Photoelectron Spectrum of the Propargyl Radical in a Supersonic Beam. *J. Phys. Chem.* **1990**, *94*, 8399−8401.

(20) Gao, H.; Lu, Z.; Yang, L.; Zhou, J.; Ng, C. Y. Communication: A Vibrational Study of Propargyl Cation Using the Vacuum Ultraviolet Laser Velocity-Map Imaging Photoelectron Method. *J. Chem. Phys.* **2012**, *137*, 161101.

(21) Garcia, G. A.; Gans, B.; Krüger, J.; Holzmeier, F.; Röder, A.; Lopes, A.; Fittschen, C.; Alcaraz, C.; Loison, J.-C. Valence Shell Threshold Photoelectron Spectroscopy of C_3H_x (*x* = 0−3). *Phys. Chem. Chem. Phys.* **2018**, *20*, 8707−8718.

(22) Wyss, M.; Riaplov, E.; Maier, J. P. Electronic and Infrared Spectra of $H_2C_3H^+$ and Cyclic $C_3H_3^+$ in Neon Matrices. *J. Chem. Phys.* **2001**, *114*, 10355−10361.

(23) Catani, K. J.; Sanelli, J. A.; Dryza, V.; Gilka, N.; Taylor, P. R.; Bieske, E. J. Electronic Spectrum of the Propargyl Cation $H_2C_3H^+$ Tagged with Ne and N_2. *J. Chem. Phys.* **2015**, *143*, 184306.

(24) Beussman, D. J.; Erickson, T. A.; Enke, C. G. 193-nm Photodissociation of Ions from Saturated and Unsaturated Aliphatic Molecules. *J. Am. Soc. Mass Spectrom.* **1996**, *7*, 114−117.

(25) Lalli, P. M.; Corilo, Y. E.; Abdelnur, P. V.; Eberlin, M. N.; Laali, K. K. Intrinsic Acidity and Electrophilicity of Gaseous Propargyl/Allenyl Carbocations. *Org. Biomol. Chem.* **2010**, *8*, 2580−2585.

(26) Pei, L.; Farrar, J. M. A Velocity Map Imaging Study of Ion-Radical Chemistry: Charge Transfer and Carbon-Carbon Bond Formation in the Reactions of Allyl Radicals with C^+. *J. Phys. Chem. A* **2016**, *120*, 6122−6128.

(27) Cunje, A.; Rodriquez, C. F.; Lien, M. H.; Hopkinson, A. C. The $C_4H_5^+$ Potential Energy Surface. Structure, Relative Energies, and Enthalpies of Formation of Isomers of $C_4H_5^+$. *J. Org. Chem.* **1996**, *61*, 5212−5220.

(28) Bieske, E. J. Electronic Spectroscopy of Size-selected Ionic Complexes. *J. Chem. Soc., Faraday Trans.* **1995**, *91*, 1−12.
(29) Frisch, M. J.; Trucks, G. W.; Schlegel, H. B.; Scuseria, G.; Robb, M.; Cheeseman, J. R.; Scalmani, G.; Barone, V.; Petersson, G. A.; Nakatsuji, H.; et al. *Gaussian 16*, Revision B.01; Gaussian, Inc.: Wallingford, CT, 2016.
(30) Fukui, K. The Path of Chemical Reactions - the IRC Approach. *Acc. Chem. Res.* **1981**, *14*, 363−368.
(31) Barker, J. R. Multiple-well, Multiple-path Unimolecular Reaction Systems. I. MultiWell Computer Program Suite. *Int. J. Chem. Kinet.* **2001**, *33*, 232−245.
(32) Barker, J. R. Energy Transfer in Master Equation Simulations: A New Approach. *Int. J. Chem. Kinet.* **2009**, *41*, 748−763.
(33) *MultiWell-2013 Software*, 2013, designed and maintained by J. R. Barker with contributors N. F. Ortiz, J. M. Preses, L. L. Lohr, A. Maranzana, P. J. Stimac, T. L. Nguyen, and T. J. Dhilip Kumar, University of Michigan, Ann Arbor, MI. http://clasp-research.engin.umich.edu/multiwell/.
(34) Stein, S. E.; Rabinovitch, B. S. Accurate Evaluation of Internal Energy Level Sums and Densities Including Anharmonic Oscillators and Hindered Rotors. *J. Chem. Phys.* **1973**, *58*, 2438−2445.
(35) Hippler, H.; Troe, J.; Wendelken, H. J. Collisional Deactivation of Vibrationally Highly Excited Polyatomic Molecules. II. Direct Observations for Excited Toluene. *J. Chem. Phys.* **1983**, *78*, 6709−6717.
(36) Lam, A. K.; Li, C.; Khairallah, G.; Kirk, B. B.; Blanksby, S. J.; Trevitt, A. J.; Wille, U.; O'Hair, R. A.; da Silva, G. Gas-phase Reactions of Aryl Radicals with 2-Butyne: Experimental and Theoretical Investigation Employing the N-Methyl-pyridinium-4-yl Radical Cation. *Phys. Chem. Chem. Phys.* **2012**, *14*, 2417−2426.
(37) Dryza, V.; Sanelli, J. A.; Robertson, E. G.; Bieske, E. J. Electronic Spectra of Gas-Phase Polycyclic Aromatic Nitrogen Heterocycle Cations: Isoquinoline$^+$ and Quinoline$^+$. *J. Phys. Chem. A* **2012**, *116*, 4323−4329.
(38) Poad, B. L. J.; Wearne, P. J.; Bieske, E. J.; Buchachenko, A. A.; Bennett, D. I. G.; Kłos, J.; Alexander, M. H. The Na^+−H_2 Cation Complex: Rotationally Resolved Infrared Spectrum, Potential Energy Surface, and Rovibrational Calculations. *J. Chem. Phys.* **2008**, *129*, 184306−8.
(39) Apeloig, Y.; Müller, T. In *Dicoordinated Carbocations*; Rappoport, Z., Stang, P., Eds.; Wiley: Chichester, 1997; Chapter 5.

https://dx.doi.org/10.1021/acs.jpca.9b11810
J. Phys. Chem. A 2020, 124, 2366−2371